NASA CR-72489

MICROFOG LUBRICANT APPLICATION SYSTEM FOR ADVANCED TURBINE ENGINE COMPONENTS

by

J. Shim and S. J. Leonardi

prepared for

NATIONAL AERONAUTICS AND SPACE ADMINISTRATION

CONTRACT NO. NAS 3 – 9400

MOBIL RESEARCH AND DEVELOPMENT CORPORATION
RESEARCH DEPARTMENT

Requests for copies of this report should be referred to:

National Aeronautics and Space Administration
Office of Scientific and Technical Information
Attention: AFSS-A
Washington, D. C. 20546

NASA CR-72489

MICROFOG LUBRICANT APPLICATION SYSTEM FOR ADVANCED TURBINE ENGINE COMPONENTS

FINAL REPORT - DETERMINATION OF THE VELOCITIES, PARTICLE SIZE DISTRIBUTIONS, AND WETTABILITIES OF MICROFOG STREAMS OF VARIOUS LUBRICANTS

by

J. Shim and S. J. Leonardi

Prepared for

NATIONAL AERONAUTICS AND SPACE ADMINISTRATION

September 30, 1968

CONTRACT NAS 3-9400

Project Management
NASA Lewis Research Center
Cleveland, Ohio
Fluid System Components Division
Dennis P. Townsend, Project Manager
William R. Loomis, Research Advisor

MOBIL RESEARCH AND DEVELOPMENT CORPORATION
Paulsboro, N. J.

FINAL REPORT

MICROFOG LUBRICANT APPLICATION SYSTEM FOR ADVANCED TURBINE ENGINE COMPONENTS

by

J. Shim and S. J. Leonardi

ABSTRACT

A test apparatus providing a range of conditions such as might be encountered in a "once-through" microfog lubrication system for the bearings of high speed aircraft, has been employed to determine the velocities, particle size distributions, and wettabilities of microfog streams of various lubricants.

Wettabilities are related to size, concentration, and velocity of the microfog particles, temperature of the wetted surface, ambient conditions, geometric considerations, and properties of the lubricants.

Table of Contents

Table of Contents (Continued)

Table of Contents (Continued)

Table of Contents (Continued)

Table of Contents (Continued)

Page

Figures (Cont'd)

Table of Contents (Continued)

Page

Figures (Cont'd)

Table of Contents (Continued)

Page

Figures (Cont'd)

I. INTRODUCTION

Lubricants as microfogs* have been employed in industrial lubrication for many years. Typical applications are the lubrication of air-operated devices and machine components such as bearings, gears, cylinders, etc. More recently, microfog lubrication has received consideration for potential use in the engine or accessory bearings of advanced aircraft, where space and weight considerations demand optimized efficiency of the lubrication system.

Although the fundamental mechanisms of atomization and collection of aerosol particles on bodies have been considered both experimentally and theoretically by a number of investigators (1, 3, 15, 20, 21, 22), these investigations, in most cases, have been restricted to simplified or narrow ranges of conditions and were directed toward different areas of application. Early work (5) has attempted to establish the wetting characteristic curve of cetane by impinging microfog upon a surface of foil. However, these experimental data are limited and relatively meager.

In order to advance the efficiency of microfog lubrication beyond the limits of existing technology, a basic knowledge of the general behavior of microfog, particularly its wetting characteristics, in terms of oil properties, microfog particle-size distribution, concentration, velocity, system geometry, and desired ambient conditions, is essential.

The purpose of the present work is, therefore, to determine the wetting characteristics of five potential high temperature lubricants on a heated metal plate as a function of system variables. The Statement of Work for this contract is attached hereto as Appendix A.

This report is the final (Task II and III) report submitted under contract NAS3-9400, "Microfog Lubricant Application System for Advanced Turbine Engine Components." The first phase of this effort (Task I) was previously reported (21) and covered the theory, equipment, and experimented approached to principal variables.

---

*Dispersion aerosols with oil particles will be called microfogs, regardless of particle size.

II. SUMMARY AND CONCLUSIONS

The wetting characteristics of five potential high temperature lubricants - XRM 177 F, Hercolube F, Sunthetic 18H (B), Ucon 50-HB-5100, and Turbo Oil 4040, in terms of oil/gas mass flow ratio, particle velocity, and particle size distribution, were determined under a variety of test conditions. Most of this work, except as otherwise indicated, was conducted at 45 psi in an inert atmosphere of nitrogen, which was employed as the atomizing and carrier gas.

A. Rate of Oil Output

The rates of oil output for the present microfog generator were determined for the five test oils at different gas flow rates. In addition to these oils at 200°F, the rates for XRM 177 F at 100 and 280°F were also determined. Rates of oil output were found to increase with decreasing kinematic viscosity of the oils and with increasing gas flow rate. These results can be expressed by an empirical relation:

$$W = 0.8\, Q_G^{1.7} \left(\frac{\mu}{\rho}\right)_L^{-0.4}$$

This relation gives agreement with the experimentally determined data within ± 10 percent. These and all other symbols used in subsequent equations are described in the Notation Section (IV).

B. Particle Velocity Distribution

Determinations of the axial distribution of microfog particle velocity in a diffusing jet, using a high speed photographic technique, were made with five different spray nozzles at gas flow rates of 2, 3, 4, 5, and 6 cfm (at 45 psig and 200°F). Gas stream velocities were also calculated by measuring the pressure drops across the spray nozzles, and assuming the expansion of gas through the nozzles to be an adiabatic process.

Comparisons between the experimental particle velocities and the calculated gas stream velocities indicate a substantially good agreement within the experimental errors, suggesting that the relative velocity between gas and particles is nearly zero. Hence, the microfog particles within the size and concentration ranges studied appear to be completely suspended in the gas stream near the spray nozzle. The limitations of both the theoretical calculations of axial velocity distribution and the high speed photographic technique are briefly reviewed.

The spray pattern and expansion angle are discussed in relation to inlet pressure. Observations on the spray angle suggest that when a converging nozzle is used, the expansion angle of a microfog spray increases with increasing inlet pressure.

C. Particle Size Distribution

Particle size distributions of the test oils were determined under various conditions in order to investigate the atomizing and reclassifying characteristics of the present experimental apparatus - specifically, the microfog generator and spray nozzles.

The particle size distributions generated by several atomizing nozzles tested were discussed in terms of various factors suggested by the well-known particle size correlation. For the commercially available generator such as the one used in this study, in addition to dynamic force of the atomizing gas, gas/oil mass flow ratio, and liquid properties, the aerodynamics of microfog flow within the generator after atomization and the design of the size-selecting impactor and supporting screen seem to play a very important role in controlling the size distribution of microfog particles.

Particle size frequency distribution curves on a number basis, in most cases, have a bi-modal distribution. This behavior, which has not been reported by others, is believed to be a reflection of either differences in generator design or coagulation of small particles, or both.

Experimental "reclassifying" nozzles of different sizes and configurations were designed and developed. These nozzles produced relatively large particles (11 μm or larger) not by coalescence, but by a mechanism whereby the particles are wetted out within the nozzles and the resulting liquid film is reatomized by the gas passing through the nozzle. Among the experimental nozzles developed, a novel type consisting of one or more layers of mistermesh, knitted wire mesh made of fine wire, plastic, or fibrous material, was particularly successful in regenerating extremely large particles (40 μm or larger).

Particle size distribution data on a number basis, determined by the present light-scattering particle counter, were sufficiently accurate for meaningful comparison. However, because of a large dilution factor required to introduce particles singly into the illuminated volume and the limited range of the counter, the particle counter could not provide information of sufficient accuracy to be translated into mass of microfog particles. Mass determinations of limited systems were, therefore, made by a cascade impactor technique.

D. Wetting Rate Determinations

Prior to a series of wetting rate studies, the optimum spray distance was determined to be 1/2". However, a spray distance of 1" was used for this study to facilitate photographic analysis. An empirical equation relating wetting rate to spray distance is given by

$$\text{Wetting Rate} = \Psi_o\left(\frac{1}{X}\right)$$

The wetting characteristics of the five test oils at 600, 700, and 800°F were investigated under a variety of test conditions. Wetting rates obtained with nozzles of different sizes and configurations vary considerably for a given operating condition. For a given spray nozzle, the rates increase with increasing oil/gas mass flow ratios established by varying gas flow rate to the microfog generator. Furthermore, for a given oil/gas mass flow and particle size distribution, increasing particle velocity by means of a nozzle greatly increases wetting rate, while relatively small increases in particle size indicate considerable improvements on the rates for a given oil/gas mass flow and particale velocity.

Wetting rate increases as plate temperature increases, but changes little with increasing plate temperature at low mass flow ratio. When impinging on a hot surface at sufficiently high oil/gas mass flow ratio, microfog particles seem to wet the surface, regardless of its temperature within the range studied.

The wettabilities of the test oils were compared in terms of the specific and minimum wetting rates listed in the following table:

Test Oil	Specific Wetting Rate* [cm^2/sec/(oil/gas) mass ratio] x 10^4	Minimum Wetting Rate* [(oil/gas) mass flow ratio] x 10^3
XRM 177 F	1.4	1.5
Hercolube F	0.9	4.7
Sunthetic 18H(B)	0.6	1.1
Ucon 50-HB-5100	0.4	0.8
Turbo Oil 4040	-0.4	16.1

*Test Conditions used: No. 1 nozzle and at 600°F.

On the basis of the minimum oil and gas flow concept, XRM 177 F as microfog, in general, possesses the best wettability under the present testing conditions.

A limited wetting study of XRM 177 F at 600°F, using air instead of nitrogen gas, indicates that the surface oxide formation and oil degradation products, to the extent that they occur under the test conditions, have little influence on wetting rate.

The mean surface velocity and thickness of thin oil films were estimated from the wetting rate data of XRM 177 F at 600°F. These estimated values vary from 0.1 to 2.8 cm/sec for the mean surface velocities and from 4 to 23 um for the film thickness.

One of the most important observations of this study is the occurrence of different wetting patterns of oil on a heated solid surface. These are broadly classified as continuous film flow, and streaky, discontinuous film flow. The typical sequential wetting patterns for thin oil films of both types are illustrated. The flow patterns of the test oils at three different temperatures are summarized as follows:

Test Oil	Flow Pattern of Thin Oil Film		
	600°F	700°F	800°F
XRM 177 F	C	C	S*
Hercolube F	S*	S	S
Sunthetic 18H(B)	C	C	S
Ucon 50-HB-5100	C	S*	S
Turbo Oil 4040	S	S	S

C: continuous, S: streaky, S*: streaky but continuous at high oil/gas mass flow ratio.

In relation to these flow patterns of thin oil films, the criterion and possible mechanism for the breakdown of thin oil films flowing over a heated solid surface are briefly discussed, and the strong dependence of viscosity, surface tension, and particularly contact angle on the minimum wetting rate and critical film thickness is cited.

III. DETAILED REPORT

A. Materials

The five potential high temperature lubricants tested were:

1. 4040 Turbo Oil, Humble Oil and Refining Co.
2. Ucon 50-HB-5100 fluid, Union Carbide Corp.
3. Sunthetic 18H (Bottoms) fluid, Sun Oil Co.
4. XRM 177 F fluid, Mobil Research and Development Corp.
5. Hercolube F fluid, Hercules Powder Co.

These oils are identified broadly by chemical type in Table 1, which also lists other pertinent physical properties for each oil. Viscosity-temperature curves for these oils appear in Figure 1, and vapor pressure-temperature curves in Figure 2.

The test specimen was a flat plate 2" x 2" x 1/4" made of hardened CVM WB-49 material and finished circumferentially ground to 4 to 8 μ in. RMS. A plate with a freshly ground surface was used for each run.

Nitrogen gas employed in this work was "purified grade," stated by the supplier (the Airco Industrial Gases Division of the Air Reduction Co.) to have a minimum purity of 99.98 mole percent, with a maximum of 10 ppm oxygen.

B. Experimental Apparatus and Procedure

The test apparatus used in this work consists of a de-aeration chamber (B), a microfog generator (C), a thermostated vacuum-pressure chamber for wetting rate studies (E), a similar chamber for particle velocity and particle size distributions (F), and a particle counter (G). An over-all view of the apparatus is shown in Figure 3, while the control panel and electronic counter appear in Figure 4. Descriptions of each major component of the apparatus were included in detail elsewhere (21). A schematic flow diagram of the apparatus is shown in Figure 5.

1. Rate of Oil Output

The rate of oil output was determined by measuring the rate of change of the oil level in a calibrated sight glass attached to the oil reservoir, after running the generator for a sufficient time to establish equilibrium in oil flow within the generator. The rates were graphically obtained from the linear portions of the change of oil level-time curves.

Table 1

Physical Properties of Test Oils

	XRM 177 F	Ucon 50-HB-5100	Hercolube F	Esso Turbo Oil-4040	Sunthetic 18H Bottoms
Chemical Type	Synthetic nonaromatic hydrocarbon containing antiwear additive	Polyglycol ether, unformulated	Dipentaerythritol ester, unformulated	Dibasic acid ester, formulated	Synthetic nonaromatic hydrocarbon, unformulated
Flash Point, °F	510	475	540	430	540
Fire Point, °F	595	545	600	470	585
Pour Point, °F	<-35	<-35	<-35	<-35	<-35
Autogenous Ignition Point, °F (ASTM D 2155, 3 Determinations)	770 745 740	700 715 750	780 850 780	740 740 730	750 750 770
Kinematic Viscosity, cs					
@ 400°F	5.87	38.39	1.96	1.03	15.29
@ 210°F	39.66	181.10	8.86	3.18	122.30
@ 100°F	444.10	1,135.0	58.07	12.05	1,411.0
@ 0°F	38,366.0	68,392.0	2,252.0	194.3	>99,000
@ -20°F	>99,000	>99,000	7,550.9	483.0	>99,000
Neutralization Number	0.05	0.0	0.03	0.21	0.0
Density @ 20°C, g/cm^3	0.8480	1.0563	1.0085	0.9266	0.8450
Surface Tension @ 25°C, dynes/cm	31.0	36.9	30.1	30.1	29.7
Specific Heat, cal/g-°C					
@ 200°F	0.579	0.492	0.496	0.527	0.584
@ 400°F	0.636	0.545	0.534	0.596	0.647

Figure 1

VISCOSITY-TEMPERATURE RELATION FOR TEST LUBRICANTS

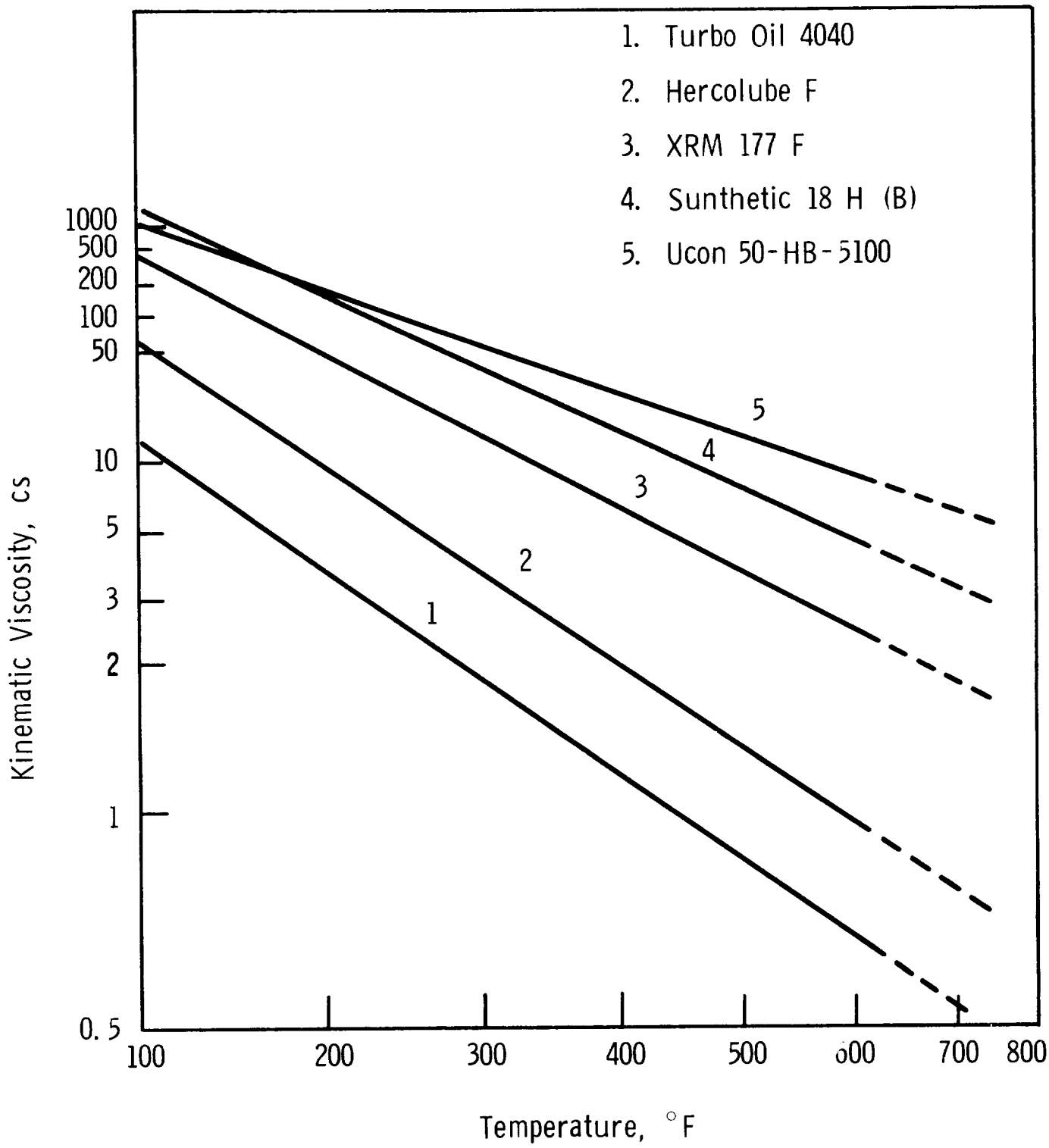

FIGURE 2

VAPOR PRESSURE VERSUS TEMPERATURE

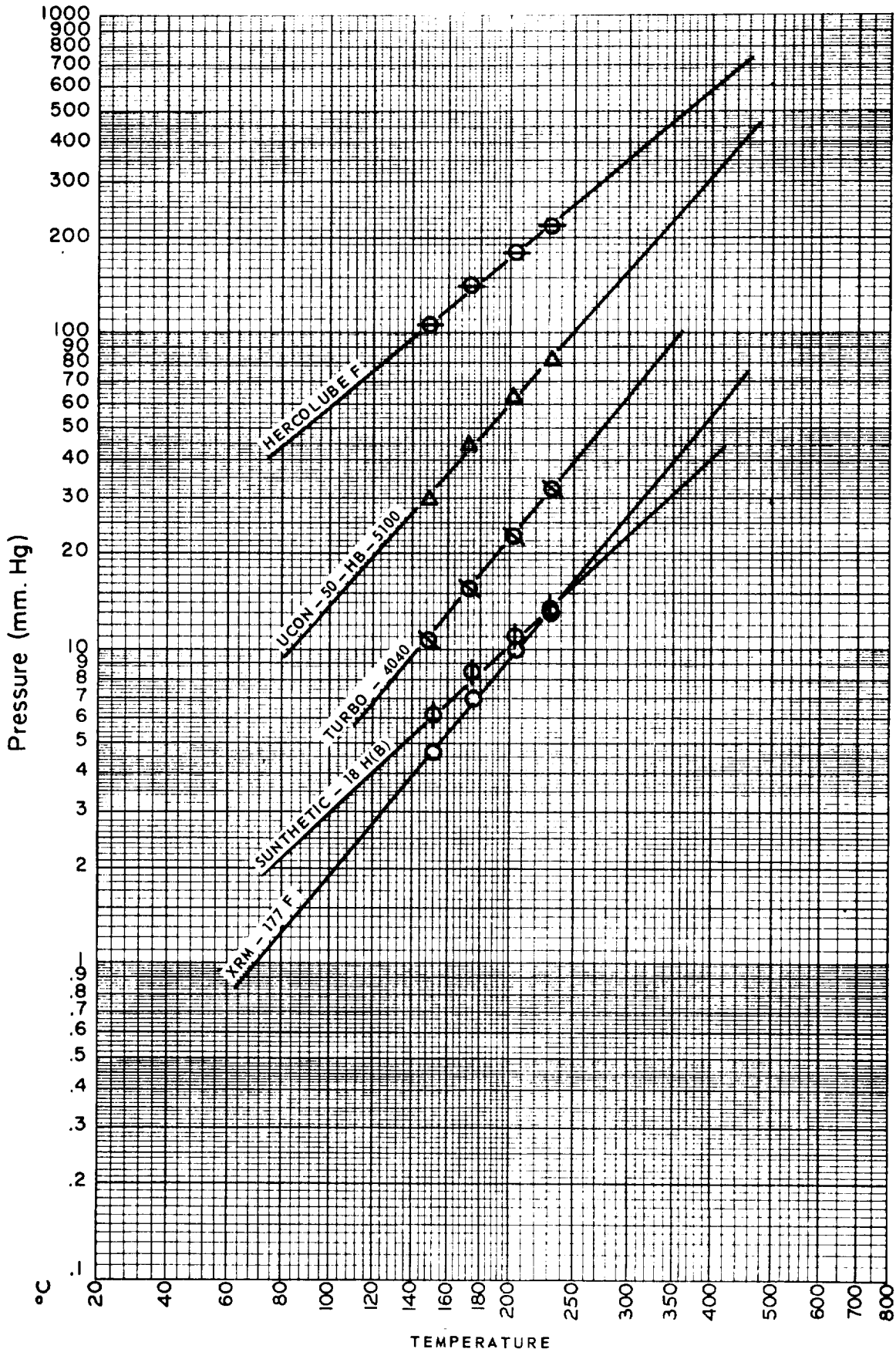

Figure 3

OVERALL VIEW OF EXPERIMENTAL APPARATUS

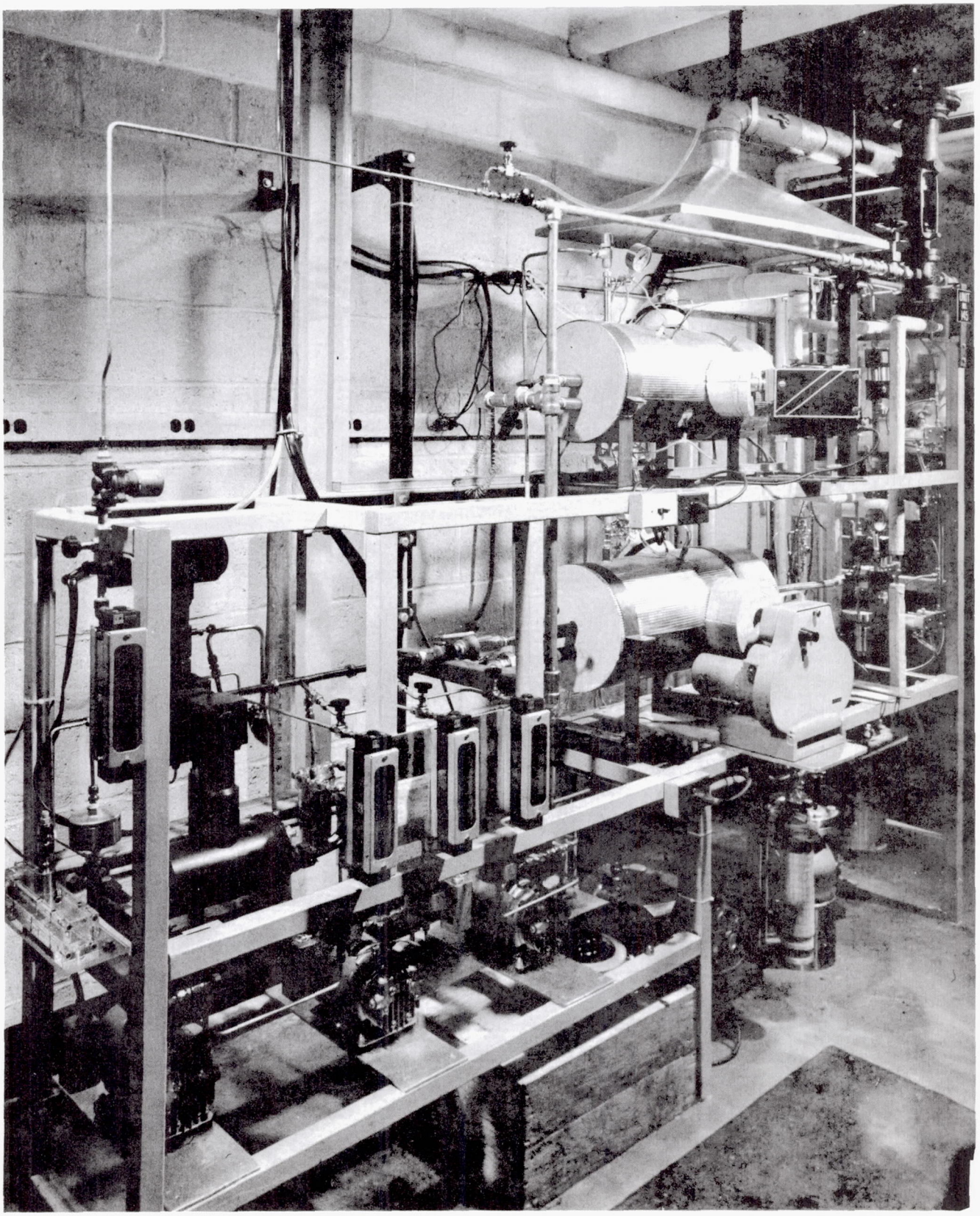

Figure 4

CONTROL CONSOLE AND ELECTRONIC COUNTER

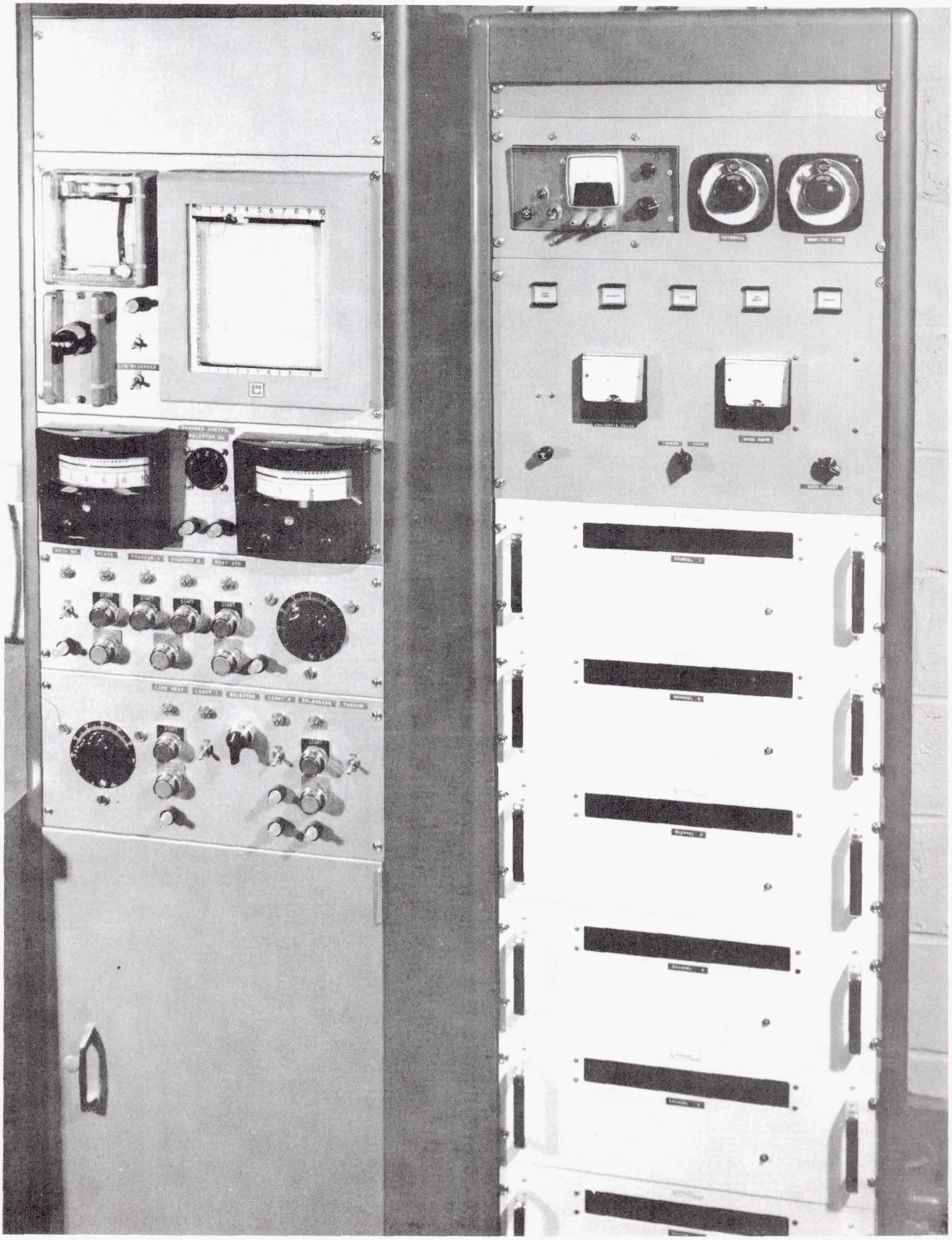

Figure 5

FLOW DIAGRAM OF EXPERIMENTAL APPARATUS

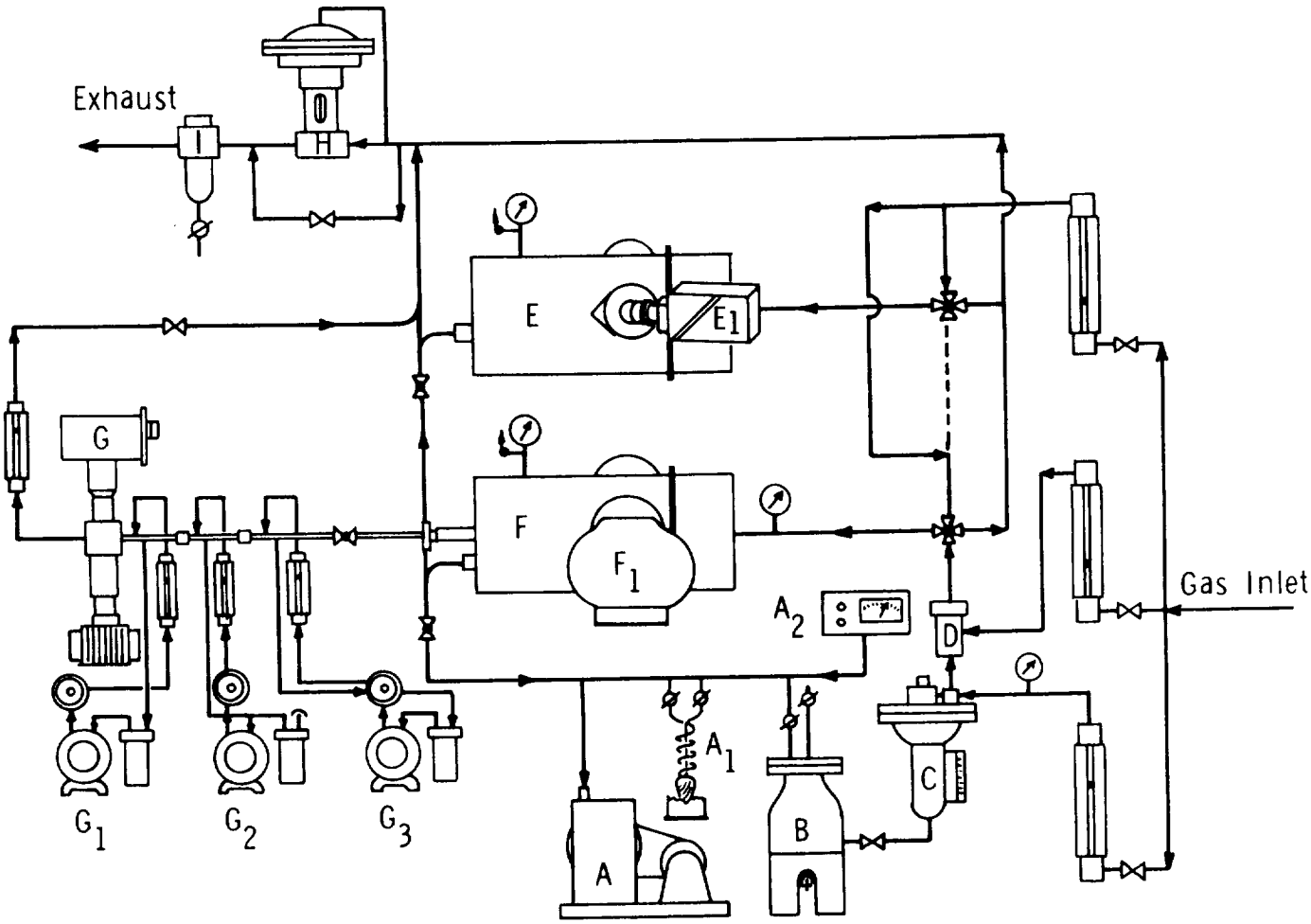

2. Particle Velocity Distribution

Average axial velocities of the microfog particles discharged from the different spray nozzles under the various gas flow rates to the microfog generator were determined in the test chamber (F), by photographing the movement of a microfog wave front propagated from the wetted tip of spray nozzle, with a Hycam high speed motion picture camera (F_1) operating at framing speeds between 8,600 and 9,400 frames per second (fps). To determine the exact film frequency throughout each test run, the camera is equipped with an input jack from a signal generator registering from 1 to 1,000 timing marks per second on the film edge.

The light source for the high speed photography was comprised of four G.E. 650 watt DVY lamps in a single reflector. Orientations of the light and camera were detailed in the Task I report (21).

To begin a typical series of particle velocity measurements, heat the microfog generator and nitrogen gas to the desired operating temperature, and now isolate the test chamber (F) from test chamber (E) and particle counter (G) by use of the appropriate valves shown in Figure 5. After focusing the camera to the nozzle axis, load the camera with 400 ft. of high speed photographic film (16 mm black and white, Eastman Kodak 4X, Negative Film Type 7224); then set to maximum film speed. After installing the spray nozzle inside the chamber, introduce nitrogen gas to the chamber via the 4-way fast acting directional valve, which is pneumatically operated and electrically controlled, raising the chamber pressure to 45 psig as regulated by diaphragm valve (H). Adjust the nitrogen gas flow to 2 cfm, and then start the microfog generator at the desired gas flow rate, with the microfog stream by-passing the test chamber and exhausting directly at 45 psig through the diaphragm valve by way of the directional valve.

As soon as the operation of the microfog comes to a steady state as indicated by the appearance of oil in exhaust trap (I), illuminate the test chamber; then activate a solenoid valve, setting the camera in operation and simultaneously delivering an electrical signal to a relay switch, which after a two-second delay, reverses the 4-way directional valve. This sends the microfog stream from the generator through the test chamber, while diverting the nitrogen stream directly to the exhaust line. Starting the camera two seconds in advance allows it to accelerate to maximum film speed before the microfog stream is introduced to the test chamber. The total camera run with a 400 foot film roll is approximately 2.6 seconds. At the end of the camera run, deactivate the solenoid controlling the 4-way valve, switching the microfog stream to the exhaust line, and open the by-pass around the diaphragm valve to exhaust the system pressure. After

purging the test chamber with nitrogen and cleaning the transport line, the apparatus is ready for the next run.

3. Particle Size Distribution

Particle size measurements were conducted by two different techniques: (1) a light scattering method, and (2) a cascade impaction technique.

Light Scattering Technique

The right-angle single-particle light scattering particle counter was constructed by the Mobil Research and Development Corporation with the cooperation of the Illinois Institute of Technology Research Institute. A series of particle counters of this type has been described by O'Konski, et al. (19) and by Fisher, et al. (6). In principle, the optical arrangement is that of Figure 6. The essential features of the technique include introduction of a sample flow through an intensively illuminated zone viewed by a photo-multiplier which picks up the scattered light from an individual particle, sorting of the electrical signal by a pulse height analyzer, and delivery of the signal to an electronic scaler counter (Nonafast Inc.) which is capable of operating in the size ranges covering from 0.5 to 32 μm with the increment of each channel at a constant factor of $\sqrt{2}$. Systems for collection, dilution, and delivery of the microfog sample to the particle counter were previously described (21).

Determinations of particle size distribution by the particle counter entail use of the lower test chamber (E). The procedure of introducing the microfog stream into the test chamber is identical to that of particle velocity measurement except that a microfog sample is allowed to flow through the particle counter via a two-stage diluter, confining the flow to a laminar region.

For a typical series of tests, calibrate the particle counter by adjusting the voltage-input to the system for maximum sensitivity; evacuate and then purge the test chamber to ensure freedom from stray particles. As soon as the particle counter reaches a thermal equilibrium, open the appropriate valve, allowing the nitrogen stream from the test chamber to flow through the two-stage diluter, gas-sheath system, and illuminated sensing zone, and finally to the exhaust line. After opening the chamber to the particle counter section, adjust the gas flow rates of the diluters to provide the dilution ratio of 10:1. Normally, the sampling timer is set at 10 seconds and the interval timer is set for 20 seconds between samplings. Before introducing the microfog to the chamber, run the counter through several sampling cycles to confirm that the system is free of particles. Then, at the beginning of a

Figure 6

SCHEMATIC DIAGRAM OF OPTICAL SYSTEM

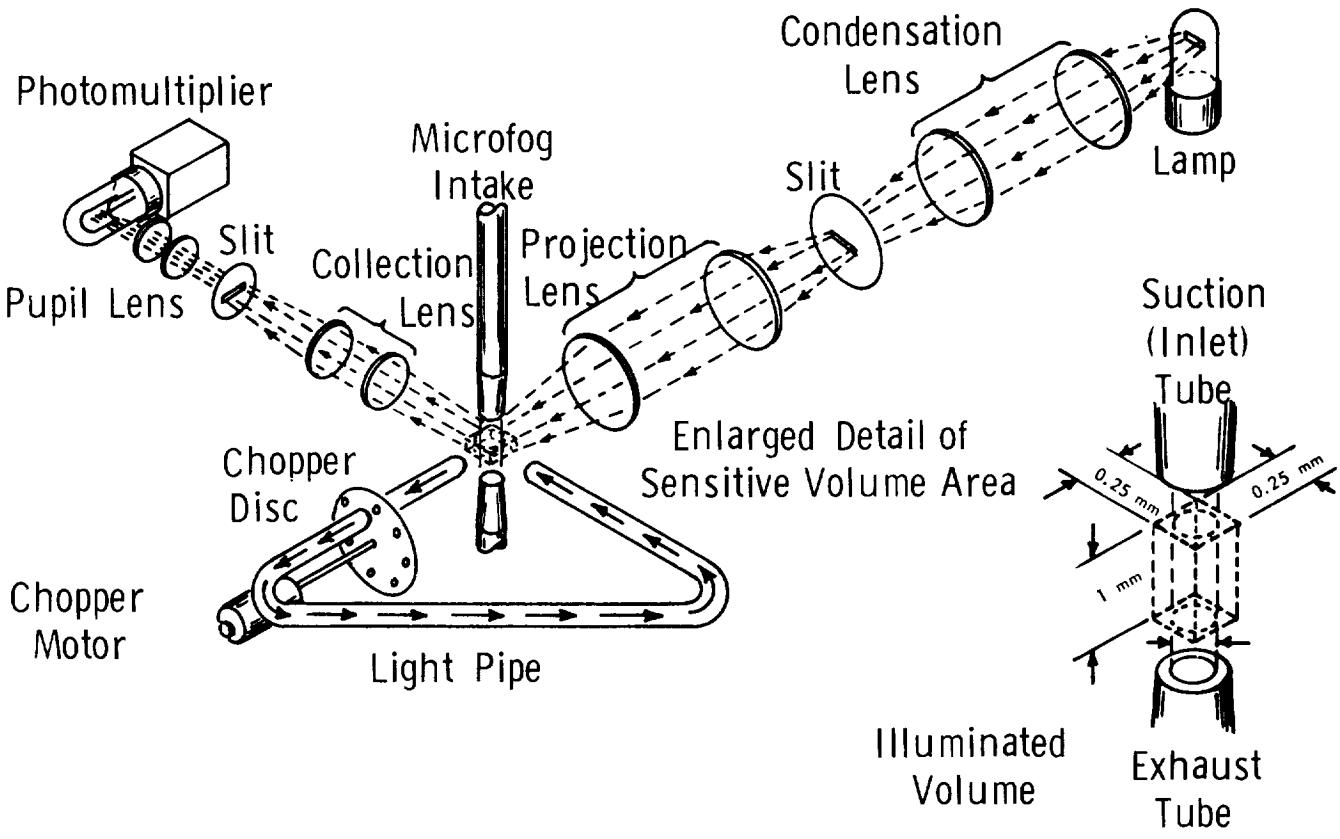

20 second interval, start nitrogen flow to the generator at the desired rates and maintain the flow rates until completing the particle size measurement. At 20 seconds elapsed on the interval timer, actuate the solenoid controlling the 4-way valve, sending the microfog stream to the chamber and switching the nitrogen stream directly to the exhaust line. A microfog sample is continuously drawn from the chamber through the two-stage dilution system, and the sample with the concentration of the microfog reduced by a factor of 100, enters the sensing zone for counting. Meanwhile, the particle counts are registering on the electronic counter. After the 10 second sampling period, deactivate the solenoid, reversing the flow directions of the two streams so that the nitrogen stream is introduced to the chamber and counter for purging. Shut off nitrogen flow to the generator and record the counts.

The light scattering technique produces number frequency data. Because it was found that number distribution data obtained in this study could not be fitted by any of the usual distribution functions (21), the number frequency data for each sample were processed by a digital computer to calculate the following statistical average diameters:

Arithmetic mean diameter

$$\bar{d}_1 = \frac{\sum d_i n_i}{\sum n_i}$$

Mean volume diameter

$$\bar{d}_2 = \left[\frac{\sum d_i^3 n_i}{\sum n_i} \right]^{1/3}$$

Cascade Impaction Technique

When it became evident, as will be later discussed, that relatively large particles (11 μm or larger) were absent in the particle counter, a cascade impaction method was developed to supplement the particle sizes determined by the particle counter. With the impaction technique, particle sizes were estimated from the amount of oil collected on an impaction cell at a given impaction velocity and with a known impaction efficiency, through the relationship established from Ranz's work (20).

This technique involved use of the upper test chamber (E). The impaction cell used in this work was a thin stainless steel plate (2" x 2" x 0.002") mounted on the test plate normally

used in wetting rate study. This light impaction cell could thus be readily removed and weighed to determine the amount of oil collected.

For a series of test runs, after the impaction cell is cleaned with naphtha and acetone, air dried, weighed, and clipped in place, the remainder of the operating procedure is identical to that of the wetting rate study except for temperature. Impaction data were obtained at 72°F. After removal of the impaction cell from the test chamber, the amount of oil collected on the cell by an impinging microfog stream at the predetermined spray distance is weighed on a microbalance.

The estimation of particle size and different properties from the data thus obtained is described in Appendix C-2.

4. Wetting Rate Determinations

Wetting rates under a variety of test conditions are determined in the upper test chamber (E) by photographing the progressive wetting of a test plate by a microfog stream, with a movie camera (E_1) operating at 64 fps. The experimental apparatus for the wetting study was fully described in the previous report (21). One minor change has been made in the experimental set-up there described. An additional light has been placed in the port originally intended for visual observation. This was found to considerably improve the quality of the photographic image. Illumination at both ports is provided by G.E. 650 watt DVY lamps in silvered reflectors.

At the start of a typical wettability test, heat the test chamber, the microfog generator, and the incoming nitrogen gas line to the desired temperature. While heating these units, clean a fresh test plate (WB-49) by following the procedure specified in Section A, Task II; then load the camera (E_1) with Eastman Kodak Ektachrome color reversal film, Type 7242, and set the film speed at 64 fps. After establishing equilibrium conditions of temperature at the chamber and microfog generator, clamp the test plate onto the plate holder mounted in front of the heater block, install the nozzle at a spray distance of 1", and quickly close the chamber door. Prior to the start of a test, the chamber is blocked off, evacuated by vacuum pump (A) to between 250 to 500 μm pressure which is held for 10 to 15 minutes, and purged with fresh nitrogen gas, slowly raising the chamber pressure to 45 psi after isolating the chamber from the vacuum pump. Heat the test plate to the test temperature (600 -800°F), while passing nitrogen through the chamber at 2 cfm. Now, start the microfog generator at the desired gas flow rate with the microfog stream exhausting directly through the 4-way valve. When reaching equilibrium conditions of temperature, pressure, and gas flow, turn on the top and side lights, and actuate the solenoid, simultaneously

starting the camera and switching the microfog stream through the spray nozzle to the test plate. When visual observation through the camera port reveals complete wetting of the test plate, deactivate the control solenoid, stopping the camera and returning nitrogen stream to the test chamber and the microfog stream to the exhaust line. Turn off the plate heater, open the by-pass around the diaphragm valve to exhaust the system pressure, and remove the test plate.

Method of Photographic Film Analysis

Particle Velocity

The filmed results of microfog particle velocity measurements were analyzed with the aid of a Photo Optical Data Analyzer (L-W Photo Corp.) and a Photo Data Quantitative Comparator, or "PDQ" screen (Photographic Analysis Co.). Images were projected at a 3:1 magnification ratio. After the microfog stream appeared to be at equilibrium, individual wave fronts were picked out and followed across the one-inch grid lines on the screen, counting off the number of frames per grid.

Wetting Rate

Analyses of the filmed wetting studies employ the same analyzer and PDQ screen. After projecting the photographic images, progressive advancement of a circular oil film on the test plate was followed at five index marks corresponding to the test plate coverages of 1, 1 1/4, 1 1/2, 1 3/4, and 2 inches. At a known film speed of 64 fps, the wetting times for these coverages are readily determined from the frame number recorded as the edge of the oil film advances across the appropriate index line on the screen.

C. Experimental Results and Discussion

1. Rate of Oil Flow

Prior to determining the wetting rate of oil at a given test condition, it is of importance to know the rate of oil flow leaving the microfog generator, since the rate of oil flow is one of the critical variables affecting the wetting characteristics of oil. Thus, the rates of oil output for the present microfog generator were determined by using Turbo Oil 4040, Hercolube F, XRM 177 F, Sunthetic 18H(B) and Ucon 50-HB-5100 at 2, 3, 4, 5, and 6 cfm* gas flow rate. In addition to these oils at 200°F,

---

*cfm here is at 45 psig and 200°F. The same unit will be used throughout this report.

the rates for XRM 177 F at 100 and 280°F were also determined. The experimental data obtained, plotting the rate of oil output versus gas flow rate for the test oils at 200°F and for XRM 177 F at 100, 200, and 280°F, are shown in Figures 7 and 8 respectively.

In determining the rate of oil output, it was observed that the more viscous oils generally required relatively longer times to establish a steady-state of oil flow within the generator, creating some difficulty in securing accurate data, particularly at 2 cfm. For these reasons, the rates for Sunthetic 18H(B) and Ucon 50-HB-5100 are sketchy, although these data are further supplemented by the rates for XRM 177 F at 100°F. On the other hand, the steady state condition for the less viscous oils such as Turbo Oil 4040, Hercolube F, and XRM 177 F at 200°F was easily reached within 2 to 5 minutes of continuous gas flow depending on the viscosity of the oil.

To investigate the effect of gas flow rate on the rate of oil flow, the rates for four test oils taken from Figure 7 are replotted in a log-log scale as shown in Figure 9. Results show excellent straight lines with the slopes approximately 1.7 for all the oils tested, and indicate that the rate of oil flow increases with increasing gas flow rate for a given oil.

In efforts to establish a simple relation representing the effect of viscosity on the rate of oil flow, all experimental data including the rates for XRM 177 F at 100 and 280°F, plotted in a log-log scale, are shown in Figure 10. Results again indicate an excellent straight line relationship having a constant slope of approximately -0.4, with the exception of 2 cfm at high viscosity ranges. Figure 10 also shows that the rate of oil flow is inversely related to the viscosity of the oil - i.e., the rate of oil flow decreases as viscosity increases.

With the aid of the experimental data obtained thus far and the straight line relationships previously indicated, it is of interest to formulate an empirical relation predicting the rate of oil output from the generator, the rates of oil flow at any given condition. Provided that the surface tension of the oil has little influence on oil flow, as a first approximation for the purpose of calculation, the rate of oil flow is then assumed to be proportional to a geometric factor, K, of the present microfog generator, and depends on the kinematic viscosity of oil and gas flow rate. This is expressed in equation form as

$$W = KQ_G^a \nu^b \qquad (1)$$

where a and b are constants to be experimentally determined from Figures 9 and 10 respectively. Thus, the general equation

Figure 7

RATE OF OIL OUTPUT VERSUS GAS FLOW RATE
FOR DIFFERENT LUBRICANTS

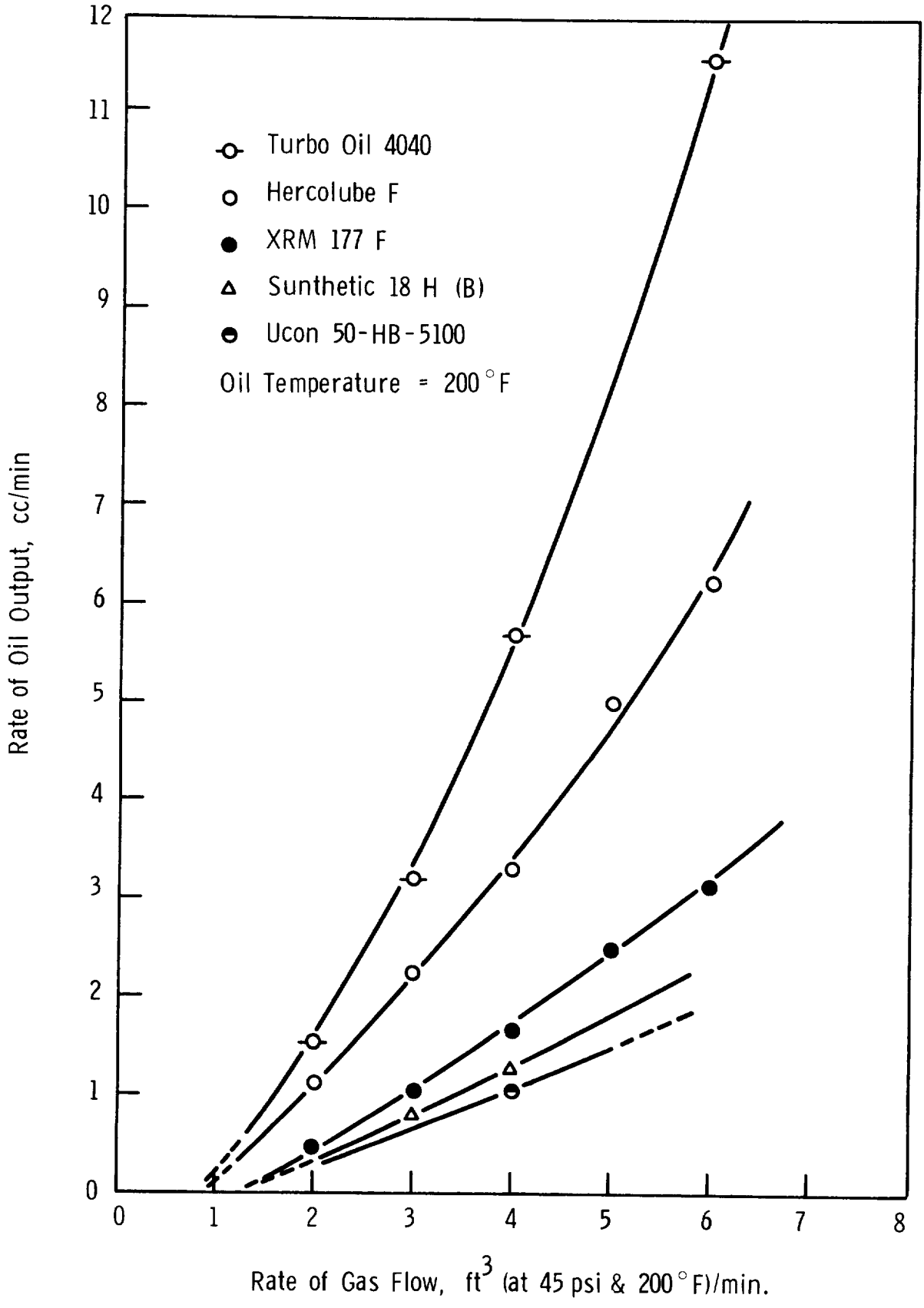

Figure 8

RATE OF OIL OUTPUT VERSUS GAS FLOW RATE
AT DIFFERENT TEMPERATURES
(XRM 177 F)

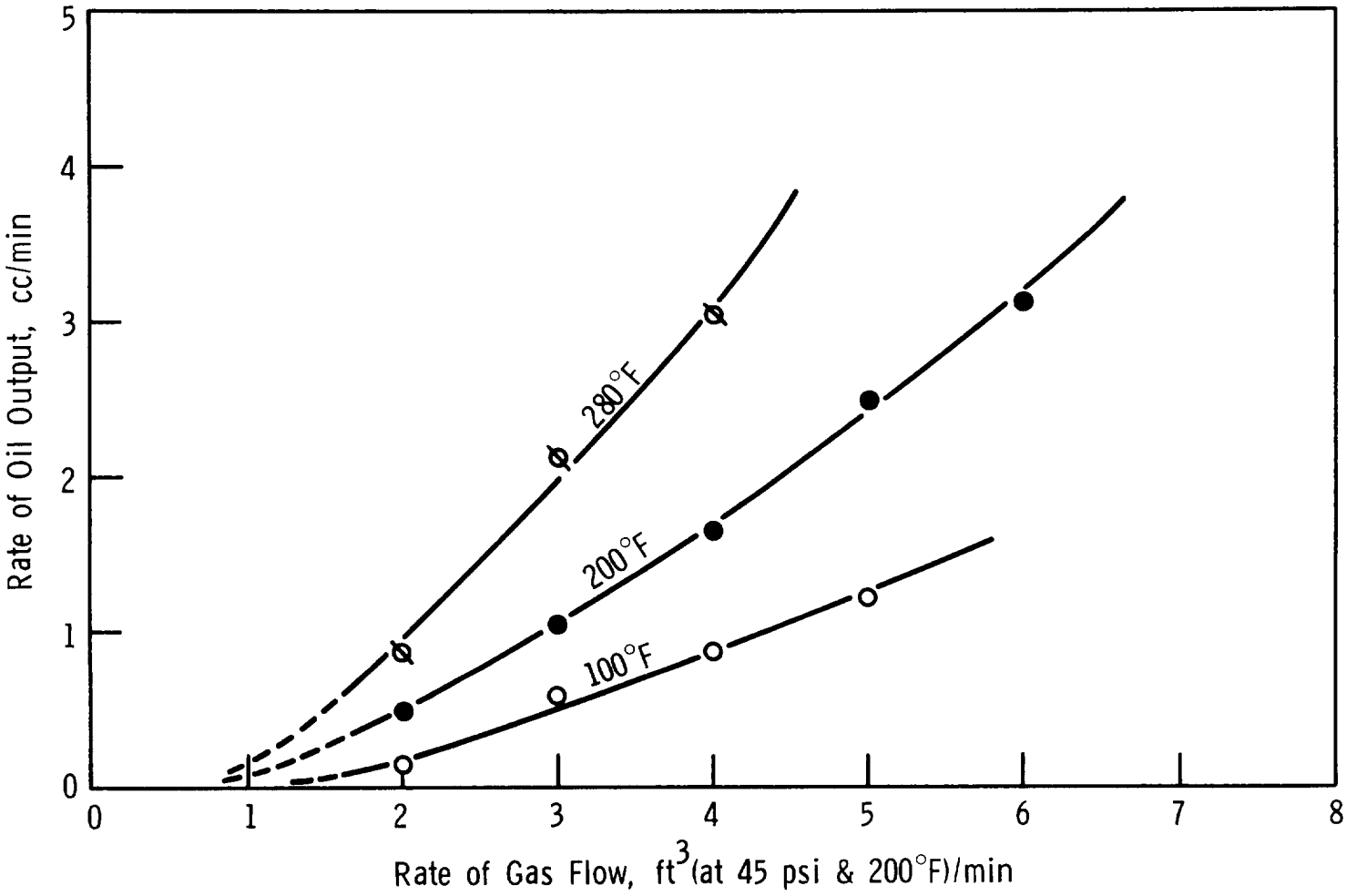

Figure 9

EFFECT OF GAS FLOW RATE ON OIL OUTPUT

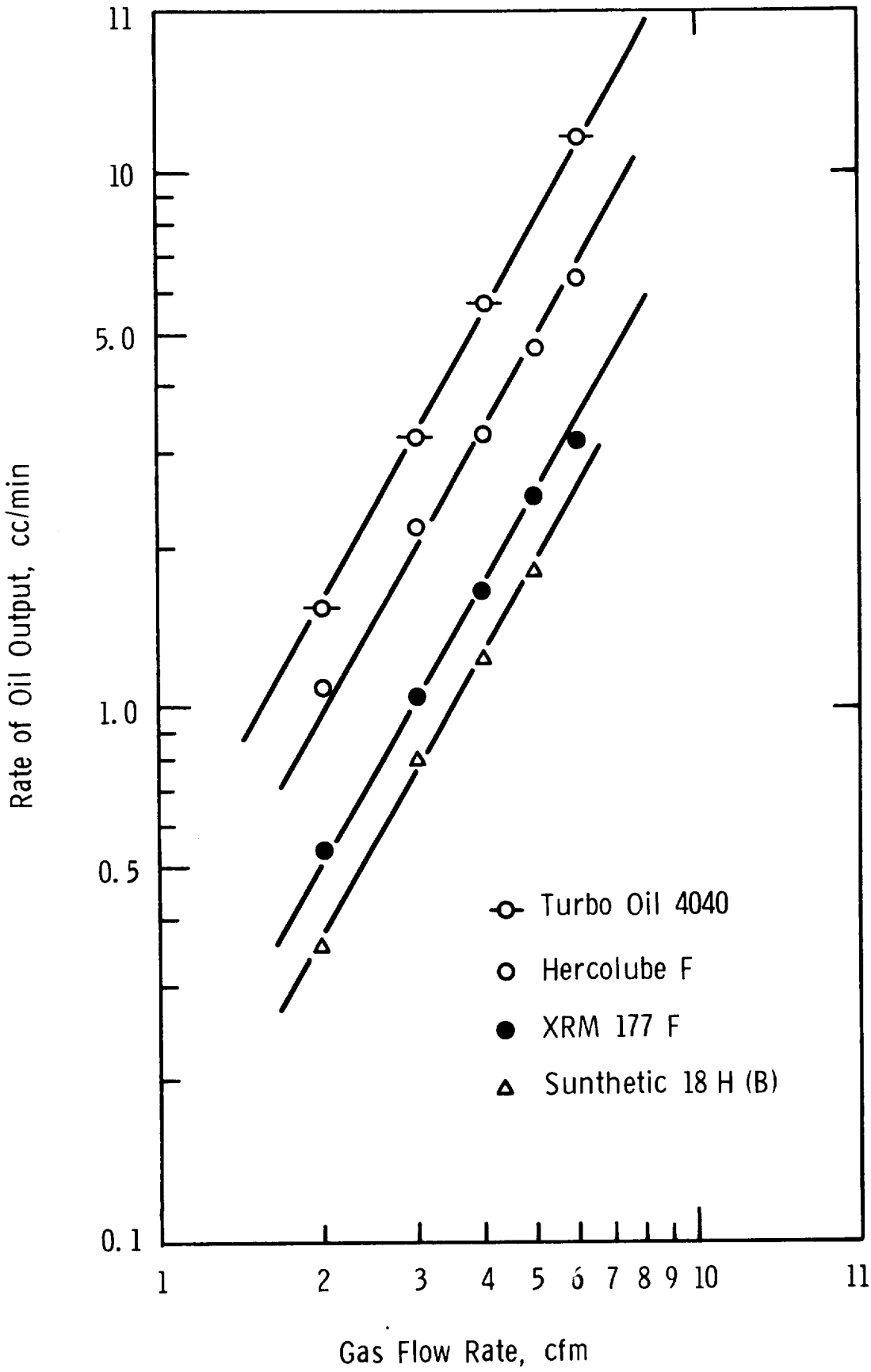

Figure 10

EFFECT OF VISCOSITY ON OIL OUTPUT

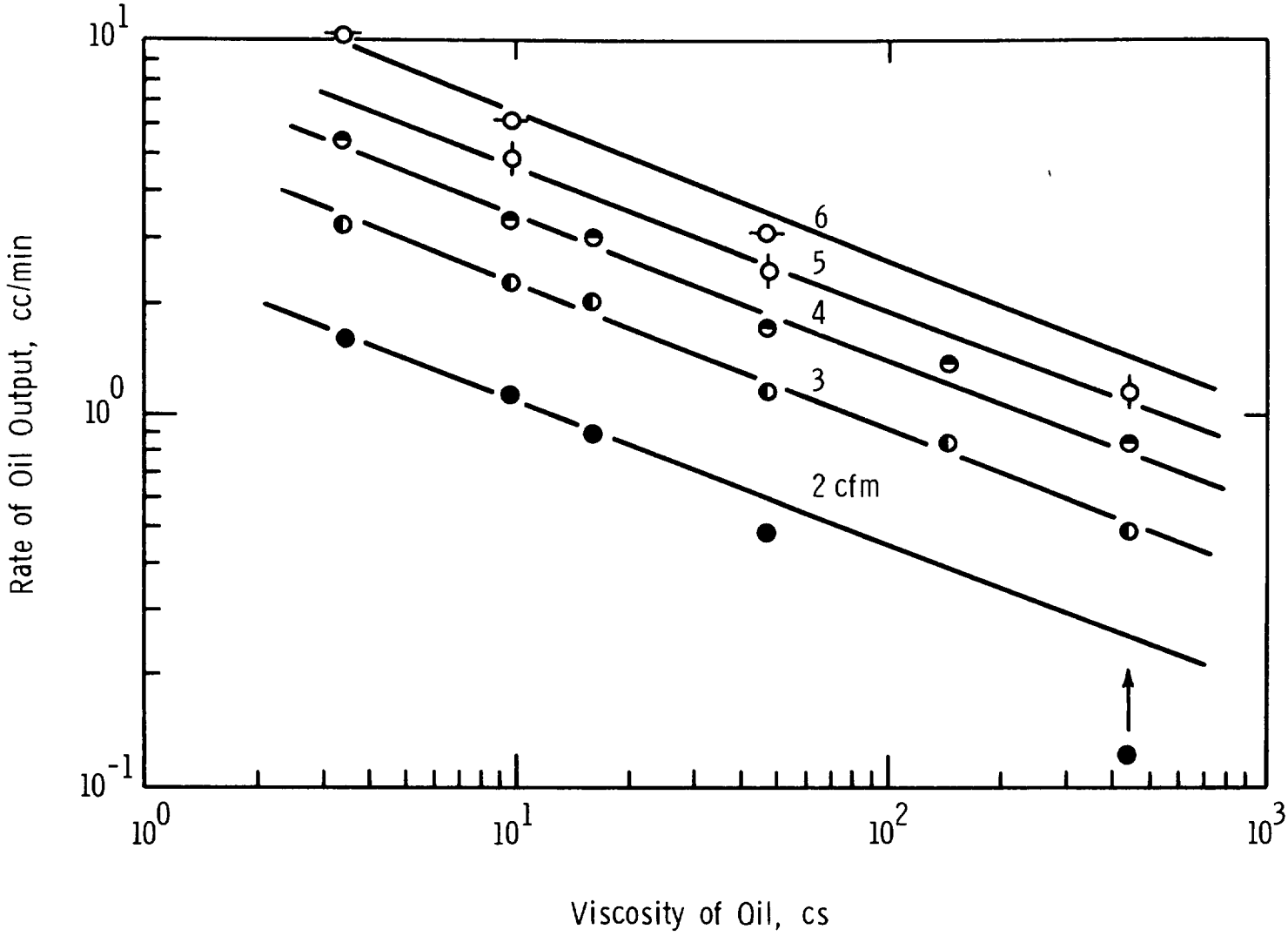

for the present generator is given by

$$W = 0.8 \left(\frac{Q_G^{1.7}}{\nu^{0.4}} \right) \qquad (2)$$

The rates of oil flow which were calculated by using Equation (2) are listed in Table 2 along with the smoothed experimental data taken from Figure 10. These include the rates for oils having viscosities of 10, 50, and 100 cs, at gas flow rates of 2, 3, 4, 5 and 6 cfm. In examining Table 2, this relation is in very good agreement with the experimental data. In order to generalize this development beyond this point, further study is needed to investigate, in detail, the geometric factor in relation to atomizing nozzles, and the aerodynamics of microfog in the generator. Since Equation (2) is certainly a first approximation, it is felt that an attempt to take surface tension of oil into account should be made for any future development of this relation.

2. Particle Velocity Distribution

As indicated by Equation (25) in Appendix B-3, accurate measurements of the values of film frequency, image movement, and number of timing marks on the high speed film, are essential in determining particle velocity by high speed photography. Thus, prior to making any measurements of particle velocity, it was of prime importance to establish the film speed curve versus time required to effectively record the motions of microfog particles. This picture frequency calibration allows selection of the proper time delay required for the film speed to reach its maximum before the event to be photographed occurs.

Since the Hy-Cam high speed camera used in this study is equipped with an input jack with a signal generator registering from 1 to 1,000 timing marks per second on the film edges, the film frequency is accurately determined by the number of frames between light impulses. Figure 11, representing film speed curve versus time, indicates that the maximum film speed is attained after 2.1 seconds of film acceleration. Similar data, not shown here, reveal that the average film frequency at this point varies from 8,600 to 9,400 fps (frames per second), depending on the roll of film used. These values of film frequency are considerably lower than the 11,000 fps specified by the Hy-Cam camera manufacturer. While the exact cause of these variations is not known as yet, differences in the physical characteristics of the film are a likely factor. In order to avoid the effects of these batch-to-batch variations, the signal generator was employed for each run.

Table 2

Comparison Between the Experimental and Calculated Values of Oil Output at Different Conditions

Gas Flow Rate (cfm)	Rate of Oil Output, cc/min					
	10 cs		50 cs		100 cs	
	Exp.(1)	Calc.(2)	Exp.(1)	Calc.(2)	Exp.(1)	Calc.(2)
2	1.1	1.0	0.6	0.5	0.5	0.4
3	2.3	2.1	1.2	1.1	0.9	0.8
4	3.5	3.4	1.8	1.8	1.4	1.3
5	4.7	4.9	2.5	2.6	1.9	2.0
6	6.6	6.7	3.5	3.5	2.6	2.7

Note: (1) Smoothed experimental data taken from Figure 10.

(2) Calculated data using Equation (2).

Figure 11

FILM SPEED CURVE VERSUS TIME

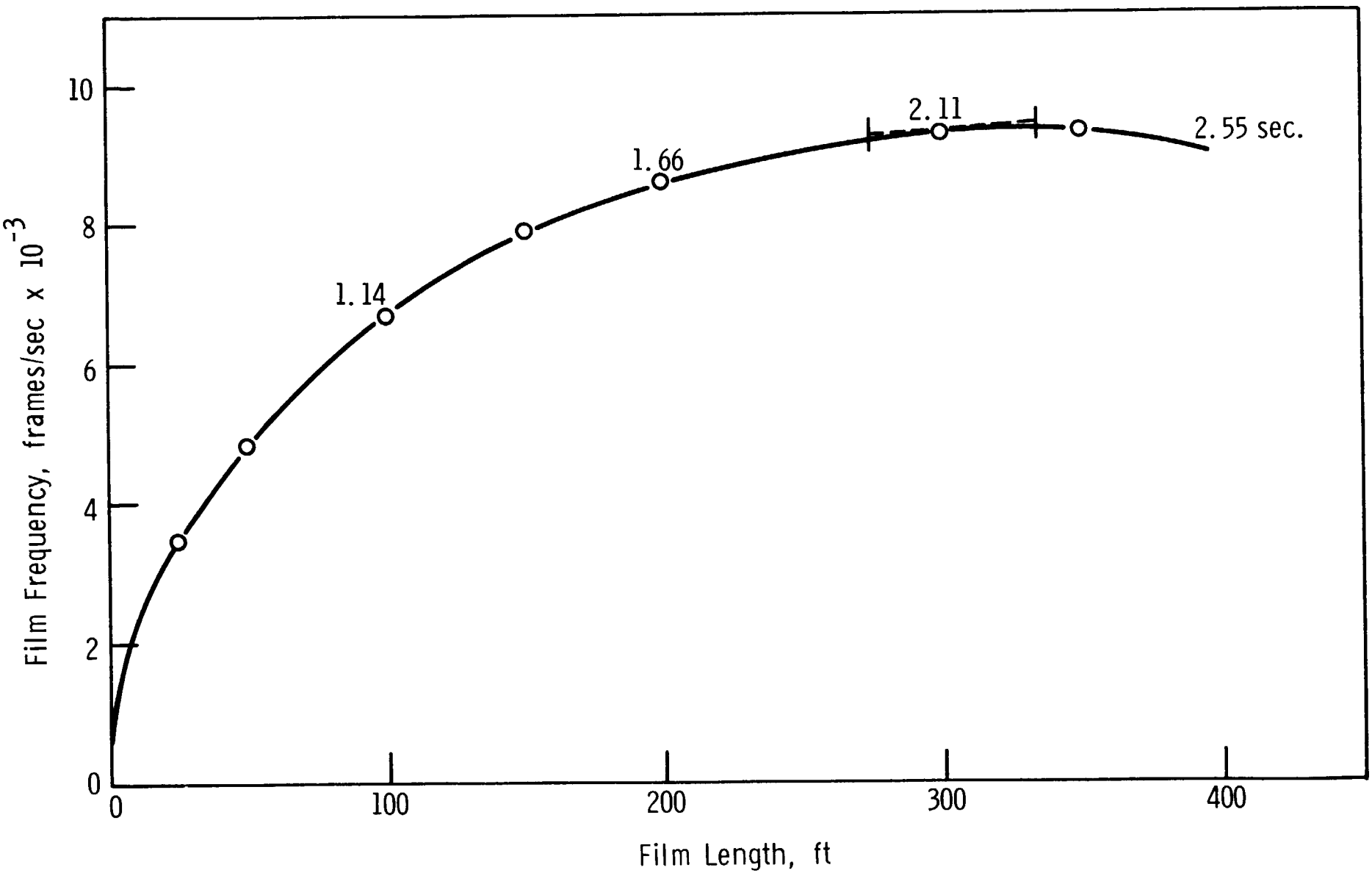

Determinations of the microfog particle velocities, using the Hy-Cam high speed movie camera, were made with five different nozzles - Nos. 1, 2, 3, 1A, and 3A, which are shown in Figures 24 and 25. The pressure drops across these nozzles were also measured at gas flow rates of 2, 3, 4, 5, and 6 cfm. The test chamber conditions were at 45 psi and 72°F. These tests, in most cases, employed XRM 177 F at a microfog generator temperature of 200°F.

Experimental results representing the local velocities at specified distances are summarized in Table 3. These also include the measurements of pressure drop, the calculated values of velocity at the nozzles, using Equations (4) and (6) of Appendix B-1, and the axial velocity distributions following Equation (22) in Appendix B-2.

In calculating the mean velocity of microfog particles we assumed, in addition to an ideal gas and adiabatic expansion, that the relative velocity between gas and particle is negligible - that is, the slip velocity is essentially zero so that no drag acts upon the particles. No attempt was made to justify these assumptions used for calculation at the present time. If an accurate correction other than the empirical one applied here is required, the work of expansion can be integrated with V expressed explicitly in terms of P by establishing adequate P-V-T relations. In spite of these fundamental premises, the calculated values of gas stream velocity, in practice, should give the minimum velocity of particles under a given condition, since the velocity correction factor used, $\epsilon_u = 0.85$, is believed to be on the low side (10). For the non-adiabatic (approximately isothermal) expansion, it is necessary to add heat to the expanding gas in order to maintain the temperature constant. For the sudden expansion of a gas in actual practice, this constancy of temperature is seldom attained, because the rate of heat transfer from the surroundings is usually not sufficiently rapid. When inlet pressure is similar to discharge pressure, so that the increase in volume is small, the slowly expanding gas is more nearly isothermal. As a matter of interest, the temperature drop of an expanded gas was estimated, assuming an adiabatic expansion with 10 psi pressure drop through a nozzle, with an inlet gas temperature of 200°F, using Equation (3) in Appendix B-1. The temperature of the gas falls approximately 28°F.

In calculating average particle velocities from high speed movie films, a straight line relationship between image movement and number of frames was assumed, despite the definite curvature of the actual experimental results, presented in Figure 12, where image movement is plotted against time. This nonlinearity is the result of acceleration of the film and decay of the axial velocity of microfog particles. Assumption of the linear relationship introduces to the determination of particle velocity a slight error which depends upon the order of magnitude of Δt_i

Table 3

Axial Distribution of Mean Particle Velocity for Different Spray Nozzles

Item	Gas Flow Rate (cfm at 45 psi & 200°F)	Pressure, psi			Calculated Gas Stream Velocity, ft/sec									Experimental Particle Velocity, ft/sec		
					Adiabatic Expansion					Non-Adiabatic Expansion						
		Generator	Nozzle	Chamber	Atomizing Nozzle	Spray Nozzle	2"	4"	6"	Spray Nozzle	2"	4"	6"	2"	3"	4"
	Nozzle No. 1	(0.171" orifice diameter)														
1	2	55	48.5	46	440	290	99	50	33	218	75	38	25	-	-	-
2	3	70	53	46.5	657	411	141	71	47	348	119	60	40	131	71	49
3	4	96	61	46.5	846	595	204	102	68	519	177	89	59	174	87	49
4	5	118	66.5	47	957	685	233	117	77	690	236	118	79	196	134	97
5*	6	110	74	48	811	755	257	128	85	889	304	152	101	200	150	94
	Nozzle No. 2	(0.390" orifice diameter)														
6	2	53.5	46.3	46	482	121	93	47	32	41	32	16	11	31	25	-
7	3	65	47	46.5	674	167	128	65	43	61	48	24	13	65	33	-
8	4	85	48	46.5	932	213	164	83	55	83	65	33	22	83	54	37
9	5	111	49	47	1110	245	188	96	64	104	81	41	27	87	65	-
10*	6	93	48.5	46.5	995	253	195	99	66	125	98	49	33	128	95	84
	Nozzle No. 3	(0.281" orifice diameter)														
11	2	54	47	46	451	168	95	47	32	79	44	22	15	-	-	-
12	3	64	48	46.5	670	213	119	60	40	119	67	34	22	120	87	52
13	4	87.5	49.5	46.5	925	268	150	75	50	163	92	46	31	147	87	65
14	5	113	50	46.5	1110	316	177	89	59	205	115	58	38	160	97	-
15*	6	93	51	47	967	348	195	98	64	247	139	70	46	165	106	95

Table 3 (Cont'd)

Item	Gas Flow Rate (cfm at 45 psi & 200°F)	Pressure, psi			Calculated Gas Stream Velocity, ft/sec					Experimental Particle Velocity, ft/sec		
		Generator	Nozzle	Chamber	Atomizing Nozzle	Spray Nozzle	2"	4"	6"	2"	3"	4"
	Nozzle No. 1A	(the de Laval type of nozzle with throat size of 0.171" and with one layer of 150 mesh screen in expansion section)										
16	2	52	47	45	444	256	87	44	38	-	-	-
17	3	64.5	49.5	45.5	640	358	122	61	41	57	40	-
18	4	85	53.5	46.5	846	462	157	79	52	75	50	-
19	5	116.5	61.5	47	956	644	219	109	73	88	64	48
20*	6	107	68.5	47.5	850	755	257	128	85	110	76	63
	Nozzle No. 3A	(No. 3 Nozzle packed with 3 layers of 150 mesh screen in converging section.)										
21	2	53	48	45	392	286	160	80	53	-	-	-
22	3	65	51.5	45.5	600	400	224	112	74	59	42	30
23	4	87	57.5	46.5	802	528	296	147	98	63	51	41
24	5	121	70	47	938	723	405	202	134	110	75	60
25*	6	117	83	47.5	762	855	478	239	158			

* A new atomizing nozzle having 1.88×10^{-2} in^2 of total flow area.

Figure 12

DISTANCE VERSUS TIME CURVES

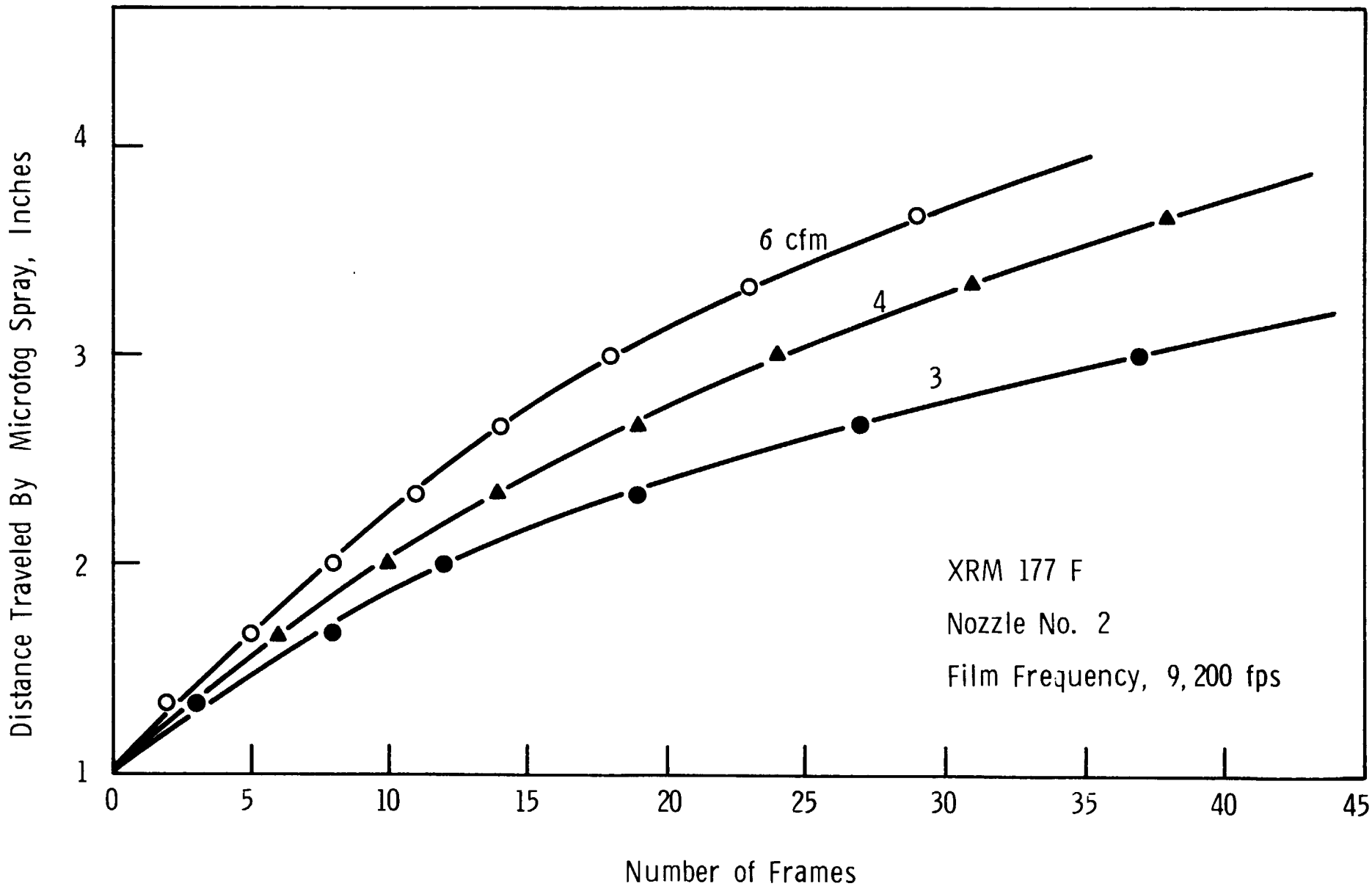

and Δx_i, and can be minimized by taking the smallest possible increments of image movement and time.

In estimating the values of image movement, careful analysis of the high speed movie films reveals an irregular pattern of the frontal demarcation line of the microfog stream leaving the spray nozzles. Moreover, low particle concentrations and blur of the moving image on the film often added to the difficulty of identifying the boundaries of the microfog stream. For example, at 2 cfm the microfog stream was so sparse that the boundaries of the stream could not be distinguished. At higher gas flow rates the axial distributions of mean particle velocity were estimated with average accuracy of + 10% at 2", 3", and 4" distances from the spray nozzle, but at closer distances to the nozzle reliable estimates were prevented by excessive image blur resulting from the higher velocity and more narrow width of the microfog stream.

When a camera is used to investigate the motions of a subject at an appreciable duration, smearing or blurring of the image inevitably results. The degree of blurring, which is greatly affected by velocity of the subject, exposure duration, and image magnification, can be expressed in mathematical terms as follows (12):

$$\xi' = t_E . M_x . u . \text{Cos } \beta \qquad (3)$$

where ξ' is the image blur; t_E, exposure duration; M_x, optical magnification; u, subject velocity; β, angle between direction of motion and film plane. Thus a camera, to be useful in photographing a high speed event, must be capable of providing a suitable number of pictures, free from excessive blur of image movement, during the time duration of the event. With the present Hy-Cam high speed movie camera at 9,500 fps, the maximum velocity of a microfog stream, which can be estimated with the minimum number of frames, is approximately 400 ft/sec. Therefore, at high gas flow rates with nozzles No. 1 and 3, the velocities of microfog particles in the vicinity of the spray nozzle could not be determined with reasonable certainty by use of the present camera.

We briefly discussed the limitations of theoretical equations (Appendix B) and experimental apparatus in determining the velocity of microfog particles. Now, as a matter of interest, the limited results from Table 3, plotting dimensionless velocity, U_m/U_o, versus dimensionless distance, X/X_0 are shown in Figures 13 and 14 for adiabatic and non-adiabatic expansions, respectively. These results are compared with the calculated values.

Figure 13

DISTRIBUTION OF MEAN PARTICLE VELOCITY ALONG THE AXIS OF SPRAY NOZZLE
(Adiabatic Expansion)

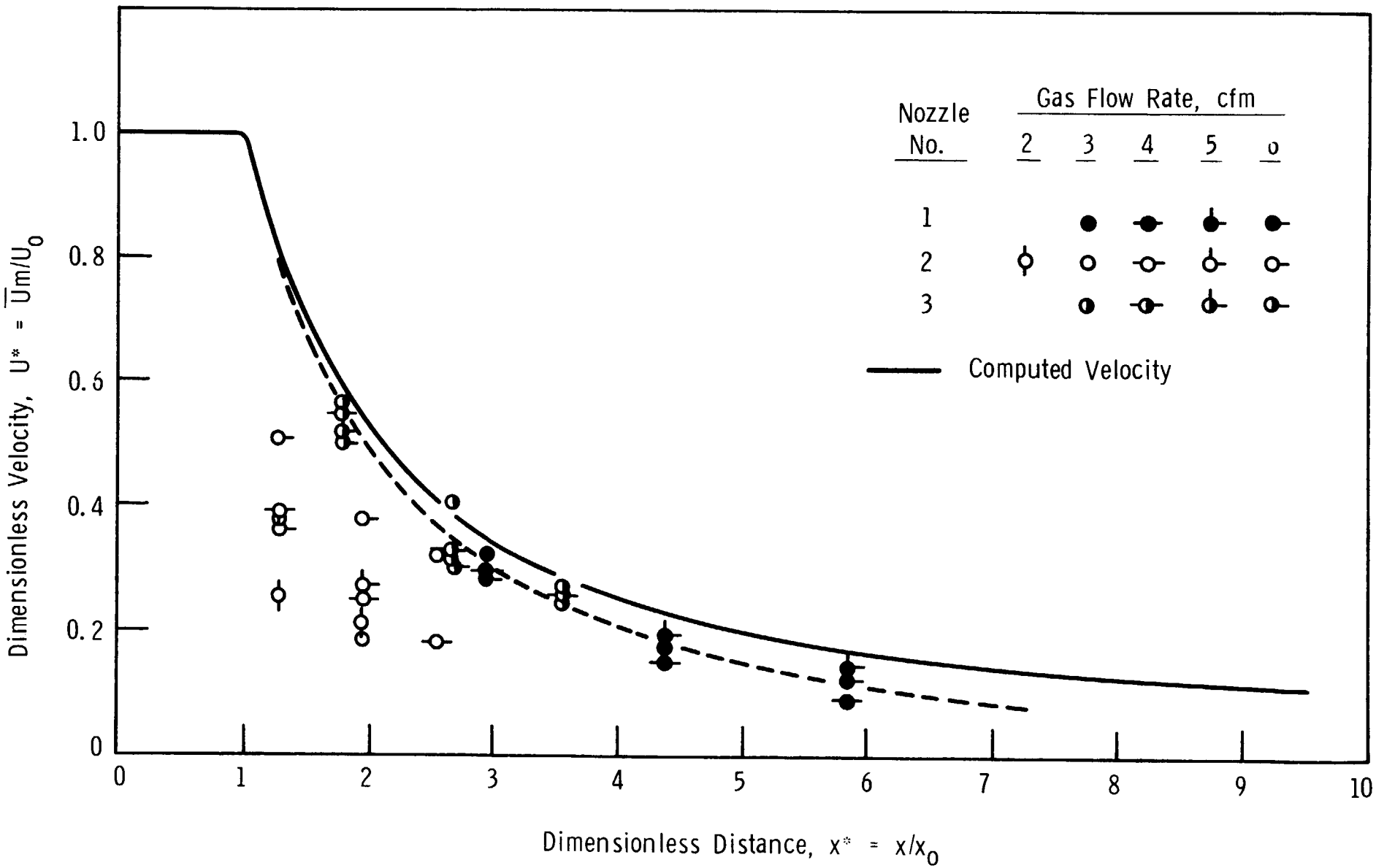

Figure 14

DISTRIBUTION OF MEAN PARTICLE VELOCITY ALONG THE AXIS OF SPRAY NOZZLE (NON-ADIABATIC EXPANSION)

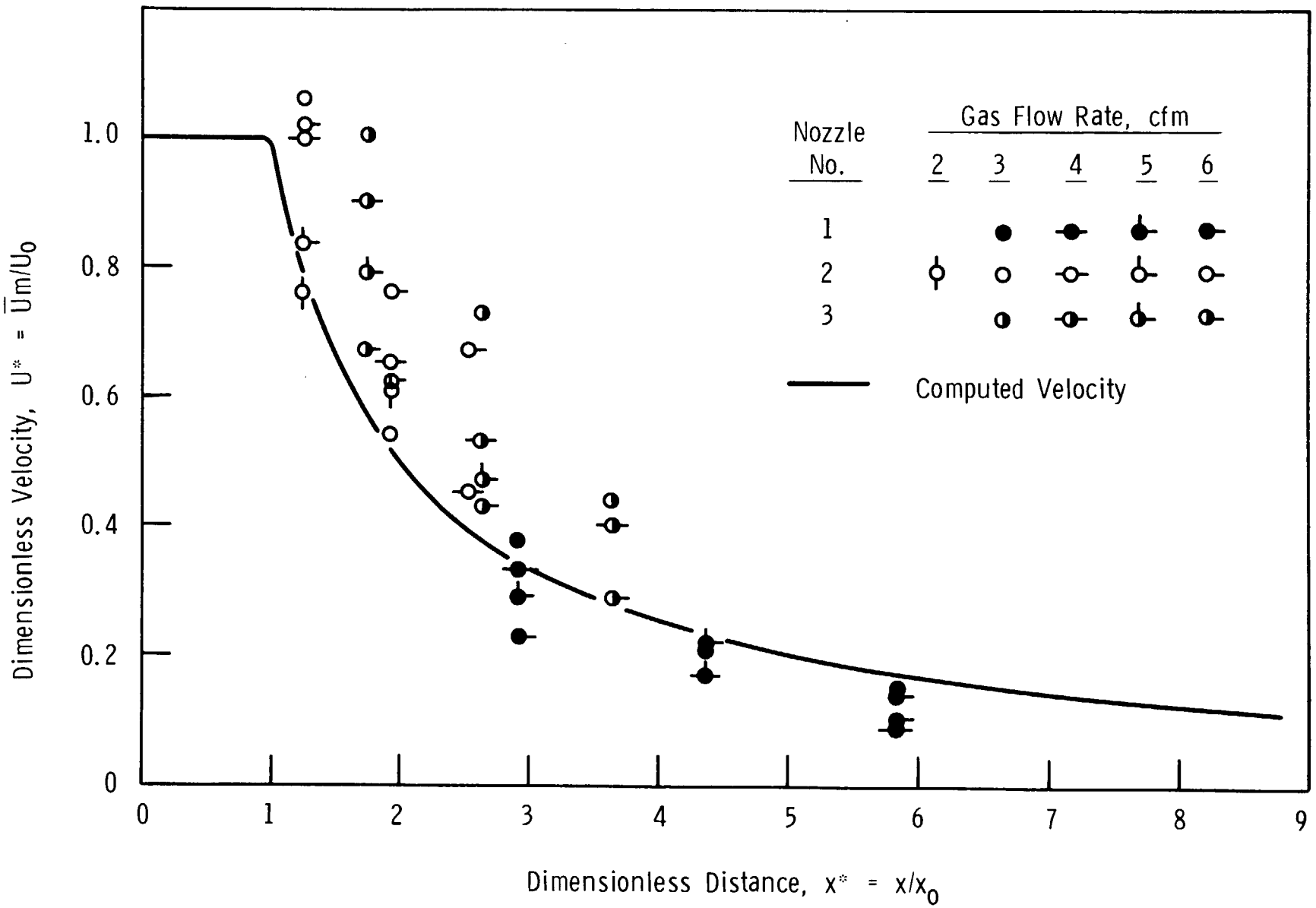

For the adiabatic expansion, the result shows good agreement between the calculated and the experimental values of particle velocity with the exception of the data for No. 2 nozzle. The excellent agreement between the calculated and the observed values for some cases at the 2 inch distance must, to some extent, be fortuitous, bearing in mind the arbitrary selection of the velocity correction factor and the assumption of $X_o = 4D_o$ at $\mu = 0$, as suggested by Forstall's work (7), without experimental verification. It is felt that representation of Forstall's empirical relation (refer to Equation 21 in Appendix B-2) is somewhat arbitrary, since this relation seems to be not entirely consistent with others, although the velocity profiles in consecutive sections of the microfog jet are basically similar to the others. For example, other experiments (2, 10) on free jets issuing in still ambient fluid disclose much greater values of X_o ranging from 6 to 8, depending on physical characteristics of the fluid and nozzle design. The results for No. 2 nozzle deviate considerably from the calculated values - that is, the experimental values of particle velocity, in all cases, are smaller than the calculated. The cause of these deviations is not clearly known except that the largest percentage error of pressure measurement occurs at the lowest pressure drop and that Equation 4 in Appendix B-1 is difficult to evaluate accurately when the inlet pressure is nearly equal to the discharge pressure.

For the non-adiabatic expansion, comparison between the calculated and the experimental values of particle velocity indicates that the experimental data scatter widely, although, contrary to the comparison for adiabatic expansion, the results for No. 2 nozzle are in good agreement with those calculated. The comparison also shows that the calculated values, in general, are lower than the observed except for No. 1 nozzle.

These comparisons lead to the conclusion that microfog particles within the size and concentration ranges studied seem to be completely suspended at high gas stream velocities, but not at lower velocities. In other words, the velocity of the microfog particles relative to that of the gas is near zero at high gas stream velocities, but not at lower velocities. The results seem to suggest that the expansion processes in this study are more nearly adiabatic when the pressure drops are relatively high, but are closer to isothermal at lower pressure drops.

The results for No. 1A and No. 3A nozzles are not included in these comparisons because of the uncertainty of friction loss due to the presence of 150 mesh screens in the nozzles. In calculating the gas stream velocities for these nozzles, it is somewhat doubtfully assumed that the entire pressure drop across the spray nozzle produces a high velocity stream by expanding a gas stream from a high pressure region. As a result of this assumption, it would be anticipated that the experimental values

of particle velocity are considerably lower than the calculated, as indicated in Table 3.

No attempt was made to determine the radial distribution of particle velocity from the high speed movie film. However, according to Equation (19) in Appendix B-2, the radial distribution can be estimated by using some sort of empirical equation similar to Equation (19). Forstall compared the measured velocity profiles with the cosine curve as suggested by Hinze (9, 10), and with the Gaussian error curve. From this comparison, he concluded that the Gaussian error curve gave very good agreement practically across the entire jet width along the axial distance, $X/D_o = 20$. Values slightly too high are obtained near the apex of the velocity-distribution curve; at the boundary region the values are too low.

i) Effect of Surrounding Temperature

Although particle velocities, in most cases, were determined at 72°F, several runs were repeated at 600° and 800°F to observe whether or not the surrounding temperatures had any influence on the velocity distribution of microfog particles due to additional turbulences created by heat- and mass-transfer at the boundary regions of an expanding jet. The movie films showed no measurable differences in particle velocity at high or low surrounding temperatures studied. This indifference may be due to the fact that under the present experimental conditions the rate of heat transfer to a rapidly expanding jet from its surroundings is not sufficiently rapid to affect the velocity distribution of the jet, as suggested in the preceding section.

ii) Effect of Oil/Gas Mass Flow Ratio (Concentration of Microfog Particles)

The concentration of microfog particles suspended in a gas stream is another important parameter to be considered in the description of two-phase flow. In order to investigate the effect of oil/gas mass flow ratio on velocity, the particle velocity of XRM 177 F at a gas flow of 4 cfm with No. 3 nozzle was compared with those of Turbo Oil 4040 and Hercolube F at the same operating conditions. In comparing these values, it is assumed that for the three oils the radial and axial concentration gradients of the microfog particles in the gas streams are uniform when time-averaged, although their oil/gas mass ratios are 3.2×10^{-3} for XRM 177 F, 7.6×10^{-3} for Hercolube F, and 12.0×10^{-3} for Turbo Oil 4040.

The results reveal that the velocities of these oils are in agreement at distances of 2" and 3" from the nozzle within the

accuracy (+ 10%) of the present experimental measurements, but the particle velocities of Hercolube F and Turbo Oil 4040 at 4" slightly lag behind the velocity of XRM 177 F, which has a lower particle concentration. Thus, it may be concluded that if the velocity of gas flow is sufficiently high ($N_{Re} > 10^6$), the oil/gas mass flow ratio is less than 12.0×10^{-3}, and the mean particle size is less than 10 μm (refer to Section 3), the concentration of particles in a microfog flow has no effect on particle velocity. In measuring the particle velocity at much higher loading, one might expect the intensity and scale of gas turbulence to be reduced by the particles through the dissipation of the kinetic energy of turbulent gas. The reduction of turbulence by large numbers of particles should tend to increase the relative velocity between the particles and the gas and create variations of the expansion angles of a diffusing jet.

In this study, it was also observed that extremely large drops (possibly 500 ∿ 2,000 μm diameter) traveled considerably slower than the gas stream. These outsized drops were occasionally formed at the tip of a spray nozzle, when the microfog was continuously sprayed for an extended period.

iii) Observations on Spray Pattern and Expansion Angle

In analyzing the high speed movie films, the spray patterns and expansion angles of microfog sprays were observed as a function of source pressure.

Figure 15, representing a typical spray pattern of microfog, shows the turbulent character of the flow in a spray nozzle, with the separate eddying domains at the boundary region still distinguishable. It is also of interest to note that streaks created by the paths of relatively large particles during exposure of 0.002 seconds appear to be localized in the boundary regions, particularly in the lower regions of the spray.

The observations made in the analyses of movie film suggest that, when a convergent nozzle is used, the expansion angle of a microfog spray increases with increasing inlet pressure. The variation of the microfog spray angle with inlet pressure may be explained qualitatively as follows, referring to the three sequential sketches shown in Figure 16: for $P_1 \sim P_2$, the gas density down stream from the nozzle is very close to the inlet gas density, and the microfog particles are large compared with the scale of turbulence. The main effect of these factors on the particles is to increase their flow resistance, and the particles, at most, more or less follow the slow turbulent motions of the gas, resulting in a bending of the particle trajectories toward the axis of the jet and a decrease of the expansion angle. With increasing inlet pressure, $P_1 > P_2$, there

Figure 15

FLOW PATTERN OF MICROFOG SPRAY IN A FREE JET

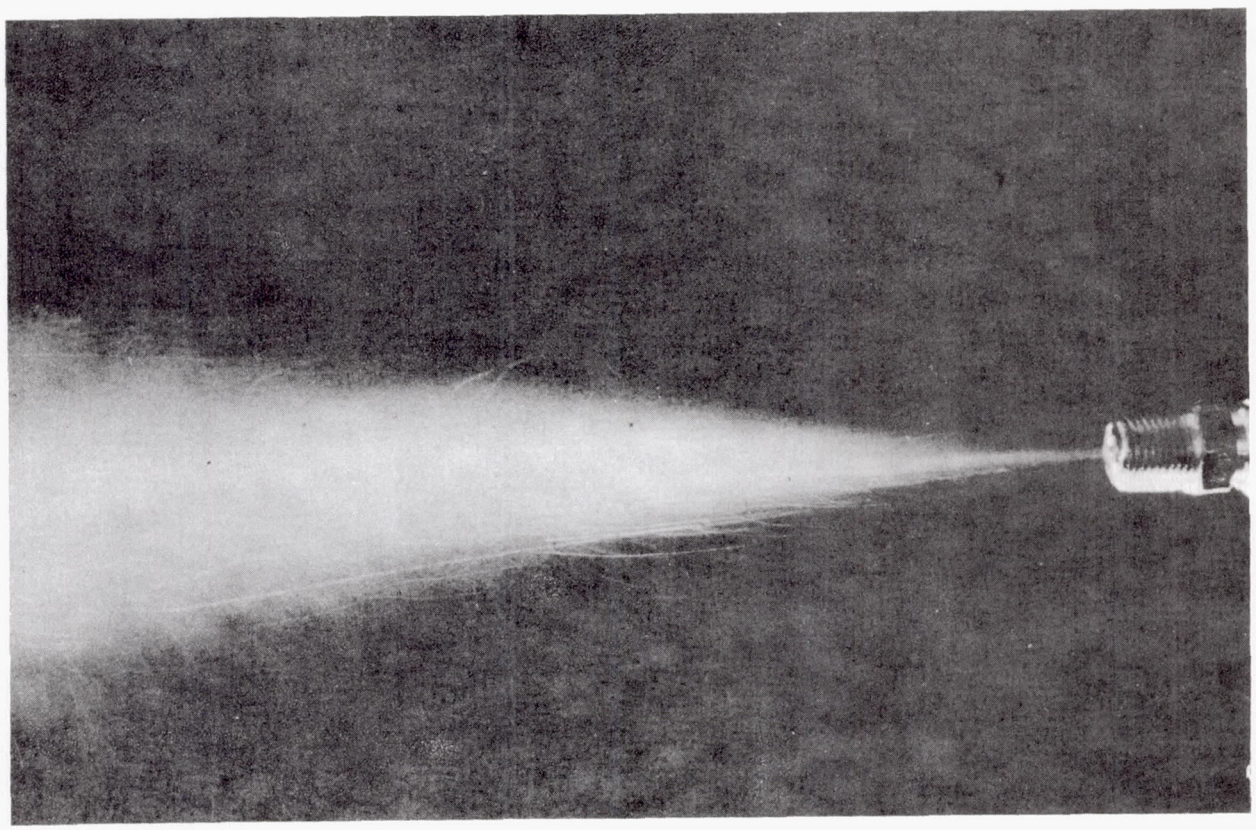

Figure 16

PARTICLE TRAJECTORIES SHOWN SCHEMATICALLY
IN THE VICINITY OF A NOZZLE THROAT

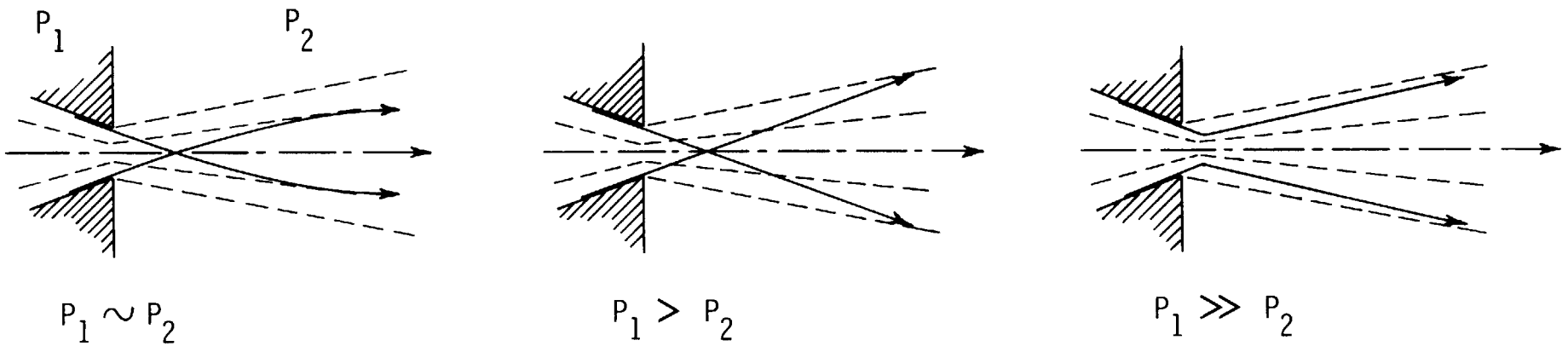

is increasing turbulence in the jet, and the particles, becoming relatively small compared with the scale of the turbulence, tend to follow all turbulence components of the gas. Consequently, the particles travel downstream from the nozzle along rectilinear extensions of the trajectories established in the nozzle until the smaller-scale turbulences are reached. Further increase of P_1 (i.e., $P_1 >> P_2$) produces a strong interaction between the jet and the microfog particles. The particles tend to follow the streamlines of the nitrogen gas in the vicinity of the throat and the expansion increases with increasing inlet pressure.

This qualitative picture has not been verified experimentally. However, it should be of considerable interest to further investigate whether or not the particle paths really cross between the nozzle inlet and a downstream target, as shown in the sketch.

3. Particle Size Distribution

In order to study the atomizing characteristics of the present experimental apparatus - more specifically the microfog generator and spray nozzles - particle size distribution data were obtained with all the test oils under a variety of conditions. All runs were made in duplicate and agreement between pairs of data was, in general, excellent.

A typical number incremental frequency distribution curve, corresponding to the particle size distribution produced by the microfog generator at a gas flow rate of 3 cfm, is shown in Figure 17. Furthermore, the cumulative particle size distribution curve, presented in Figure 18, is plotted in a log-probability graph to show what fraction of a particle (by number) possesses radii greater than a given value.

It is of interest to note, as illustrated by Figure 17, that particle size frequency distribution curves on a number basis, in most cases tested in this study, have a bimodal distribution - i.e., two peaks. This behavior, which is rare for pneumatic atomization, may stem from differences in the design of the generator where, for example, size screening by the impactor, which is supposed to allow only small particles to leave the generator, may be ineffective. An alternative or additional possible cause of bimodal size distribution could be coagulation of particles brought about by gas turbulence which may be created by high volumetric gas flow through the 1/2" tubing traveled by the microfog stream.

i) Microfog Generator

Particle size correlation by Nukiyama (18), probably has been the most widely quoted work in pneumatic atomization, expressed in the following form:

Figure 17

n_i VERSUS PARTICLE DIAMETER

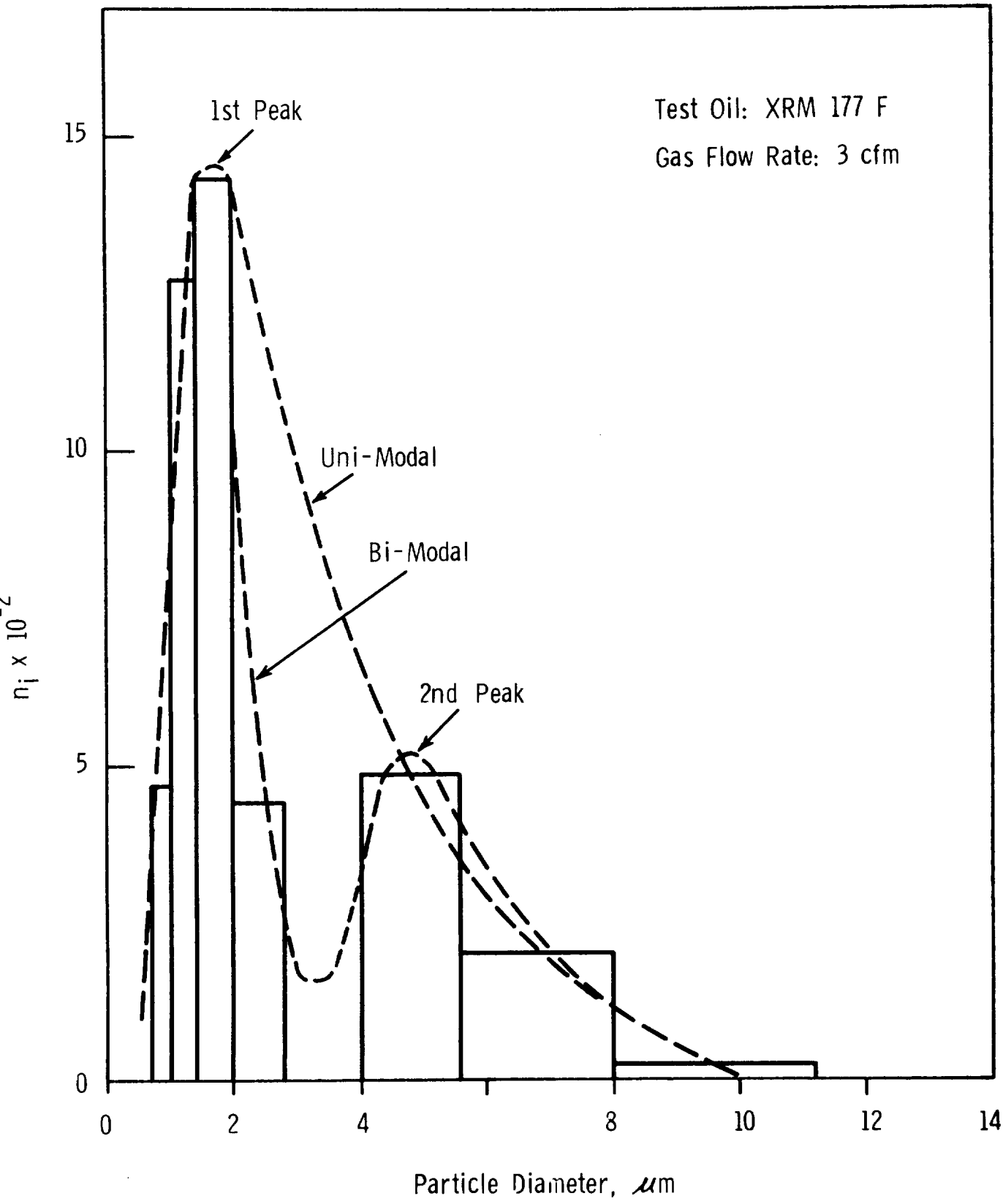

Figure 18

CUMULATIVE PARTICLE SIZE DISTRIBUTION CURVE

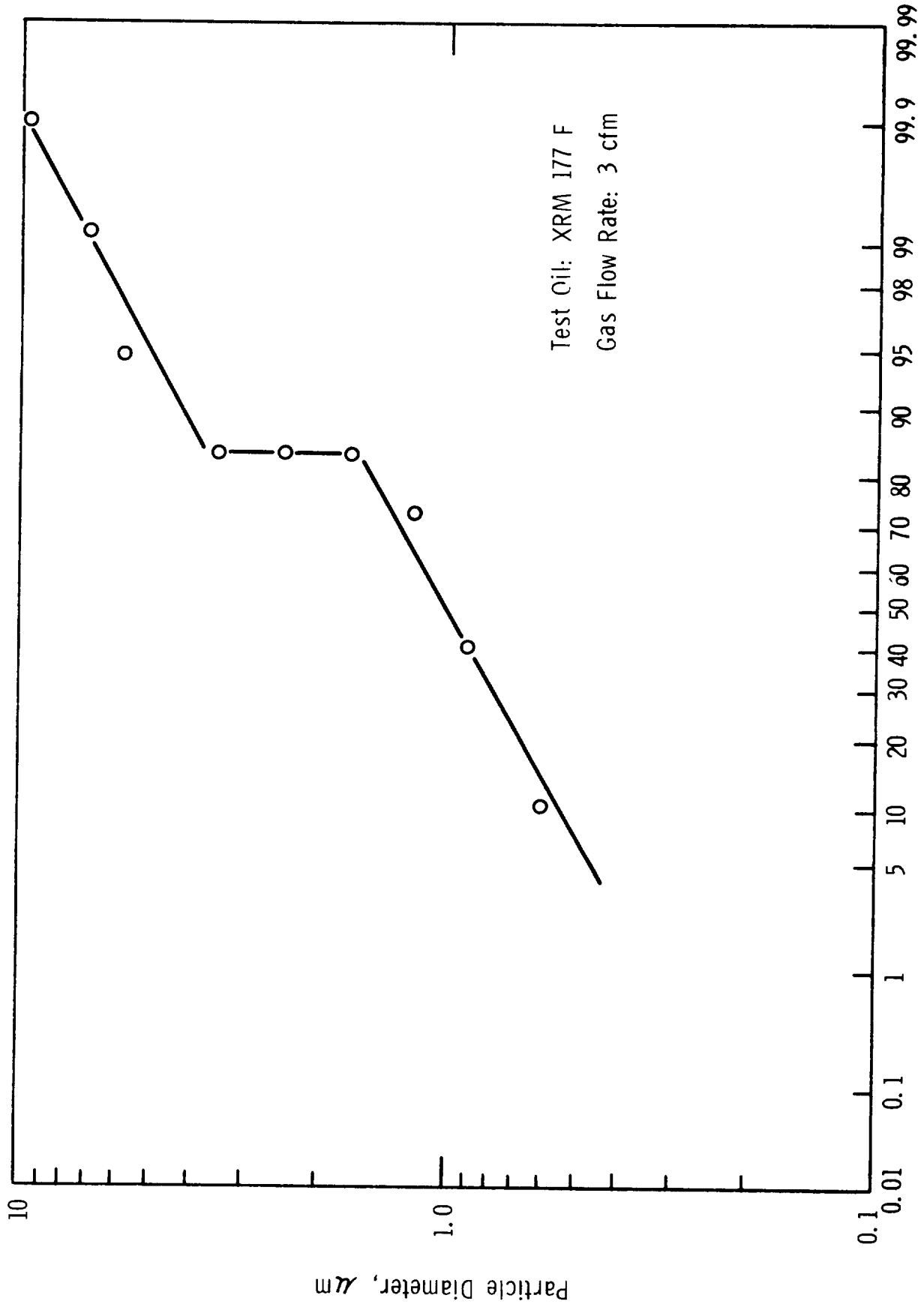

$$\bar{d} = \frac{585}{(U_G - U_L)}\left(\frac{\sigma}{\rho}\right)_L^{1/2} + 597\left(\nu\sqrt{\frac{\rho}{\sigma}}\right)_L^{0.45} \cdot \left(\frac{Q_L}{Q_G} \times 1000\right)^{3/2} \quad (4)$$

A close analysis of this equation shows that if $Q_G/Q_L > 5{,}000$, the second term has slight influence on particle size, which is then mainly determined by relative velocity, $U_R = U_G - U_L$, and liquid properties. Nozzle dimensions do not enter the correlation. The relation also suggests that the average particle size from a pneumatic atomizing nozzle decreases with increase of gas/oil ratio, while increase in relative velocity decreases particle size. More recent work by Kim and Marshall (13) indicates that the most important operating variables in pneumatic atomization are (1) the dynamic force of the atomizing gas, and (2) the mass flow ratio of gas to liquid, and suggests an empirical modification of the Nukiyama relation. Most investigations to date, however, suggest that the particle sizes from pneumatic nozzles are primarily a function of liquid flow rate, gas flow rate, nozzle dimensions, flow ratios, and viscosity of the liquid. Thus, the heart of a microfog generator is the atomizing nozzle which basically controls each of the variables listed above.

The most commonly used atomizing nozzles in commercially available generators are shown in Figure 19. The nozzles usually contain different numbers and sizes of orifices in conjunction with a solid impactor supported by grids or screens, depending upon gas flow rate and size ranges desired.

In efforts to examine these atomizing factors, and to gain the knowledge needed to control the particle size range of the present microfog generator, particle size distribution data for XRM 177 F were obtained under a variety of generator conditions. Included in this study were the effects of impactor design, oil flow, and dynamic force of the atomizing gas. The experimental results are summarized in Table 4.

Items (1) to (3) represent the effects of the design of the impactor in the generator on particle size distribution. As previously indicated, the purpose of an impactor in the generator is to screen out large particles leaving the atomizing nozzle, allowing only particles below some maximum size to leave the generator. In these tests, the screen size and distance between nozzle and impactor were varied, while the flow rate of gas and oil for a given size of atomizing nozzle were maintained constant, thereby holding constant the dynamic force of the atomizing gas. The dynamic force, in this case, is approximately 61 psi, surpassing the critical pressure ratio and therefore reaching, at the throat of the atomizing nozzle, the critical velocity, equivalent to the velocity of sound at the temperature of the

Table 4

Characterizations of Microfog Generator

Item	Misting Head				Flow Rate		Pressure, psi		Mean Particle Size			
	Orifice Diameter (in)	No. of Orifice	Impactor (in)	Screen	Oil[a]	Gas[b] (cfm)	Microfog Generator	Chamber	n_i[c]	$\frac{\sum n_i d_i^3}{(\mu m)^3 \times 10^{-3}}$	$\bar{d}_i$ (μm)	$\bar{d}_z$ (μm)
1	0.0635	2	None	None	2	2	73	12	5,811	147.2	1.73	2.94
2	"	"	1	150 mesh	2	2	72	11.5	6,303	89.4	1.37	2.42
3	"	"	2	¼" grid	2	2	72	12	6,233	189.7	1.81	3.12
4	0.0635	2	2	¼" grid	½	2	73	12	4,903	62.7	1.38	2.34
5	"	"	"	"	1	2	73	12	6,002	224.9	1.91	3.34
6	"	"	"	"	2	2	73	12	6,282	217.7	1.88	3.26
7	"	"	"	"	4	2	73	12	5,271	155.4	1.73	3.08
8	0.0635	2	2	¼" grid	2	2	72	12	6,233	189.7	1.81	3.12
9	"	3	"	"	2	2	27	11	4,015	8.7	0.95	1.28
10	0.0890	2	"	"	2	2	20	11	3,480	52.6	1.41	2.47
11	0.0635	2	2	¼" grid	2	2	72	12	6,233	189.7	1.81	3.12
12	"	"	"	"	2	2.6	130	13	5,183	77.7	1.50	2.47
13	0.0635	3	2	¼" grid	2	2	27	11	4,015	8.7	0.95	1.28
14	"	3	"	"	2	3	68	13	5,414	92.6	1.55	2.58
15	"	3	"	"	2	4	120	15	3,557	18.0	1.27	1.72
16	0.0890	2	2	¼" grid	2	2	20	11	3,480	52.6	1.41	2.47
17	"	"	"	"	2	3	37	12	6,493	349.7	2.20	3.77
18	"	"	"	"	2	4	71	14	4,595	103.6	1.97	3.48
19	"	"	"	"	2	5	113	17	3,881	48.0	1.35	2.31

Note: (a) the number of turns of set-screw.

(b) ft^3/min at 45 psi and 200°F.

(c) the number of particles counted in 10 sec. period.

Figure 19

ATOMIZING NOZZLES AND IMPACTORS

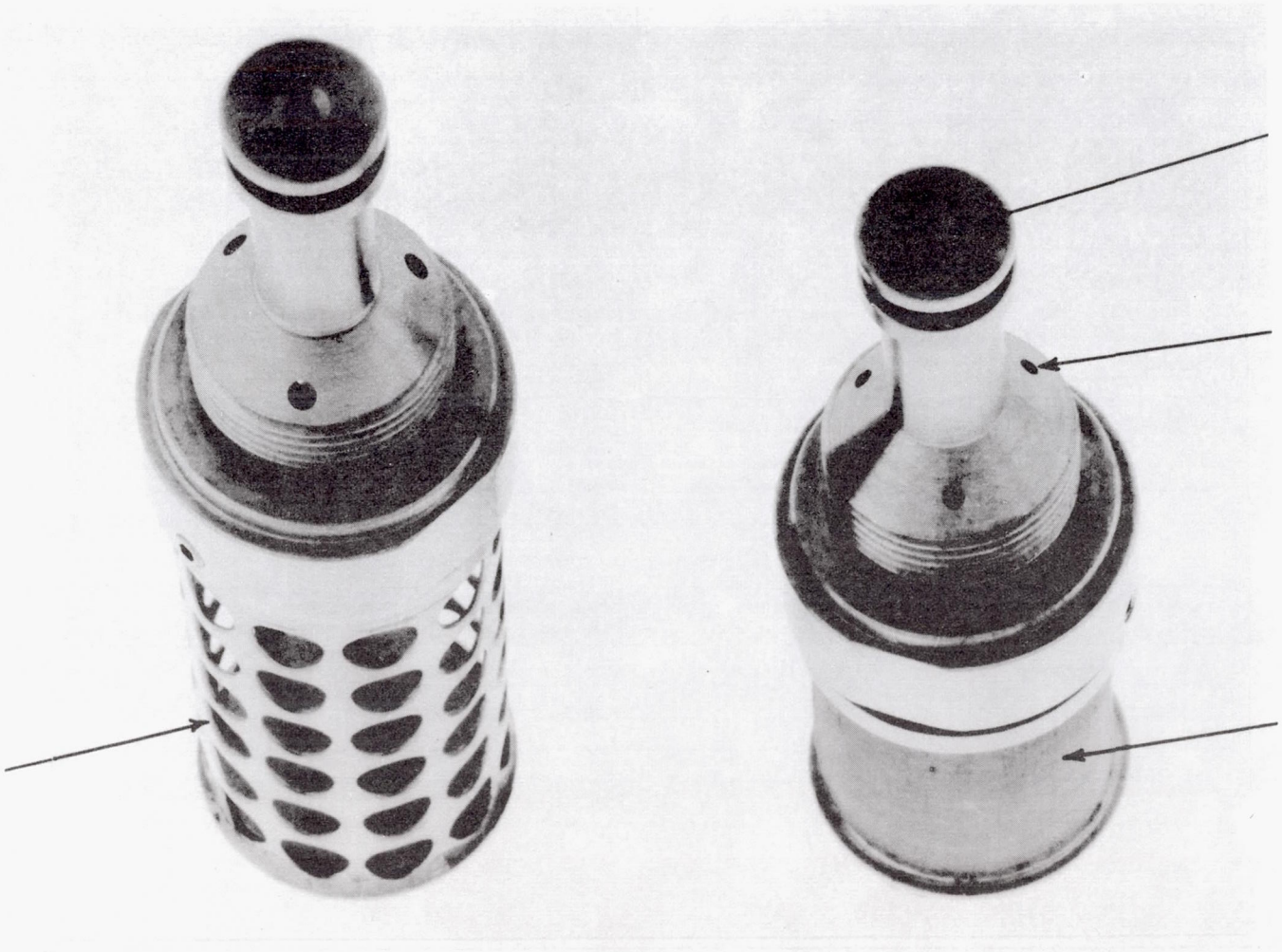

nozzle, and estimated to be 1,300 ft/sec at 200°F. Decreased values of $\sum_{i=1}^{N} n_i d_i^3$, $\bar{d}_1$, and $\bar{d}_2$ in Item (2) suggests that the combination of a finer screen (150 mesh instead of 1/4" grid) and a shorter impactor distance (1" instead of 2") does effectively screen out large particles. An increase in $\sum_{i=1}^{N} n_i$ further affirms this conclusion. However, comparison between Items (1) and (3) suggests that the 2" impactor with 1/4" grid has little effect on particle size distribution, apparently failing to effectively screen out large particles under the conditions tested.

In the series of runs represented by Items (4) to (6), an effort was made to investigate the effect of oil flow rate on particle size, although the amount of oil flow is critically limited by operating gas pressure. With the internal-siphon types, which include the generator used in this study as well as most commercially available generators for mist lubrication, it must be recognized that the operating variables are interlocked so that one variable cannot be changed without affecting the others. For this reason, it is extremely difficult to study independently the effects of these operating variables on particle size distribution. Nevertheless, an attempt was made to establish a functional relationship, hoping to better understand the roles of the atomizing nozzle in a microfog generator.

Prior to the measurements of particle size distribution for this study, the basic relations for flow of oil through an atomizing nozzle were examined in order to estimate the rates of oil flow under various conditions. Following the schematic diagram of oil flow through the orifice of an atomizing nozzle, shown in Figure 20, and assuming no other energy loss except friction, for steady mass flow the total energy balance can be simply expressed as:

$$\Delta h + \frac{\Delta P}{\rho} = \frac{(\Delta U_L)^2}{2g_c} + \frac{32(\Delta h)\nu U_L}{g_c D_o^2} \qquad (5)$$

Using Equation (5), the calculated values of ΔP and U_L for the present generator (Δh = 1" and D_o = 0.0635") and for XRM 177 F at 200°F are listed below:

Figure 20

SCHEMATIC DIAGRAM OF OIL FLOW
THROUGH THE ORIFICE OF AN ATOMIZING NOZZLE

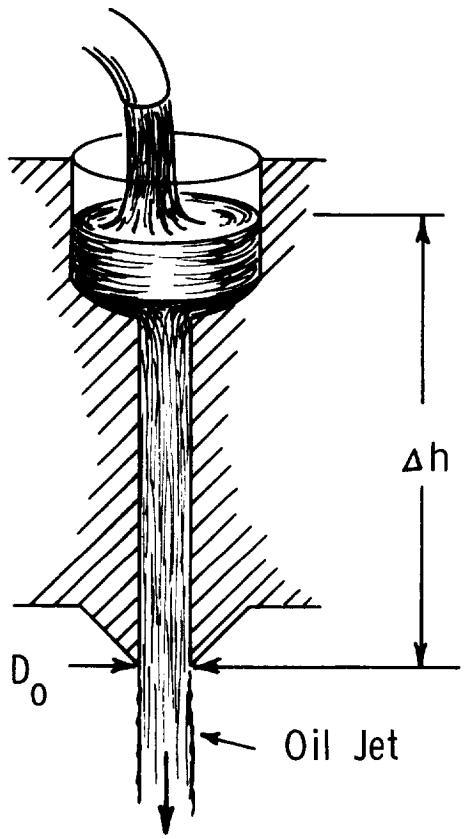

U_L (ft/sec)	Rate of Oil Flow thru Orifice (cm^3/sec)	ΔP (lb/in^2)
0.1	0.06	0.023
1	0.6	0.49
2	1.19	1.03
4	2.36	2.14

The above table is for a limited case and is incomplete. However, it clearly indicates that the atomizing nozzle does not require a very high pressure drop across the nozzle to establish a considerable amount of oil flow through the orifice. For example, at a pressure drop of 1.0 psi, the rate of oil flow can be 1.2 cm^3/sec for the present generator with the adjusting screw set for a wide-open orifice. The adjusting screw for the orifice controls the rate of oil flow by changing the cross-sectional area of oil flow in accordance with the opening of the orifice. Thus, knowing the values of ΔP and D_o, the total oil flow through the orifice can be estimated using Equation (5).

For Items (4) to (7), the rate of oil flow was varied by adjusting the orifice set-screw at different points while maintaining all other operating variables the same as Item (3). Under these conditions, estimated values of total oil flow rate at 1/2 and 1 turns of the set-screw are 2 and 5 cm^3/min, respectively. As shown in Table 4, increasing oil flow seems to increase particle size as well as $\sum_{i=1}^{N} n_i d_i^3$ up to a point. Comparison of Items 4 and 5 shows an abrupt increase of particle size and $\sum_{i=1}^{N} n_i d_i^3$, when the set-screw is opened from 1/2 turn to 1 full turn. However, with the set-screw opened further, values of particle size and especially $\sum_{i=1}^{N} n_i d_i^3$ tend to decrease, as indicated by Item 7. This result may be an indication that, as Equation (4) suggests, increasing relative velocity decreases particle size.

Items (8) to (10) represent a study of geometrical configurations and sizes of the atomizing nozzle. The study was conducted by varying both the size of orifices through which the atomizing gas passed and the number of orifices, which were placed in a

symmetrical configuration, while other conditions were maintained constant. The values of particle sizes and $\sum_{i=1}^{N} n_i d_i^3$ are widely divergent, and may not be a true reflection of the study intended, as the dynamic forces of the atomizing gas vary depending upon the total cross-sectional area available for the atomizing gas, which, in turn, changes the rate of oil flow through the orifice. Thus, these results emerge from the combined effects of these various factors.

The effect of atomizing gas pressure (or power requirement) on particle size is indicated through Items (11) to (19). In order to obtain different atomizing gas pressures, the total flow area of gas was varied by selecting three different atomizing nozzles, and gas flow rates were varied between 2 and 5 cfm. Here again, it is difficult to single out the effect of power requirements on particle size because the rate of oil flow is affected whenever the atomizing gas pressures change. Test results, however, indicate that particle size increases with increased dynamic force of the atomizing gas up to a critical pressure which is a function of atomizer design, and beyond which particle size decreases with increasing gas pressure. These results are in agreement with Nukiyama's correlation, but fail to show why an inflection point at a critical pressure (or a critical particle size) exists with this type of generator. This behavior may, however, be merely a reflection of differences in generator design.

At a glance, the particle sizes after the inflection point can be expressed in a mathematical form of the following type:

$$\bar{d} = \alpha_1 P^{\alpha_2} \qquad (6)$$

where $P = \frac{1}{M_W} \frac{M_G}{M_L} RT \ln \frac{P_2}{P_1}$

The parameters α_1 and α_2 may be dependent upon atomizer design, α_1 also may change as physical properties of the oil change.

ii) Effect of Nozzle Sizes and Configurations

In efforts to gain the knowledge needed to extend the available microfog particle size range, particle size distribution data for XRM 177 F were obtained with a number of different spray nozzles. All five nozzles shown in Figure 21 were tested to determine whether or not these nozzles would influence particle

Figure 21

NOZZLE SIZES AND CONFIGURATIONS

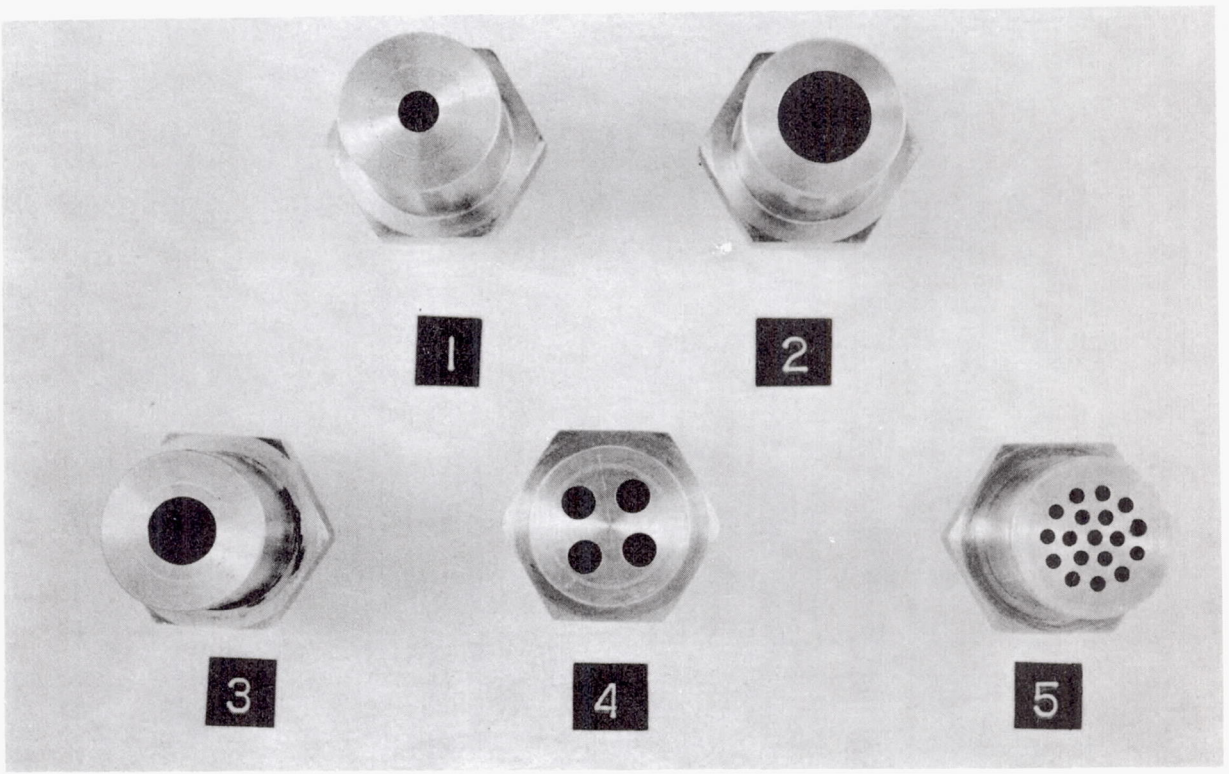

Nozzle No.	Orifice Diameter (in.)	No. of Orifices	Total Flow Area ($in.^2$)
1	0.171	1	0.023
2	0.390	1	0.120
3	0.281	1	0.062
4	0.141	4	0.062
5	0.067	18	0.063

size distribution, and if so, by what physical processes. Experimental results revealed that differences in the configurations of Nos. 3, 4, and 5 nozzles had virtually no effect on particle size distribution. This probably means that there is no measurable degree of coalescence among microfog particles. However, when microfog was sprayed continuously for an extended period, the propagation of periodic bursts of large particles was observed. These large particles clearly were formed by the mechanism of wetting-out and not by coalescence as claimed by some. The frequencies of propagation were, however, not high enough to affect overall particle size. It is apparent from these results that so called "reclassifying" nozzles, of the types shown in Figure 21, which are claimed commercially to increase particle size through coalescence, cannot sufficiently extend the particle size range available for wetting rate studies.

In an effort to develop nozzles with the required effects on particle size, several nozzles were crudely modified to increase impaction and turbulence within the nozzle. This investigation included nozzle Nos. 1, 3, and 5, No. 5 nozzle packed with 0.2 gm. of superfine steel wool, and with 30 glass beads of 1.5 ∿ 2.0 mm diameter, and No. 3 nozzle packed with a combination of 150 mesh screens and 10 glass beads of 4 mm diameter.

All particle size distribution data were obtained at a gas flow rate of 3 cfm, with the generator pressure between 37 and 40 psi, and the test chamber at 12 psi. Results, reported as the average of 2 runs, are summarized in Table 5.

The mean particle sizes, $\bar{d}_1$, $\bar{d}_2$ and $\bar{d}_3$ (refer to definition of these terms), not only fail to increase with the use of the standard reclassifying nozzles, but slightly decline, as illustrated in Items (1) to (4). There also is no great difference in the particle size distribution. However, comparisons of the total volumes of the particles, $\sum_{i=1}^{N} n_i d_i^3$, in Table 5, reveal reductions in the total volume of the particles counted where standard reclassifiers are employed. When the nozzles packed with materials to increase impaction and turbulence within the nozzles are employed, reductions in $\sum_{i=1}^{N} n_i$ and $\sum_{i=1}^{N} n_i d_i^3$ are more dramatic, as indicated in Items (5), (6), and (7). These drastic reductions in n_i are graphically illustrated in Figures 22 and 23, by taking particle size distribution data obtained for the runs represented by Items (4) and (5). Figure 22, representing an incremental frequency curve on a number basis, clearly shows re-distribution

Table 5

Effect of Nozzle Configurations on Particle Size*

Item	Spray Nozzle	Pressure, psi			Mean Particle Size				
		Generator	Nozzle	Chamber	n_1+	$n_1 d_1^3$ $(\mu m)^3 \times 10^{-3}$	$\bar{d}_1$ (μm)	$\bar{d}_2$ (μm)	$\bar{d}_3$ (μm)
1	None	37	12	12	6,535	330.9	2.15	3.71	5.5
2	Nozzle No. 1 (0.171" dia)	40	22	12	4,949	174.3	1.89	3.31	5.4
3	Nozzle No. 3 (0.281" dia)	38	13	11	5,481	178.0	1.80	3.16	5.1
4	Nozzle No. 5 (18 holes)	37	13	11	5,813	150.0	1.78	2.95	5.0
5	Nozzle No. 5 packed with 0.2 gm of superfine steel wool	39	18	12	2,461	7.7	0.95	1.46	3.7
6	Nozzle No. 5 packed with 30 glass beads (1.5 ~ 2.0 mm dia)	39	19	12	2,608	23.2	1.15	2.07	-
7	Nozzle No. 3 packed with a combination of 150 mesh screen and 10 glass beads (4 mm dia)	40	22	12	3,409	37.6	1.25	2.15	-

* This study was made on XRM-177F at 3 cfm with a Misting head having two orifices (0.0890" diameter) and 2" impactor with $\frac{1}{4}$" grid.

+ The number of particles counted in 10 second period.

Note: $\bar{d}_1$ - Arithmetic mean diameter

$\bar{d}_2$ - Mean Volume diameter

$\bar{d}_3$ - Mass Median diameter

Figure 22

n_i VERSUS PARTICLE SIZE
XRM 177 F; 3 cfm

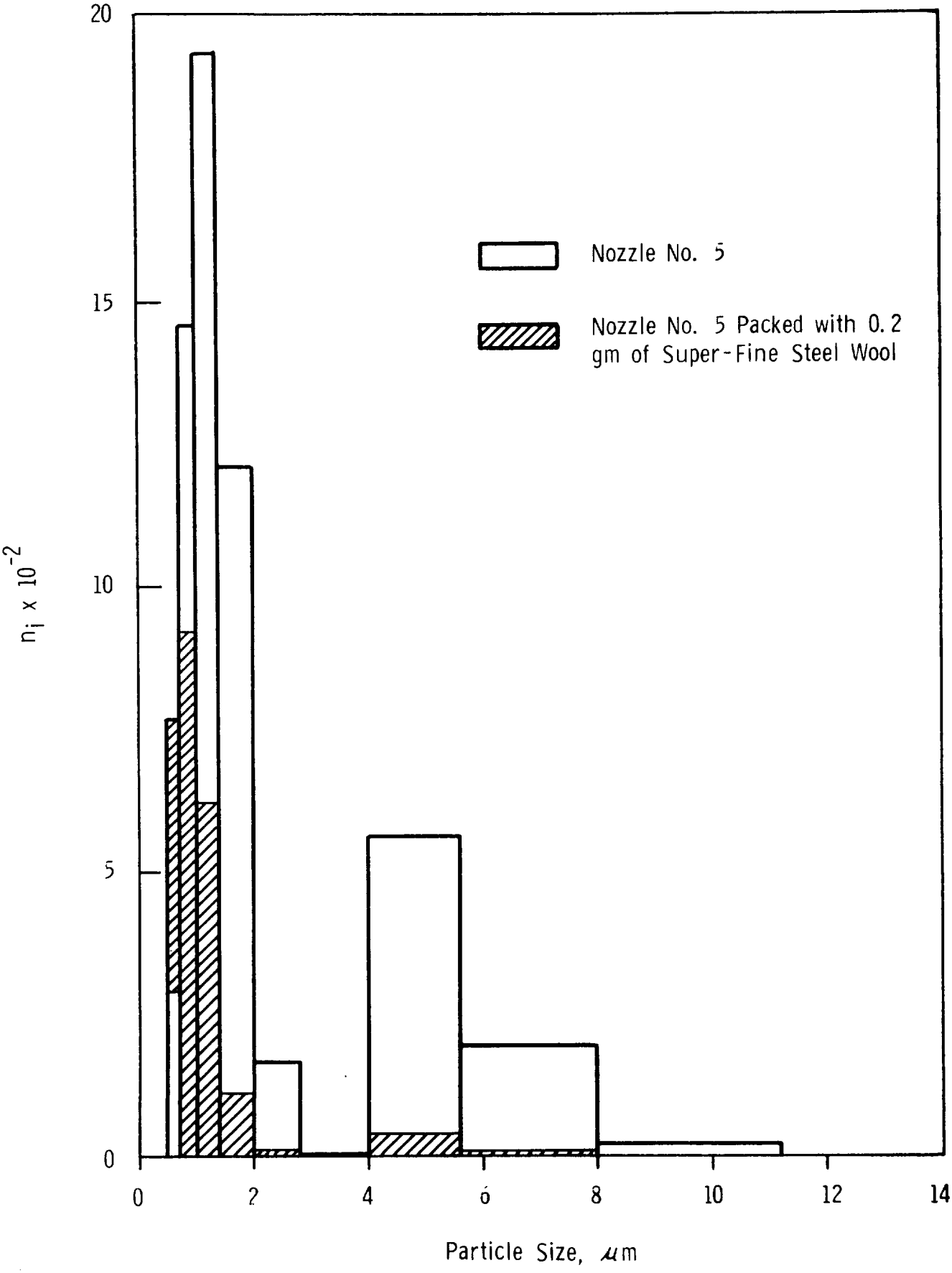

Figure 23

CUMULATIVE PARTICLE SIZE DISTRIBUTION CURVES

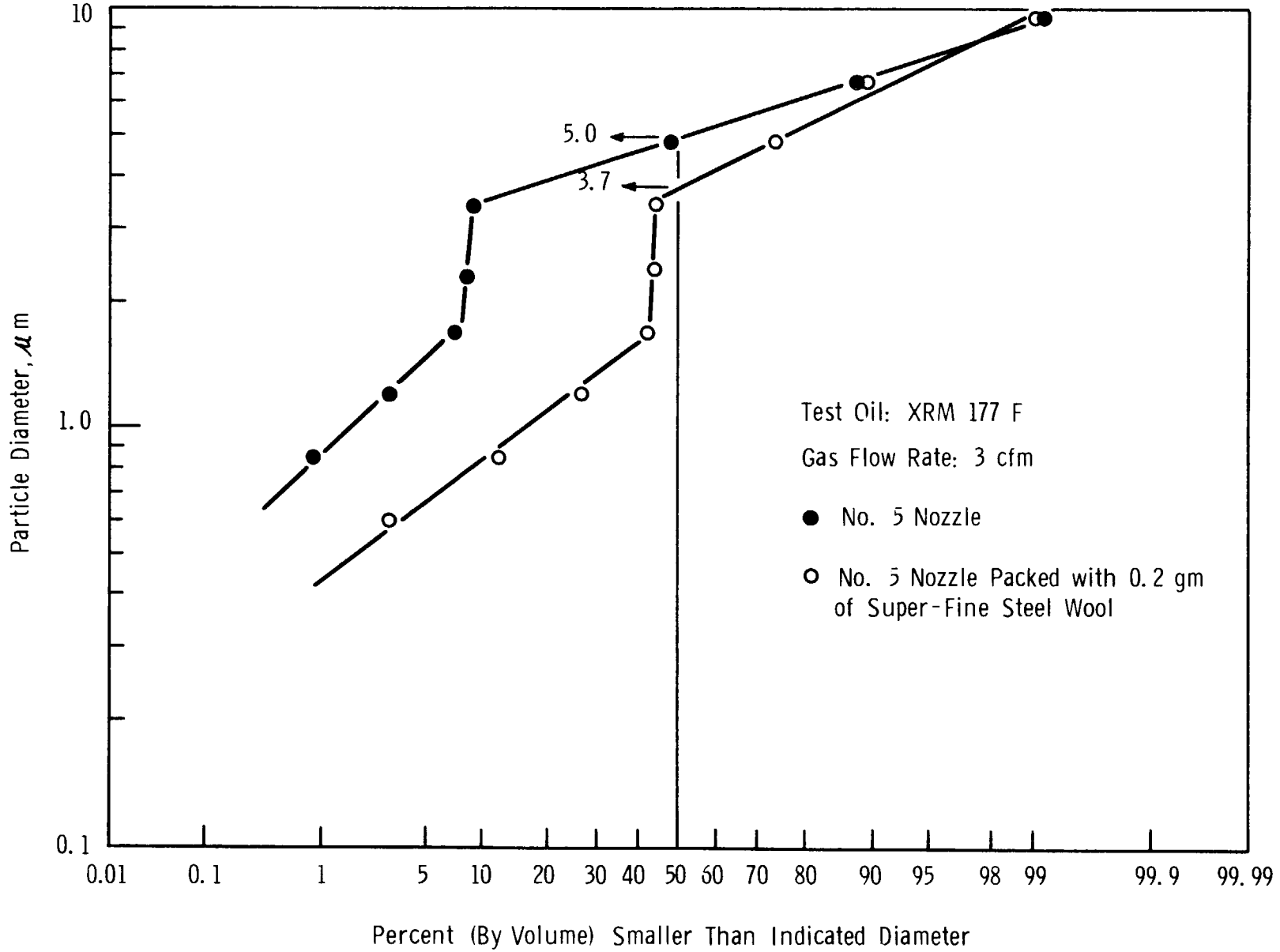

of the particle sizes when the packing material is introduced into the No. 5 nozzle. The curves shown in Figure 23 correspond to cumulative (integral) distribution curves (by volume) in a log-probability scale for the same data, and indicate a shift of particle size distribution, reflecting the reclassifying actions of the nozzles. Figure 23 also gives the mass median diameters of these systems, 5.0 μm for No. 5 nozzle and 3.7 μm for No. 5 nozzle packed with superfine steel wool, respectively. These mass median diameters are usually established from the 50 percent point on the cumulative curve, as shown in Figure 23.

In considering the dramatic reductions in total volume counted for the modified nozzles, it should be noted that extra precautions were taken in obtaining these data in order to eliminate a possibility that the reduced counts with the modified reclassifying nozzles are caused by collection of oil particles within the nozzles. By counting particles at different times, it was shown that for each nozzle the particle count reaches equilibrium before determination of the particle size distributions here compared. Furthermore, it can reasonably be assumed that the different nozzles tested in this series have no effect on the quantities and sizes of the particles produced by the microfog generator, although there are slight differences in power requirements for atomization. This leads to the conclusion, based on mass balance data, that modified reclassifiers are producing particles larger than the 32 μm upper limit of the present counter, but are not producing appreciable numbers of particles in the 11 to 32 μm range. Hence, although these modified reclassifying nozzles apparently can be quite efficient in converting small to much larger particles, they do not appear to provide a feasible approach to average particle sizes in the upper portion of the range chosen for study - i.e., 11 to 32 μm. Presumably, considerably higher kinetic energy (or power) than that available in the nozzles at present flow rates is required to re-atomize to suitable particle sizes the oil collected in the nozzles by impaction.

Keeping these power requirements for re-atomization in mind, nozzle Nos. 1A and 3A, shown in Figure 24, were designed. A schematic diagram of these nozzles is depicted in Figure 25, where they are compared with nozzle Nos. 1, 2, and 3. Following the results described in Table 5, the designs of nozzles 1A and 3A aim primarily at improved re-atomization of the oil collected in the packing materials within the nozzles and at better defined configurations of the nozzles, moving away from random packings. The five nozzles shown in Figure 24 were employed for the studies of particle velocity distribution, size distribution, and wetting rate throughout this project.

Figure 24

SIZE AND CONFIGURATION OF EXPERIMENTAL SPRAY NOZZLES

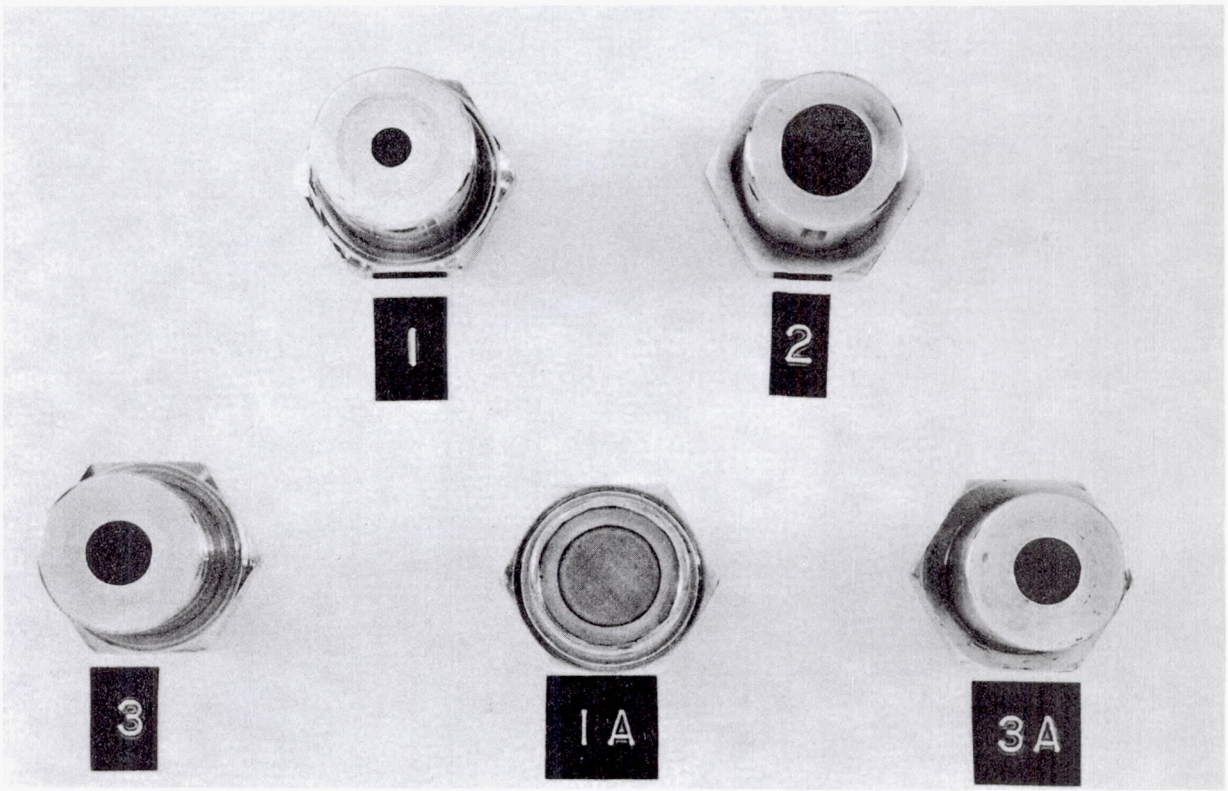

Nozzle No.	Nozzle Type	Orifice Diameter (in.)	No. of Orifices	Total Flow Area (in.^{2})
1	Convergent	0.171	1	0.023
2	Convergent	0.390	1	0.120
3	Convergent	0.281	1	0.062
1 A	deLaval type of nozzle with one layer of 150 mesh screen in expansion section	0.171	1	0.023
3 A	No. 3 nozzle packed with 3 layers of 150 mesh screen in converging section	?	?	?

Figure 25

SCHEMATIC DIAGRAM OF EXPERIMENTAL SPRAY NOZZLES

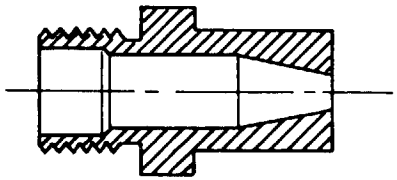

1

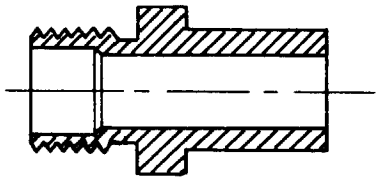

2

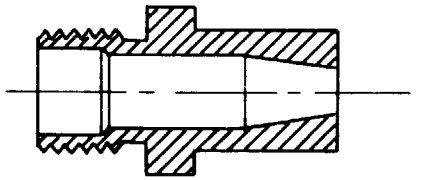

3

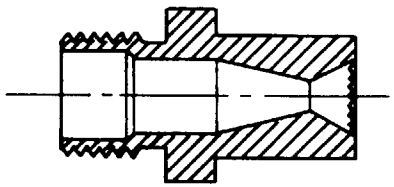

1A

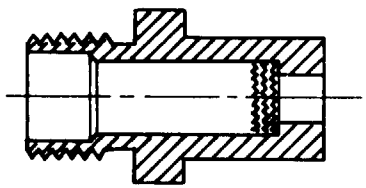

3A

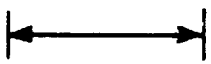

1" Scale

iii) Particle Size Distributions of Different Test Oils

Determinations of the microfog particle sizes and distributions for the five test oils were made with five different nozzles at gas flow rates of 2, 3, 4, 5, and 6 cfm. The nozzles included are Nos. 1, 2, 3, 1A, and 3A. Particle size distribution data obtained in this series are listed in Appendix C-3, and the mean particle sizes determined by different methods are summarized in Table 6.

As was described in the previous report (21), representations of particle size distributions by different methods have considerably different physical significances depending upon their applications. For instance, arithmetic mean diameter is suggested for comparison of particle size distribution on a number basis relating to the evaporation of liquid drops. For comparison of the distribution of mass in a spray, however, the application of mean volume diameter is more meaningful. In addition to arithmetic mean and mean volume diameters, median diameter data also are included in Table 6. The median diameter of a spray is that diameter which divides the spray into two equal portions by either number: volume, or mass.

Although mean volume diameters are most meaningful for the study of wetting rate, they may not be as accurate as desired for translation into other properties, such as total mass flow, since an optical analyzer such as the one used in this study is primarily designed for number countings.

Because general discussion or comparison of the great mass of particle size distribution data would be exceedingly cumbersome, the data are best considered independently as individual cases. From the summary of mean particle sizes*, we can, however, draw the general conclusions that for a given condition, XRM 177 F and Turbo Oil 4040, in general, produce the largest particle size and that the physical properties of the oil and the concentration of oil particles suspended in the gas stream are the important factors affecting the action of the nozzle in regulating particle size. The results also suggest that the spray nozzles respond quite differently to operating conditions, depending upon gas flow rate and type of oil used, and consequently the design of an optimum nozzle becomes a function of operating variables. Thus, each given set of conditions will have its own optimum nozzle design. Table 6 also indicates that none of the nozzles used in this study could effectively generate mean particle sizes (in any form of mean sizes) of approximately 8 and 16 μm, which originally were to be included in this study. It is, however, not clear at present whether the absence of large particles in these particle

*No specific type of average size is referred to here.

Table 6

Summary of Mean Particle Sizes

Item	Test Oils	Nozzle No.	Arithmetic Mean Diameter, μm					Mean Volume Diameter, μm					Mass Median Diameter, μm				
			2 cfm	3 cfm	4 cfm	5 cfm	6 cfm	2 cfm	3 cfm	4 cfm	5 cfm	6 cfm	2 cfm	3 cfm	4 cfm	5 cfm	6 cfm
	XRM-177F																
1		1	0.87	1.89	2.09	2.04	2.05	0.94	3.31	3.68	3.65	4.12	0.88	5.40	5.80	5.80	7.00
2		2	1.08	1.80	1.62	1.25	1.38	1.89	3.21	2.84	2.12	2.47	4.05	5.40	5.15	4.20	4.70
3		3	0.90	1.80	1.65	1.29	1.52	1.62	3.16	2.96	2.24	2.82	4.70	5.10	5.10	4.30	4.85
4		1A	0.88	1.41	1.52	1.70	1.82	1.71	2.63	2.86	3.13	3.40	5.60	5.00	5.30	5.60	5.80
5		3A	0.75	1.26	1.68	2.09	1.84	1.13	2.42	3.10	3.68	3.43	1.20	5.00	5.60	4.50	5.70
	Hercolube-F																
6		1	1.02	1.42	1.32	1.40	1.33	1.13	2.06	2.02	2.35	2.12	1.10	4.00	4.20	4.70	4.50
7		2	0.98	1.21	1.11	1.03	0.97	1.08	1.80	1.59	1.49	1.18	1.05	3.90	3.70	3.65	1.25
8		3	0.99	1.19	1.13	1.10	1.01	1.08	1.69	1.68	1.45	1.42	0.70	3.80	3.90	3.50	3.90
9		1A	0.93	1.30	1.48	1.41	1.67	1.03	2.06	2.36	2.86	2.75	1.02	3.50	4.30	4.60	4.85
10		3A	0.83	1.24	1.44	1.43	1.72	1.03	2.08	2.30	2.17	2.73	1.10	4.85	4.65	4.50	4.85
	Sunthetic 18H(B)																
11		1	0.89	0.98	0.99	0.91	1.00	0.99	1.27	1.24	1.14	1.63	0.95	1.30	1.60	1.35	4.00
12		2	0.91	0.97	0.90	0.87	0.88	0.99	1.22	1.25	1.26	0.98	0.98	1.40	1.70	3.50	0.97
13		3	0.92	0.94	0.87	0.86	0.87	1.01	1.03	0.96	0.95	0.97	1.00	0.98	0.99	0.92	1.03
14		1A	0.94	0.95	0.99	0.94	1.25	1.05	1.05	1.32	1.04	2.14	1.05	1.10	1.90	1.00	3.70
15		3A	0.89	0.96	0.93	0.88	0.96	1.01	1.08	1.04	0.99	1.07	1.05	1.07	1.05	0.97	1.05
	Turbo Oil 4040																
16		1	1.54	1.65	1.52	1.49	2.00	2.55	2.64	2.52	2.58	3.37	4.50	4.40	4.50	4.80	5.60
17		2	1.48	1.37	1.23	1.19	1.25	2.45	2.15	1.81	1.60	2.51	4.50	4.10	3.90	3.80	6.10
18		3	1.44	1.33	1.31	1.19	1.28	2.33	2.16	2.06	1.76	2.31	4.30	4.50	4.10	3.90	4.85
19		1A	1.00	1.27	1.78	2.52	2.93	1.62	2.19	3.02	4.10	4.77	4.25	4.50	5.00	6.10	6.50
20		3A	0.90	1.23	1.75	2.26	2.43	1.55	2.10	2.98	3.59	4.01	5.00	4.40	4.85	5.70	5.70
	Ucon 50-HB-5100																
21		1	0.77	1.08	1.24	1.18	1.28	0.83	1.62	2.09	1.96	2.10	0.78	3.60	4.30	4.20	4.20
22		2	0.77	1.17	1.04	0.84	0.92	0.84	1.91	1.59	0.91	1.19	0.78	4.10	3.85	1.15	1.45
23		3	0.78	1.15	1.14	0.88	0.90	0.84	1.77	1.86	1.15	1.16	0.80	4.00	4.00	1.40	1.20
24		1A	0.73	0.90	1.03	1.14	1.18	0.79	1.33	1.63	1.96	2.06	0.74	3.70	4.20	4.30	4.40
25		3A	0.73	0.83	1.03	1.12	1.10	0.78	1.27	1.72	1.93	1.85	0.74	3.90	4.20	4.30	4.20

size distributions is due to inability of the nozzles to produce the large particles or to limited capability of the particle counter. This question will be further discussed in the following section.

iv) Comparison of the Particle Size Distributions of Test Oils

Listed in Table 7 are the particle size distribution data for the different test oils, and their mean particle diameters in several forms, determined with No. 3 nozzle at a gas flow rate of 3 cfm. This particular operating condition was chosen to illustrate the effects of different oils on particle size distribution in view of the fact that all other data show basically a similar trend. The corresponding cumulative (integral) particle size distribution curves are also shown in Figure 26, where particle diameter is plotted against percent (by volume) of the particles smaller than the indicated diameter in a log-probability scale. Results, in general, indicate that as described in Table 7, XRM 177 F produces the largest mean particle size under the given operating condition, and that the number frequency curves of these oils represent a bi-modal distribution with the exception of that for Sunthetic 18H(B), which exhibits a uni-modal distribution.

From Appendix C-3, the data of Table 8 have been selected to show the effect of nozzle configurations on particle size distribution. It is found that not only the values of $\sum_{i=1}^{N} n_i$, but the mean particle sizes generated by nozzle Nos. 1A and 3A are smaller than those produced by the other nozzles. Reduction in number counted and decrease in mean particle size are somewhat confusing and are entirely opposite to what originally was intended with these nozzles, which were aimed at increasing the number of large particles in the size range of 4 μm or higher.

The results cited create an uncertainty regarding the entire particle size measurement by the present particle counter because the absence of relatively large particles (11 μm or larger) in particle size distribution, particularly with No. 1A or No. 3A nozzles, is unexplained. Hence, several aspects of the particle sampling technique were examined in an attempt to determine the probable causes of this result.

The absence of the large particles may be attributable to one or a coupling of the following factors: (1) anisokinetic sampling, (2) gravitational settling, (3) discriminatory dilution of particle concentration, and (4) failure of the experimental spray nozzles to generate the large particles.

Figure 26

CUMULATIVE PARTICLE SIZE DISTRIBUTION CURVES

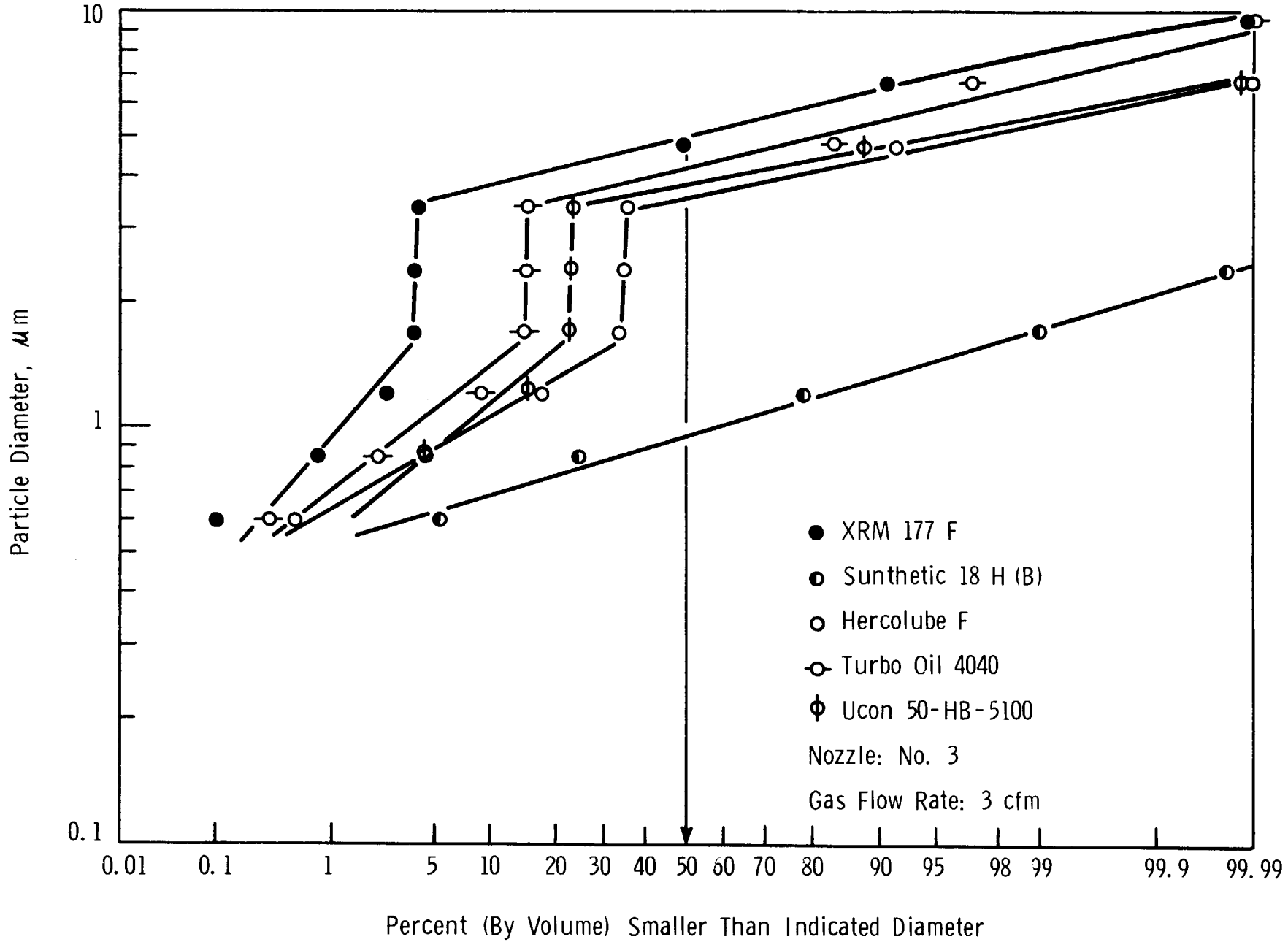

Table 7

Particle Size Distribution of Different Test Oils*

Channel No.	Particle Size (μm)	XRM-177F	Hercolube-F	Sunthetic 18H(B)	Turbo Oil 4040	Ucon 50-HB-5100
1	0.6	460	612	768	691	955
2	0.9	1083	1680	991	1665	1571
3	1.2	1109	2024	995	2131	1853
4	1.7	280	777	135	586	398
5	2.4	5	30	2	16	4
6	3.4	0	1	0	0	0
7	4.8	474	132	0	349	165
8	6.8	149	7	0	23	10
9	9.6	12	0	0	2	0
10	13.6	0	0	0	0	0
11	19.2	0	0	0	0	0
12	27.2	0	0	0	0	0
Arithmetic Mean Diameter, μm		1.8	1.2	0.9	1.3	1.1
Mean Volume Diameter, μm		3.2	1.7	1.0	2.2	1.8
Mass Median Diameter, μm		5.0	3.6	1.0	4.2	4.0

*Test Conditions: No. 3 Nozzle, 3 cfm, and 10 sec. sampling time.

Table 8

Effect of Nozzle Configuration on Particle Size Distribution*

Channel No.	Particle Size (μm)	Nozzle No.				
		1	2	3	1A	3A
1	0.6	443	469	460	602	587
2	0.9	1305	1267	1083	1018	824
3	1.2	1681	1427	1109	906	660
4	1.7	583	442	280	140	83
5	2.4	15	7	5	0	2
6	3.4	0	0	0	0	0
7	4.8	578	485	474	254	133
8	6.8	252	200	149	56	35
9	9.6	33	25	12	7	6
10	13.6	0	0	0	0	0
11	19.2	0	0	0	0	0
12	27.2	0	0	0	0	0
Arithmetic Mean Diameter, μm		1.9	1.8	1.8	1.4	1.3
Mean Volume Diameter, μm		3.3	3.2	3.2	2.6	2.4
Mass Median Diameter, μm		5.4	5.4	5.1	5.0	5.0

*Test conditions: XRM-177F, 3 cfm, and 10 sec. sampling time.

Phenomena taking place at the inlet of a sampling tube, depending on the ratio of flow rates inside and outside the sampling tube, and on the angle between the sampling tube and flow direction, must create some difference in concentration and particle size distribution between a microfog stream and the microfog sample withdrawn. The relationship between the efficiency of sampling by a tube and the ratio of the flow rates outside and inside the tube, shown in Figure 27, which is taken from Watson's work (15 & 25) indicates that the sampling efficiency increases with increasing ratio of stream velocity to sampling velocity and with increasing particle size. According to this work, we would expect samples to show an increase, rather than a decrease, of the relatively large particles in the particle size measurements, since the ratio of the stream velocities used in this study ranges from 1 to 3. For this reason, anisokinetic sampling does not appear to be the main cause for the absence of the relatively large particles in the particle counter.

Assuming that the relatively large particles are introduced in a sampling tube, then the particles must be transported through a tube to an optical sensing zone. When the particle stream consists of large particles moving slowly through the tube (N_{Re} $<2,400$), we may experience decreases in the average concentration of the particles because of gravitational settling. Figure 28, taken from Mitchell's work (16), shows that at the transport velocity of 600 ft/min the loss due to settling for particles of 12 and 25 μm does not exceed, at most, 5 and 13 percent of the original concentration, respectively. This evidence seems to suggest that gravitational settling cannot explain entirely the absence of the large particles.

By the process of elimination, if these large particles are known to exist in a spray system, the two preceding conclusions lead to the further conclusion that discriminatory dilution by the two dilution stages seems to play a principal role in eliminating the large particles from the microfog stream - i.e., the large particles are selectively removed from the microfog stream, possibly because of particle size distributions along the tube and pressure gradients induced by the dilution pumps. No effort has been made to confirm this conclusion at present. However, when an opportune time arises, this possible behavior of the particle counter will be investigated. If discriminatory dilution occurs, it may seriously limit the applicability of a particle counter with two-stage diluters to the higher ranges of particle size.

Before accepting these conclusions, efforts were made to insure that relatively large particles actually are produced under certain spray conditions, and to estimate the sizes of these particles. With these objectives, determinations of particle size distribution for relatively large particles (11 μm or larger) were made with XRM 177 F by employing a cascade impactor technique as

Figure 27

ANISOKINETIC SAMPLING ERROR (15 and 25)

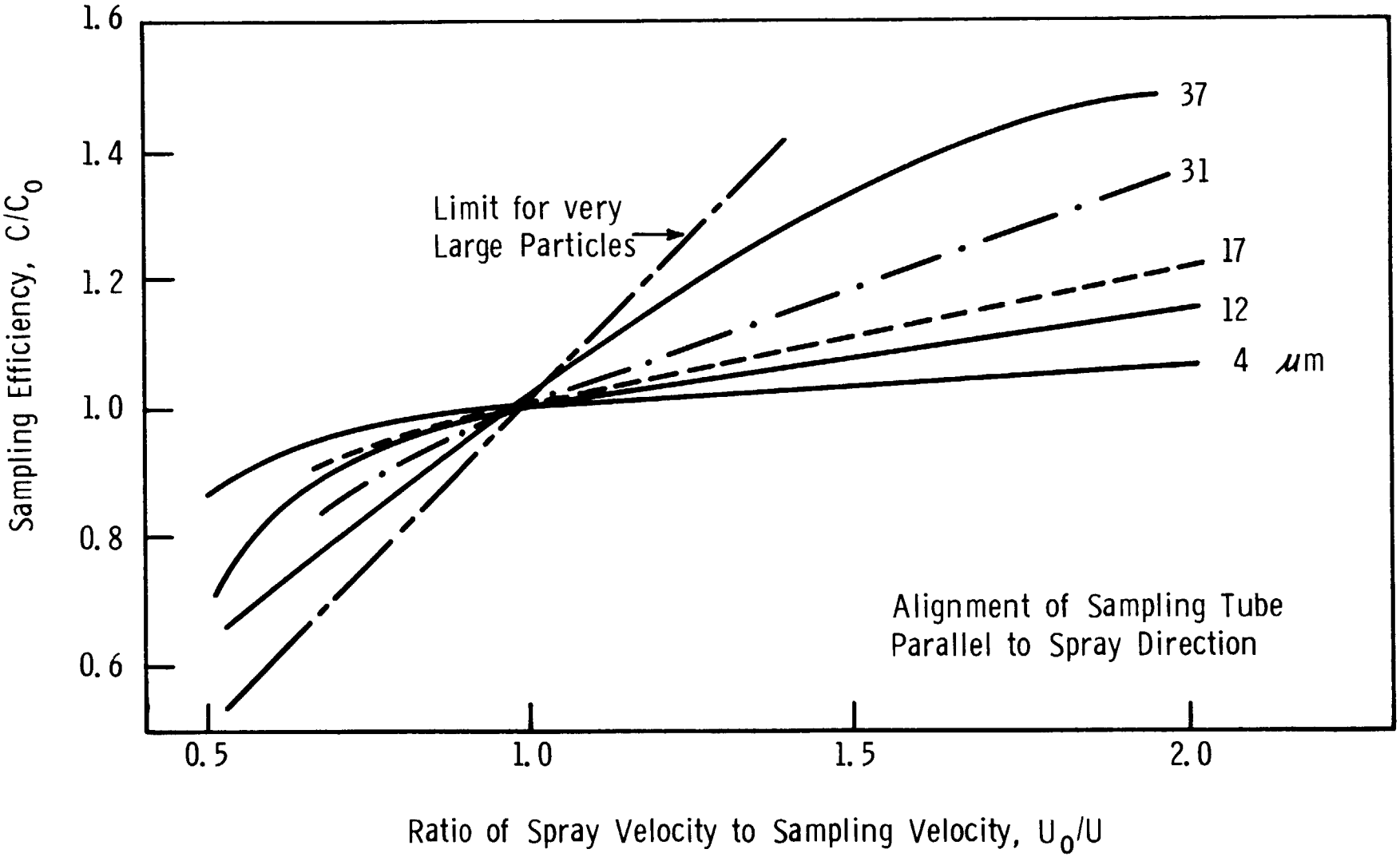

Figure 28

DECAY OF OIL PARTICLE CONCENTRATION AS A FUNCTION OF TRANSPORT VELOCITY

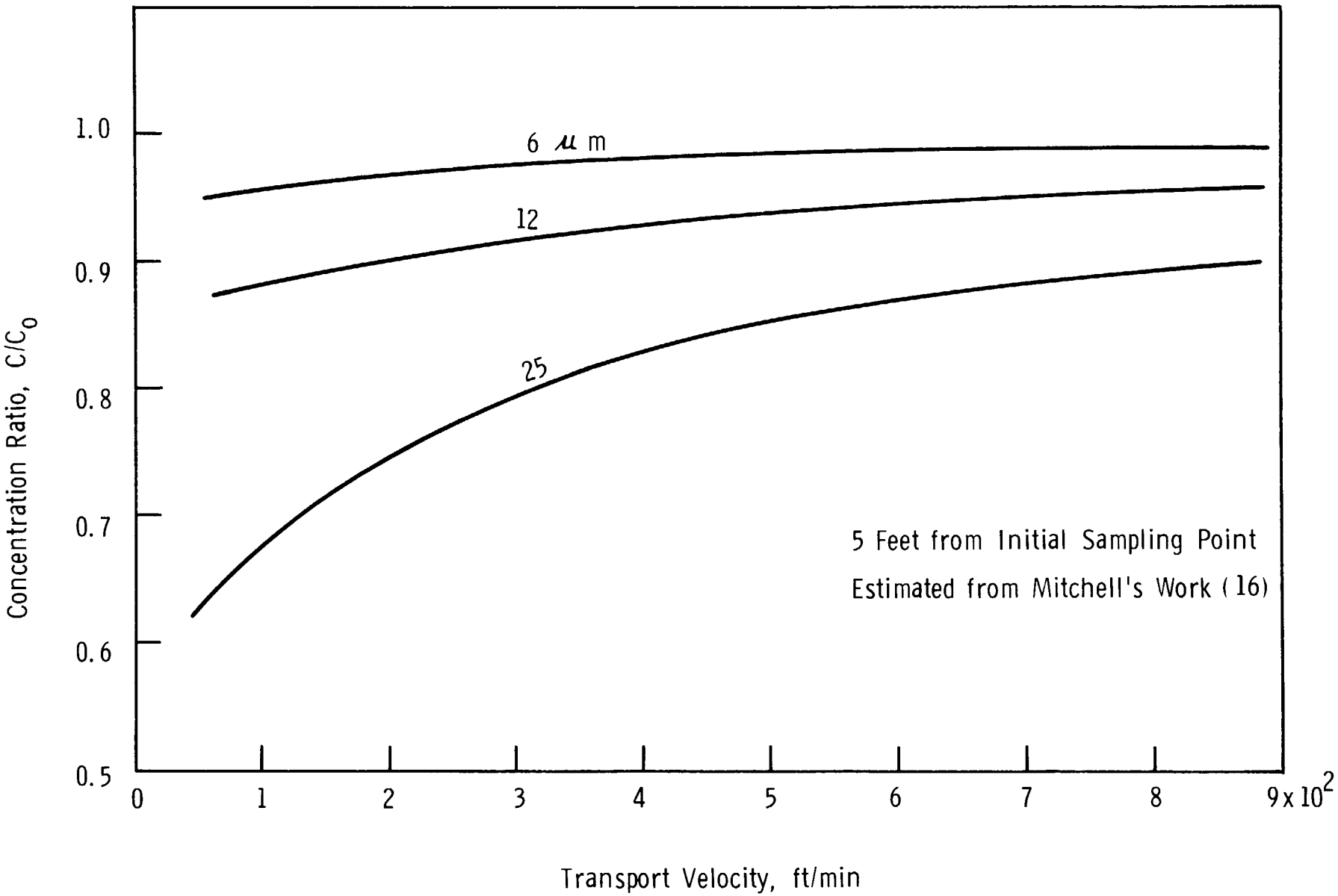

described in Section B. The collections of oil on the impactor were made at 45 psi and 72°F.

Prior to the determinations of particle size, collection efficiency* at different spray distances was established by taking the ratio of the initial impaction area of oil particles to the total area of the impaction cell. The initial impaction areas of microfog particles were estimated by analyzing the area covered by thin oil films with a microscope after spraying microfog on the collection cell for a short time (approximately 1.5 seconds). Results show collection efficiency for all nozzles tested to be approximately 0.9 at spray distances of 1" or longer. At spray distance of 1/2", the collection efficiency is estimated to be about 0.5. For simplicity, as a first approximation for calculation, $\eta = 0.9$ is used. Knowing collection efficiency and stream velocity, we can now calculate the ranges of particle size which should impact on a collection plate. For the case of a microfog stream of infinite extent, using the work of Ranz and Wong (20, 26), calculated results for a 5 cm (approximately 2") collector are shown in Figure 29. Diameters at zero efficiency, $(\bar{d})_{\eta=0}$, can be considered to be the minimum sizes which can be collected at a specified velocity. For example, particles smaller than 6 μm cannot be expected to be collected in a gas stream at 100 ft/sec velocity. In a similar manner, value of particle size at $\eta = 0.9$, $(\bar{d})_{\eta=0.9}$, for a given velocity can be estimated. Preliminary results (not included in this report) obtained with Nos. 1A and 3A nozzles conclusively indicate that the relatively large particles can be produced by a proper nozzle design, and that considerable quantities of particles larger than 11 μm are produced by these nozzles.

The estimated values of particle sizes at $\eta = 0.9$, with the rates of total oil collection at a specified velocity, are presented in Table 10. These data represent the segment of the experimental results obtained with No. 1 nozzle at gas flow rates of 2, 3, 4, 5, and 6 cfm. Also included in Table 10 are the particle size distribution data counted by the optical particle counter and various terms signifying the physical meanings of the spray systems. The methods of calculating these terms are presented in Appendix C-2.

---

*The collection efficiency, η, is defined theoretically as the ratio of the cross-sectional area of the original microfog stream from which particles of a given size are removed because their trajectories intersect the collection surface to the projected area of the collector in the direction of flow in the case.

Figure 29

COLLECTION EFFICIENCY OF AN IMPACTOR
ESTIMATED FROM RANZ'S WORK (20)

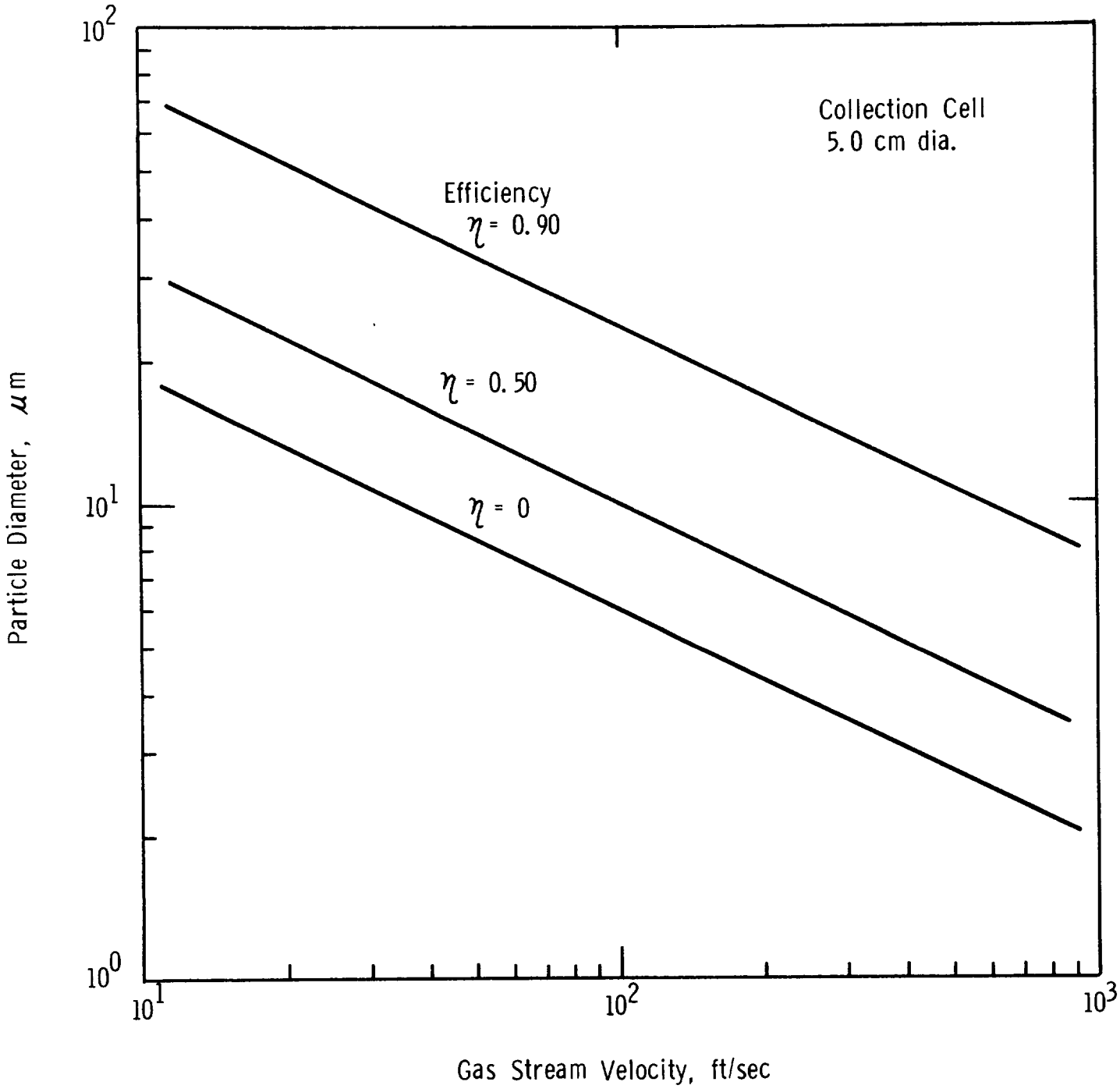

Table 9

Particle Size Distribution of XRM-177F

Nozzle No. & Gas Flow Rate	Item	Particle $\bar{d}$ (μm)	Counter n_i	Cascade Impactor $(\bar{U}_m)$calc. (ft/sec)	Cascade Impactor $(\bar{d})_{\eta=0.9}$ (μm)	Cascade Impactor (dw/dt) (mg/sec)	Cascade Impactor Δ(dw/dt) (mg/sec)	(dn_i/dt) (p/sec) x 10^{-5}	$(dQ_L/dt)_i$ (cm³/sec) x 10^{4}	(dn_i/dQ_g) (P/cm³) x 10^{-2}	$(dQ_L/dQ_g)_i$ (cm³/cm³) x 10^{7}
Nozzle No. 1 2 cfm											
	1	0.6	486					241	0.03	255	0.03
	2	0.9	638					316	0.10	333	0.11
	3	1.2	357					177	0.07	187	0.07
	4	1.7	24					11.9		12.6	
	5	2.4	1					0.5		0.4	
	6	3.4	0								
	7	4.8									
	8	6.8									
	9	9.6									
	10	13.6									
	11	19.2									
	12	27.2									
	13			290	14	0.57	0.15	1.3	1.86	1.3	1.97
	14			197	17	0.42	0.25	1.2	3.10	1.2	3.29
	15			99	24	0.17	0.17	0.3	2.11	0.2	2.24
	16										
	17										
	18										
Total			1506					749.2	7.3	790.7	7.7

Table 9 (Cont'd)

Particle Size Distribution of XRM-177F

Nozzle No. & Gas Flow Rate	Item	Particle $\bar{d}$ (μm)	Counter n_i	Cascade Impactor $(\bar{U}m)$calc. (ft/sec)	Cascade Impactor $(\bar{d})_{\eta=0.9}$ (μm)	Cascade Impactor (dw/dt) (mg/sec)	Cascade Impactor Δ(dw/dt) (mg/sec)	(dn_i/dt) (p/sec) x 10^{-5}	$(dQ_L/dt)_i$ (cm^3/sec) x 10^4	(dn_i/dQ_g) (P/cm^3) x 10^{-2}	$(dQ_L/dQ_g)_i$ (cm^3/cm^3) x 10^7
Nozzle No.1 3 cfm	1	0.6	365					272	0.03	193	0.02
	2	0.9	1386					1033	0.33	737	0.24
	3	1.2	1747					1300	1.17	925	0.82
	4	1.7	840					626	1.60	444	1.11
	5	2.4	36					26.8	0.19	19.1	0.13
	6	3.4	0					0	0	0	0
	7	4.8	591					440	25.5	313	18.0
	8	6.8	239					178	29.2	127	20.6
	9	9.6	30					22.4	10.4	16	9.3
	10	13.6	0					0	0	0	0
	11	19.2	0					0	0	0	0
	12	27.2	0					0	0	0	0
	13			411	12	6.13	0.62	8.2	7.70	5.8	5.4
	14			279	14	5.51	2.57	21.4	31.8	15.2	22.6
	15			141	20	2.94	1.89	5.4	23.4	3.8	16.6
	16			71	28	1.05	0.48	0.5	5.9	0.2	4.1
	17			47	34	0.57	0.29	0.2	3.6	0	2.6
	18			35	40	0.28	0.28	0.1	3.5	0	2.5
Total			5234					3934.0	144.3	2799.1	104.0

Table 9 (Cont'd)

Particle Size Distribution of XRM-177F

Nozzle No. & Gas Flow Rate	Item	Particle $\bar{d}$ (μm)	Counter n_i	Cascade Impactor (Um)calc. (ft/sec)	Cascade Impactor $(\bar{d})\eta=0.9$ (μm)	Cascade Impactor (dw/dt) (mg/sec)	Cascade Impactor Δ(dw/dt) (mg/sec)	(dn_i/dt) (p/sec) x 10^{-5}	$(dQ_L/dt)_i$ (cm^3/sec) x 10^4	(dn_i/dQ_g) (P/cm^3) x 10^{-2}	$(dQ_L/dQ_g)_i$ (cm^3/cm^3) x 10^7
Nozzle No. 1 4 cfm	1	0.6	358					355	0.04	188	0.02
	2	0.9	1385					1375	0.44	728	0.23
	3	1.2	1829					1812	1.45	960	0.77
	4	1.7	976					960	2.46	508	1.31
	5	2.4	84					83.5	0.60	44.2	0.32
	6	3.4	3					3	0.06	1.6	0.03
	7	4.8	657					652	37.8	345	20.0
	8	6.8	362					359	58.9	190	31.2
	9	9.6	100					99.2	46.0	52.5	24.6
	10	13.6	0					0	0	0	0
	11	19.2	0					0	0	0	0
	12	27.2	0					0	0	0	0
	13										
	14			405	12	6.63	1.21	15.9	15.0	8.4	7.94
	15			204	17	5.42	3.86	17.9	47.9	9.5	25.4
	16			102	23	1.56	0.90	1.7	11.2	0.9	5.93
	17			68	29	0.66	0.24	0.2	3.0	0.1	1.60
	18			50	33	0.42	0.42	0.2	5.2	0.1	2.75
Total			5754					5734.6	230.1	3036.3	122.1

Table 9 Cont'd

Particle Size Distribution of XRM-177F

Nozzle No. & Gas Flow Rate	Item	Particle $\bar{d}$ (μm)	Counter n_i	Cascade Impactor $(\bar{U}m)_{calc.}$ (ft/sec)	Cascade Impactor $(\bar{d})_{\eta=0.9}$ (μm)	Cascade Impactor (dw/dt) (mg/sec)	Cascade Impactor Δ(dw/dt) (mg/sec)	(dn_i/dt) (p/sec) x 10^{-5}	$(dQ_L/dt)_i$ (cm^3/sec) x 10^4	(dn_i/dQ_g) (P/cm^3)$_{-2}$ x 10^{-2}	$(dQ_L/dQ_g)_i$ (cm^3/cm^3) x 10^7
Nozzle No. 1 5 cfm											
	1	0.6	412					511	0.05	217	0.02
	2	0.9	1285					1590	0.51	674	0.21
	3	1.2	1618					2010	1.8	851	0.77
	4	1.7	734					935	2.39	396	1.01
	5	2.4	62					77	0.55	32.8	0.23
	6	3.4	0					0	0	0	0
	7	4.8	564					700	40.6	297	17.20
	8	6.8	339					420	68.9	178	29.20
	9	9.6	80					99.2	46.0	42	19.50
	10	13.6	1					1.2	1.6	0.5	0.68
	11	19.2	0					0	0	0	0
	12	27.2	0					0	0	0	0
	13			685	9.2	-	-	-	-	-	-
	14			466	11	6.30	1.90	32.4	23.6	13.7	10.0
	15			233	16	4.40	3.51	19.4	43.5	8.2	18.4
	16			117	22	0.89	0.58	1.3	7.2	0.5	3.05
	17			77	27	0.31	0.07	0.1	0.8	-	0.34
	18			58	31	0.24	0.24	0.2	3.0	0.1	1.27
Total			5115					6396.8	240.5	2710.8	101.9

Table 9 (cont'd)

Particle Size Distribution of XRM-177F

Nozzle No. & Gas Flow Rate	Item	Particle $\bar{d}$ (μm)	Counter n_i	Cascade Impactor $(\bar{U}m)$calc. (ft/sec)	Cascade Impactor $(\bar{d})_{\eta=0.9}$ (μm)	Cascade Impactor (dw/dt) (mg/sec)	Cascade Impactor Δ(dw/dt) (mg/sec)	(dn_i/dt) (p/sec) x 10^{-5}	$(dQ_L/dt)_i$ (cm^3/sec) x 10^4	(dn_i/dQ_g) (P/cm^3) x 10^{-2}	$(dQ_L/dQ_g)_i$ (cm^3/cm^3) x 10^7
Nozzle No. 1 6 cfm											
	1	0.6	531					790	0.09	279	-
	2	0.9	1120					1665	0.53	588	0.19
	3	1.2	1027					1528	1.38	539	0.49
	4	1.7	273					406	1.04	143	0.37
	5	2.4	17					25.3	0.18	8.9	0.06
	6	3.4	0					0	0	0	0
	7	4.8	380					565	32.8	196	11.95
	8	6.8	219					326	53.8	115	19.0
	9	9.6	100					148.8	69.0	52.5	24.40
	10	13.6	22					32.7	43.5	11.5	15.35
	11	19.2	0					0	0	0	0
	12	27.2	0					0	0	0	0
	13			755	8.8	-	-	-	-	-	-
	14			514	10	6.25	3.11	70.6	38.5	25.0	13.60
	15			257	15	3.14	2.24	15.2	27.8	5.3	9.82
	16			128	21	0.90	0.51	1.3	6.3	0.5	2.26
	17			85	26	0.39	0.12	0.1	1.5	-	0.53
	18			64	29	0.27	0.27	0.2	3.3	-	1.17
Total			3689					5574.2	279.7	1963.7	99.2

Experimental results obtained by the cascade impactor technique, together with data from the particle counter, show that mean particle size of a spray system changes little in the ranges of gas flow rates studied except at 2 cfm, and that the geometrical configuration of a nozzle seems to have a great influence on particle size distribution. For the purpose of comparison and of characterizing spray systems, both the mass median diameters and the mean partial diameters obtained from the particle counter will be adjusted according to the values of $\sum_{i=1}^{N} n_i$ and $(d)_{\eta=0.9}$.

In addition, calculated values of $(\frac{dn_i}{dt})$, $(\frac{dn_i}{dQ_G})$, and $(\frac{dQ_L}{dQ_G})_i$ provide the insight to spray system. For example, in the case of XRM 177 F with No. 1 nozzle at 3 cfm, the rate of microfog particles introduced into test chamber, $(\frac{dn_i}{dt})$, is 3.9×10^8 particles per second; particle concentration, $(\frac{dn_i}{dQ_G})$, 2.8×10^5 particles per cm^3; and oil/gas volumetric flow ratio, $(\frac{dQ_L}{dQ_G})_i$, 1.0×10^{-5}.

A comparison between the total mass flow rates calculated from these particle size distributions and those determined by measuring the amount of oil flow at the microfog generator is made and listed below:

	Rate of Oil Flow,* $(\frac{dQ_L}{dt})$, cc/min		
Gas Flow Rate (cfm)	Measured	Calculated from Particle Size Distribution Data	% Difference
2	0.5	0.1	80
3	1.1	0.9	18
4	1.7	1.4	18
5	2.5	1.5	40
6	3.1	1.7	45

*Test conditions used = No. 1 nozzle and XRM 177 F.

It is noted that there are considerable quantities of oil lost (not collected on impactor or test plate), depending on gas flow rates used. A part of this loss, of course, occurs in the pipe line, but most of the loss can be attributable to the loss of large oil drops formed at the bottom tip of the spray nozzle, which will be further discussed with the wetting rate studies. As previously described, the extremely large drops (approximately 500 ∿ 1000 μm) formed at the bottom tip of the spray nozzle do not impact on the collector plate, but instead, drift away from the plate because of high gas velocity along the plate. Apparently, when the large drops formed at the tip break away from the nozzle, they are not entrained back into the main stream of gas flow. The horizontal position of the spray nozzle obviously is partly responsible for this behavior. Thus, the situation should be improved when the nozzle is vertically positioned and microfog sprays downward. The introduction of a secondary gas flow around the boundary regions of an expanding microfog spray also should aid the entrainment of large particles back into the main stream. A study of this kind of microfog delivery system should be included in efforts to advance the efficiency of microfog lubrication.

v) Radial Distribution of Particle Size in a Microfog Spray

When a microfog sprays and expands as illustrated in Figure 16, the radial velocity gradient of the microfog spray may create a radial distribution of particle sizes depending upon scales of gas turbulence along the radial direction. Thus, it is of great interest, although not required by the contract, to investigate whether or not there exists a measurable difference in particle size in the radial direction of the microfog spray.

The particle counting chamber is equipped with a sampling tube consisting of 9 small thin-wall tubes giving good coverage of an area corresponding to the test plate (2" x 2") used in the wetting rate studies. The sampling tube is described in detail elsewhere (21). With the sampling tube at a distance of 6" from the spray nozzle in the axial direction, the possibility of radial variation of particle size distribution was briefly studied using XRM 177 F and No. 3 nozzle at a gas flow rate of 3 cfm.

Preliminary results obtained in this study suggested that particle size distribution at the center of an expanding spray is composed of slightly more of the smaller particles than that near the boundaries of the spray. Distribution data, however, reveal that when mean particle sizes at different points are compared, there is practically no difference in particle size - i.e., the microfog spray is homogeneous in the radial direction. In order to substantiate this preliminary conclusion, further study of the subject was indicated. In the course of the study, it was

felt that orthokinetic sampling may introduce an error into particle size measurement because in some cases the sampling tubes are not parallel to the direction of microfog flow. The effect of sampling angle between sampling tube and flow direction was therefore briefly reviewed. It is found from Watson's work (25) that sampling efficiency at angles of less than 10 degrees, providing isokinetic flow, is nearly 1.0, as illustrated in Figure 30. This means that, at least for this study, the effect of sampling angle on particle size distribution is insignificant.

vi) Effects of Other Factors

The effects of several operating variables was briefly examined during the particle size measurements. These variables included sampling time, and ambient temperature and pressure in the particle counting chamber. For this study, sampling times of 2, 10, and 15 seconds were used, the chamber pressures were at 12 and 45 psi, and the chamber temperatures at 72 and 700°F. Test results reveal that these variables, with the exception of ambient temperature, have no measurable effect on particle size distribution. When the test chamber is operated at 700°F, the mean particle size seems to decrease slightly. This slight decrease in mean particle size is probably caused by re-entrainment of smaller particles after "repulsion" of particles from a hot chamber surface, or vaporization of particles (oil droplets) suspended in the stream.

4. Wetting Rate Determinations

i) Factors Involved in Wetting Rate

Before attempting to measure the wetting rates of oil on a hot surface, we must critically review many factors involving wettability* (or spreadability) of oil drops on the surface. Impaction efficiency and evaporation are two of the most important of such factors in this study. When the microfog particles impact on the surface, adhesion of the particles to the surface, and coagulation and spreadability of the particles on the surface to form a thin film, will control the amount of oil film available for lubrication. In addition, the spreading of these microfog particles to form a uniform oil film is greatly influenced by the dynamic action of a high velocity gas stream. Thus, the velocity distribution of the gas stream along the hot surface is important in determining the rate of wetting. Considering these factors, the wetting rate now can be expressed in mathematical form as:

*Wettability here does not necessarily follow the classical thermodynamic definition of wetting. Wettability and spreadability are interchangeably used.

Figure 30

SAMPLING EFFICIENCY VERSUS ANGLE BETWEEN THE AXIS OF THE SAMPLING TUBE AND THE FLOW DIRECTION (25)

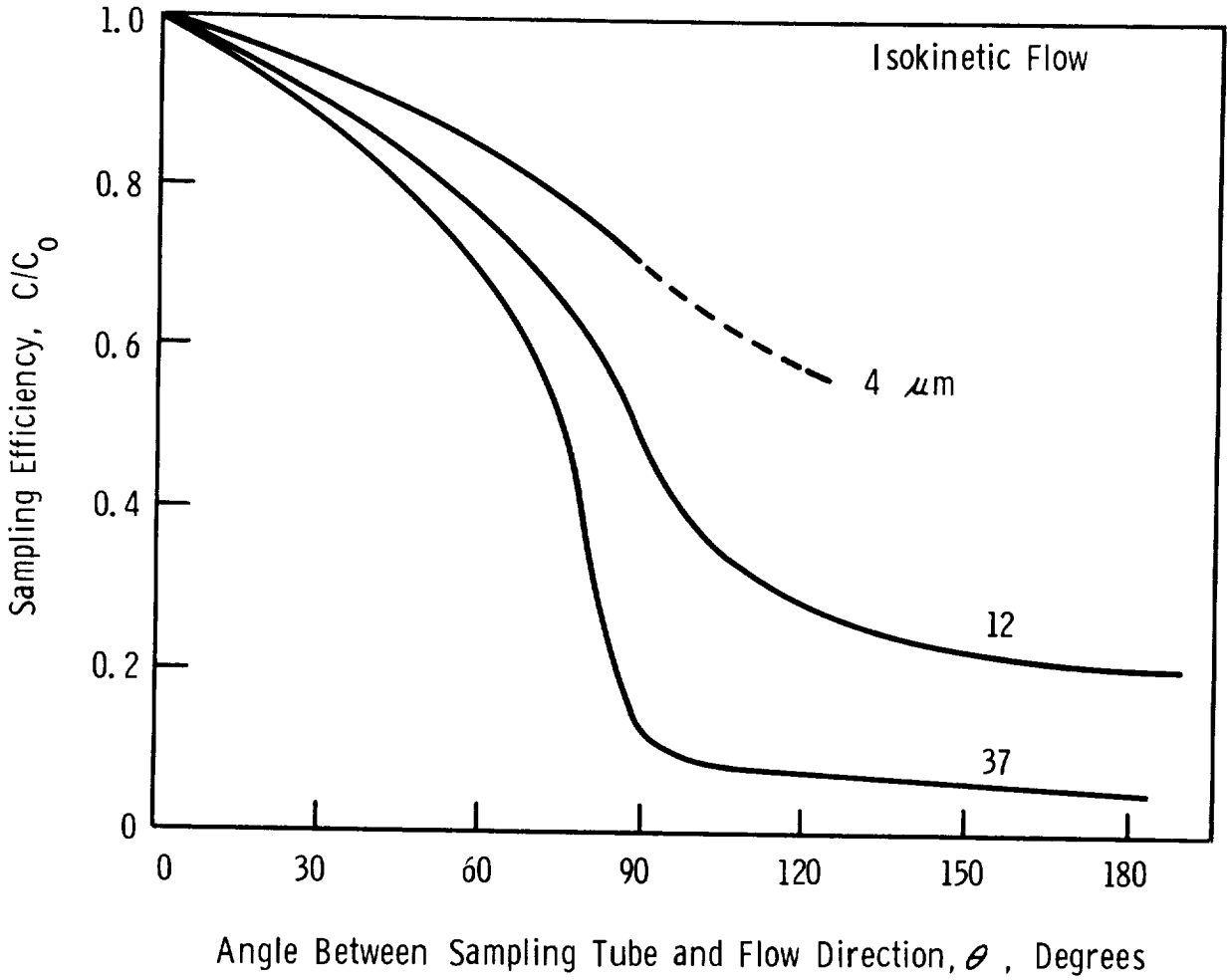

$$\text{Wetting rate} \equiv \left(\frac{dA}{dt}\right) = F[U_L, U_G, \rho_L, \rho_G, M_L, M_G, \bar{d}, L, \lambda] \quad (7)$$

Introducing functional variables to form dimensionless groups, Equation (7) becomes

$$\frac{dA}{dt} = f\left[\frac{LU_L}{\nu_L}, \frac{\nu_L}{d}, \frac{U_G \rho_G \bar{d}^2}{\mu_G \rho_L L}\right] \quad (8)$$

$$\text{or} = f\left[N_{Re}, N_{Sc}, N_{Stk}\right] \quad (9)$$

Thus, the general expression for wetting rate can be given by:

$$\frac{dA}{dt} = K\, N_{Stk}^{a} \cdot N_{Sc}^{b} \cdot N_{Re}^{c} \quad (10)$$

where N_{Stk} signifies inertial impaction; N_{Sc}, evaporation; and N_{Re}, characterization of film flow on a surface, respectively. Since the microfog particles spread out on a heated surface in this study, in addition to all these factors, rate of heat transfer in terms of N_{Nu} and N_{Pr} must be considered and incorporated with Equation (10).

ii) Optimum Spray Distance

Prior to a series of wetting rate studies using each of the five test oils under specified conditions, preliminary wetting studies were made to determine the optimum spray distance between nozzle and test plate. These tests were made, as specified by Section B, Task II, Exhibit A under the contract, under the following conditions:

Spray distance	: 1/2", 1", 2", 3", 4", and 6"
Spray nozzle	: No. 3
Test lubricant	: XRM 177 F
Oil flow rate	: 0.85 gm/min (0.0019 lb/min)
Gas flow rate	: 3 ft^3/min
Mean volume diameter	: 3.2 μm
Plate temperature	: 700°F

Test results are shown in Figure 31 by plotting the fraction of the area covered - i.e., the ratio of areas, (A/A_o), versus spray time. Figure 31 indicates that, as expected, wetting time increases with increasing spray distance. The lines, shown in

Figure 31, give an excellent linear relationship with varying slopes at different spray distances beyond 25 percent of area covered (25% of area corresponds to 1" diameter of test plate). At a spray distance of 3", although the test plate was sprayed for 10 seconds, the movement of the oil film could not be photographed after 7 seconds, by which time the test chamber was completely filled with microfog particles. At spray distances of 4" or longer, when the test plate was sprayed for 15 seconds, no visible movement of oil film was detected. In analyzing photographic films of wetting tests, it was particularly difficult to identify and to follow an oil film flow within a 1" radial distance from the center of the plate. In this region, where microfog particles impact, wetting time is very short and the flow pattern of an oil film is not uniform. However, the wetting times outside this region, varying from 3 to 7 seconds, are accurately recorded after a continuous oil film covering the entire test plate. Although there is evidence in the photographic films that this continuous film is preceded on the plate by streaks of discontinuous oil film (or oil vapor), possible wetting by these streaks is disregarded, since, besides being discontinuous, there is strong doubt that these streaks wet the test plate at all. The time required for these streaks to appear out to the edges of the plate is merely 0.2 ∿ 0.3 seconds.

When impacting on a hot surface, the microfogs appear to have definitely more tendency toward drift caused by "repulsion" and particles seem to re-entrain back to the microfog streams. In such a case, the heat- and mass-transfer processes between phases near the hot surface may play a significant role in controlling the wetting rates. A detailed study of this area should yield characteristic wetting curves of greater value and is essential to the development of microfog lubrication beyond present limitations.

Following Equation (10), an attempt was made to relate the wetting rates of microfogs on a hot surface to spray distance. Equation (10) simply suggests that the wetting rate becomes a function of only the inertial parameter defined as

$$\psi = \frac{\rho_L \bar{d}^2 \bar{U}_m}{72 \mu_G L} \tag{11}$$

provided that evaporation and flow characteristics of oil films remain constant under a given condition. In such a case, as described in Appendix B, only the velocity distribution of a diffusing microfog in the axial direction decreases in inverse proportion to the spray distance x; that is

$$\frac{\bar{U}_m}{U_o} \sim \frac{1}{x} \tag{12}$$

Figure 31

EFFECT OF SPRAY DISTANCE ON WETTING

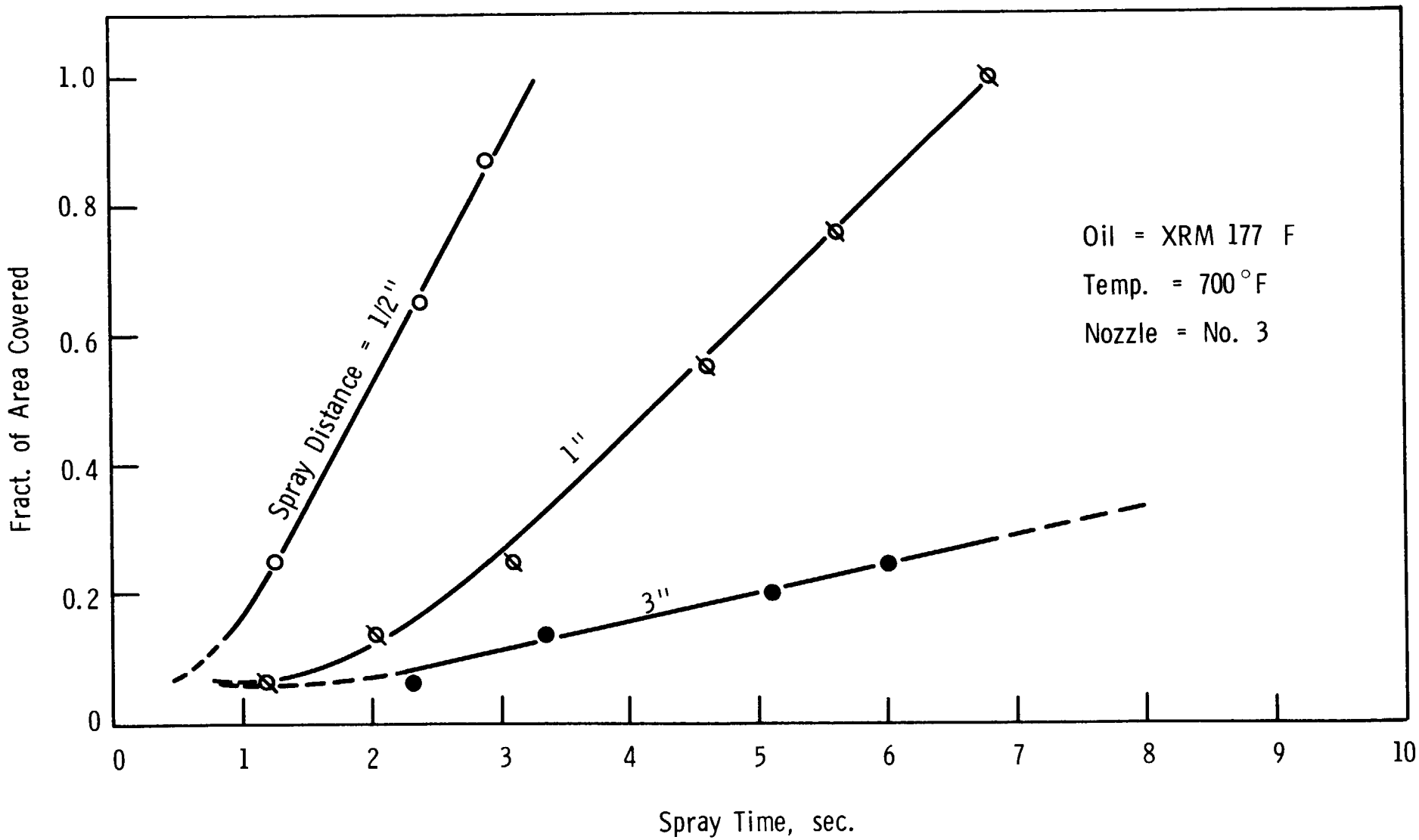

Thus, an empirical equation relating wetting rate to spray distance is expressed as

$$\frac{dA}{dt} = \psi_o \left(\frac{1}{x}\right) \qquad (13)$$

where ψ_o is a parametric constant to be determined experimentally. According to Equation (13), we should get a family of similar curves depending upon operating conditions such as particle size, oil/gas mass flow ratio, etc.

In order to test Equation (13), wetting rates, the slopes of the wetting curves shown in Figure 31, are plotted against spray distance. These curves are shown in Figure 32, which also includes the wetting rate data obtained with Nos. 1 and 2 nozzles under the limited conditions specified by Section B, Task II, Exhibit A. The plot gives excellent straight lines with the slope approximately unity. Furthermore, it is interesting to note that there appears to be a lower and upper limiting point of wetting in these straight lines. According to Equations (11) and (13), the lower and upper limiting points of wetting depend upon two critical factors, particle size and impaction velocity, which are inter-related as far as impaction is concerned. As described in Section D-3, a minimum impaction velocity required to impinge on a surface exists for a given particle, while for an excessively high impaction velocity the wetting rate may approach an asymptotic value. Evidence for the existence of lower and upper limiting points in wetting rate is that no measurable wetting is observed when microfogs are sprayed through No. 3 nozzle at 4" and 6" spray distances for 15 seconds, and that with No. 1 nozzle at 1" and 1/2", the increase in wetting rate is relatively small, although the impaction velocity increases from 290 to 411 ft/sec. For this test series, the minimum velocity required for measurable wetting seems to be 120 ft/sec, but is subject to variations depending on operating conditions as well as oil properties. Thus, determination of these limiting boundaries is of great value in designing a microfog lubrication system.

The study of the optimum spray distance between spray nozzle and test plate shows that the test plate was completely wet in the shortest time at 1/2", the shortest distance tested, which should therefore be considered as the optimum distance. However, the spray distance of 1" is selected for wetting studies throughout this project because of photographic considerations. With the present camera and lighting angles, the spray nozzle at a 1/2" distance from the test plate interferes with the camera view by casting a shadow on the test plate.

Figure 32

WETTING RATE AS A FUNCTION OF SPRAY DISTANCE

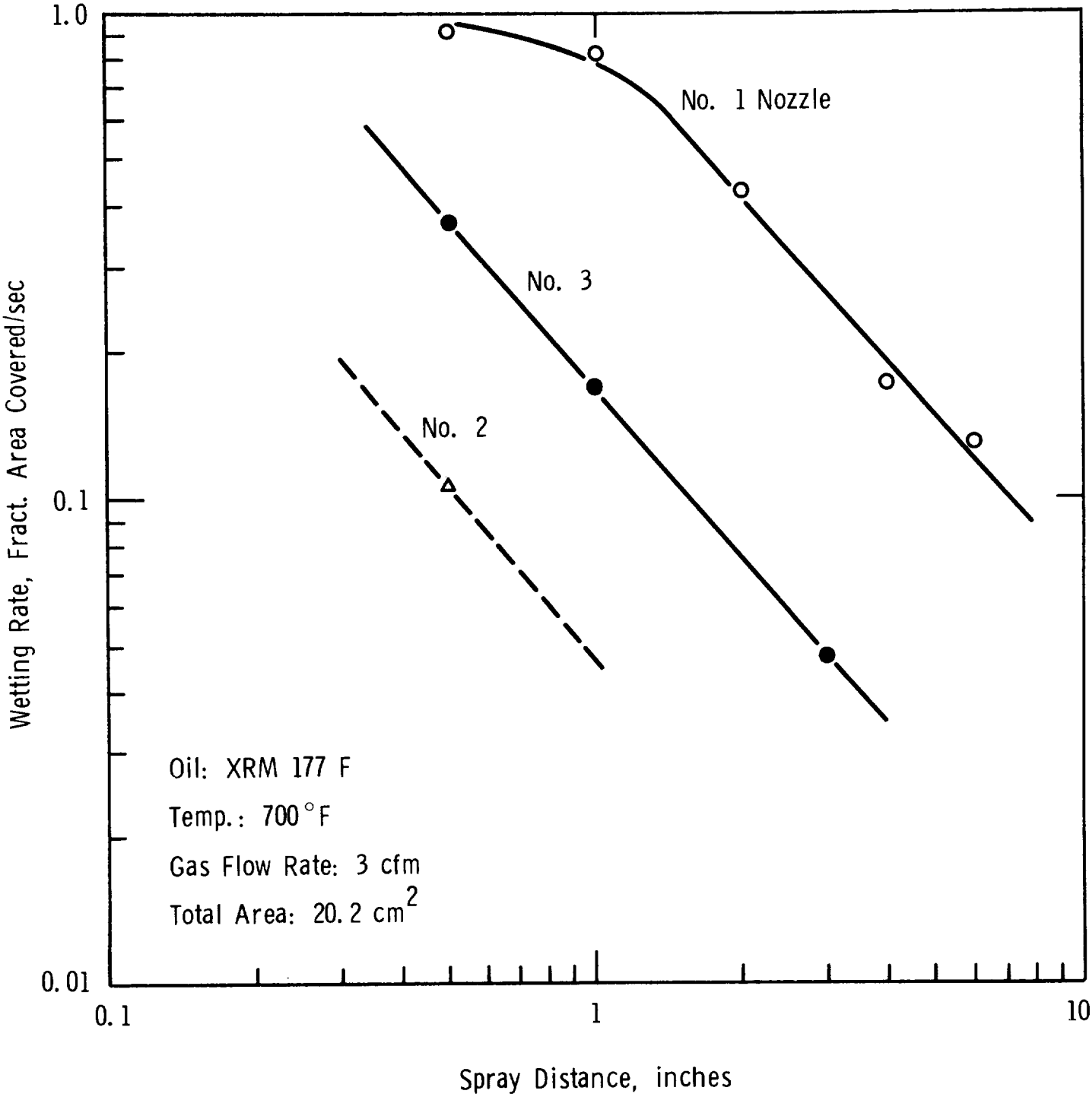

iii) Wetting Rates of Different Test Oils

After fixing the spray distance at 1", measurements of the wetting rates of the five test lubricants (XRM 177 F, Hercolube F, Sunthetic 18H(B), Ucon 50-HB-5100, and Turbo Oil 4040) were made with the five different spray nozzles at a variety of test conditions as specified in Section A, Task II.

Test results, reporting wetting time at different radial distances, are listed in Appendix D-1, with other pertinent data. The wetting rates estimated graphically by taking the slopes of the fraction of area covered-spray time curves for these oils are also included. Typical experimental results are illustrated by the data for XRM 177 F with No. 3 nozzle at 700°F, shown in Figure 33. In general, similar curves represent the test data for all other oils.

Average temperature variations of the test plate from a desired temperature in most cases were less than $\pm$ 10°F except for the runs which had long spray times at 800°F. In such cases, plate temperature dropped sharply by approximately 40°F, but gradually recovered and remained constant before completion of the experiment. The temperatures of spray nozzles under different chamber temperatures varied considerably depending upon gas flow rates and the times required to bring the system to a steady-state condition. Average ranges of the temperature variation were as follows:

Chamber °F	Spray Nozzle °F
600	310 -350
700	380 -450
800	430 -540

As indicated in the above table, the widest variation, 110°F, occurred at 800°F.

In discussing the test results summarized in Appendix D-1, it is necessary to define some sort of reference point so that these data are justly compared. To do so, a method was developed to compare these data on the basis of the values of specific wetting rate and minimum oil/gas mass ratio. The specific wetting rate and minimum oil/gas mass ratio designate the wetting rate established by expending a unit oil/gas mass flow ratio and the minimum amount of oil/gas mass required to wet a hot surface under a given condition, respectively. Using these terms as references, discussion of these data will be based only on significant factors which may play an important role in microfog lubrication, instead of specific experimental runs.

Figure 33

WETTING RATE OF XRM 177 F AT DIFFERENT GAS FLOW RATE

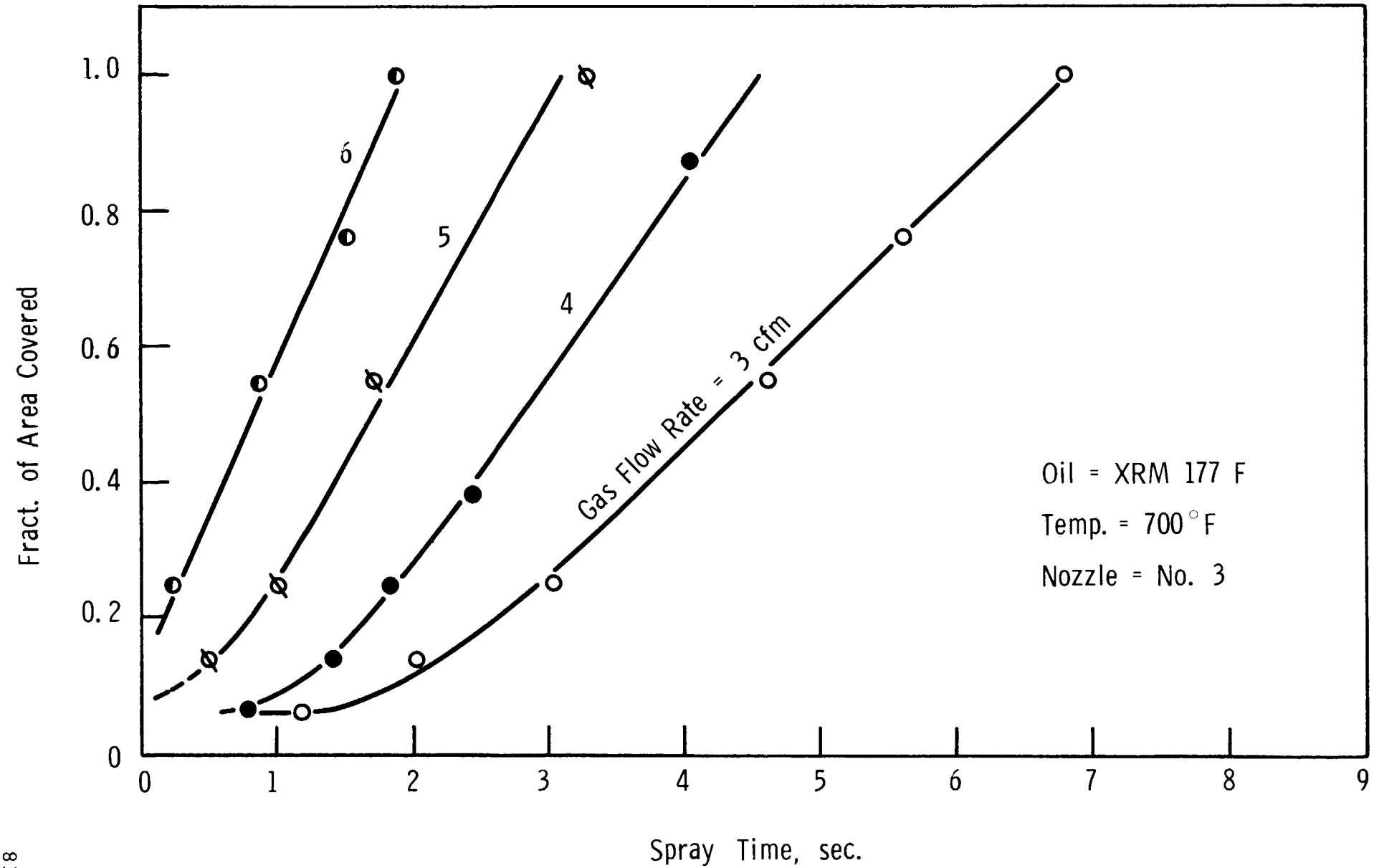

iv) Effect of Nozzle Configurations

Since five different spray nozzles are employed in the wetting rate study, it is of interest to investigate how these nozzles affect the wetting rates of a test oil at different oil/gas mass flow ratios. When discussing the wetting rates of oils, as previously described, we must remember the importance of impaction efficiency, in which the impaction velocity and particle size are the key variables controlling wetting rate. Wetting rate can, therefore, be discussed only in conjunction with particle velocity and size distribution, which have already been treated in the preceding sections.

Results representing the effect of nozzle configurations on wetting rate, summarized from the experimental data obtained for XRM 177 F at 600°F, are shown in Figure 34. It is clear from Figure 34 that wetting rate increases with increasing oil/gas mass flow ratio for all the nozzles shown. An exception to this behavior was experienced with Nozzle No. 2, which in wetting studies at different gas flow rates, produced no visible wetting. This seems to be due almost entirely to the impaction efficiency, indicating that for a given particle size, the efficiency may approach zero if impaction velocity is not sufficiently high. A comparison between the results of No. 2 nozzle and those of No. 3 nozzle is clear indication of an important role that impaction velocity plays in determining the wetting rate. In this case, the specific wetting rates with Nos. 2 and 3 nozzles are 0 and 4×10^{3} cm^2/sec. - unit (oil/gas) mass, respectively, while the particle size distribution data (refer to table 6) with these nozzles show little differences. Thus, for a given oil/gas mass flow and particle size distribution, increasing particle velocity by means of a nozzle greatly increases wetting rate. For example, at the gas flow rate of 3 cfm, corresponding to the oil/gas mass flow ratio of 2.65×10^{-3}, the wetting ratios with Nos. 2 and 3 nozzles are 0 and 2.4 cm^2/sec., respectively, while the particle velocities vary from approximately 160 ft/sec. for No. 2 nozzle to 213 ft/sec. for No. 3, and the arithmetic mean particle diameter for both nozzles remains fairly constant at 1.80 um. Test results obtained with No. 3A also show considerable increase in wetting rate, but here no clear cut comparison can be made as the particle velocity distributions of this nozzle are not well-defined because of the packing materials within the nozzle.

Although we discussed here only the results of XRM 177 F at 600°F, the test results of other oils indicated, to a greater or lesser degree, a similar general trend in the effects of nozzle configurations on wetting rate.

Figure 34

EFFECT OF NOZZLE CONFIGURATIONS ON WETTING RATE AT 600°F

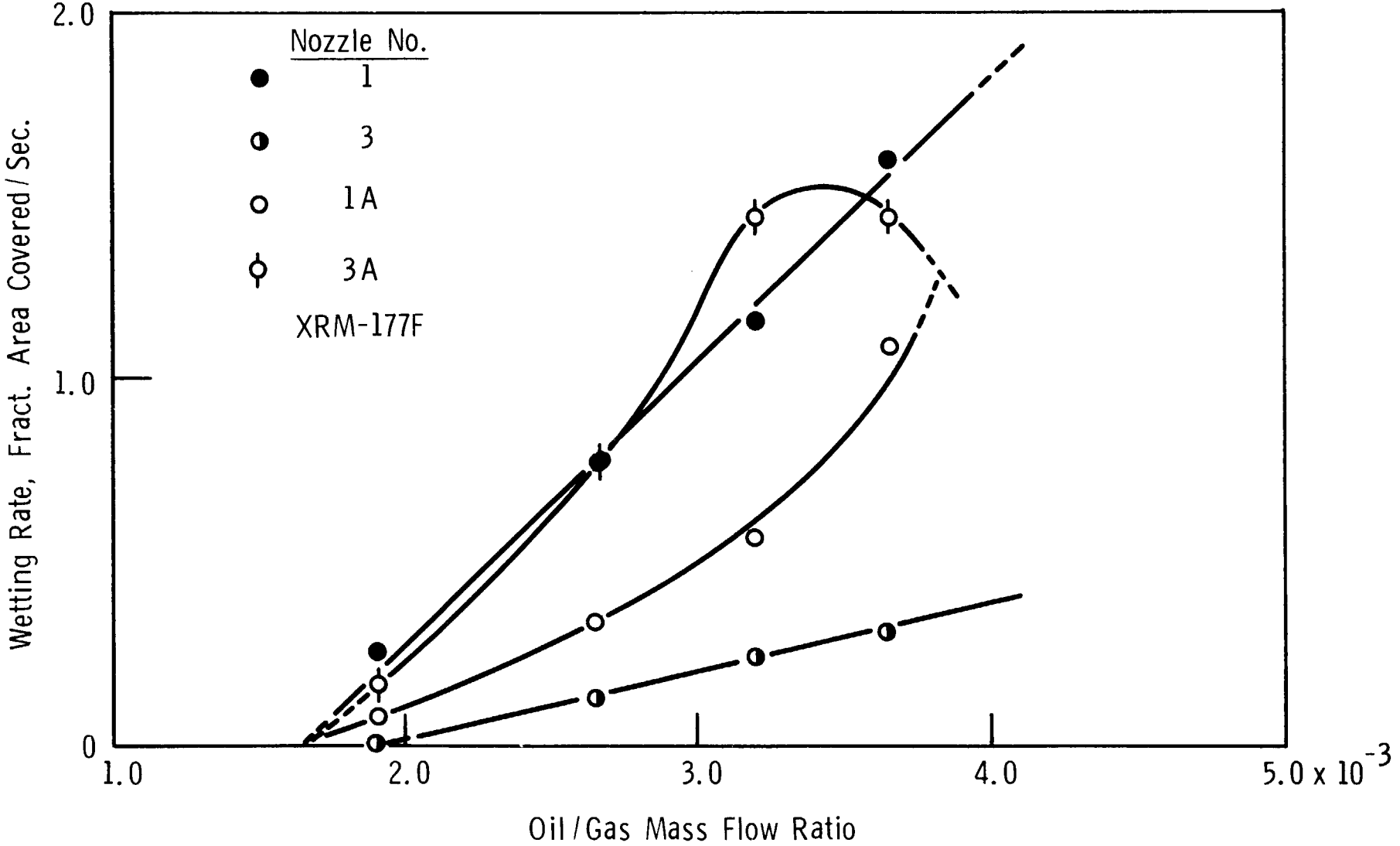

v) Effect of Particle Size

In the preceeding section, we have indicated that the impaction velocity and particle size have a profound effect on wetting rate. Thus, an effort was made to determine to what extent particle size influences wetting rate for a given particle velocity and (oil/gas) mass flow ratio, although the variations of particle size are critically limited by means of a reclassifying nozzle and by dynamic forces of atomizing gas within the microfog generator. With the present microfog generator which is similar to commerically available generators for mist lubrication, it must be remembered that the operating variables are interlocked so that one variable cannot be altered without affecting the others - that is, for a given (oil/gas) mass flow particle size cannot be varied, without changing particle velocity. For this reason, it is extremely difficult to study independently the effect of particle size on wetting rate. Nevertheless, an attempt was made to demonstrate a trend, hoping to better understand the important roles of the particle size in the microfog lubricant application.

For convenience in discussing the effect of particle size on wetting rate, the wetting rate data obtained with Nos. 1 and 1A for XRM-177 F at 600°F, shown in Figure 34, are chosen. A comparison between the wetting rates with No. 1 nozzle and those with No. 1A nozzle is an indication that a relatively slight variation in particle size by means of the nozzles having different configurations contributes considerably to the determination of wetting rate. In this case, the specific wetting rates with Nos. 1 and 1A nozzles are 14×10^3 and 9.4×10^3 cm^2/sec - unit (oil/gas) mass, respectively. The increase in the specific wetting rate with No. 1 nozzle seems to be due partly to increased particle velocity, but due mostly to increased particle size, indicating that for a given oil/gas mass flow and particle velocity, an increase in particle size greatly improves wetting rate. For example, at the gas flow rate of 4 cfm corresponding to the oil/gas mass flow ratio of 3.20×10^{-3}, the wetting rates with Nos. 1 and 1A nozzles are 23.2 and 11.3 cm^2/sec respectively, while the arithmetic mean particle diameter vary from 2.09 μm for No. 1 nozzle and 1.52 μm for No. 1A nozzle, and the particle velocities with Nos. 1 and 1A range from 400 to 320 ft/sec. respectively. In these examples, no precise comparison can be made as the particle velocity distributions of these nozzles are not identical owing to presence of one layer of 150 mesh screen in the expansion section of No. 1A nozzle. Nevertheless, it is evident from these comparisons that increasing particle size improves wetting rate.

In addition to these comparisons discussed, with the other wetting rates individually selected in relation to the particle sizes and velocities obtained with different nozzles for other oils, a similar comparison can be made to demonstrate the importance of particle size on wetting rate.

Up to this point, we have principally discussed wetting rate in relation to impaction efficiency which is greatly influenced by

impaction velocity, and particle size and distribution. However, we must realize that this alone would not be sufficient to describe the amount of oil film available for lubrication because the surface velocity and thickness of thin oil films vary considerably depending on the operating conditions employed. Thus, in addition to these factors discussed, we must introduce hydrodynamics of thin oil films with the wetting rate study. This will be discussed in the section X.

vi) Effect of Oil/Gas Mass Flow Ratio, and of Plate Temperature

In order to aid discussion of wetting rate as a function of oil/gas mass flow ratio and of plate temperature, wetting rates for XRM 177 F at 600, 700, and 800°F, with No. 1 nozzle at gas flow rates of 2, 3, 4, 5, and 6 cfm, are shown in Figure 35. In a similar manner, the wetting rates of other oils and nozzles, constructed from Appendix D-1, are shown in Figures 36 through 53. As anticipated, the wetting rates increase with increasing mass flow ratios established by increasing gas flow rates to the microfog generator. This seems to be true up to a certain region of mass flow ratio, beyond which the wetting rates tend to level off or decline in some cases as the mass flow ratios further increase. This asymptotic behavior seems to suggest that there is an upper limiting value of wetting rate under the present operating conditions. The asymptotic behavior of the wetting rates at high mass flow ratio can be attributed, at least in part, to a combination of particle size distribution and impaction pressure, $P/U_o^2\rho/2$ (indicated in Ref. 21), along the test plate. When a microfog stream having a given particle size distribution is sprayed on the test plate, only the particles in certain size ranges can carry sufficient momentum to penetrate through the layers of impaction pressure created by the gas stream along the plate, and then impact on the plate. Now, with the same given particle size distribution, if gas stream velocity increases, in turn increasing the impaction pressure, the range of particle sizes which have sufficient momentum to impact on the plate may change in such a way that the total amount of particles collected on the plate remains fairly constant. Results similar to this asymptotic behavior were noted in determining size distribution of relatively large particles (11 μm or larger) by use of the cascade impactor.

The results also show that differences in wetting rate with respect to temperature are relatively unimportant at low mass flow ratios - i.e., 1.91 and 2.67×10^{-3}, but become significant at mass flow ratios of 3.2×10^{-3} or higher.

Another interesting point to note in Figure 35 is a shift of the order of wetting rates at different temperatures. The point of crossover is probably dependent upon oil properties and the amount of oil available for wetting, which, at a given impaction efficiency, is mainly controlled by the rate of mass transfer through evaporation. Once an amount of oil sufficient for wetting is accumulated on the test plate, the flow of the oil film is principally controlled by the

Figure 35

WETTING RATE AS A FUNCTION OF OIL/GAS MASS FLOW RATIO AND OF PLATE TEMPERATURE

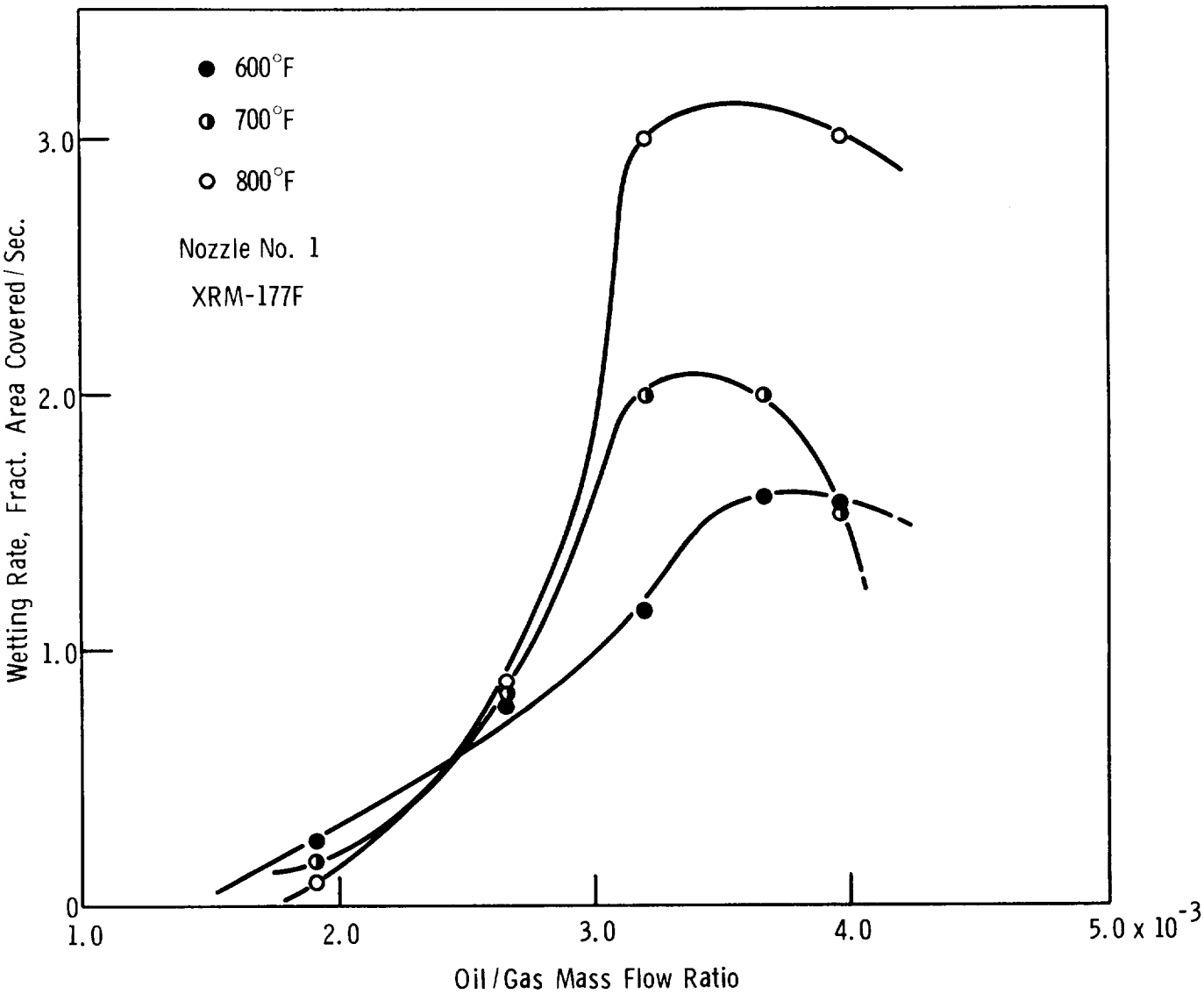

Figure 36

WETTING RATE AS A FUNCTION OF OIL/GAS MASS FLOW RATIO AND OF PLATE TEMPERATURE

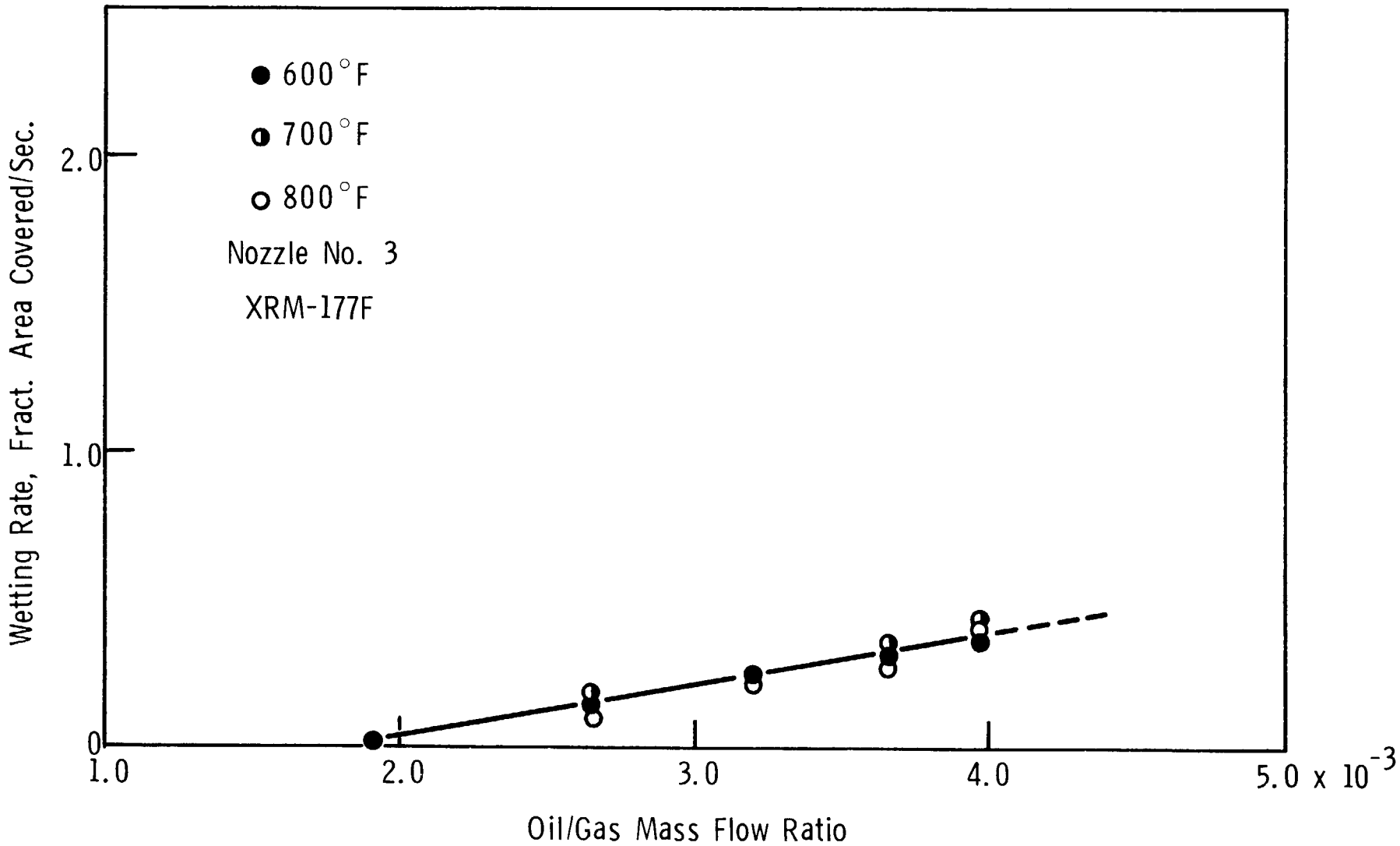

Figure 37

WETTING RATE AS A FUNCTION OF OIL/GAS MASS FLOW RATIO AND OF PLATE TEMPERATURE

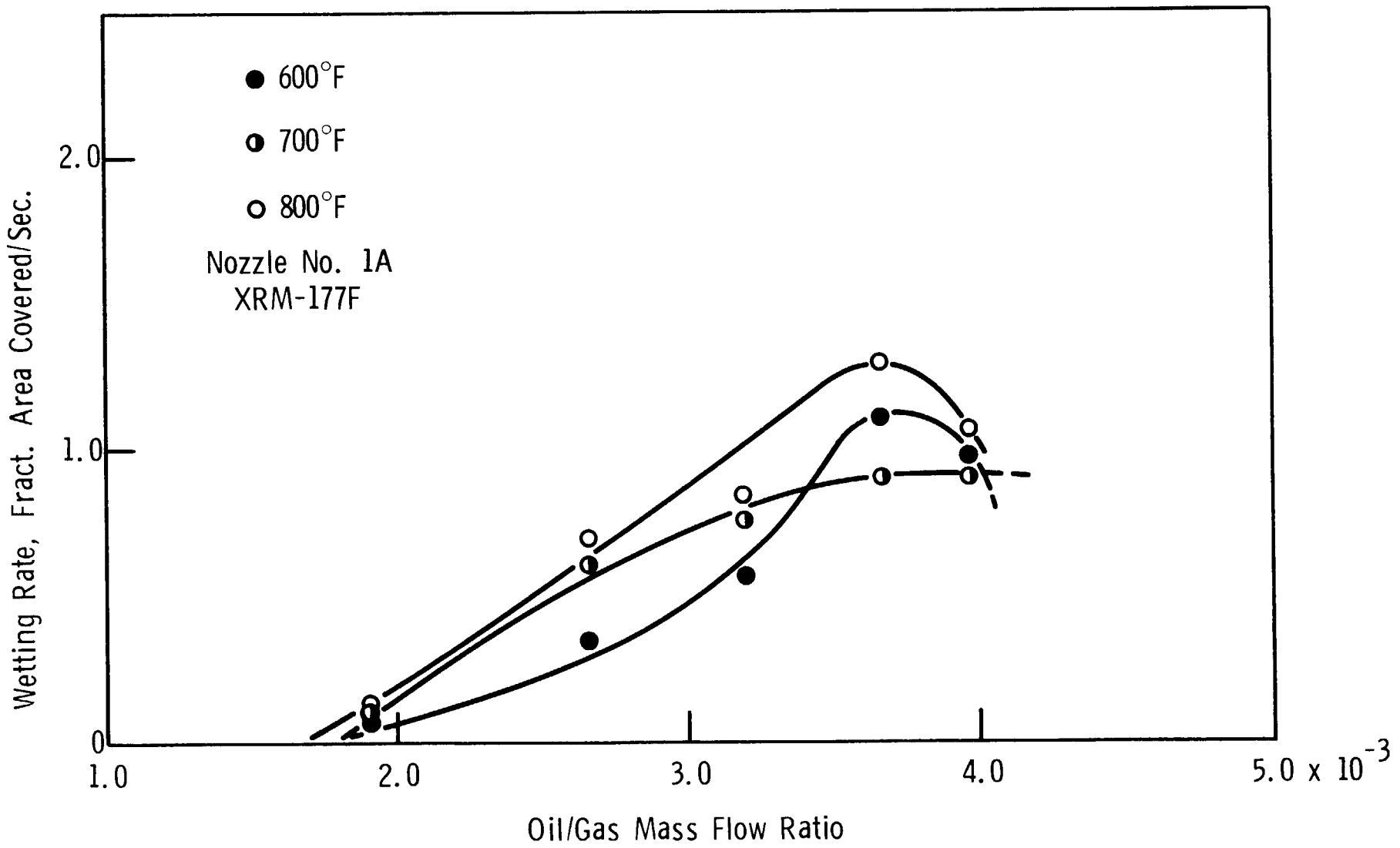

Figure 38

WETTING RATE AS A FUNCTION OF OIL/GAS MASS FLOW RATIO AND OF PLATE TEMPERATURE

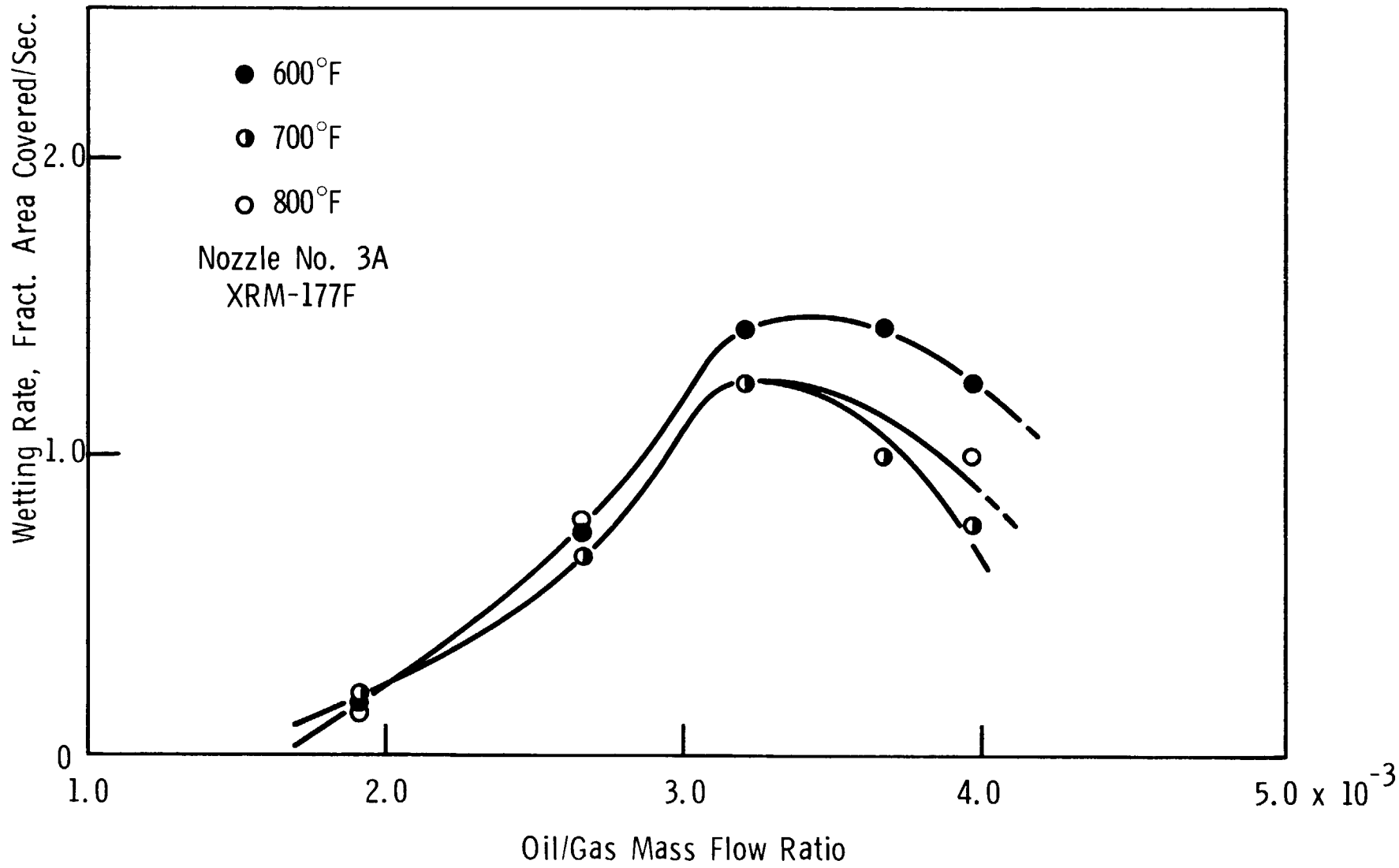

Figure 39

WETTING RATE AS A FUNCTION OF OIL/GAS MASS FLOW RATIO AND OF PLATE TEMPERATURE

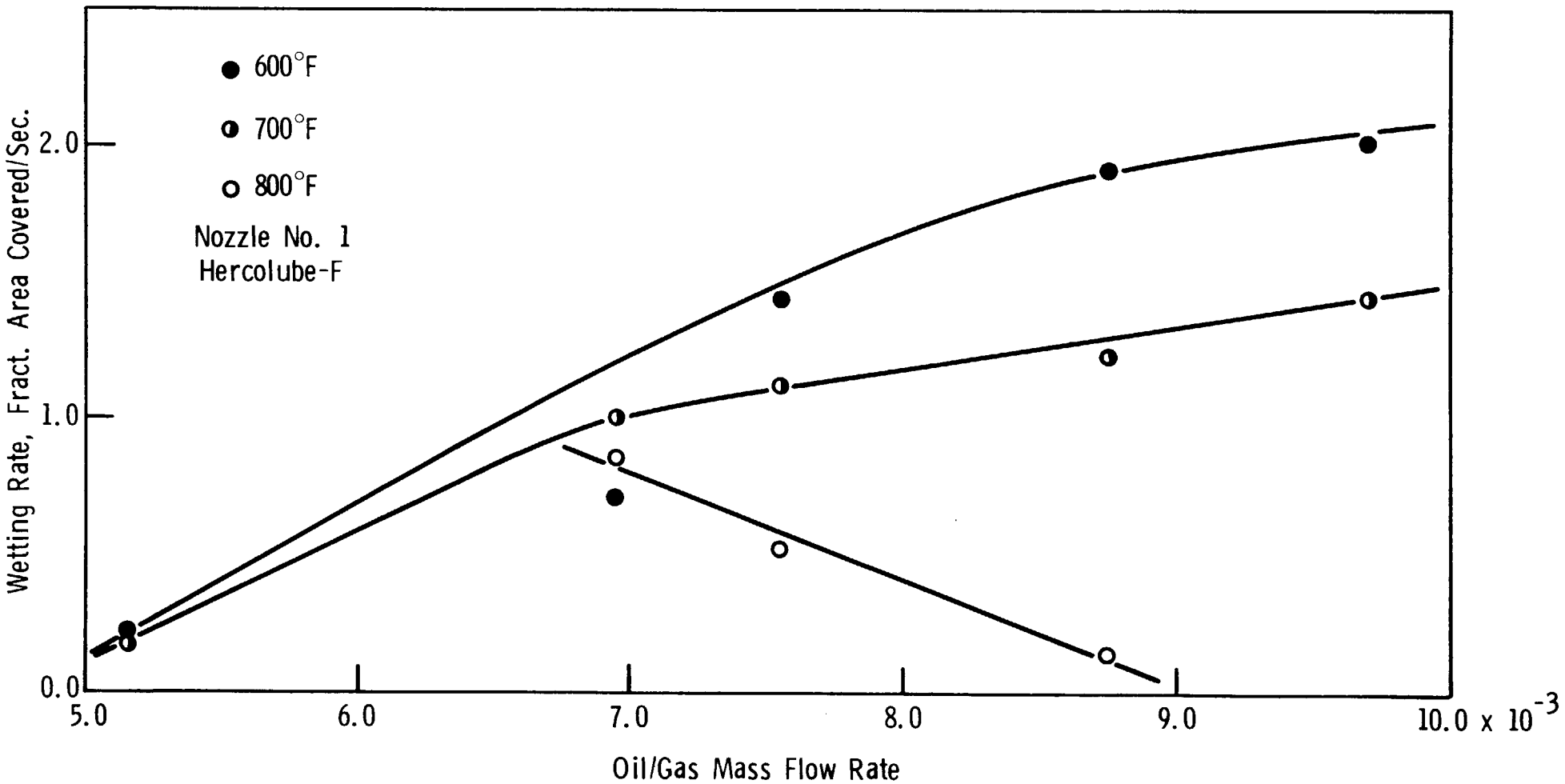

Figure 40

WETTING RATE AS A FUNCTION OF OIL/GAS MASS FLOW RATIO AND OF PLATE TEMPERATURE

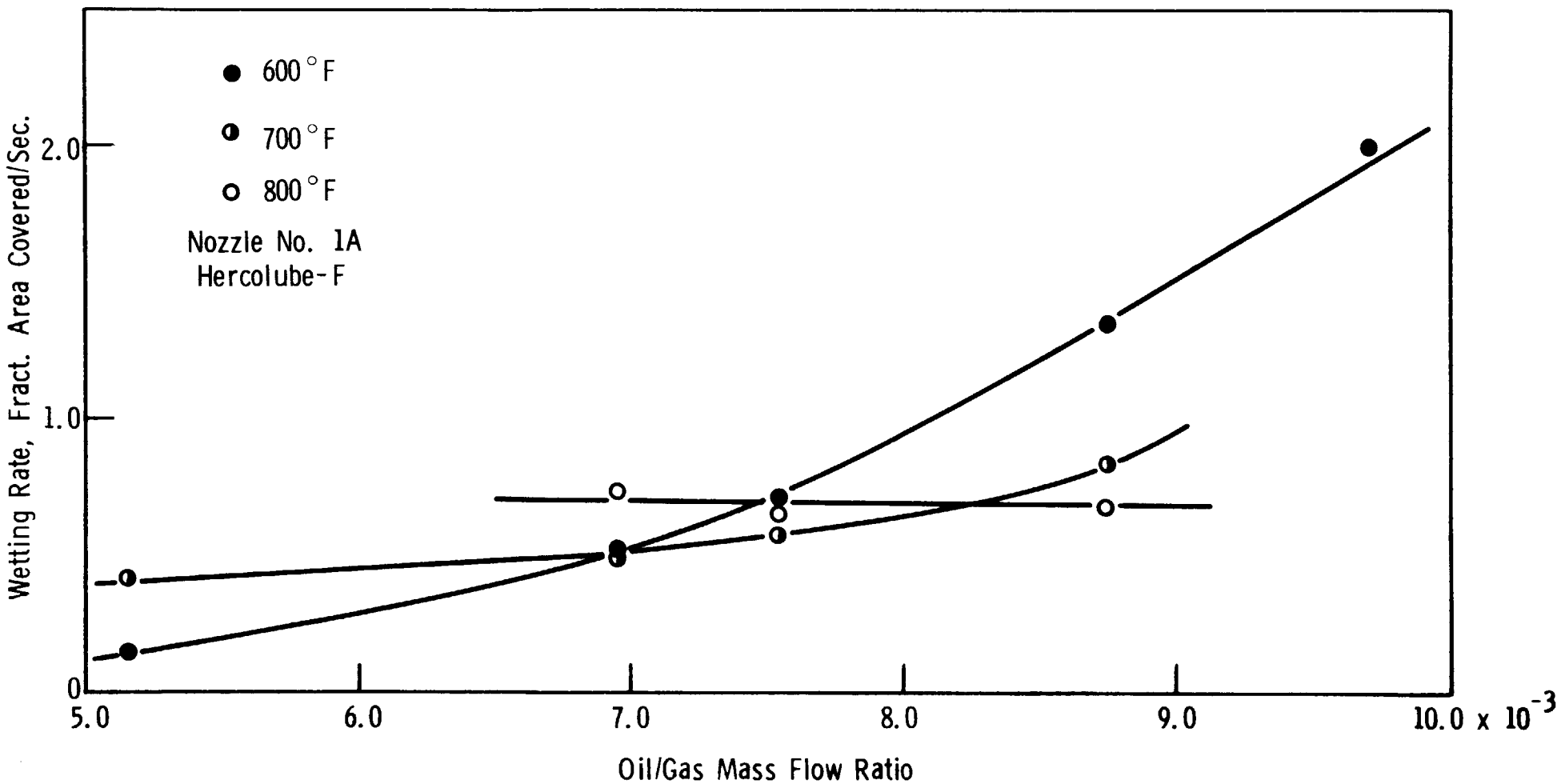

Figure 41

WETTING RATE AS A FUNCTION OF OIL/GAS MASS FLOW RATIO AND OF PLATE TEMPERATURE

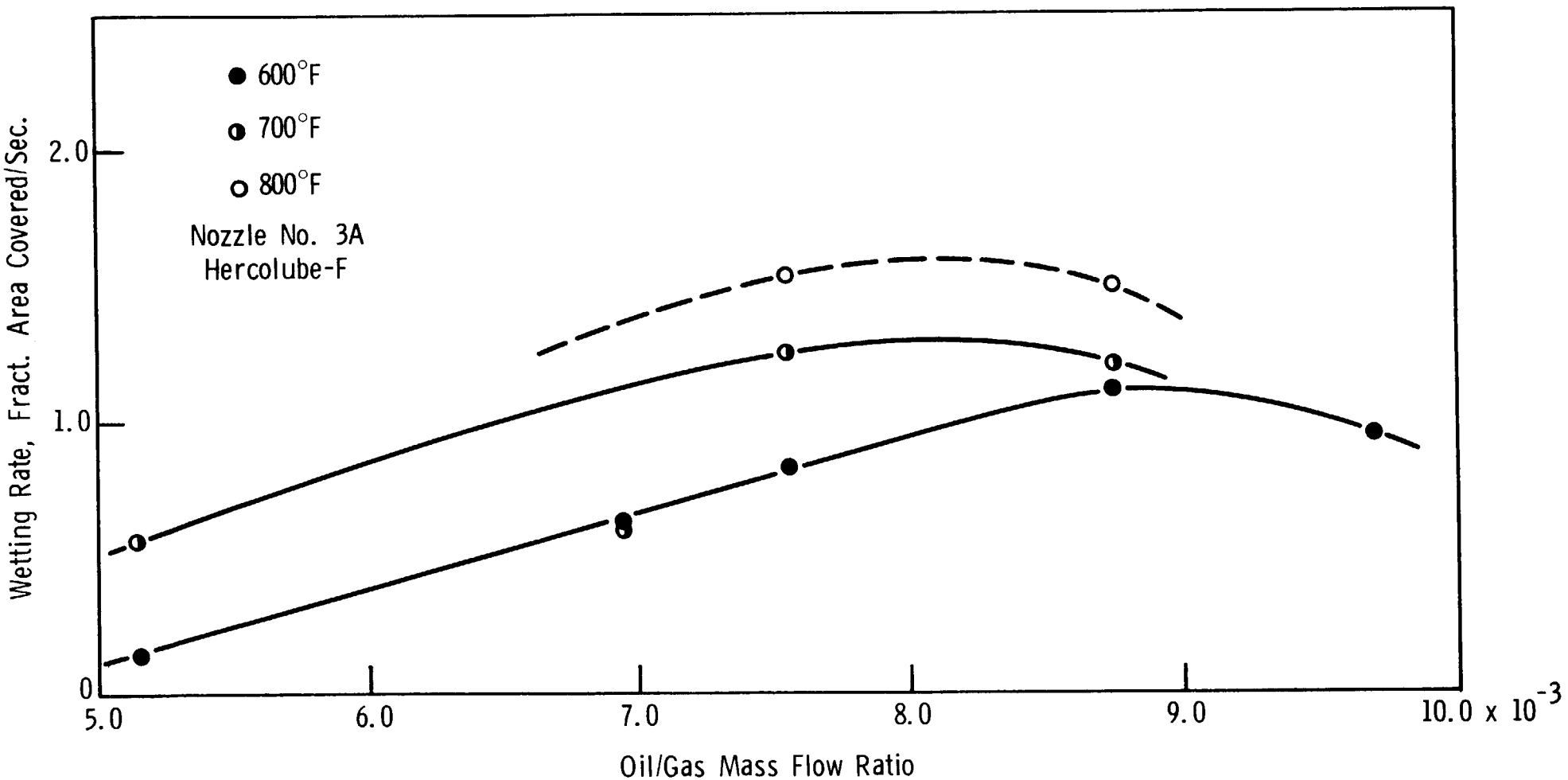

Figure 42

WETTING RATE AS A FUNCTION OF OIL/GAS MASS FLOW RATIO AND OF PLATE TEMPERATURE

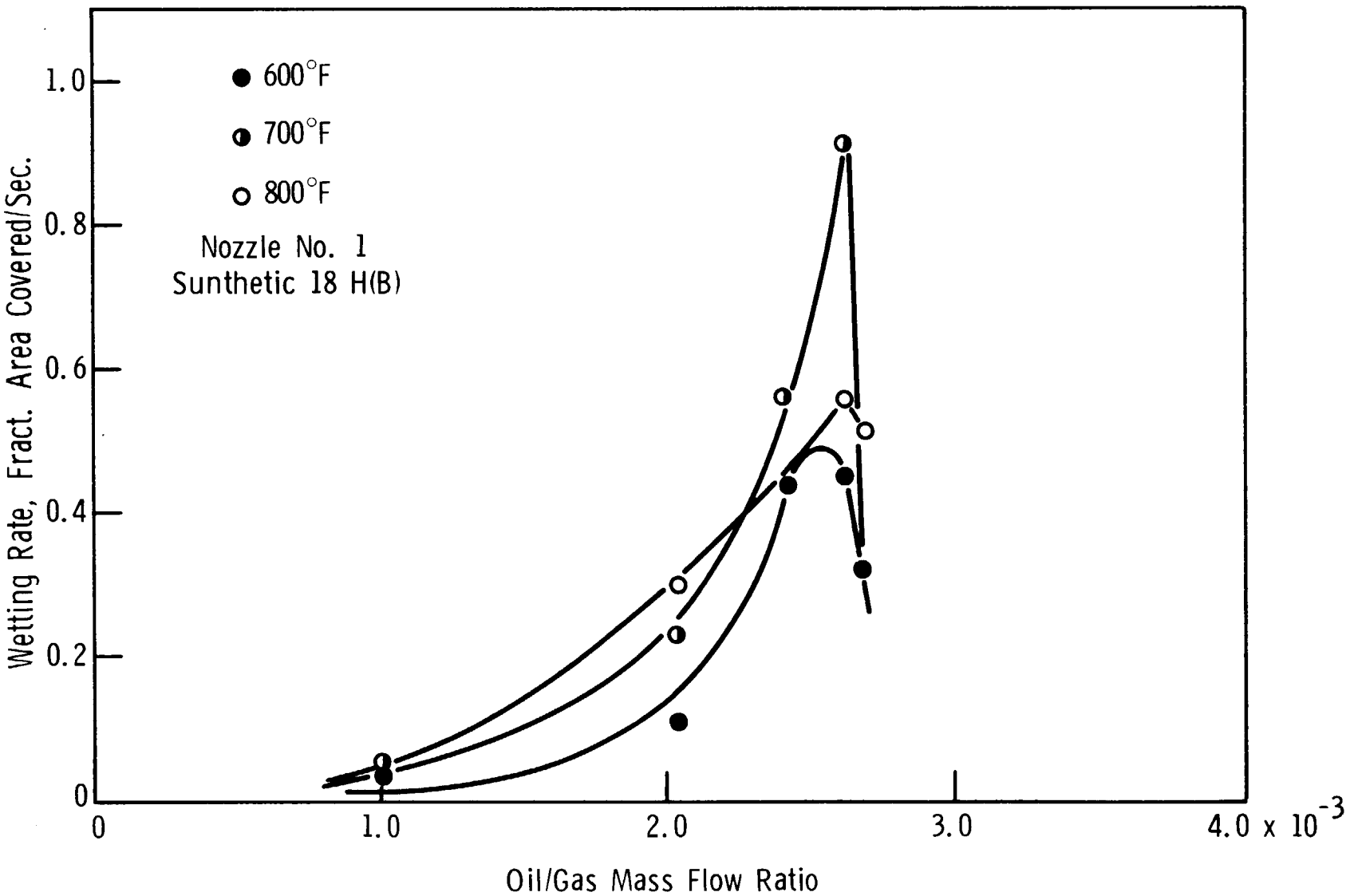

Figure 43

WETTING RATE AS A FUNCTION OF OIL/GAS MASS FLOW RATIO AND OF PLATE TEMPERATURE

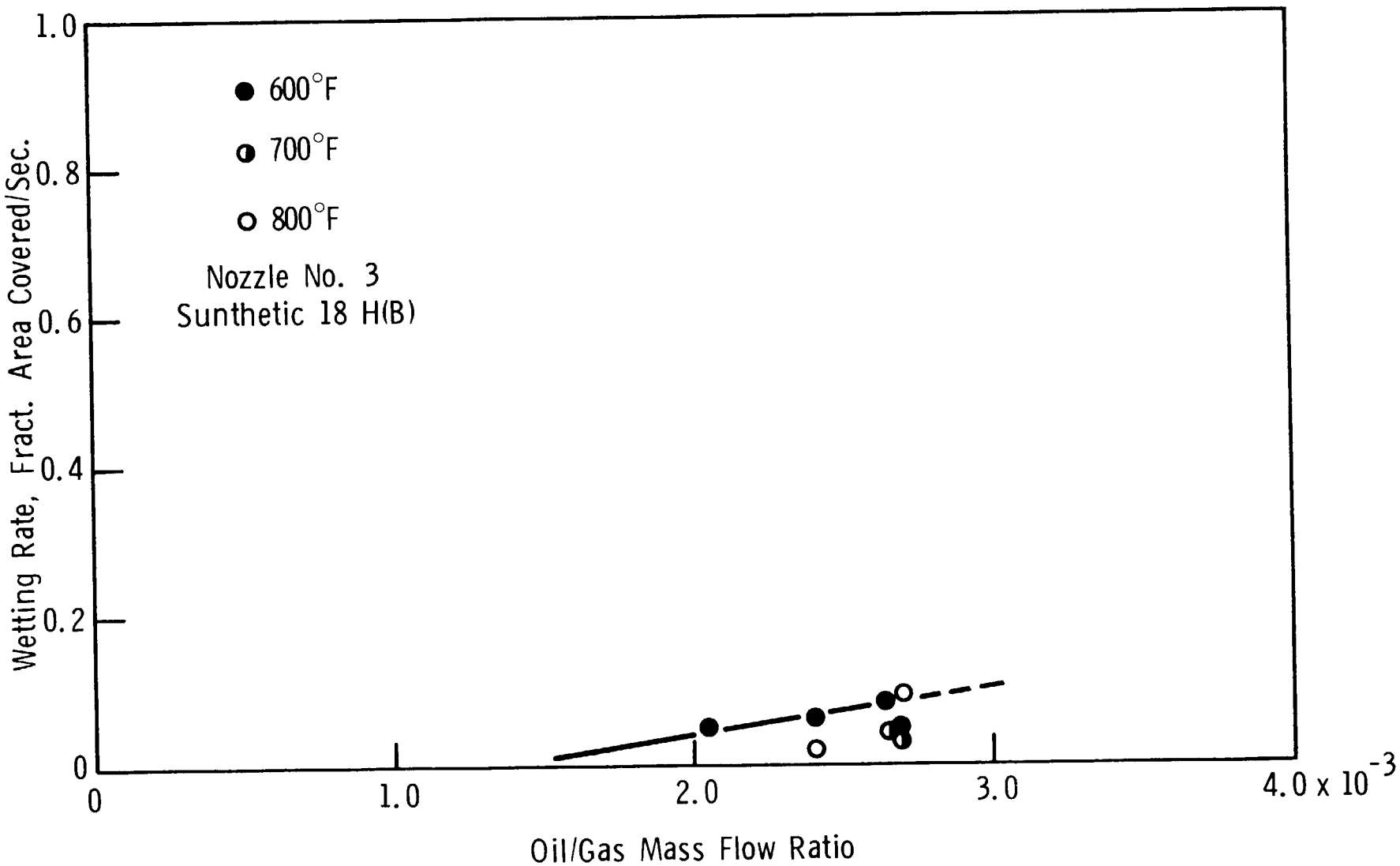

Figure 44

WETTING RATE AS A FUNCTION OF OIL/GAS MASS FLOW RATIO AND OF PLATE TEMPERATURE

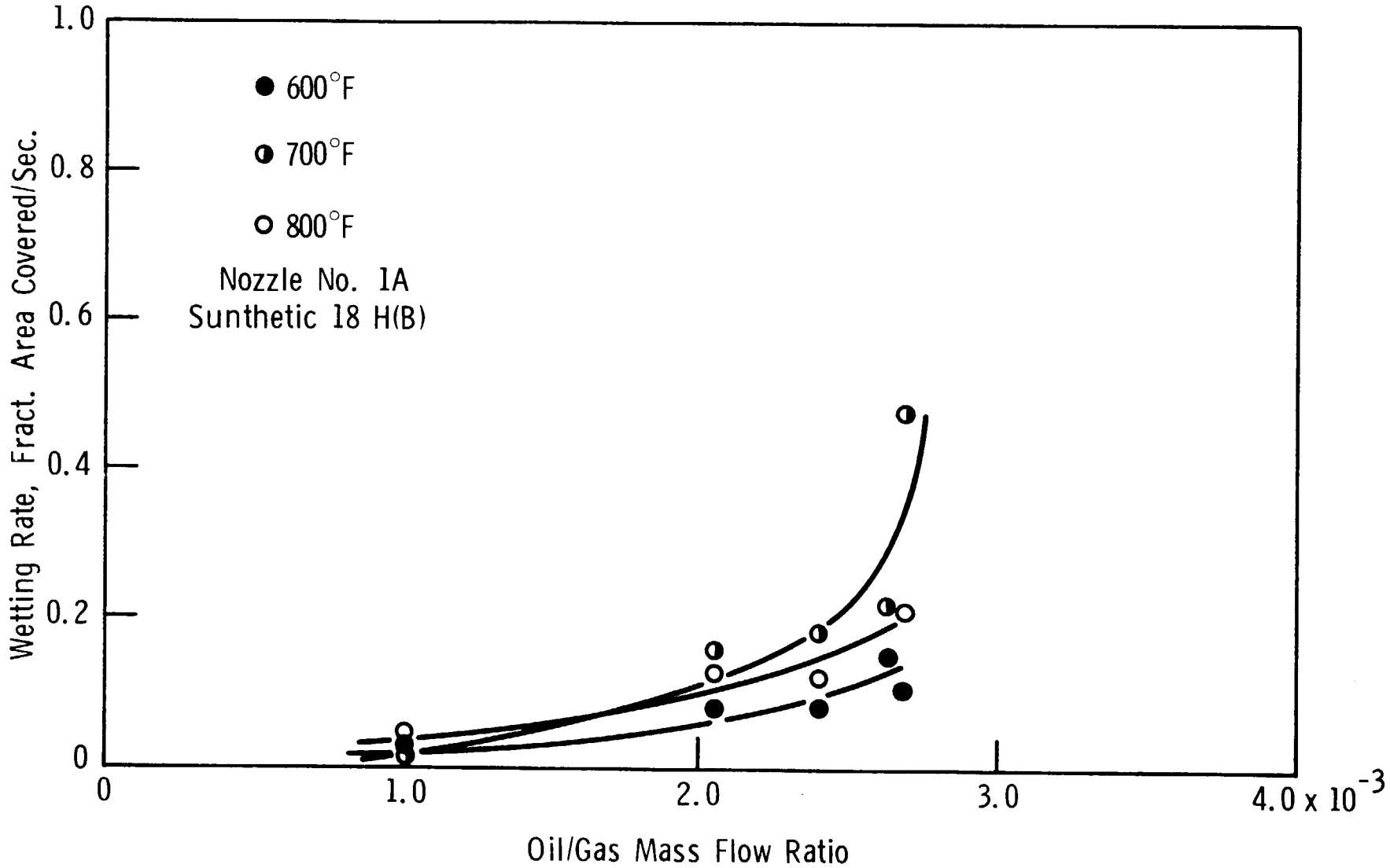

Figure 45

WETTING RATE AS A FUNCTION OF OIL/GAS MASS FLOW RATIO AND OF PLATE TEMPERATURE

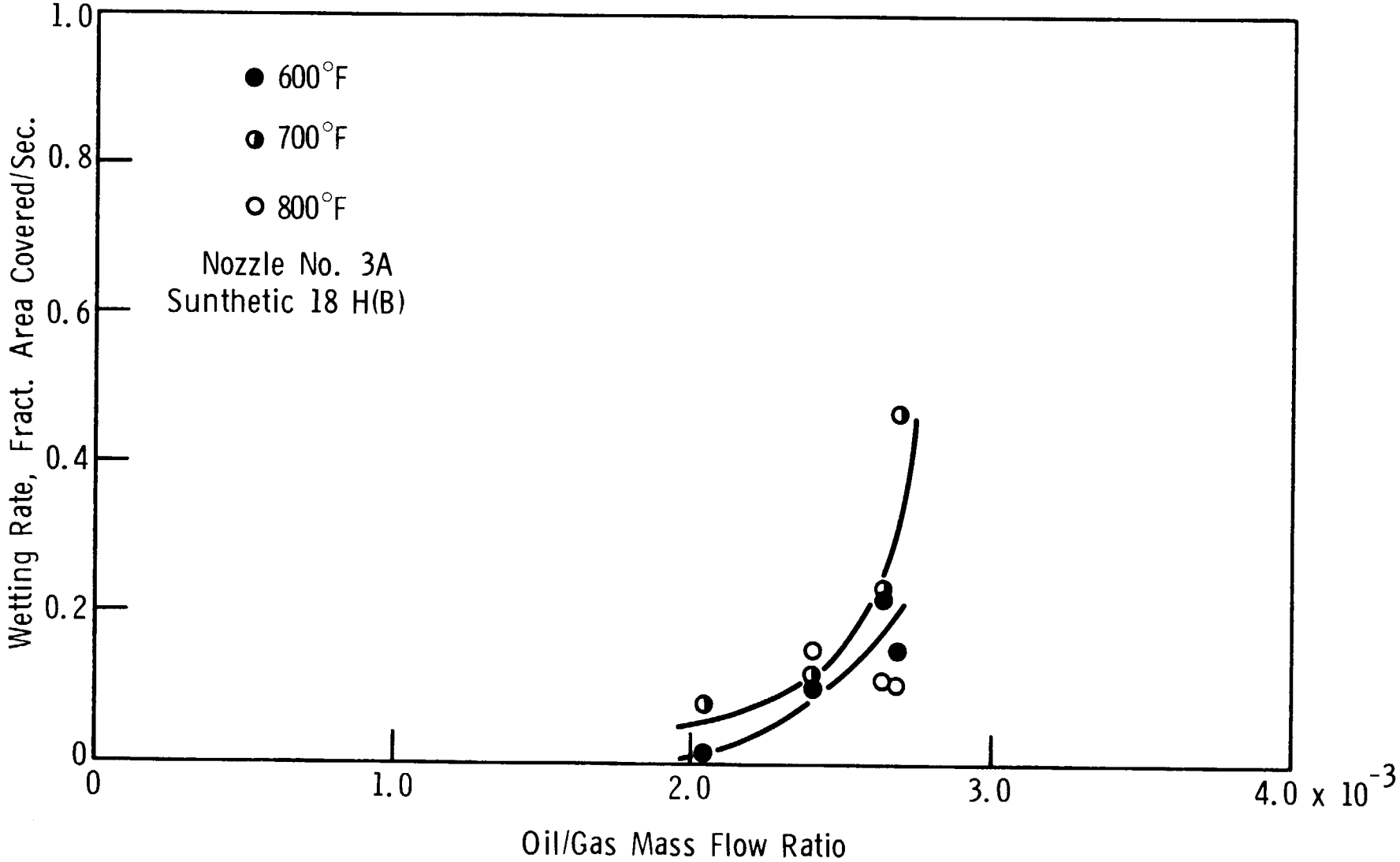

Figure 46

WETTING RATE AS A FUNCTION OF OIL/GAS MASS FLOW RATIO AND OF PLATE TEMPERATURE

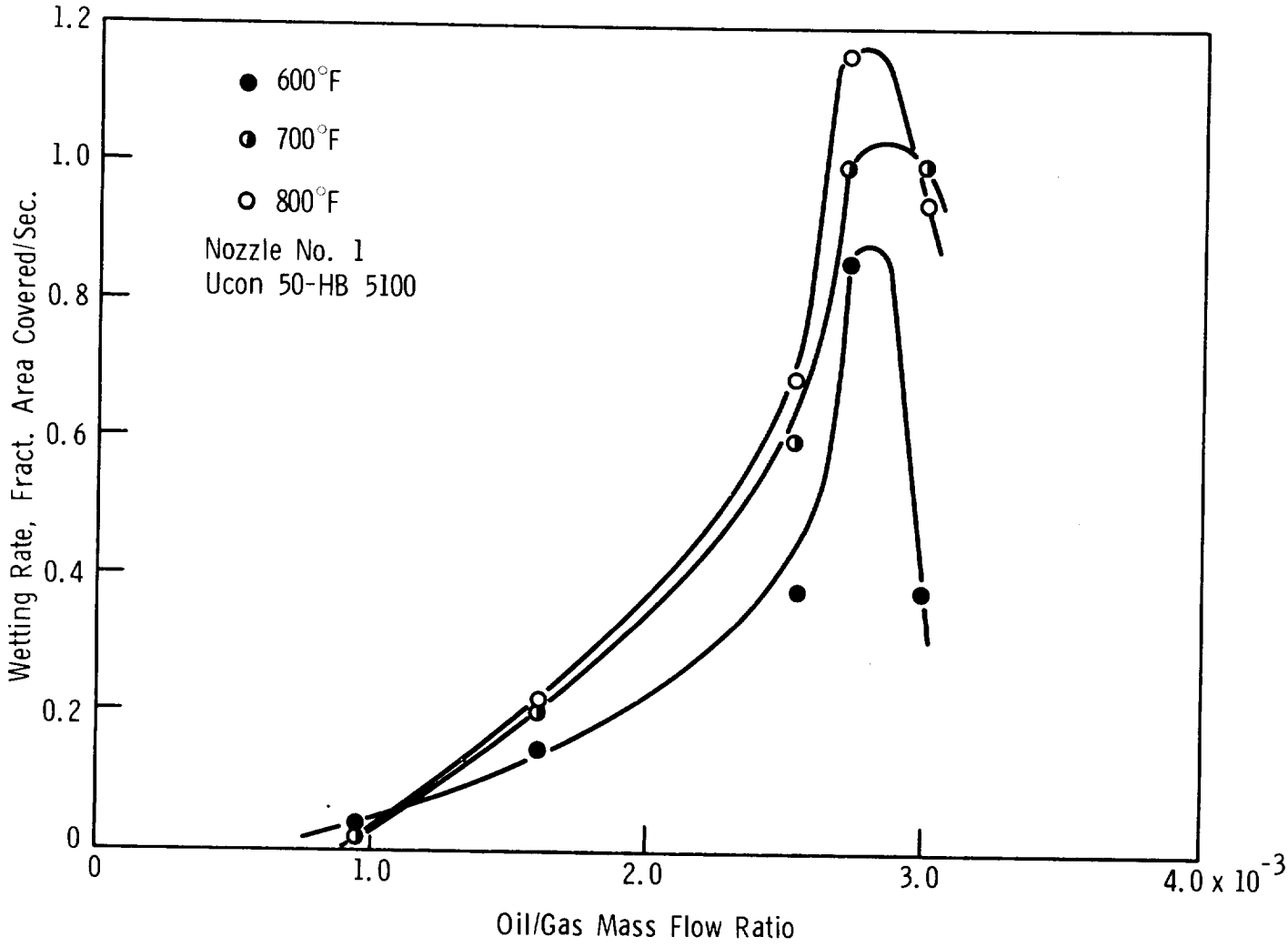

Figure 47

WETTING RATE AS A FUNCTION OF OIL/GAS MASS FLOW RATIO AND OF PLATE TEMPERATURE

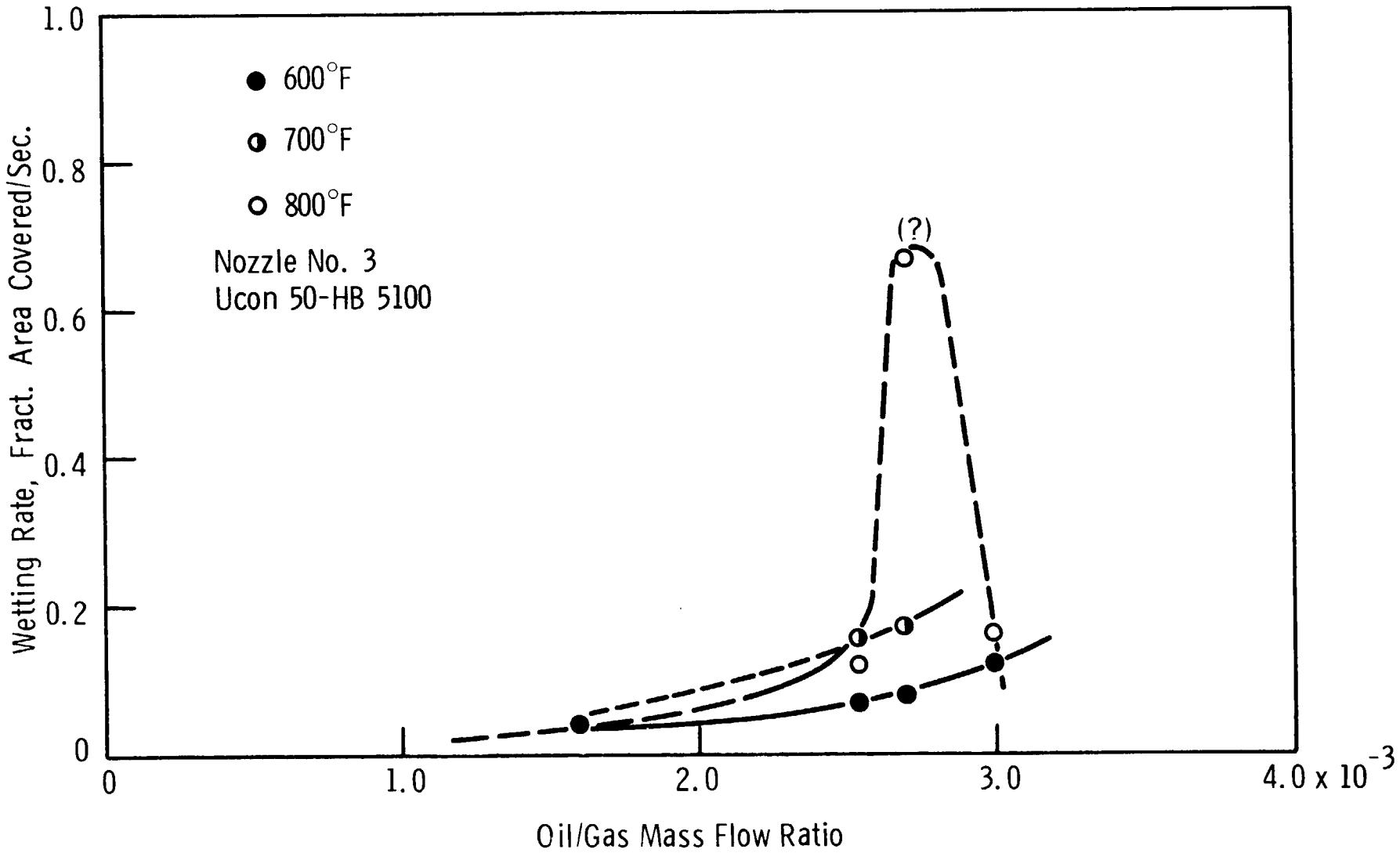

Figure 48

WETTING RATE AS A FUNCTION OF OIL/GAS MASS FLOW RATIO AND OF PLATE TEMPERATURE

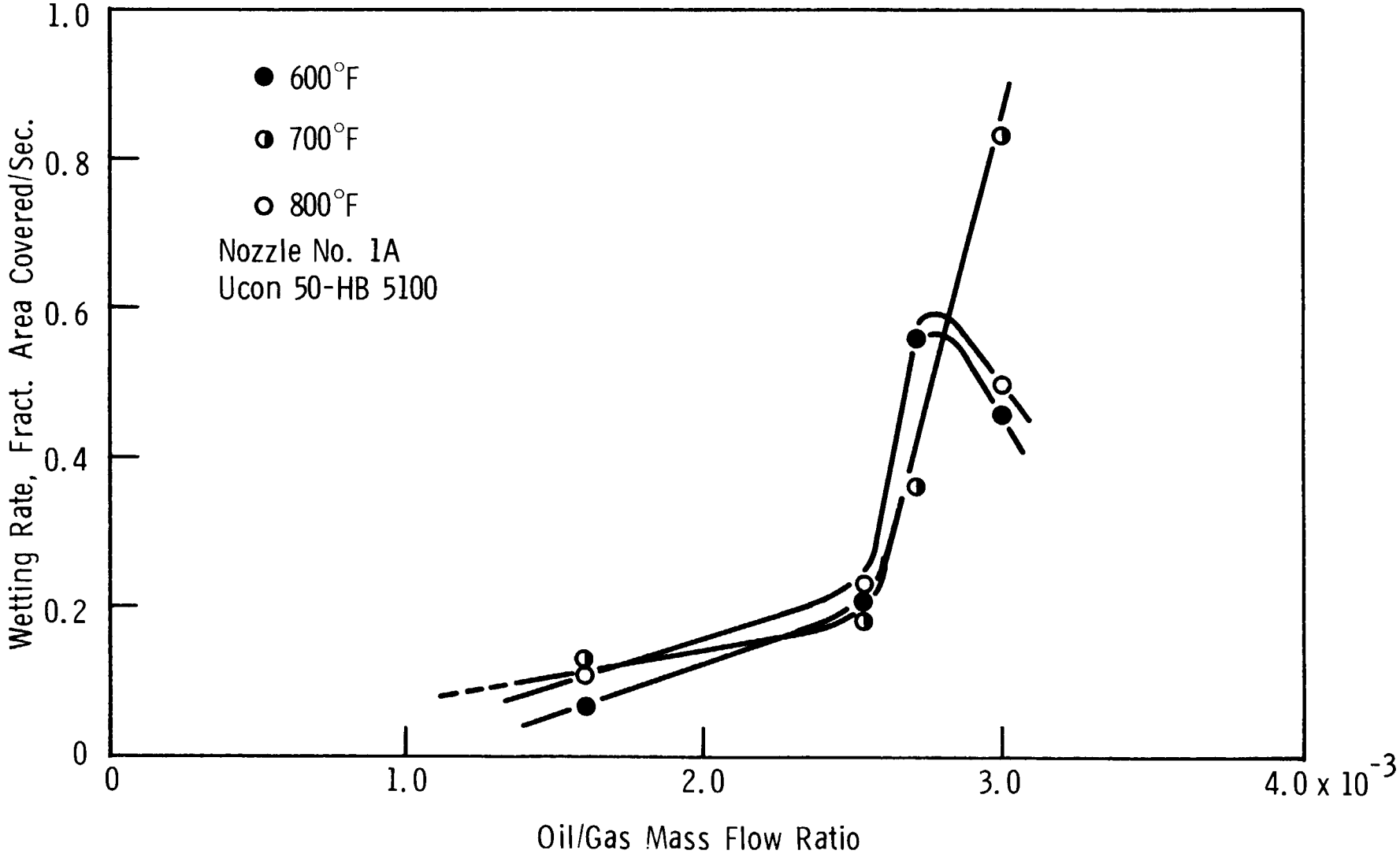

Figure 49

WETTING RATE AS A FUNCTION OF OIL/GAS MASS FLOW RATIO AND OF PLATE TEMPERATURE

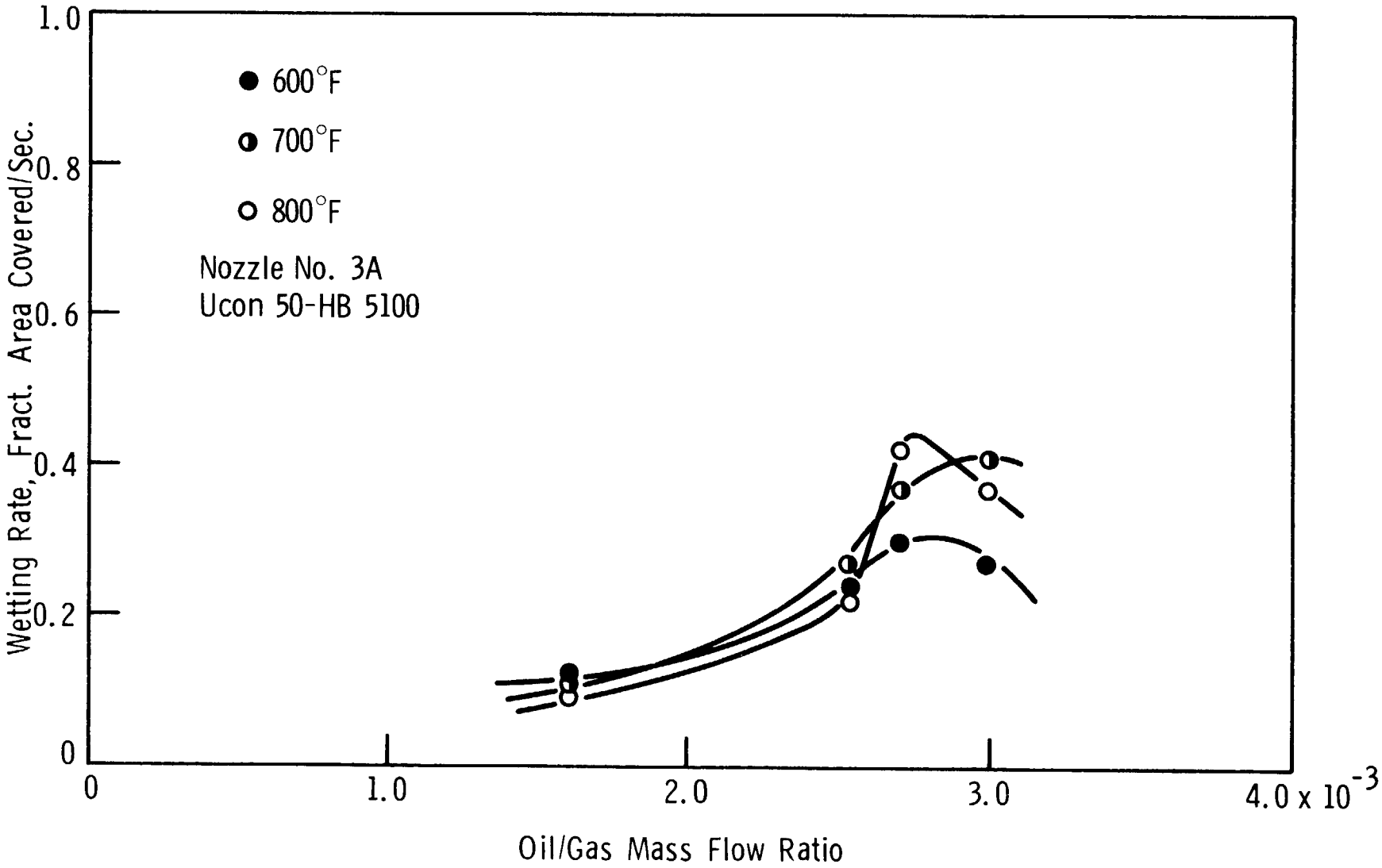

Figure 50

WETTING RATE AS A FUNCTION OF OIL/GAS MASS FLOW RATIO AND OF PLATE TEMPERATURE

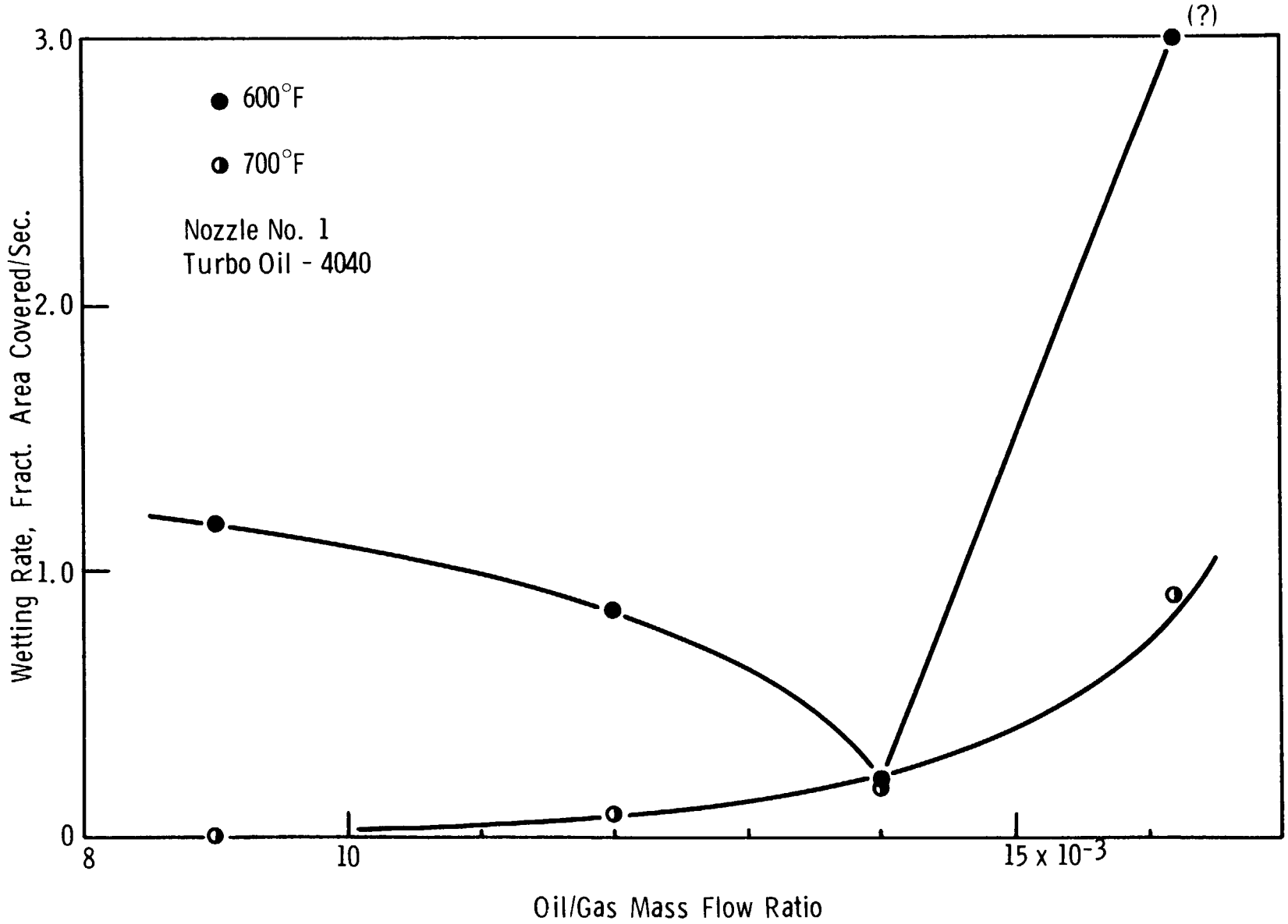

Figure 51

WETTING RATE AS A FUNCTION OF OIL/GAS MASS FLOW RATIO AND OF PLATE TEMPERATURE

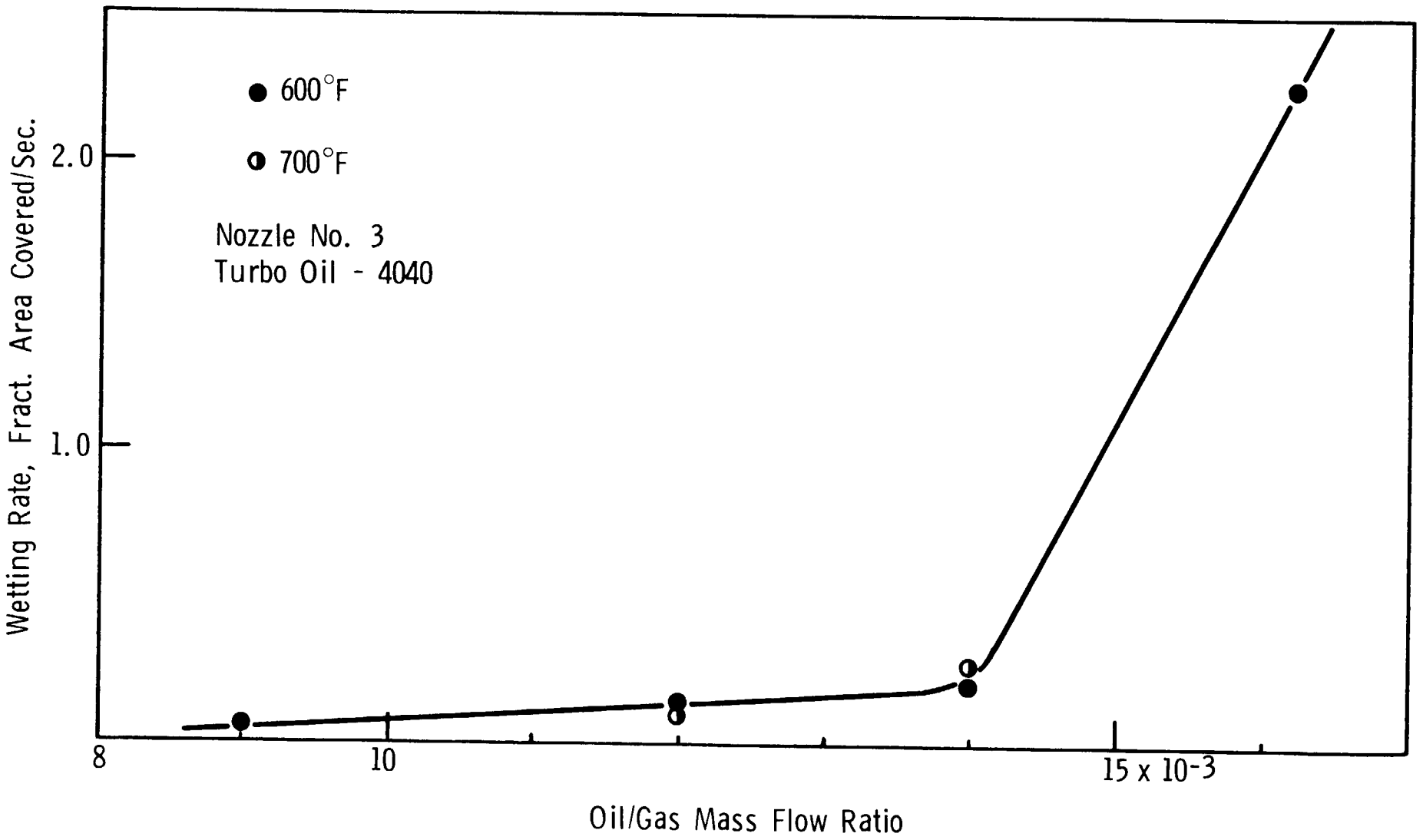

Figure 52

WETTING RATE AS A FUNCTION OF OIL/GAS MASS FLOW RATIO AND OF PLATE TEMPERATURE

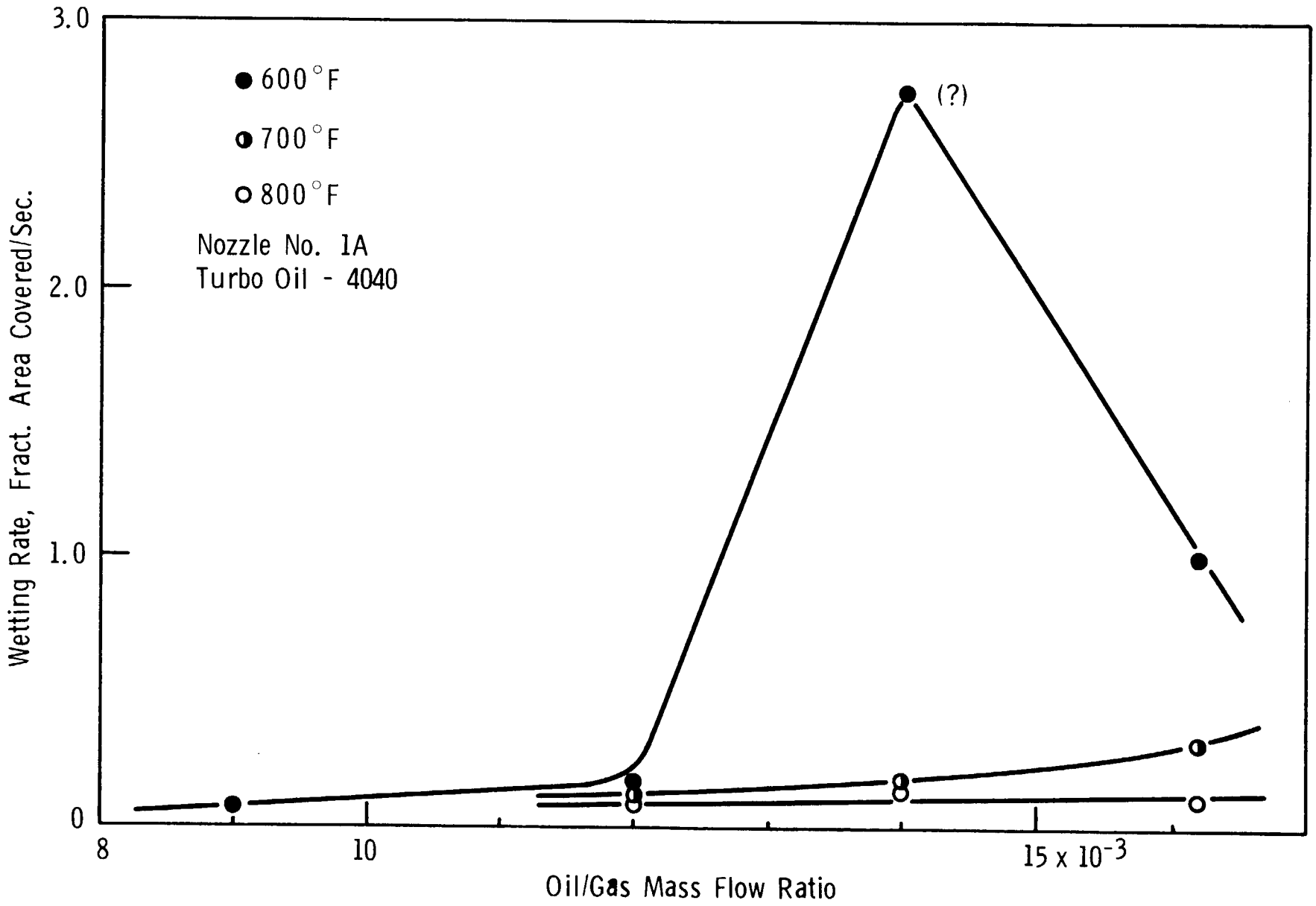

Figure 53

WETTING RATE AS A FUNCTION OF OIL/GAS MASS FLOW RATIO AND OF PLATE TEMPERATURE

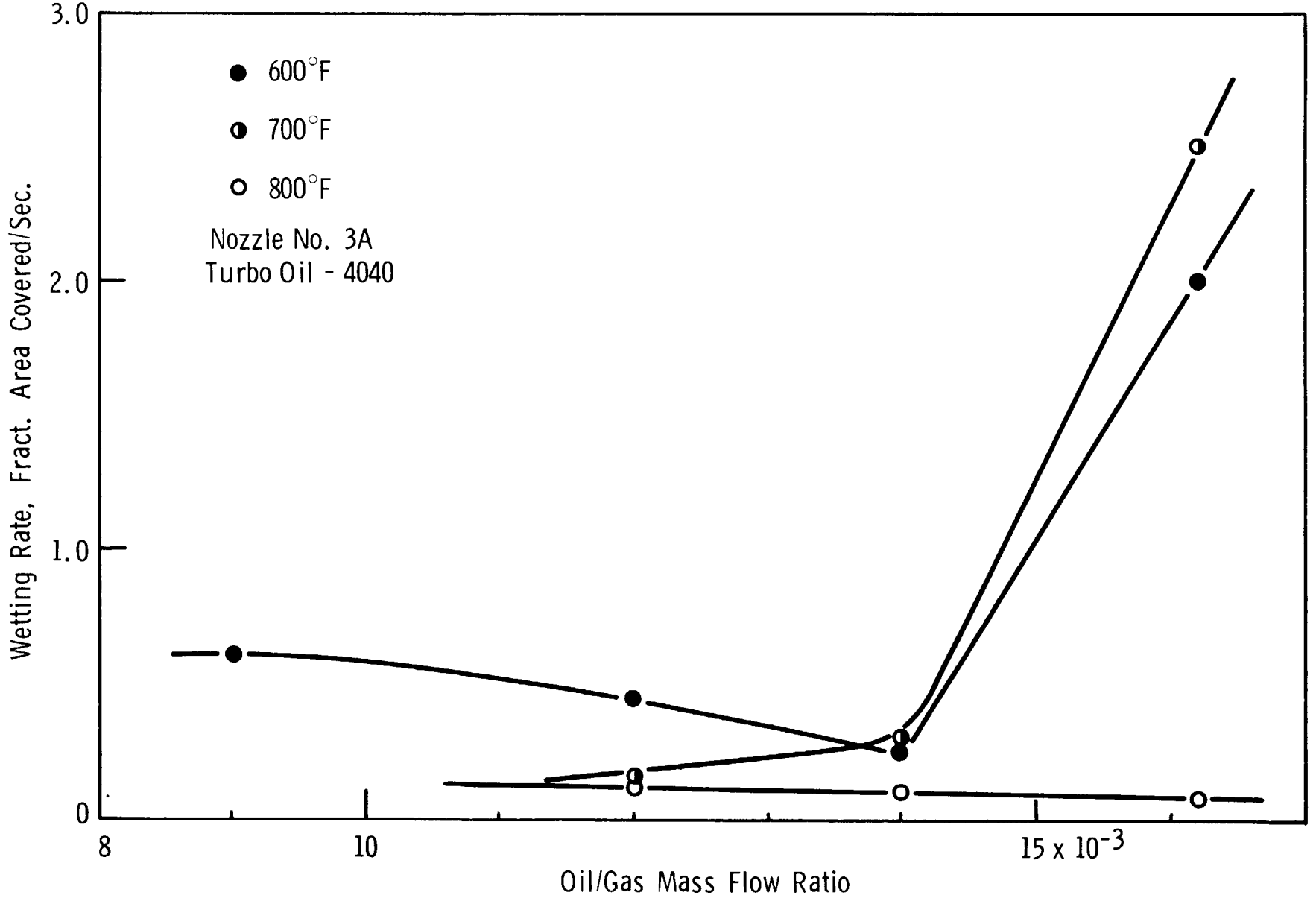

fundamental properties of the oil film and by the interfacial shear produced by the adjacent high velocity gas flow. This shifting phenomenon involving the hydrodynamic behavior of a thin oil film on a heated surface and the rate of mass transfer at an interface between oil film and gas, is more dramatic for light oils such as Hercolube F or Turbo oil 4040 than for the more viscous oils, XRM 177 F, Sunthetic 18 H(B), and Ucon 50HB-5100, as shown by Figures 36 through 53.

In discussing the effect of plate temperature on wetting, the importance of the heat transfer process at the interface between the test plate and the moving oil film cannot be ignored. Careful review of the motion picture films reveals that streaks of discontinuous oil film on the test plate at the early stage of spraying are not influenced only by impaction pressure and heat flux, $q = h\Delta T$, along the test plate. The filmed experiments seem to indicate that when a microfog drop impinges upon the test plate at 800°F, where most evaporation of the oil occurs, direct contact is obstructed by immediate formation of an oil vapor layer between the oil drop and the plate, a process similar to the Leidenfrost phenomenon* (14). A study of heat transfer in this area could add significantly to our understanding of high temperature lubrication.

The results discussed in this section would lead to the conclusion that when impinging on a hot surface at sufficiently high oil/gas mass flow ratio, microfog particles seem to wet the surface, regardless of its temperature within the range where the Leidenfrost phenomenon (or film boiling) does not occur.

vii) Comparison of the Wetting Rates of Different Test Oils

For convenience in comparing the wettabilities of the five test oils having widely different properties, their wetting times, obtained with No. 1 nozzle at 600°F, are chosen for discussion. The wetting rates versus the oil/gas mass flow ratios for these oils are also plotted in Figure 54 in an attempt to establish a correlation similar to those obtained in the previous sections. The curves shown in Figure 54 give the values of the specific wetting rate (wetting rate per unit mass flow ratio) and minimum wetting rate (minimum oil/gas mass flow ratio required to wet a solid surface), which are determined by taking slope and intercept at zero wetting rate, respectively. These values are listed in the following table.

*This phenomenon observed in a study of the spontaneous spreading of oil drop on a hot surface, was briefly discussed in Reference (21). The Leidenfrost phenomenon is the occurence of a "repulsion" between a liquid and a hot solid. In such a case, the liquid is supported on a layer of vapor formed by evaporation from the lower surface of the liquid by conduction through the vapor film and by radiation from the hot surface.

Figure 54

WETTING RATE OF DIFFERENT OILS
AS A FUNCTION OF OIL/GAS MASS FLOW RATIO AT 600°F

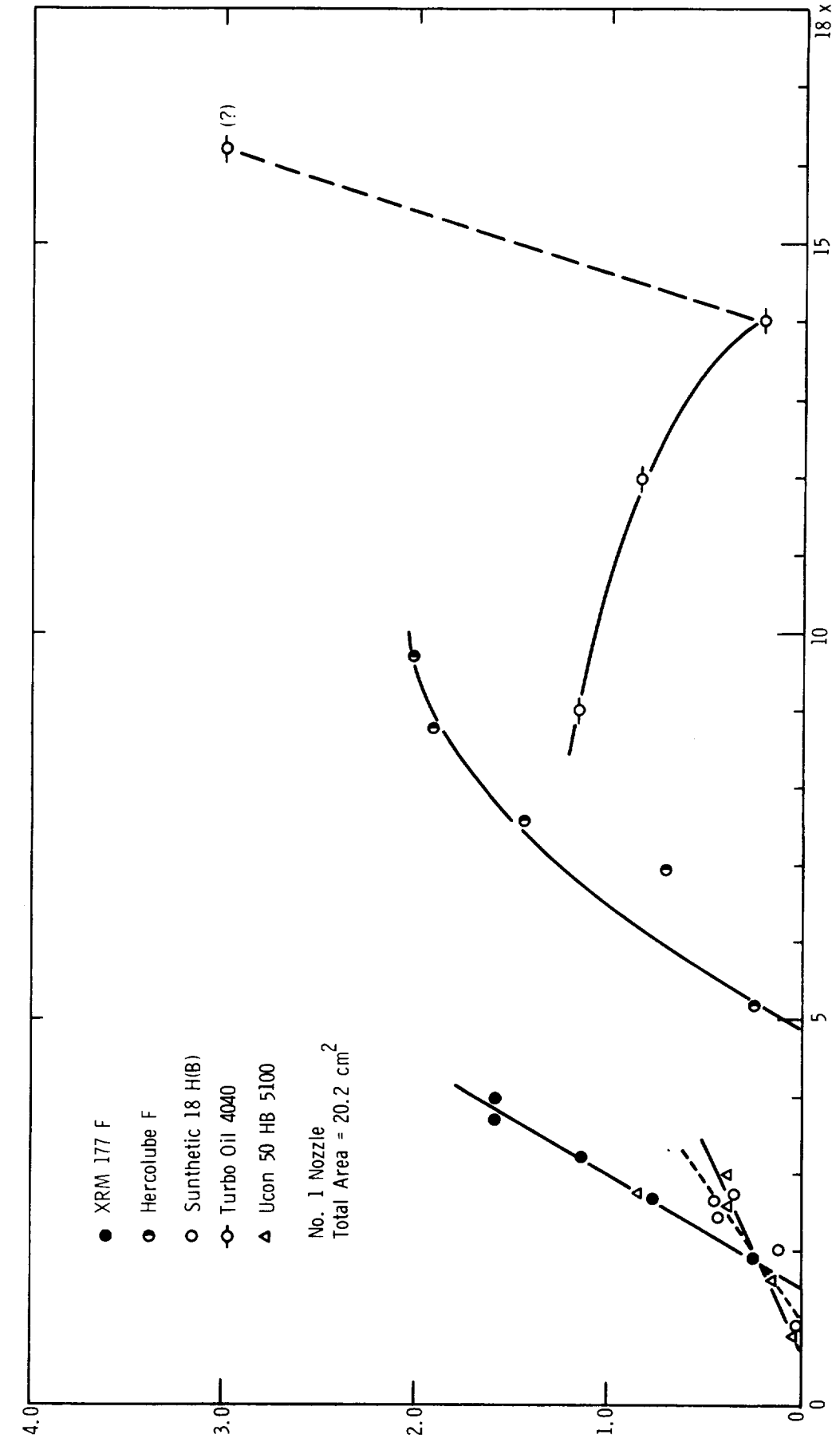

Test Oil	Specific Wetting Rate* [cm^2/sec/(oil/gas) mass ratio] x 10^{-4}	Minimum Wetting Rate* [(oil/gas) mass flow ratio] x 10^{3}
XRM 177 F	1.4	1.5
Hercolube F	0.9	4.7
Sunthetic 18H(B)	0.6	1.1
Ucon 50-HB-5100	0.4	0.8
Turbo Oil 4040	-0.4	16.1

*Test conditions used: 600°F and No. 1 nozzle.

Results of wetting studies, in general, show that the wetting times of Ucon 50-HB-5100 and Sunthetic 18H(B) are considerably longer than those of Hercolube F and Turbo Oil 4040 at a given condition, while the heavy oils usually require lower minimum (oil/gas) mass flow ratio to wet the test plate than the light oils. Reasons for the longer wetting times of the heavy oils can be attributable chiefly to their low fluidity which unfavorably influences several important factors such as the rate of oil output, particle size, and velocity of the oil film on the test plate. However, the heavy oils seem to have an advantage in minimum wetting rate - i.e., they require lower minimum oil/gas mass flow ratio to wet a given test plate. This apparently is due to lower oil loss by evaporation and/or streaking. The wetting rate data for XRM 177 F suggest that its physical properties are such that it possesses the advantages of both the light and heavy oils, combining excellent fluidity with low oil loss by evaporation or streaking. These properties are clearly reflected in the above table where, for a unit oil/gas mass flow ratio, XRM 177 F has the fastest wetting rate, and requires a minimum (oil/gas) mass flow ratio of only 1.5×10^{-3} to wet the test plate at 600°F. On the basis of the specific and minimum wetting rates, the comparison of these test oils leads to the conclusion that at 600°F with No. 1 spray nozzle XRM 177 F has the best overall wetting characteristics. In the same manner, conclusions concerning the wetting characteristics of the five oils at different conditions can be based on similar comparisons of their wetting rates.

It is of interest to find that the specific wetting rate of Turbo Oil 4040 is a negative value, -0.4×10^{4} cm^2/sec - unit mass flow, implying that the wetting rate decreases with increasing oil/gas mass flow ratio, as shown in Figure 54. This phenomenon may be explained by relating wetting rate to particle size distribution and impaction pressure, which jointly control the amount of oil collected on the test plate, and to the flow pattern of the oil film (the latter will be discussed in greater detail in a later section). When increasing the oil/gas mass

flow ratio, for Turbo Oil 4040 a great increase in oil streaking was observed. As a result, less oil was accumulated on the plate and hence less was available for the formation of a continuous oil film wetting the test plate. This may account, at least in part, for the negative value of the specific wetting rate.

viii) Effect of Surface Oxide Formation and Oil Degradation Products

A series of test runs under the conditions outlined in Task II, Section A, but using air instead of nitrogen gas, and with the test oil not degassed, was made to determine the effects on wetting rate of surface oxide formation and oil degradation products, which may modify oil properties or form surface deposits. These tests were made with four different nozzles - Nos. 1, 3, 1A, and 3A, at gas flow rates of 3 and 5 cfm, and employed XRM 177 F at test plate temperatures of 500, 550, and 600°F. Originally specified determinations of the wetting rates of XRM 177 F with air at 700 and 800°F were replaced by those at 500 and 550°F, with the approval of the NASA project manager, in view of the 750°F autogeneous ignition temperature (ASTM-D2155) of XRM 177 F, indicating a possibility of explosion hazard.

A summary of the test results is presented in Appendix D-2. Comparison of these results with wetting rate data obtained under the identical conditions with nitrogen as the atomizing gas, indicates that any surface oxides and oil degradation products that might be formed have little influence on the wetting rates of XRM 177 F at 600°F. Thus, surface oxides and oil degradation products, at least in the quantities formed in the short duration of exposure to air as the atomizing gas, appear to have little effect on wetting rate. There was, however, a very slight variation in the appearance of the test plate after exposure to these test conditions for 10 seconds. At 500 and 550°F, the plate appeared oily with a trace of tarnish, while the appearance of the plate tested at 600°F was oily with light tarnish.

ix) Effect of Gas Flow Rate to Diffuser

In order to investigate the effects of gas flow rate to the microfog diffuser on wetting, determinations of the wetting rates of XRM 177 F were augmented by wetting rate tests using the No. 3 nozzle at 600 and 700°F. The gas flow rates to the diffuser were 1, 2, and 3 cfm, while the gas flow rates to the microfog generator were varied from 2 to 6 cfm. In this way, the process of atomization is kept constant, while the particle velocity of the spray is varied by introducing another nitrogen gas stream to the transporting line. In this way, particle concentration (or oil/gas

mass flow ratio) in the gas streams is altered accordingly, but mean particle size presumably remains constant. Experimental results are listed in Appendix D-3.

A typical experimental result, plotting the fractions of area covered versus spray time at different gas flow rates to the diffuser, is shown in Figure 55. The plot indicates that increased gas stream velocity has little effect on total wetting time, but intermediate points seem to scatter more. The increased scattering of these points is probably due to increased impaction pressure, generating, in turn, more streaking and discontinuity of the oil film on the test plate. Since this creates difficulties in photographically identifying a true continuous oil film, the experimental data in this particular study are the least accurate of the wetting rate data obtained thus far.

In an effort to establish a simple relation indicating the effects of various factors on wetting rate, the wetting rates as a function of particle concentration (or oil/gas mass flow ratio) and of impaction velocity at 600 and 700°F are presented in Figures 56 and 57. These figures also include the constant velocity lines designated by the dotted lines. Although the figures appear to be somewhat sketchy and confusing, we can nevertheless draw several general conclusions: (1) wetting rate increases as impaction velocity increases at a constant mass flow ratio, (2) wetting rate increases with increasing mass flow ratio at a constant impaction velocity, and (3) for a given particle size wetting rate changes little when increasing impaction velocity, in turn, correspondingly decreases particle concentration in the gas stream.

The first and second remarks merely confirm the previous conclusions on the importance of impaction velocity and of oil/gas mass flow ratio. The variations of impaction velocity, while maintaining mass flow ratio constant, but not free from changes in particle size, were achieved by using different nozzle sizes. The last observation simply suggests that introduction of additional gas flow to a transporting line for the purpose of increasing impaction velocity has no advantage in wetting rate. In general, the best wetting can be achieved through the maximum loading of oil particles suspended in the gas stream (or the highest mass flow ratio under a given condition) and the proper choice of nozzle size to develop the appropriate impaction velocity in accordance with the particle size distribution.

x) Surface Velocity and Thickness of Thin Oil Films

Since the velocity distribution of an oil film is expressed in mathematical form for the case of laminar film flow motivated by interfacial shear, it is of interest to apply these relations

Figure 55

EFFECT OF NITROGEN FLOW RATE TO DIFFUSER ON WETTING

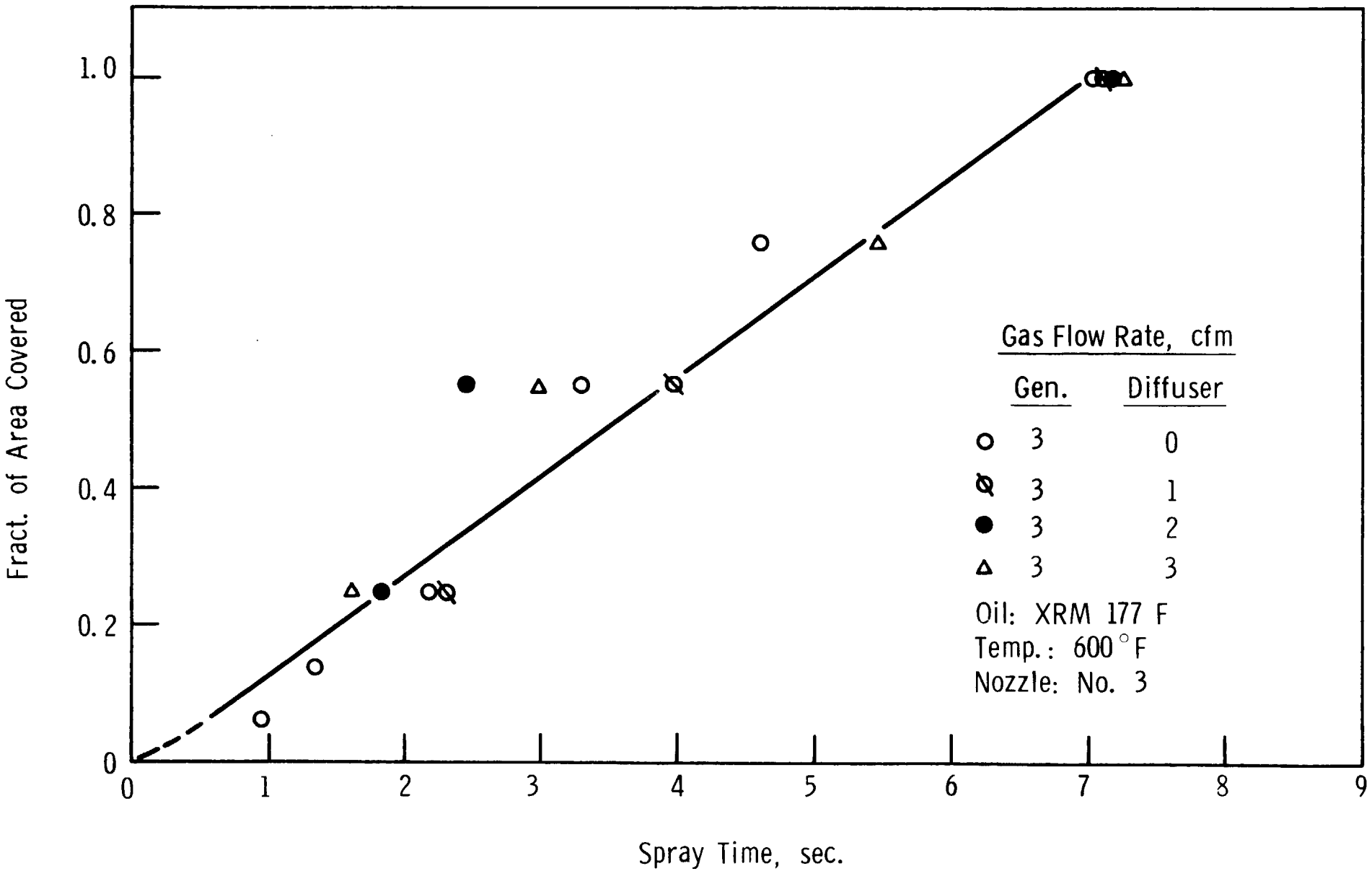

Figure 56

WETTING RATE AS A FUNCTION OF OIL/GAS MASS FLOW RATIO AND OF IMPACTION VELOCITY AT 600 ° F

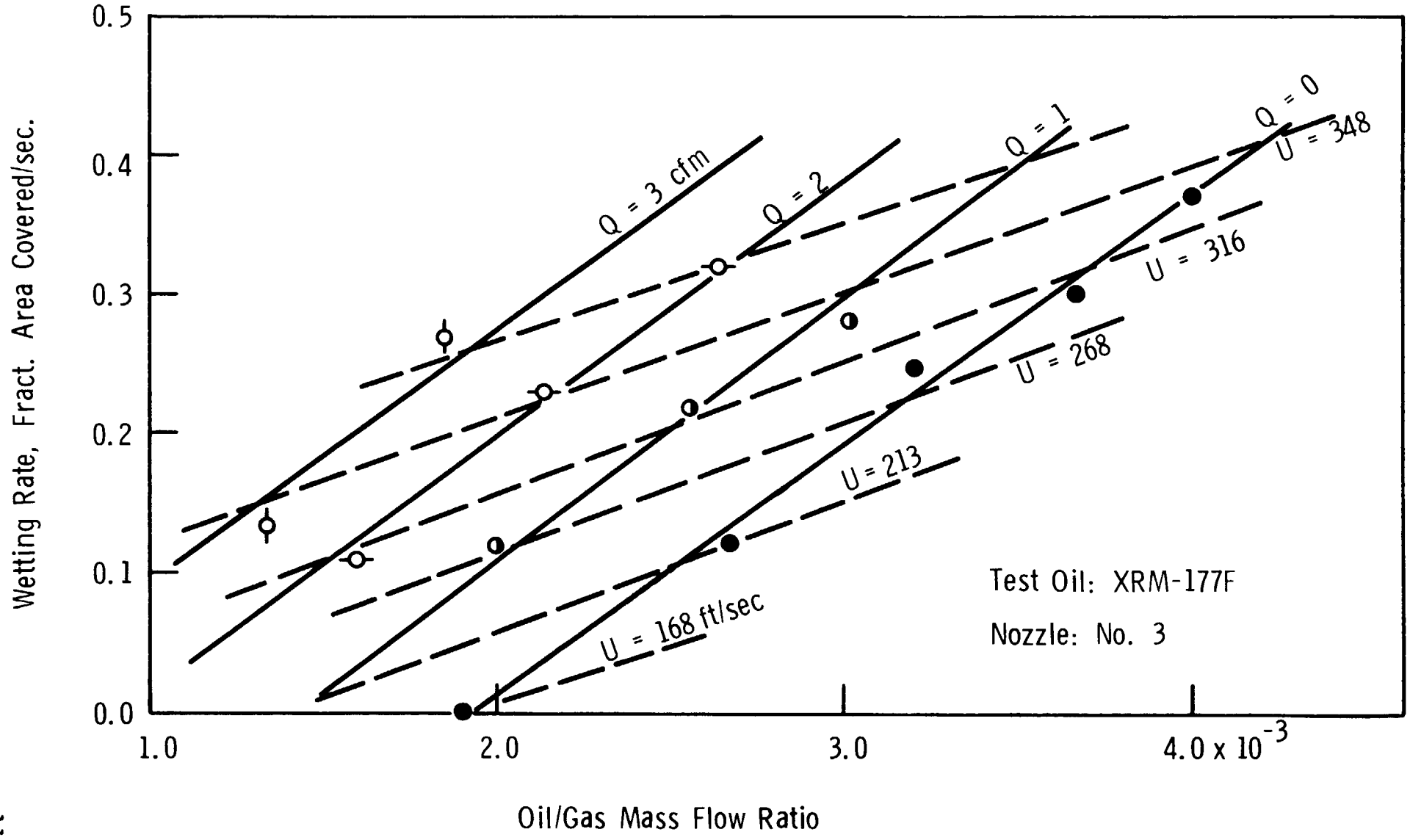

Figure 57

WETTING RATE AS A FUNCTION OF OIL/GAS MASS FLOW RATIO AND OF IMPACTION VELOCITY AT 700 ° F

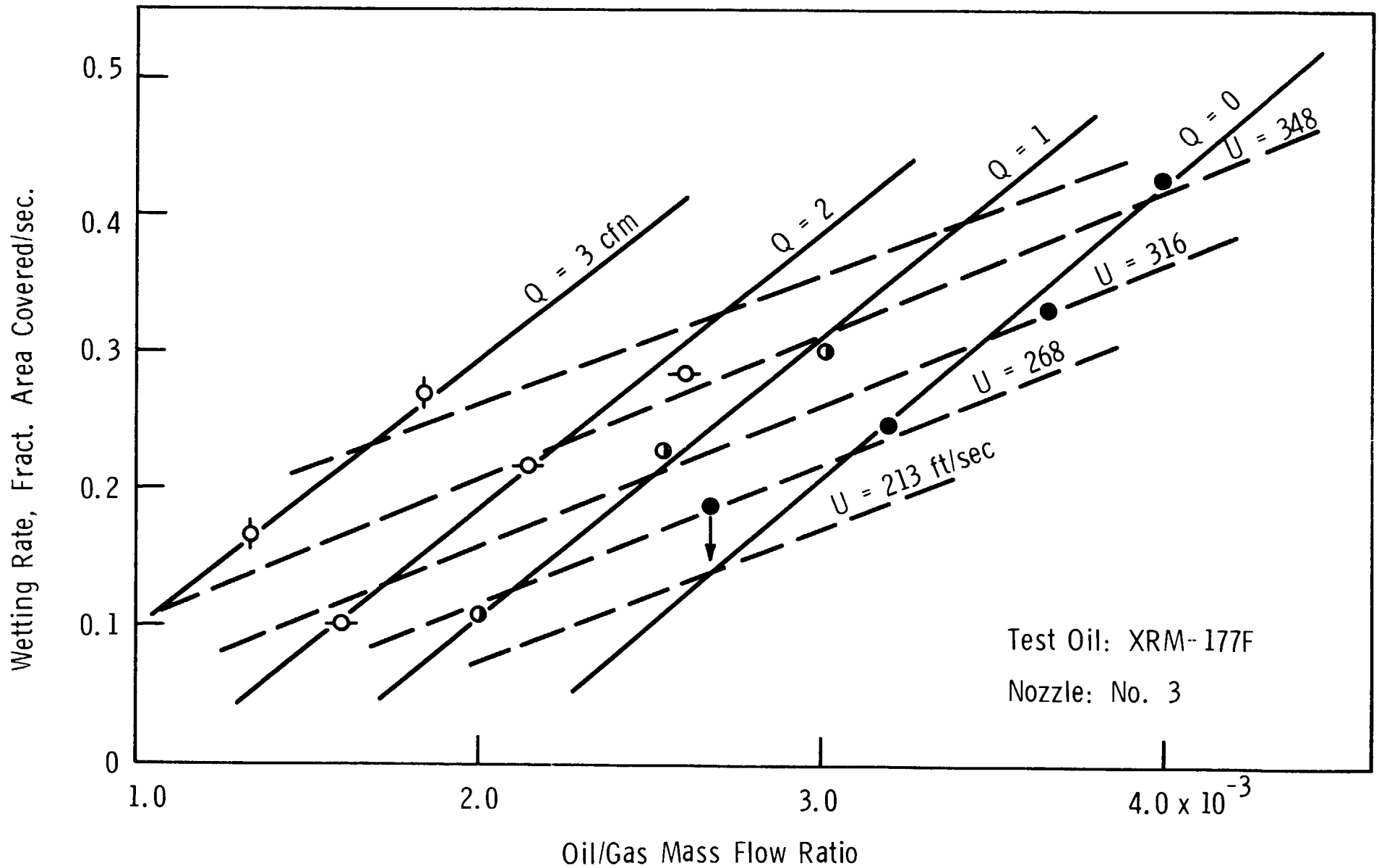

in a limited way to existing experimental data in order to estimate surface velocities and thicknesses of thin oil films flowing isothermally over heated plates.

In the earlier section (iii), we indicated that in the wetting rate studies of XRM 177 F, the relationship between wetted area and wetting time is linear and a corresponding relation can therefore be expressed as:

$$\frac{dA}{dt} = \frac{d(\pi r^2)}{dt} = k_1 \tag{14}$$

where k_1 is the slope of a straight line. From Equation (14), the velocity of the oil film, U_r, along radial distance, r, is given by:

$$U_r \equiv \frac{dr}{dt} = \frac{k_1}{2\pi r} \tag{15}$$

Since the local velocities of an oil film vary along the radial direction as shown in Figure 58, an average surface velocity must be determined by taking the integration of U_r along r

$$\langle \bar{U}_r \rangle = \frac{1}{r_2 - r_1} \int_{r_1}^{r_2} U_r(r)\,dr \tag{16}$$

Using Equations (15) and (16), the average (log-mean) surface velocities are calculated from the wetting data for XRM 177 F with Nos. 1 and 3 nozzles and listed in Table 9 along with other pertinent data. Additional calculated data for nozzles 1A and 3A are listed in Appendix D-4. Since the film thicknesses were not determined experimentally, it was necessary to calculate values with the aid of wetting rate and specific oil flow rate (oil flow rate to test plate per unit radius of plate) by employing Equation (5) in Appendix D-5, that is,

$$\delta = \frac{\Gamma}{\rho_L \langle \bar{u} \rangle}$$

At this point, we must make a distinction between mean film velocity, $\langle \bar{u} \rangle$, and mean surface velocity, $\langle \bar{u}_r \rangle$, which are related in the form of

$$\langle \bar{u} \rangle = \frac{\langle \bar{u}_r \rangle}{2} \tag{17}$$

Figure 58

RADIAL SPREADING DISTANCE VERSUS TIME

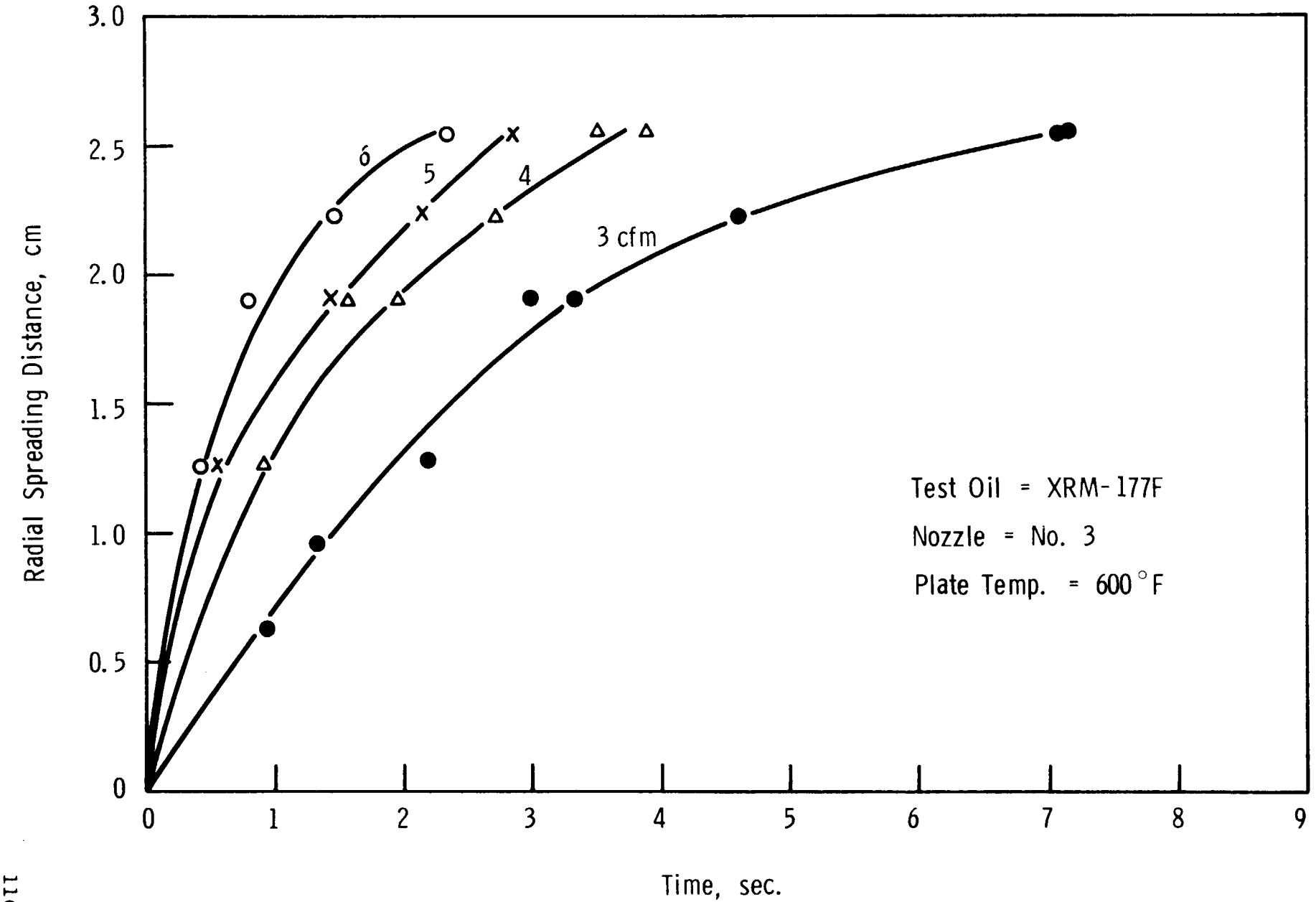

providing our system is similar to a case of laminar film flow motivated by interfacial shear alone. In calculations of the film thicknesses, it is also assumed that the temperature of the oil film is in equilibrium with the operating temperature, and that no oil is lost through evaporation, and the values of density at 600°F are extrapolated by taking a straight line relation, even though the validity of this type of extrapolation to these temperatures is in doubt.

The results listed in Tables 9, calculated from the wetting rate data for XRM 177 F with Nos. 1 and 3 nozzles at temperature of 600°F, reveal that mean surface velocity increases with increasing gas flow rate. The tabulated results also show that at 4 cfm the specific oil flow to the plate is highest and, in turn, the oil film flowing over the plate at 600°F is thickest. It is, however, somewhat surprising to find that the specific oil flow rate varies little in the range of 4 to 6 cfm gas flow despite a considerable increase in the rate of oil output from the generator from 1.35 to 2.52 gm/min. This finding seems to suggest that an excess of gas flow may improve the wetting rate of an oil not by increasing specific flow rate, but by increasing mean surface velocity through higher interfacial shear at the free surface. An increase in wetting rate by this means is, of course, brought about at the expense of film thickness. This implies that each set of operating conditions has its optimum point depending on surface velocity and the oil film thickness required for lubrication.

The calculated values of Reynolds number, using mean surface velocity and extrapolated kinematic viscosity of XRM 177 F at 600°F, indicate that the film flow is mainly laminar in nature - i.e., $N_{Re} \cong 100$ at 600°F. Visually, however, the film seems to exhibit not a smooth laminar flow, but a wavy laminar flow, or the flow in a laminar-turbulent transition zone. The appearance of wavy laminar flow may be, in part, due to instability of the oil film at high temperature. In addition to the critical Reynolds number, the general dependence of the Weber and Froud numbers may be important in characterizing this type of film flow (4).

xi) Wetting Pattern of Test Oils

During analyses of the photographic films recording the wetting rate studies, considerable differences in oil film flow among the oils tested were observed. Two different types could be broadly classified - streaky flow for the light oils, and uniform (continuous) film flow for the heavy oils. The light oils include Hercolube F and Turbo Oil 4040; while XRM 177 F, Sunthetic 18H(B), and Ucon 50-HB-5100 are classified as heavy oils.

Table 10

Surface Velocity and Thickness of Thin Oil Films*

Item	Plate Temp. (°F)	Gas Flow Rate (cfm)	Wetting Rate (fract. area covered/sec.)	Specific Flow Rate (g/cm-sec.) x 10^4	Mean Surface Velocity (cm/sec.)	Oil Film Thickness (μm)
1	600	2	0.25	0.83	0.44	5.5
2	600	3	0.77	10.86	1.35	23.3
3	600	4	1.15	13.00	2.01	18.8
4	600	5	1.60	12.40	2.80	12.8
5	600	6	1.58	12.30	2.76	12.9
6	700	2	0.16	0.83	0.28	
7	700	3	0.82	10.86	1.43	
8	700	4	2.00	13.00	3.50	
9	700	5	2.00	12.40	3.50	
10	700	6	1.54	12.30	2.70	
11	800	2	0.10	0.83	0.18	
12	800	3	0.84	10.86	1.47	
13	800	4	3.00	13.00	3.88	
14	800	5	2.00	12.40	5.83	
15	800	6	3.00	12.30	5.83	

*Test conditions used: XRM-177F, No. 1 Nozzle, and total cross-sectional area of the test plate = 20.2 cm^2.

Table 10 (Cont'd)

Item	Plate Temp. (°F)	Gas Flow Rate (cfm)	Wetting Rate (fract. area covered/sec.)	Specific Flow Rate (g/cm-sec.) x 10^4	Mean Surface Velocity (cm/sec.)	Oil Film Thickness (μm)
1	600	2	-	-	-	-
2	600	3	0.15	1.18	0.26	13.2
3	600	4	0.25	2.16	0.44	14.4
4	600	5	0.29	1.81	0.51	10.4
5	600	6	0.37	2.03	0.65	9.0
6	700	2	-	-	-	-
7	700	3	0.19	1.18	0.33	11.0
8	700	4	0.25	2.16	0.44	15.2
9	700	5	0.33	1.81	0.58	9.6
10	700	6	0.43	2.03	0.75	8.4
11	800	2	-	-	-	-
12	800	3	0.10	1.18	0.18	
13	800	4	0.23	2.16	0.40	
14	800	5	0.28	1.81	0.49	
15	800	6	0.40	2.03	0.70	

*Test Conditions used: XRM-177F, No. 3 Nozzle, and total cross-sectional area of test plate = 20.2 cm^2.

An excellent photograph showing a continuous oil film spreading over a test plate is presented in Figure 59. Careful review of the photographic evidence shows that when a continuous oil film spreads out to the edge of the plate, multi-layers of oil rings having different film thicknesses are formed and seem to propagate at regular intervals. Although no attempt has been made to investigate the reasons for this type of oil film movement at this time, the phenomenon observed may be partly due to the periodic variations in particle size distribution which occur when a microfog stream wets out at the tip of the spray nozzle, and may be partly initiated and controlled by the drag of gas flow at interface (for the interfacial shear, refer to Appendix D-5).

Schematic representation of the typical sequential spreading patterns of an oil film is given in Figure 60, showing, in Part (A), a continuous oil film gradually spreading out to the edge and in Part (B), a streaky flow or discontinuous oil streaks rapidly extending out to the edge of the test plate. In Part (1), the initial wetted area equivalent to the main impaction area of a microfog spray appears at a very early stage of spraying. Here, we can already notice differences in wetting pattern between Parts (A) and (B). While Part (B) exhibits irregular patterns of "oil fingers" covering a relatively wider area, Part (A) displays a comparatively uniform and thicker oil film. As soon as sufficient oil film is accumulated on the plate, the primary oil film starts to spread out. Differences between Parts (A) and (B) at this stage are more dramatic. In Part (B) it is very difficult to define the boundary region of the primary film because relatively heavy oil streaks (discontinued oil fingers) overshadow the entire wetting pattern. As spraying continues, the areas covered by the oil films, as well as areas of streaking and impaction, generally increase until the plate is completely covered.

From the photographic results obtained for all the wetting rate studies, the more viscous oils, including XRM 177 F, Sunthetic 18H(B), and Ucon 50-HB-5100, generally display a wetting pattern similar to Part (A), while the light oils follow Part (B). These wetting patterns do change somewhat depending upon the temperatures of the test plate and the gas flow rate. The wetting patterns of the different test oils at three temperatures are summarized as follows:

	Wetting Pattern of Oil Film		
Test Oil	600°F	700°F	800°F
XRM 177 F	C	C	S*
Hercolube F	S*	S	S
Sunthetic 18H(B)	C	C	C
Ucon 50-HB-5100	C	S*	S
Turbo Oil 4040	S	S	S

Figure 59

WETTING PATTERN OF AN OIL

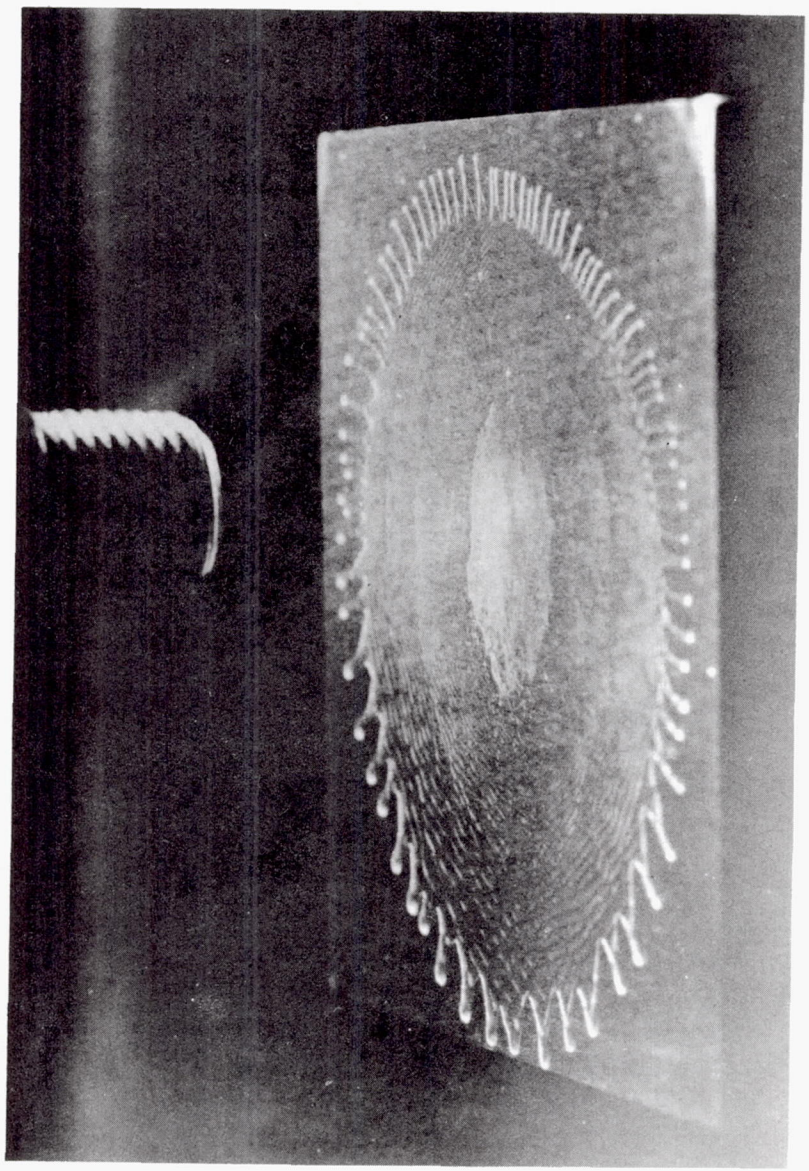

Figure 60

SCHEMATIC DIAGRAM OF THE WETTING PATTERNS OF THE TEST OILS

A Type

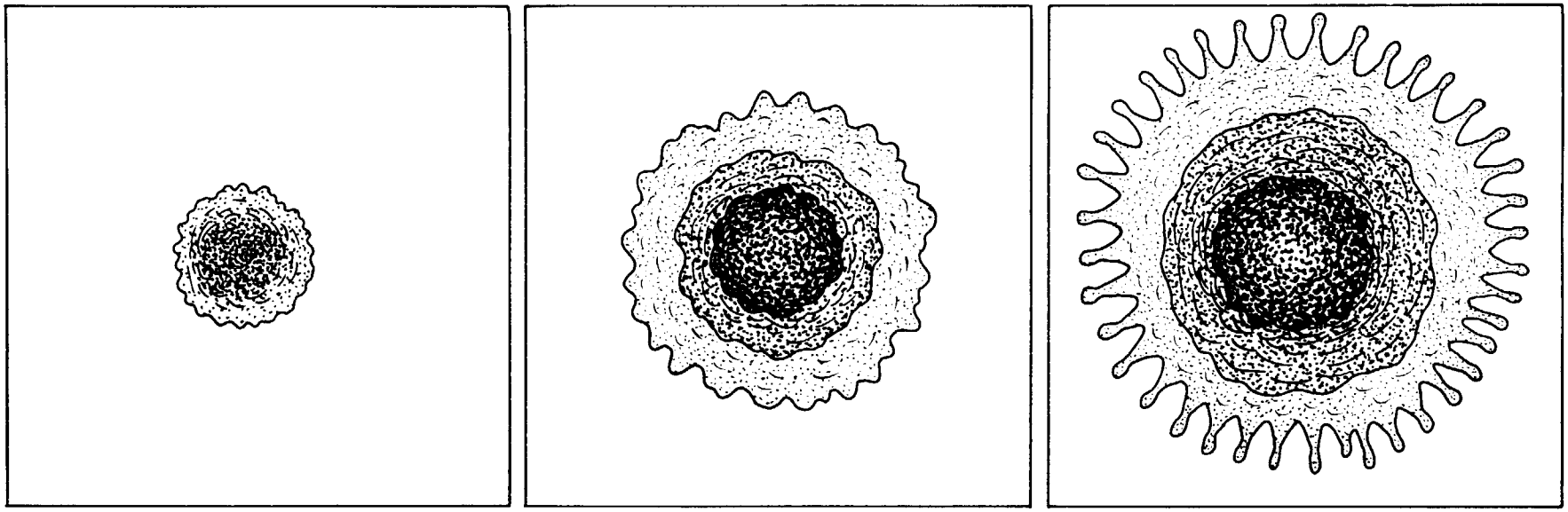

B Type

1 2 3

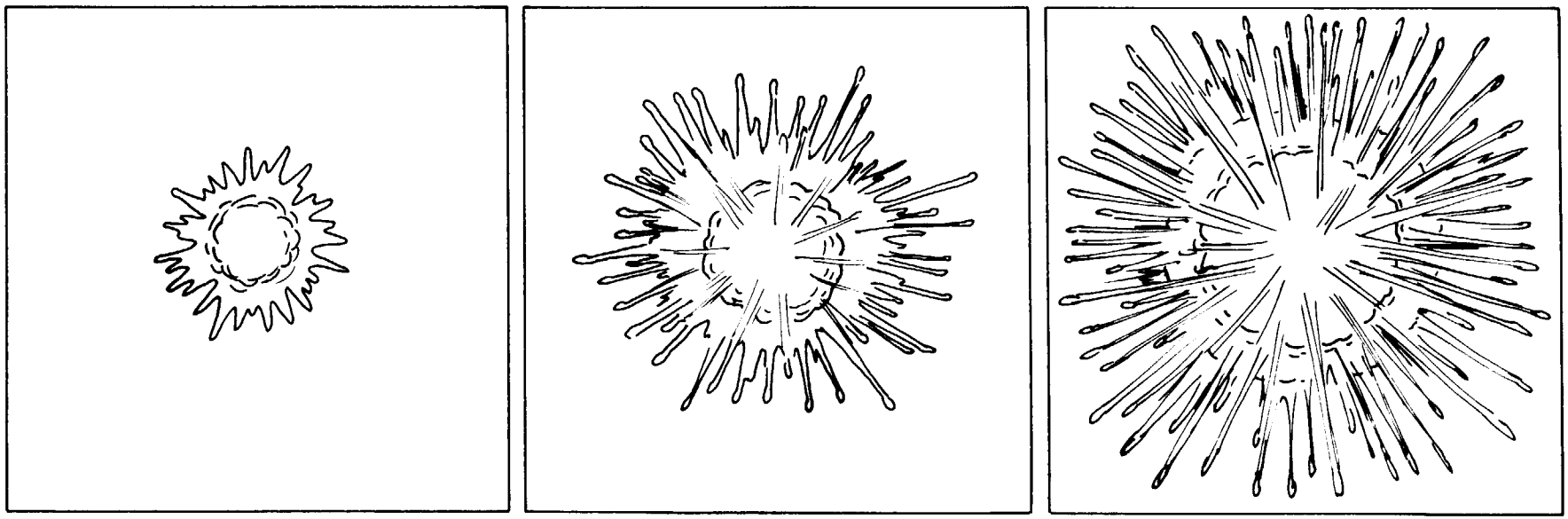

C : continuous film flow
S* : streaky but continuous flow at high oil/gas mass flow ratio
S : streaky film flow

In view of the relatively high fluidities and vapor pressures of Turbo Oil 4040 and Hercolube F, and the earlier experimental data on the spontaneous spreading of oil drops on a heated surface (21), it is extremely doubtful that the streaky oil films of Turbo Oil 4040 and Hercolube F actually wet the test plate even at 600°F, although streaks of the oil film flooding the test plate appear to wet the plate in the photographic results. Thus, the wetting times of the test oils with streaky flow, without considering the flow patterns of the oil films, may be completely misleading as far as this study is concerned.

From the observation of these wetting patterns, it may be concluded that for a given condition, a minimum viscosity and surface tension must be required to form a continuous oil film at a minimum wetting rate. Hence, a study relating the wetting patterns of oil films to actual performances of lubricants at high temperature may be attractive and useful for predicting the failure or success of a lubricant in a high temperature lubrication system.

As a matter of interest, wetting patterns were photographed when distilled water as a microfog was sprayed on the test plate at 400 and 600°F. The photographic results strongly resemble Part (B) in Figure 60 with more extensive streaking. This behavior is generally referred to as the convective Leidenfrost phenomenon, or fog flow with dry wall boiling. In this case, the vapor fraction is superheated almost to the wall temperature, while most of the original liquid does not evaporate (14, 24).

xii) Criterion for the Break-up of Thin Oil Films Flowing Isothermally over Solid Surfaces

In order to have a better understanding of the streaky flow of thin oil films on a hot surface, efforts were made to define theoretically a stability criterion for a thin oil film flowing over a hot surface, and to briefly examine the mechanisms initiating the streaky flow.

When a thin oil film flows over a solid surface under the actions of, for example, a shear applied by a high speed gas, streaky film flow (or dry patches) can form and spread. Hartley and Murgatroyd (8) have considered the stability of a flowing film in terms of two criteria, based respectively on a force balance at a dry patch and on energy flow considerations. In the present study, we shall confine attention to the first case.

On the basis of the theory of Hartley and Murgatroyd, if the dry patch is stable, the surface tension forces and the stagnation pressure of the oil film at the stagnation point must be in static equilibrium (refer to Appendix D-6), that is,

$$\sigma\ (1 - \cos\ \theta) = \int_0^{\delta^*} \frac{\rho u^2(y)}{2}\ dy \tag{18}$$

The equation above is very interesting in its simplicity and strong dependence on contact angle, the left-hand side of the equation being capable of values ranging from zero to 2σ. The criterion presented leads to theoretical estimates of the minimum film thickness and flow rates of oil films in motion. As an example, the minimum film thickness and wetting rate for the case of a laminar film flow motivated by interfacial shear, illustrated in Appendix D-5, are given, respectively, by

$$\delta^* = 1.82 \left[[\sigma\ (1 - \cos\ \theta)] \left(\frac{\mu}{\tau_i}\right)^2 \right]^{1/3} \tag{19}$$

and

$$\Gamma^* = 3.30 \left[\left(\frac{\rho\mu}{\tau_i}\right) [\sigma(1 - \cos\ \theta)]^2 \right]^{1/3} \tag{20}$$

It is of interest to note that the oil film thickness and the maximum wetting rate* are greatly dependent upon viscosity, surface tension, and particularly contact angle. Since no experimental data are available, it is therefore not possible to compare these equations with the experimental data. Nevertheless, these equations suggest the upper and lower limits of δ^* and Γ^*, ranging from:

$$\left.\begin{matrix}\delta^* \\ \Gamma^*\end{matrix}\right\} \rightarrow 0 \qquad \text{as } \theta \rightarrow 0 \text{ (for free spreading)}$$

*The minimum wetting rate is defined as the minimum oil flow rate required to re-wet the surface after the formation of a dry patch.

and

$$\delta^* = 1.82 \left[2\sigma \left(\frac{\mu}{\tau_i}\right)^2\right]^{1/3} \quad \text{as } \theta \to 180° \text{ (for spheroidal-state)}$$

$$\Gamma^* = 3.30 \left[\left(\frac{\rho\mu}{\tau_i}\right) (2\sigma)^2\right]^{1/3}$$

The equations also suggest that the minimum wetting rate decreases with increasing gas flow rate which in turn increases interfacial shear. In comparing these equations with the experimental data, the validity of using the measured static contact angle is in question. It is quite possible that the static contact angle is not the appropriate one for use in the Hartley-Murgatroyd theory; a film edge in motion, however, may experience a larger contact angle than the static one. The theoretical treatment may not, therefore, be valid in such a case although it seems to predict the general trends correctly.

It may be noted that the existence of a dry patch is an essential condition in the above-mentioned analysis; if the surface is already wetted, then the flow rate could quite possibly be reduced below the minimum wetting rate without breakdown of the film. The film in this case would be metastable and some mechanism for breaking it down would be required. The upper limit of δ^* and Γ^* considered immediately leads to one mechanism for breaking oil film down - i.e., for the case of the spheroidal state. Although it is believed that every oil wets to some extent - that is, $\theta \neq 180°$ - the spheriodal state may exist when the oil film layers are supported on a film of vapor formed by evaporation from the lower surface of the oil layers. The phenomenon was briefly discussed in the earlier section (v) in relation to the effects of plate temperature on wetting rate. The oil film will possibly not break down when it becomes metastable, but evaporation may continue until the film is depleted to zero flow. This conclusion assumes, of course, that the heat transfer process itself cannot provide the initiating forces for breakdown. Breakdown might be started by bubble nucleation or by the film instability caused by inhomogeneous development of surface tension gradient within the film - that is, Marangoni forces as discussed by Norman and McIntyre (17).

At this point, we must recognize the limitations of the theoretical analysis of the breakdown of a thin oil film flowing over a solid surface - for example, when the film flow is either wavy or turbulent, no simple solutions such as Equations (19) or (20) can be obtained. Discussion here is merely a brief attempt to establish a simple relation so that we might have a better

understanding of the breakdown of an oil film flowing over a solid surface. It is, however, worthwhile to consider more sophisticated models, perhaps simulating actual bearings, in future efforts.

IV. NOTATIONS

a : constant in Equation (1)

A : surface area

A_o : total crosss-sectional or surface area

b : constant in Equation (1)

c : constant

C : particle concentration

C_o : initial particle concentration

C_p : specific heat capacity at pressure constant

C_v : specific heat capacity at volume constant

d : notation of differential

$\bar{d}$: average particle size

$\bar{d}_1$, $\bar{d}_2$, $\bar{d}_3$: arithmetic mean, volume mean, and mass median diameter

D_o : orifice diameter

D : diffusion coefficient

f : film frequency

F : denoting a function

g_c : gravitational constant

h : head of oil column, convective heat transfer coefficient

H, H_1, H_2 : enthalpy

k : frequency of timing light impulses, thermal conductivity

k_1, k_2 : constants

K : geometric factor of microfog generator

l : variable defined in Equation (8), Appendix B-2

L : length of impacting body, heat transfer path

M : molecular weight

M_G, M_L : mass of gas and liquid

M_X : optical magnification

n_i : number of microfog particles

N : total number of microfog particles

N_f : number of frames

N_{Nu} : Nusselt number = (hL/k)

N_{Pr} : Prandtl number = $(C_p\mu/k)$

N_{Re} : Reynolds number = (UL/ν)

N_{Sc} : Schmidt number = (D/ν)

N_{Stk} : Stokes number = $(2\ N_{Re}\rho G\ \bar{d}^2/72\ \rho_L L^2)$

N_t : total number of timing marks

P : pressure of a fluid at any point, power

P_1, P_2 : pressure of a fluid at reference 1 and 2, respectively

q : rate of heat transfer, $q = h\Delta T$

Q_G : gas volumetric flow rate

Q_L : liquid volumetric flow rate

r : radial distance, radius

R : gas law constant

R_o : radius of total wetted area

t : time

t_i : time at reference i

t_E : exposure duration

T : absolute temperature

u : velocity

U_G : gas velocity

U_L : liquid velocity

U_r : relative velocity $U_r = U_G - U_L$

$\bar{U}_m$: average maximum velocity along the axis of spray

U_o : velocity at throat of nozzle

U_s : secondary flow velocity

U^* : dimensionless velocity = $\bar{U}_m/U_o$

v : radial velocity, velocity to y direction

V_o : specific volume

V_j : average volume of droplet j

V : volume (gas or liquid)

W : rate of oil output, weight rate

x, x_i : transfer path

X_o : distance of irrotational core

X : distance image moved between frames

y : y-direction

z : z-direction

Greek Letters

α	:	specific heat capacity ratio = Cp/C_v
α_1, α_2	:	constants in Equation (6)
β	:	angle between direction of motion and film plane
Γ	:	total specific flow rate
Γ^*	:	minimum wetting rate
δ	:	film thickness
δ^*	:	critical film thickness
Δ	:	denoting a small increment
ϵ_N	:	nozzle coefficient
ϵ_u	:	velocity correction factor, $\epsilon_u = \sqrt{\epsilon_N}$
η	:	collection efficiency, variable defined in Equation (8), Appendix B-2
θ	:	contact angle
λ	:	rate of evaporation
μ	:	dynamic viscosity, $\mu = U_s/U_o$, micron
ν	:	kinematic viscosity
ξ	:	variable $= \eta/c^{2/3}$
ξ'	:	image blur, expressed in Equation (3)
π	:	3.14
ρ	:	density
ρ_G, ρ_L	:	density of gas and liquid, respectively
σ	:	surface tension
τ_i	:	interfacial shear $= \mu_i(\frac{\partial u}{\partial y})$
ϕ	:	angle
$\underline{\psi}$, $\underline{\psi}_o$	:	variable defined in equation (9), Appendix B-2, parametric wetting constant
Ω	:	external force

V. REFERENCES

1. Alder, C. R. and W. R. Marshall Jr.: Chem. Eng. Progr., 47, 515, 601 (1951)

2. Corrsin, S. and L. Lumby; Appl Sci. Res.; 6A, 114 (1956)

3. Davies, C. N. and M. Aylwood; Proc. Phys. Soc.; 64B, 889 (1951)

4. Drew, T. B.; "Advances in Chemical Engineering", Vol. 5, Academic Press, New York, p.155 (1964)

5. Faust, D. G.; Lubrication Engineering; 183, Aug. (1952)

6. Fisher, H. A., S. Katz, and A. Liederman; Proc. 3rd Natl. Air Poll. Symp.; 112 (1955)

7. Forstall, W. and A. H. Shapiro; J. Appl. Mechanics, 17, 399 (1950); 18, 219 (1951)

8. Hartley, D. E. and W. Murgatroyd; Int. J. Heat Mass Transfer, 7, 1003 (1964)

9. Hinze, J. O.; "Turbulence", McGraw Hill, New York, p. 423 (1959)

10. Hinze, J. O. and B. G. van der Hegge Zijnen; Appl. Sci. Res.; 1A, 435 (1949)

11. Hougen, O. A. et al.; "Chemical Process Principles", Part II, John Wiley, New York, p. 698 (1959)

12. Hyzer, W. G.; "Engineering and Scientific High Speed Photography", MacMillan, New York, p. 26 (1962)

13. Kim, K. Y. and W. R. Marshall Jr.; J.A.I.Ch.E. (to be published)

14. Leidenfrost, J. G.; "De Aquae Communis Nonnullis Qualitatibus Tractatus, Duisburg on Rhine" (1956); this treatise in English was published in Int. J. Heat Mass Transfer, 9, 1153 (1966)

15. May, K. R.; J. Appl. Phys.; 20, 932 (1949)

16. Mitchell, R. I., R. E. Thomas, and A. A. Putman; Ind. Eng. Chem. Process Design & Dev.; 3, 339 (1964)

17. Norman, W. S. and V. McIntyre; Trans. Inst. Chem. Eng.; 38, 301 (1960)

18. Nukiyama, S. and Y. Tanasawa; Trans. Jap. Soc. Mech. Eng.; 4, No. 14, 86 and No. 15, 138 (1938)

19. O'Konski, C. T. and G. J. Doyle; Amal. Chem.; 27, 694 (1955)

20. Ranz, W. E. and J. B. Wong; Ind. Eng. Chem.; 44, 1371 (1952)

21. Shim, J. and S. J. Leonardi; "Microfog Lubricant Application System for Advanced Turbine Engine Components", NASA CR-72291, Sept. (1967)

22. Soo, S. L.; Ind. Eng. Chem. Fundamentals, 3, 75, 98 (1964)

23. Tollmien, W.; Zangeu Math. u. Mech.; 6, 468 (1926)

24. Watchers, L. H. J., H. Bonne, and H. J. van Nouhuis; Chem. Eng. Sci., 21, 923 (1966)

25. Watson, H; Amer. Ind. Hyg. Ass., Quart., 15, 21 (1954)

26. Wong, J. G., W. E. Ranz, and H. F. Johnstone; J. Chem. Phys.; 26, 244 (1955)

VI. APPENDICES

APPENDIX A

APPENDIX A

Statement of Work
Contract NAS3-9400

I. SCOPE OF WORK

The Contractor shall furnish the necessary personnel, facilities, service, material and otherwise do all things necessary for or incident to, design, fabricate, and put into operation an oil-mist application test system. This equipment shall be used to determine the wetting characteristics of five potential high temperature lubricants covering a range of physical and chemical properties appropriate for use in a "once-through" minimum-oil and gas flow lubrication system of aircraft turbine type engines.

Task I - Test Rig

The Contractor shall design and fabricate a microfog lubricant applicator test rig which shall simulate the "once-through" oil mist lubrication system required for a high speed aircraft engine, and determine by measurements the requirements for efficient wetting, of several lubricants. Essential elements required for this rig are given in the following section. The test rig design shall be subject to NASA Project Manager approval prior to fabrication.

A. Oil Mist Generator

A standard oil-mist generator shall be used. The generator shall be modified by replacing the reservoir with one of heavier construction to allow for higher temperature, higher pressure and material compatibility with the lubricants, and by adding heaters and a temperature regulator to control reservoir temperature. The mist generator shall be capable of operating with internal pressure to 80 psig and oil temperature to 300°F. The generator shall be capable of supplying nitrogen at optimized flow rates.

B. Nitrogen Gas System

Nitrogen gas shall be supplied to the generator to produce the oil mist and then to the specimen test chamber as an oil carrier and for inert blanketing of the cavity. From there, it exhausts to atmosphere via an oil collector. Quality of the nitrogen gas shall be at least 99.99 percent by volume nitrogen, oxygen content of not more than 50 ppm by volume, hydrocarbon content (as methane) of not more than 5 ppm by volume, and a dew point of -90°F or better.

C. Mist Nozzle

An optimum nozzle configuration shall be obtained for discharging the gas-oil mist inside the test chamber and onto the test specimens. Corrosiveness of the test lubricants at the test operating conditions in the chamber shall determine the nozzle's material of construction. The nozzle material shall be a stainless steel such as 18-8-C or 25-12-C. If these materials are inadequate, a material such as Inconel or Hastalloy shall be substituted. Three different types of "wet" fog nozzle configurations shall be tested to determine the optimum nozzle. The nozzle design shall include a converter, or reclassifier, tailored to give average particle sizes and velocities in a critical region with respect to wetting so as to insure good sensitivity in comparing the wettabilities of different oils and the effects of physical parameters such as particle size, particle velocity, plate temperature, and system geometry, as well as the effects of oil properties such as density, surface tension, and viscosity. The nozzle shall be tailored to provide even delivery over a optimum angle for efficient coverage of the test specimen.

D. Test Chamber

The test chamber is to be a thermostatically and pressure controlled oven for simulation of pressures (up to 80 psia and temperatures up to 1000°F). The chamber shall have an observation port through which visual and photographic observations of the test specimen can be made, during the mist generator tests. Heaters shall be supplied for the test specimen and shall be capable of maintaining the desired temperature during operation. A method shall be provided to change the distance between the nozzle and test specimen such as changing pipe lengths to the nozzle. The chamber shall have reasonable temperature response and accessability to the test specimen so as to minimize time between runs.

E. Instrumentation

1. Particle size and concentration - The particle size and concentration shall be determined by using a multi-channel particle counter with a size range of 0.5 to 32 microns. The particle size shall be taken at the same condition as the test chamber. (80 psia max and 1000°F max.) Conditions in the particle counter shall be within the temperature and pressure limits of the Royco instrument.

2. Particle Velocity - The particle velocity shall be determined at test specimen condition of carrier gas velocity, temperature and pressure and at approximately the same distance from the nozzle as the specimen. The average impact velocity of particles shall be determined by measuring the time for a demarcation line of a swarm of particles to travel through a measured distance by the use of either a high speed motion picture camera or a pair of photoelectric cell's whose separation can be varied. The two photoelectric cells circuits shall be used to start and stop an electric timer, which is graduated in 0.001 sec. intervals. Two verticle slits at both ends of the measured horizontal distance traveled by the swarm of particles and a strong vertical beam of light projected through each slit shall be provided in a glass cylinder with a nozzle. On the opposite side of the tube, there shall be placed a photoelectric cell (type 1/2-6F8G).

3. Wettability - Wettability shall be determined using photographic techniques. An alternate or backup shall be by photoelectric cell measurement of a light source reflected from the test specimen. The photographic method shall use motion pictures taken of the test specimen during exposure to the mist flow. A small amount of dye may be used in the lubricant if required, provided the dye has no measurable effect on the lubricant.

4. Oil Flow Rate - The oil flow rate shall be determined by measuring the amount of oil required to maintain a given level in the mist reservoir for a specified time.

F. Test Specimen

The test specimen shall be a flat plate 2 inches by 2 inches ($\pm$ 1/2) by 1/8 ($\pm$ 1/16) inch thick made of hardened consumable electrode vacuum melted (CVM) WB-49 material and finished circumferentially ground to 4 to 8 RMS. The NASA Project Manager may select a material other than WB-49 prior to the start of the testing operations. The specimen shall be mounted in a vertical position in the test chamber with a flat side facing the end of the mist nozzle at a distance from the nozzle, to be determined in Task II.

G. Test Lubricants

The following five lubricants shall be used in this investigation:

1. Humble Oil and Refining Co., 4040 Turbo Oil
2. Union Carbide Corp., UCON 50-HB 5100 fluid
3. Sun Oil Co., Sunthetic 18H (bottoms) fluid
4. Mobil Research and Development Corp., XRM 177F
5. Hercules Powder Co., Hercolube F

These fluids cover the range of physical properties appropriate for fluids to be used in a once-through lubrication system (e.g. viscosity and surface tension). Substitution of this list shall be made if recommended by the Contractor and approved by the NASA Project Manager.

Task II - Mist Generator Tests

The Contractor shall investigate the wettability of the five test lubricants on the static metal surface under a range of ambient conditions simulating engine bearing operation as described below.

A. Test Procedure

The Contractor shall perform a series of wettability tests using each of the five test lubricants listed in Task I, paragraph G, under each set of conditions listed below:

1. Five (5) flow rates for each lubricant in the flow range up to 0.02 lbs/min (± 10%) to be recommended by the Contractor and approved by the NASA Project Manager.

2. Four (4) nitrogen flow rates and/or other considerations for each oil flow to give approximately 2, 4, 8, 16 microns average drop particle sizes as recommended by the Contractor and approved by the NASA Project Manager.

3. Three (3) test plate specimen temperatures of 600°, 700°, and 800°F (± 10°F) as monitored with a thermocouple imbedded in the surface of the specimen.

Prior to the start of each run, the test chamber and specimen shall be brought to the desired temperature. A stream of pure nitrogen, at the same rate as the nitrogen stream to be introduced from the mist generator, is then passed through the nozzle. The run shall be started by switching to the nitrogen stream carrying fog from the fog generator when the specimen temperature has recovered to the control temperature, and the nozzle temperature has reached equilibrium.

One or more nozzles shall be used as required to cover the range of test conditions. The test chamber pressure shall be held at 45 ($\pm$ 5) psig and the test fluid at a temperature of 200° ($\pm$ 10°) F in the generator reservoir during a run. All lubricants shall be degassed for a 72 hour period immediately before running by means of a mechanical vacuum pump capable of maintaining a pressure of 10^{-3} mm Hg, while vibrating the fluid. The test chamber shall be pumped down with a mechanical vacuum pump prior to a run and then purged with nitrogen during the run.

Metal test specimens shall be cleaned before each test in the following manner:

1. Rinsed with acetone.
2. Scrubbed with moist levigated alumina and a soft polishing cloth.
3. Thoroughly rinsed with tap water.
4. Rinsed briefly with distilled water.
5. Rinsed with ethyl alcohol.

A run shall consist of operating the generator with a test lubricant under a set of conditions while impinging the mist on the specimen. After reaching equilibrium conditions of pressure, temperature and flow, the particle size and velocity shall be determined and the wettability recorded by measuring the time required to cover the metal specimen with a complete film of oil. A total of 300 runs shall be made to include all test conditions in A1, A2, and A3 above. Up to a maximum of 60 additional runs shall be made as required by the Contractor, or directed by the NASA Project Manager.

B. Optimum Distance Tests

Prior to the above tests, a series of seven preliminary tests shall be made to determine the optimum distance between the end of the nozzle and the test plate that shall be used in the test runs. These test conditions shall be as follows:

1. Distance between nozzle and plate

   0.5 in., 1 in., 1-1/2 in., 2 in., 3 in., 4 in., and 6 in. (± 1/16 in.)

2. Suggested Lubricant

   Mobil XRM-177F

3. Lubricant Flow Rate

   .002 lbs/min (± 10%)

4. Average Particle Drop Size (regulated by nitrogen flow rate)

   Approximately 4 microns

5. Temperature of Test Plate

   700° (± 10°) F

C. Nozzle Tests

Prior to the tests in A above, the following tests shall be run. Three types of nozzles with a maximum of four variations each shall be tested to determine the optimum nozzle configuration with respect to minimum oil and gas flow, good dispersion of fluid particles and range of particle size generation. More than one nozzle may be required to obtain the complete particle size range. The nozzle tests shall be conducted with two oil flow rates, 0.001 and 0.002 lbs/min and nitrogen flow to give the particle size range required. These tests may be conducted at room temperature, but shall be checked at 700°F to assure compliance at high temperature.

Changes in the test conditions, procedures and test equipment shall be made if recommended by the Contractor and approved by the NASA Project Manager.

Task III - Base Line Tests

The Contractor shall obtain base-line data on one fluid, to be selected by the NASA Project Manager, for a series of runs following the test outline in Task II, paragraph A, but with the test chamber not blanketed with nitrogen and the oil not degassed. Only two lubricant flow rates shall be studied (0.001 and 0.002 lbs/min). These runs are to determine the effect of surface oxide formation and fluid degradation products, such as fluid changes and surface deposits, on the wettability of the fluid.

II. Specific Data to be Reported

As a part of the data to be reported under Article VI, "Reports of Work", of this contract, the Contractor shall specifically include the following data:

1. Average drop particle size (microns) and size range for each condition of nozzle operation.

2. Wettability of fluid on metal test specimen as a function of particle size, gas velocity, metal temperature and other parameters as can be determined from the data such as vapor pressure, viscosity, density and surface tension.

3. Velocity of impingement on surface of the specimen.

APPENDIX B

PARTICLE VELOCITY DISTRIBUTION

B-1. Gas Flow Through an Expansion Nozzle

When a gas undergoes an expansion through a nozzle as shown in Figure 61, the first law of thermodynamics suggests that we can consider two different thermodynamic expansion processes - i.e., adiabatic and non-adiabatic (in most cases, isothermal) expansion.

i) Adiabatic Expansion

In an adiabatic process, potential energy changes are negligible and no work is done. Thus for the adiabatic and frictionless flow of a gas, the velocity of the gas at the throat of an expansion nozzle is given by

$$\Delta\left(\frac{u^2}{2g_c}\right) = -\int_{P_1}^{P_2} Vdp = -(\Delta H)_s \qquad (1)$$

or

$$U_o = [2g_c(H_1-H_2)_s + U_1^2]^{1/2} \qquad (2)$$

for the adiabatic expansion of an ideal gas

$$\frac{T_2}{T_1} = \left(\frac{P_2}{P_1}\right)^{\frac{\alpha-1}{\alpha}} = \left(\frac{V_2}{V_1}\right)^{\alpha-1} \qquad (3)$$

Combining Equations (1) and (3) we get

$$U_o = \left[\frac{2g_c\alpha RT_1}{M(\alpha-1)}\left\{1 - \left(\frac{P_2}{P_1}\right)^{\frac{\alpha-1}{\alpha}}\right\} + U_1^2\right]^{1/2} \qquad (4)$$

since

$$C_p = \frac{\alpha R}{M(\alpha-1)}$$

Figure 61

DEFINITION SKETCH OF A DIFFUSING ROUND JET

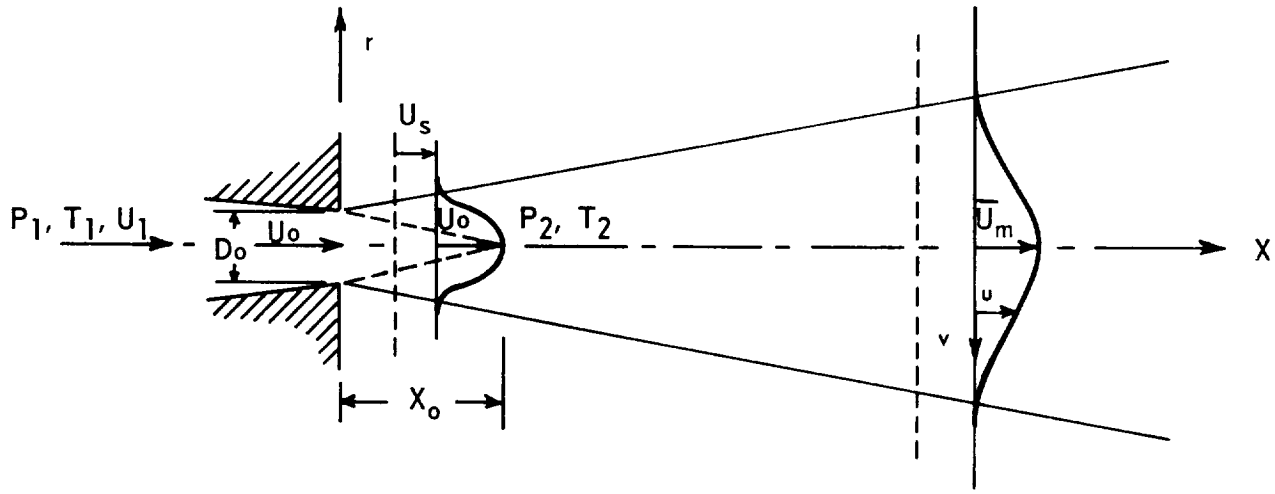

Equation (4) represents the velocity of an ideal gas at throat of the nozzle, assuming that provision is made for maintaining the desired pressure at the throat of the nozzle, and for removing the gas discharged without influencing flow, and that there is no heat absorbed or given off by the system.

Actual Velocity in Nozzles

In a well-designed nozzle, the flow is very nearly adiabatic, yet inevitably the performance of actual nozzles differs from the ideal because of friction, turbulence, radial flow, and heat transfer. Thus, to estimate the velocity of flow from the actual nozzle, we may apply a "nozzle co-efficient", ε_N, expressed as an empirical relation (10)

$$\varepsilon_N = \frac{(U_o^2)\text{actual}}{(U_o^2)\text{ideal}} = \frac{H_1 - H'_2}{H_1 - H_2} \qquad (5)$$

where (H_1-H_2) is the ideal enthalpy drop and $(H_1-H'_2)$, the actual. These corrections depend largely on the design and shape of the nozzle, the characteristics of the fluid, and the operating conditions. For well designed nozzles, the normal range of nozzle coefficients is about 0.72 to 0.96. Therefore, the corresponding values of the velocity correction factor, which is defined as $\varepsilon_u = \sqrt{\varepsilon_N}$ chosen for this study were 0.85 for all spray nozzles and 0.92 for atomizing nozzles respectively.

ii) Non-adiabatic Expansion

When a gas is expanded through a nozzle, the temperature change can be estimated on th e basis of frictionless adiabatic flow for an ideal gas. However, this temperature change is negligible when the drop in pressure is so slight that the accurate evaluation of velocity becomes difficult. In such cases, the velocity of the ideal gas can be obtained by applying the conservation of mass (or the equation of continuity) as follows:

$$W = \frac{A_o U_o}{V_o}$$

$$\therefore U_o = \frac{W V_o}{A_o} = \frac{Q_G}{\left(\frac{\pi D_o^2}{4}\right)} \left(\frac{P_1}{P_2}\right) \qquad (6)$$

It is sufficiently accurate for calculating the ideal velocity of gases when P_2 is very nearly equal to P_1 so that the increase in volume is small.

iii) Illustration

Consider Item 4 (gas flow of 5 cfm with nozzle No. 1) in Table No. 3.

Inlet pressure = 81.2 psia
Discharge pressure = 61.7 psia
Inlet temperature = 660°F
Inlet velocity = 100 ft/sec
Orifice diameter = 0.171"
α (for nitrogen) = 1.4

For an adiabatic expansion process, substitution of these values into Equation (4) produces

$$U_o = \left[\frac{2x32.2x1.4x1542x660}{28x(1.4-1)}\left\{1 - \left(\frac{61.7}{81.2}\right)^{\frac{1.4-1}{1.4}}\right\} + 100^2\right]^{1/2}$$

$$= 806 \text{ ft/sec}$$

Thus, the actual velocity is

$$\bar{U}_o = 806 \times 0.85 = \underline{685} \text{ ft/sec}$$

For a non-adiabatic expansion, Equation (6) gives

$$U_o = \frac{5}{60 \times \frac{3.14}{4} \times \left(\frac{0.171}{12}\right)^2}\left(\frac{81.2}{61.7}\right)$$

$$= \underline{690} \text{ ft/sec}$$

No further correction is necessary.

B-2. Velocity Distribution of a Diffusing Jet

For a diffusing jet symmetrical about an axis, as shown in Figure 62, if x is measured along the axis of the jet and r at right angles to it, and u, v are the components of mean velocity in the direction of x and r, respectively, then the approximate equation of motion on the momentum-transport theory, with Prandtl's assumption for the coefficient of eddy diffusion, is

$$u \frac{\partial u}{\partial x} + r \frac{\partial u}{\partial r} = \frac{1}{r} \frac{\partial}{\partial r} \left[\rho^2 r \left| \frac{\partial u}{\partial r} \right| \left| \frac{\partial u}{\partial r} \right| \right] \qquad (7)$$

U being the greatest on the axis and zero at the edge of the jet, and $\frac{\partial u}{\partial r}$ negative.

With the same basic assumptions as in the application of Prandtl's mixing length hypothesis, that is, l and the breadth of the jet are proportional to x, and the maximum velocity to 1/x. Hence we put

$$l = cx \qquad \eta = r/x \qquad u = \frac{1}{x} f(\eta) \qquad (8)$$

The stream function is given by

$$\psi = xF(\eta) \qquad F(\eta) = \int_0^\eta f(\eta)\, \eta\, d\eta \qquad (9)$$

so that

$$u = \frac{F'(\eta)}{x\eta} \qquad v = \frac{1}{x\eta} \left\{ \eta F'(\eta) - F(\eta) \right\} \qquad (10)$$

Substitution of the above expressions in Equation (1) results in the differential equation

$$C^2 \left[\frac{d^2F(\eta)}{d\eta^2} - \frac{1}{\eta} \frac{dF(\eta)}{d\eta}\right]^2 = F(\eta) \frac{dF(\eta)}{d\eta} \quad (12)$$

or with $\xi = \eta/C^{2/3}$

$$\left[\frac{d^2F(\eta)}{d\xi^2} - \frac{1}{\xi} \frac{dF(\xi)}{d\xi}\right]^2 = F(\xi) \frac{dF(\xi)}{d\xi} \quad (13)$$

The boundary conditions which must be satisfied are as follows:

At the centerline $r = o$, $v = \frac{\partial u}{\partial r} = o$;

Therefore

$$\text{at } \xi = o, F(o) = o \quad F'(\xi) = \frac{F(\xi)}{\eta} \quad F''(\xi) = \frac{F'(\xi)}{\xi} \quad (14)$$

where $r > o$, the partial derivative $\partial u/\partial r < o$, so that

$$\xi > o \qquad F''(\xi) < \frac{F'(\xi)}{\xi} \quad (15)$$

Tollmien (22) integrated Equation (13) with the resulting boundary conditions by putting

$$F(\xi) = \rho^{\int Z d\xi} \quad (16)$$

Equation (13) becomes

$$\frac{dZ(\xi)}{d\xi} = \frac{Z(\xi)}{\xi} - Z^2(\xi) - \sqrt{Z(\xi)} \quad (17)$$

It is then found that

$$Z(\xi) = \frac{2}{\xi} - \frac{2\sqrt{2}}{7} \xi^{1/2} - \frac{1}{245} \xi^2 \frac{\sqrt{2}}{1,715} \xi^{7/2} + \ldots (18)$$

Finally, the velocity distribution in terms of ξ is given by

$$\left(\frac{U}{\bar{U}_m}\right) = \frac{1}{C^{2/3} x} \left(\frac{1}{\xi}\right) \frac{dF(\xi)}{d\xi}$$

$$= \frac{1}{\xi_o}\left[1 - \frac{\sqrt{2}}{7}\xi^{3/2} - \frac{1}{490}\xi^3 + ..\right] \exp.\left[-\frac{4\sqrt{2}}{21}\xi^{3/2} - ..\right] \quad (19)$$

where $\xi_o = \frac{C^{2/3} X_o U_o}{2}$ and C, X_o, and U_o are characteristic variables to be experimentally determined.

In order to determine the values of C, X_o and U_o, perhaps the first to make an extensive investigation of a diffusing jet in a secondary stream as well as a single fluid issuing in a still ambient fluid was Forstall and Shapiro (7).

When, as shown in Figure 61, a gas is discharged from a nozzle, the maximum axial velocity, U_m, of a jet must decrease as the diffusing zone further expands. The process of diffusion is continuous, theoretically at least, until there is at infinity an infinitely broad jet of zero velocity. Following the Taylor's mixing-length hypothesis, Forstall and Shapiro obtained empirical relations for the spread of a single fluid jet in a secondary stream as a function of the distance from the nozzle and for the decrease in the jet velocity, both for different ratios, μ, between the velocity of the secondary flow and the issuing velocity of the jet.

According to Forstall's measurements, the relative velocity of the jet at the axis decreases hyperbolically with increasing x

$$\left(\frac{\bar{U}_m}{U_o - U_s}\right) = \frac{X_o}{X} \quad \text{for } X > X_o \quad (20)$$

and the following empirical relation holds

$$\frac{X_o}{D_o} = 4 + 12\,\mu \quad (21)$$

Hence, for the case of $U_s = 0$, Equation (20) becomes

$$\left(\frac{\bar{U}_m}{U_o}\right)_{calc.} = \frac{4D_o}{X} \tag{22}$$

Using Equations (19) and (22), the distribution of mean particle velocity can be estimated, assuming th at the relative velocity between gas and particles is negligible.

B-3. Method of Determining Mean Particle Velocity from High Speed Movie Films

The mean velocity of the microfog particles discharged from a nozzle is determined by photographing the movement of the microfog front and/or the propagations of a surge front created from a wetted surface of the spray nozzle, with the Hycam high speed motion picture camera. Following an idealized flow pattern of the microfog spray in a jet, as shown in Figure 62, the local distribution of mean particle velocity along the axis of the nozzle is simply determined by the distance movement between frames, ΔX_i, divided by the time duration between exposures, Δt_i, that is,

$$\left(\bar{U}_m\right)_{exp} = \frac{\Delta X_i}{\Delta t_i} = \frac{fX}{N_f} \tag{23}$$

where X is the distance image moves between frames; f, the film frequency; and N_f, the number of frames, the film frequency is estimated by the following equation:

$$f = \frac{kN_f}{N_t} \tag{24}$$

where k is the frequency of timing light impulses and N_t, the number of timing marks printed on the film edge. Combining Equations (23) and (24), we get

$$\left(\bar{U}_m\right)_{exp.} = \frac{\Delta X_i}{\Delta t_i} = \frac{kX}{N_t} \tag{25}$$

Figure 62

IDEALIZED FLOW PATTERN OF MICROFOG SPRAY IN A FREE JET

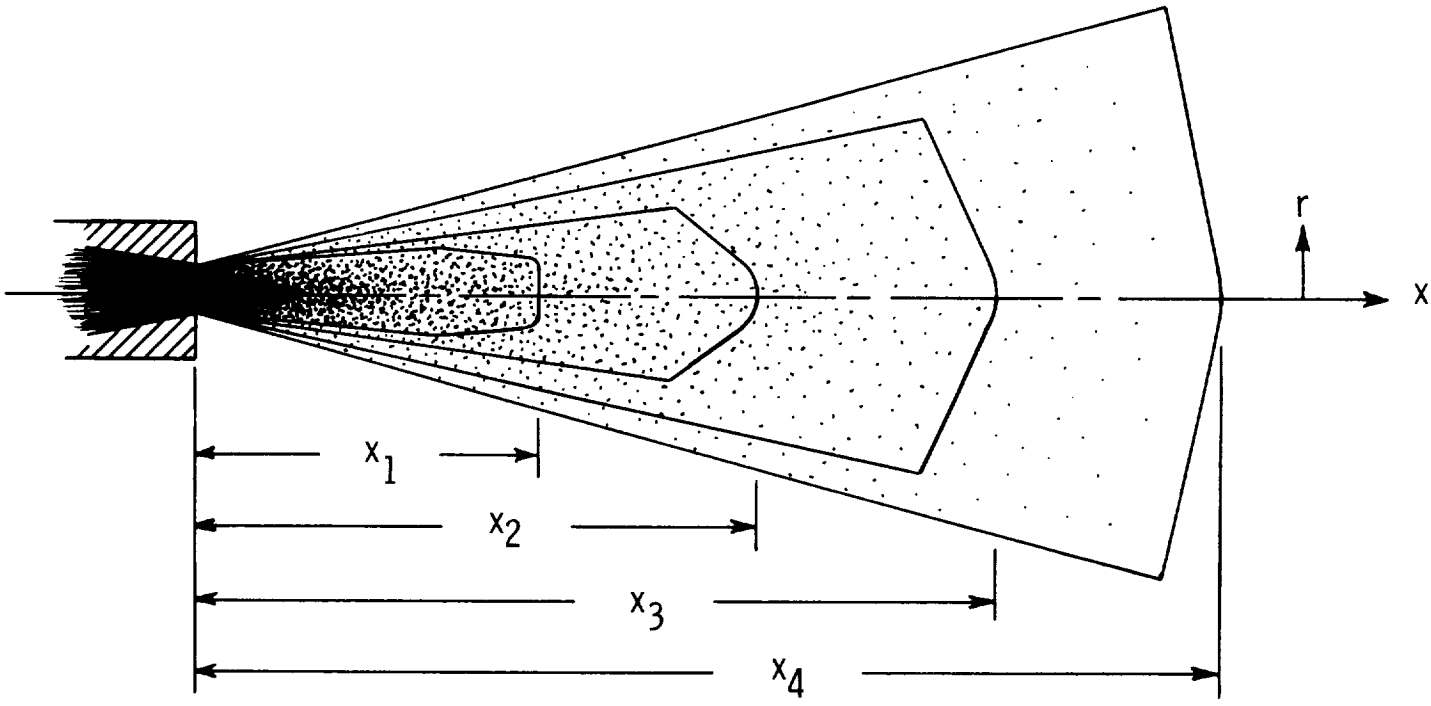

Equation (25) suggests that accuracy in determining particle velocity is principally dependent on the values of film frequency, image movement, and number of timing marks from the quantitative analysis of the high speed motor picture films.

APPENDIX C

PARTICLE SIZE DISTRIBUTION

C-1. Calibration of the Particle Counter

The purpose of the particle counter calibration is to adjust the electronic gain of the system to compensate for refractive index of the particles, lamp intensity, and geometric configurations. This ensures that each channel records only particles within a known size range which corresponds to the size distribution of microfog particles as measured optically by a microscope.

Prior to the calibration, a dependable technique for generating and sampling particles had to be developed. The actual microfog particles are ideal, but collection difficulties caused by spreading of oil droplets make spherical glass powder more attractive. Hence, the glass powders (3M Co. Superbrite 500, refractive index = 1.4 ~ 1.6) were employed for calibration. The generator employed in this study was a simple solid suspender - a glass U-tube having a nozzle inserted in one end with the other end mounted on the 1/2" transport line of the experimental apparatus. The nozzle and the pipe were connected to a gas supply line in generating particles. The glass particles of 0.3 to 30 μm were placed in the U-tube and were suspended into a gas stream when a needle valve in the gas supply line was opened. After passing through the particle counter for determining size distribution, the particles were collected on a sliding impactor, shown in Figure 63, coated with a uniform thin layer of tacky grease. The particles collected on the impactor were analyzed and counted by a bench microscope (1,000X power). An eye piece graticule was used for sizing the particles in a $\sqrt{2}$ size progression. In order to minimize statistical sampling errors, a count of 200 particles was made to adjust the overall system gain of the particle counter, so that the particle size distributions observed by the counter would coincide with those counted by the microscope.

Figure 64 shows a typical photomicrograph of spherical glass particles collected on an impactor. It is important that an efficient, uniform, tacky film be applied on the impactor when the glass particles are sampled, as there is a marked tendency in the impactor for the particles to be blown from one place to another, thereby spoiling the size-gradings. With too thick a layer of grease on the impactor, accurate grading is also prevented by formation of grease rings around the particles as shown in Figure 64. Of a wide variety of materials tried, films of a silicone stockcock grease gave best results and were successfully applied by warming the microscope slide and spreading the molten grease with a smooth glass rod. In this way, a uniform tacky film was formed on the slide plate.

The particle size distribution data shown in Figure 65 were obtained by the two independent methods - particle counter and

Figure 63

PHOTOGRAPH OF A SLIDING IMPACTOR

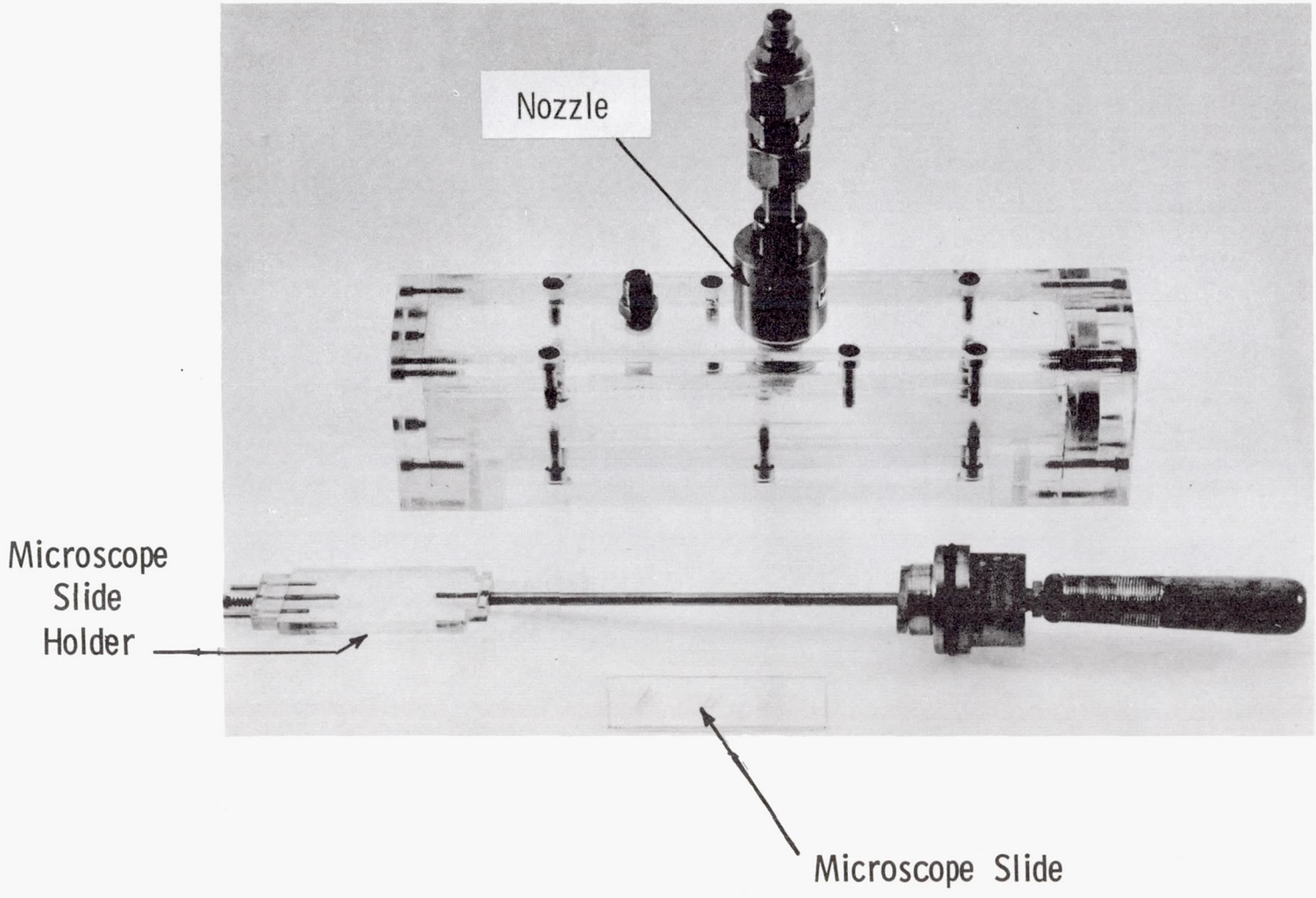

Figure 64

PHOTOMICROGRAPH OF SPHERICAL PARTICLES
COLLECTED ON AN IMPACTOR

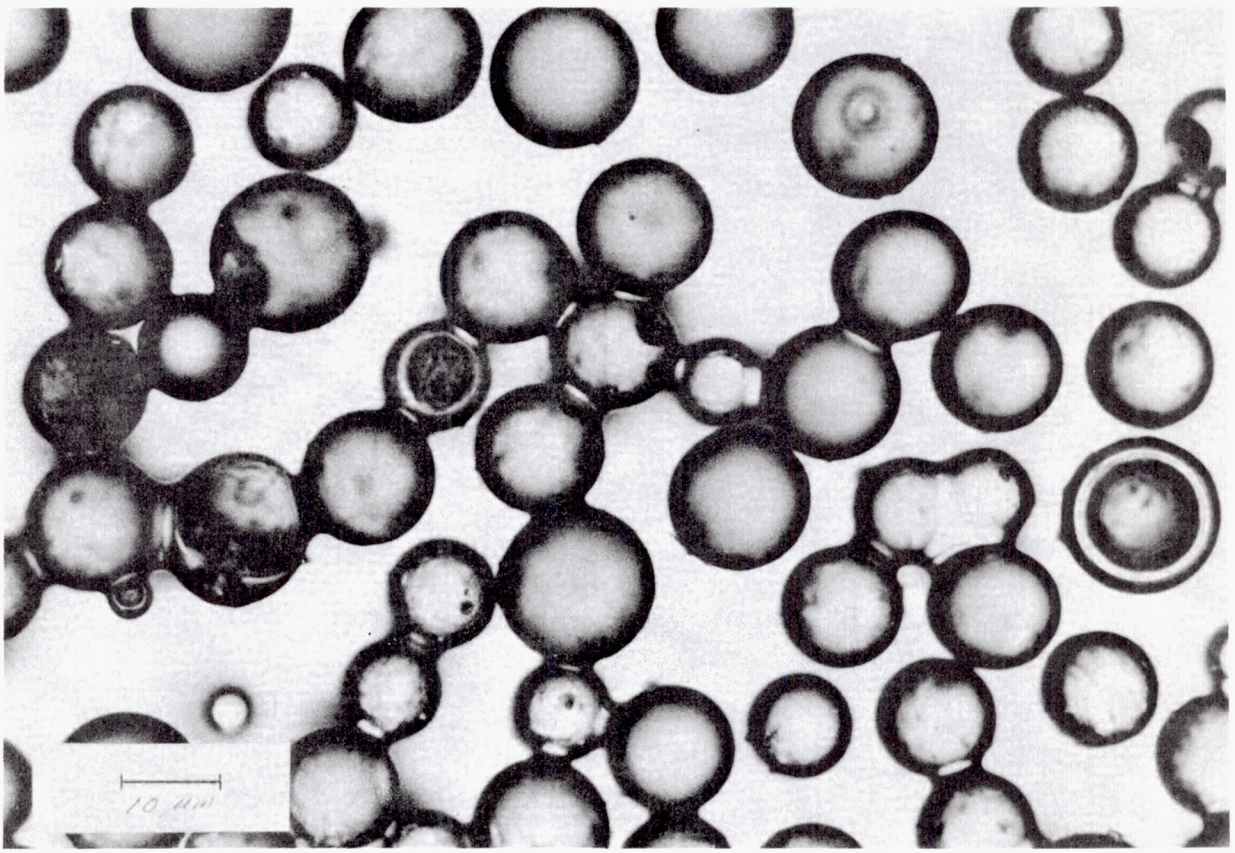

Figure 65

CUMULATIVE PARTICLE SIZE DISTRIBUTION DATA FOR CALIBRATION OF THE PARTICLE COUNTER

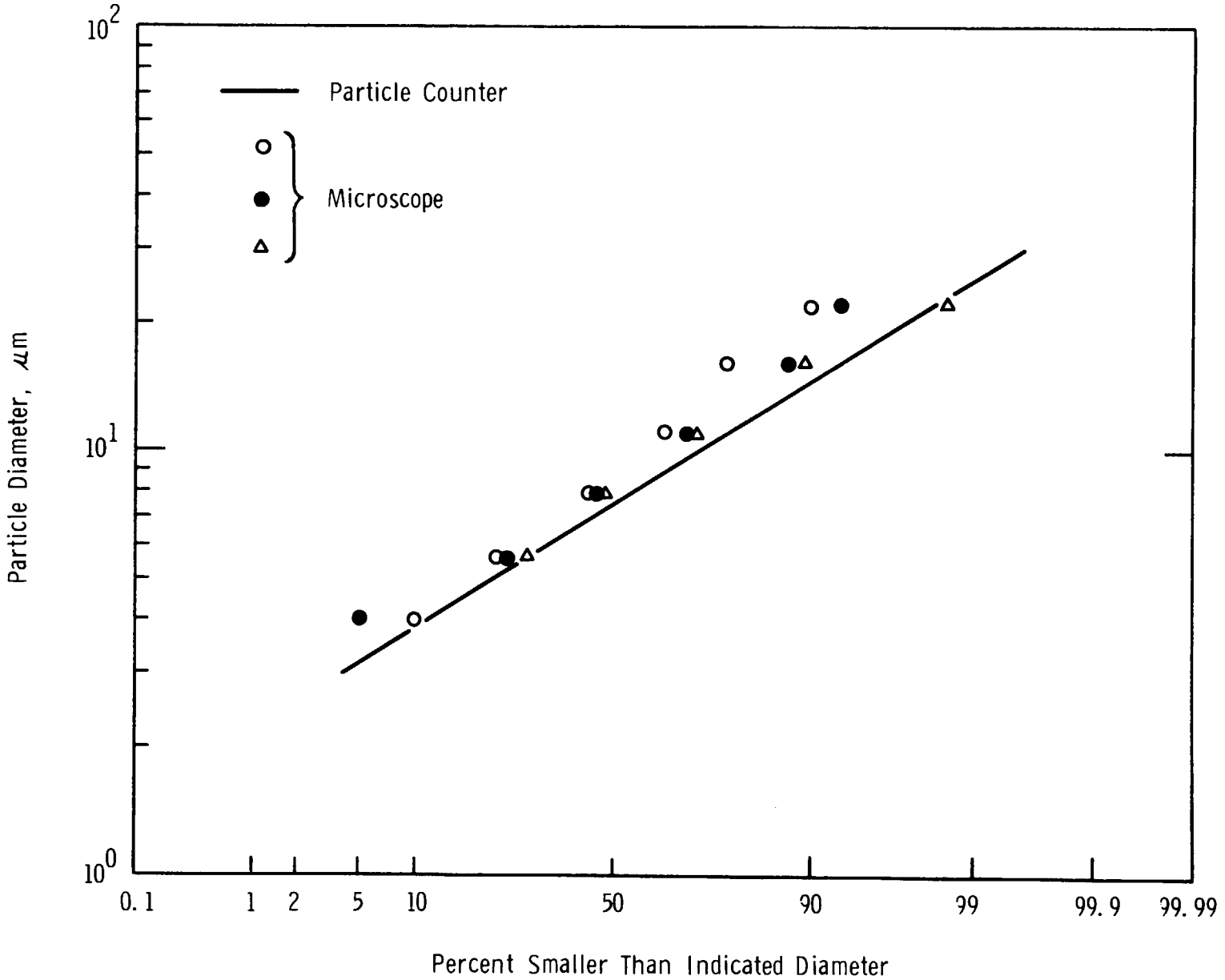

microscope - after making the final adjustment on the particle counter. Although a count of only 200 particles was made, the results seem to indicate sufficient proximity for the observed and microscopically determined distributions to coincidence. Thus, however large the sample counted by the particle counter, accuracy of the distribution estimate cannot exceed that of the primary calibration.

C-2. Method of Calculating Various Terms Used in Table 9

1. $\sum_{i=1}^{N} n_i$ from particle size distribution data

obtained by a cascade impactor technique

$$\Delta \left(\frac{dV}{dt}\right)_i = \frac{1}{\rho}\left(\frac{dW}{dt}\right)_i = \sum_{i=1}^{N} n_i \bar{V}_i$$

$$\therefore \sum_{i=1}^{N} n_i = \frac{\frac{1}{\rho}\Delta\left(\frac{dW}{dt}\right)_i}{\frac{1}{6}\pi (\bar{d}_i)^3_{\eta=0.9}}$$

$$\left(\because \bar{V}_i = \frac{1}{6}\pi (\bar{d}_i)^3_{\eta=0.9}\right)$$

2. Total counting rate of microfog particle,

$$\sum_{i=1}^{N}\left(\frac{dn_i}{dt}\right)_{\text{total}}$$

$$\sum_{i=1}^{N}\left(\frac{dn_i}{dt}\right)_{\text{total}} = \sum_{i=1}^{N_1}\left(\frac{dn_i}{dt}\right)_{\text{counter}} + \sum_{i=1}^{N_2}\left(\frac{dn_i}{dt}\right)_{\text{impactor}}$$

APPENDIX C-3

3. Flow rate of oil particles in a microfog stream, $\left(\frac{dQ_L}{dt}\right)_i$

$$\left(\frac{dQ_L}{dt}\right)_i = \left(\frac{dn_i}{dt}\right) \bar{V}_i$$

4. Particle Concentration of a microfog stream, $\left(\frac{dn_i}{dQ_G}\right)$

$$\left(\frac{dn_i}{dQ_G}\right) = \left(\frac{dn_i}{dt}\right) \Big/ \left(\frac{dQ_G}{dt}\right)$$

5. Oil/gas mass flow ratio, $\left(\frac{dQ_L}{dQ_G}\right)$

$$\left(\frac{dQ_L}{dQ_G}\right) = \left(\frac{dQ_L}{dt}\right) \Big/ \left(\frac{dQ_G}{dt}\right) = \frac{\left(\frac{dn_i}{dt}\right) \bar{V}_i}{\left(\frac{dQ_G}{dt}\right)}$$

Particle Size Distributions of Microfog Sprays

Channel	Size (μm)	Particle Size Distribution* 2 cfm	3 cfm	4 cfm	5 cfm	6 cfm
XRM-177F						
Nozzle No. 1						
1	0.6	486	365	358	412	531
2	0.9	638	1386	1385	1285	1120
3	1.2	357	1747	1829	1618	1027
4	1.7	24	840	976	754	273
5	2.4	1	36	84	62	17
6	3.4	0	0	3	0	0
7	5.8	0	591	657	538	380
8	6.8	0	239	362	276	219
9	9.6	0	30	100	85	100
10	13.6	0	0	0	0	22
11	19.2	0	0	0	0	0
12	27.2	0	0	0	0	0

*The number of particles counted in 10-second period.

Particle Size Distributions of Microfog Sprays

Channel	Size (μm)	Particle Size Distribution* 2 cfm	3 cfm	4 cfm	5 cfm	6 cfm
XRM-177F						
Nozzle No. 2						
1	0.6	724	464	396	478	399
2	0.9	866	1267	1229	991	1083
3	1.2	627	1427	1417	903	1041
4	1.7	53	442	472	184	232
5	2.4	0	7	17	1	4
6	3.4	0	0	0	0	0
7	5.8	104	485	371	153	202
8	6.8	9	200	125	20	55
9	9.6	0	25	9	0	3
10	13.6	0	0	0	0	0
11	19.2	0	0	0	0	0
12	27.2	0	0	0	0	0

*The number of particles counted in 10-second period.

Particle Size Distributions of Microfog Sprays

Channel	Size (μm)	Particle Size Distribution* 2 cfm	3 cfm	4 cfm	5 cfm	6 cfm
XRM-177F						
Nozzle No. 1A						
1	0.6	300	602	528	497	425
2	0.9	208	1018	1069	1104	1135
3	1.2	85	906	871	1143	1147
4	1.7	5	140	179	423	444
5	2.4	0	0	9	25	27
6	3.4	0	0	0	0	0
7	5.8	8	254	262	334	336
8	6.8	3	56	97	152	187
9	9.6	1	7	10	28	55
10	13.6	0	0	0	0	0
11	19.2	0	0	0	0	0
12	27.2	0	0	0	0	0

*The number of particles counted in 10-second period.

Particle Size Distributions of Microfog Sprays

Channel	Size (μm)	Particle Size Distribution*				
		2 cfm	3 cfm	4 cfm	5 cfm	6 cfm
XRM-177F						
Nozzle No. 3						
1	0.6	573	460	522	432	497
2	0.9	395	1083	1285	1011	960
3	1.2	193	1109	1393	1095	685
4	1.7	13	280	292	192	62
5	2.4	0	5	2	2	0
6	3.4	0	0	0	0	0
7	5.8	29	474	434	157	286
8	6.8	1	149	144	40	66
9	9.6	1	12	10	0	4
10	13.6	0	0	0	0	0
11	19.2	0	0	0	0	0
12	27.2	0	0	0	0	0

*The number of particles counted in 10-second period.

Particle Size Distributions of Microfog Sprays

Channel	Size (μm)	Particle Size Distribution*				
		2 cfm	3 cfm	4 cfm	5 cfm	6 cfm
XRM-177F						
Nozzle No. 3A						
1	0.6	69	587	454	353	449
2	0.9	30	824	1063	1120	1180
3	1.2	8	660	1054	1292	1237
4	1.7	0	83	331	552	422
5	2.4	0	2	15	56	16
6	3.4	0	0	0	9	0
7	5.8	1	133	309	524	400
8	6.8	0	35	127	291	187
9	9.6	0	6	26	61	58
10	13.6	0	0	0	1	0
11	19.2	0	0	0	0	0
12	27.2	0	0	0	0	0

*The number of particles counted in 10-second period.

Particle Size Distributions of Microfog Sprays

	Channel	Size (μm)	Particle Size Distribution* 2 cfm	3 cfm	4 cfm	5 cfm	6 cfm
Hercolube F							
Nozzle No. 1							
	1	0.6	930	395	528	568	561
	2	0.9	1555	1648	1730	1498	1567
	3	1.2	1761	2318	2190	1570	1746
	4	1.7	513	1702	1054	724	870
	5	2.4	13	173	101	133	141
	6	3.4	0	0	0	6	6
	7	5.8	0	286	195	240	176
	8	6.8	0	35	48	67	51
	9	9.6	0	0	1	7	4
	10	13.6	0	0	0	0	0
	11	19.2	0	0	0	0	0
	12	27.2	0	0	0	0	0

*The number of particles counted in 10-second period.

Particle Size Distributions of Microfog Sprays

	Channel	Size (μm)	Particle Size Distribution*				
			2 cfm	3 cfm	4 cfm	5 cfm	6 cfm
Hercolube F							
Nozzle No. 2							
	1	0.6	886	643	651	721	708
	2	0.9	1398	1575	1552	1370	1488
	3	1.2	1371	1895	1678	1138	1268
	4	1.7	329	630	407	130	156
	5	2.4	6	14	6	1	0
	6	3.4	0	0	0	0	0
	7	5.8	0	169	92	66	4
	8	6.8	0	9	4	2	2
	9	9.6	0	0	0	0	1
	10	13.6	0	0	0	0	0
	11	19.2	0	0	0	0	0
	12	27.2	0	0	0	0	0

*The number of particles counted in 10-second period.

Particle Size Distributions of Microfog Sprays

	Channel	Size (μm)	Particle Size Distribution*				
			2 cfm	3 cfm	4 cfm	5 cfm	6 cfm
Hercolube F							
Nozzle No. 3							
	1	0.6	851	612	668	671	678
	2	0.9	1299	1680	1565	1587	1198
	3	1.2	1388	2024	1655	1699	1037
	4	1.7	282	777	384	481	169
	5	2.4	3	30	5	15	3
	6	3.4	1	1	1	1	2
	7	5.8	0	132	115	60	34
	8	6.8	0	7	8	2	5
	9	9.6	0	0	0	0	0
	10	13.6	0	0	0	0	0
	11	19.2	0	0	0	0	0
	12	27.2	0	0	0	0	0

*The number of particles counted in 10-second period.

Particle Size Distributions of Microfog Sprays

	Channel	Size (μm)	Particle Size Distribution* 2 cfm	3 cfm	4 cfm	5 cfm	6 cfm
Hercolube F							
Nozzle No. 1A							
	1	0.6	871	643	443	459	450
	2	0.9	1147	1709	1778	1684	1520
	3	1.2	993	2063	2348	2088	1991
	4	1.7	158	795	1287	1261	1540
	5	2.4	3	21	158	186	243
	6	3.4	0	0	4	5	10
	7	5.8	0	260	381	218	472
	8	6.8	0	34	82	41	161
	9	9.6	0	1	5	8	19
	10	13.6	0	0	0	0	0
	11	19.2	0	0	0	0	0
	12	27.2	0	0	0	0	0

*The number of particles counted in 10-second period.

Particle Size Distributions of Microfog Sprays

	Channel	Size (μm)	Particle Size Distribution*				
			2 cfm	3 cfm	4 cfm	5 cfm	6 cfm
Hercolube F							
Nozzle No. 3A							
	1	0.6	509	766	546	413	284
	2	0.9	409	1329	1681	1653	1593
	3	1.2	219	1481	2192	2189	2088
	4	1.7	19	396	1085	1458	1813
	5	2.4	1	23	105	197	468
	6	3.4	0	0	2	9	13
	7	5.8	1	179	383	264	491
	8	6.8	1	32	56	51	169
	9	9.6	0	3	4	5	17
	10	13.6	0	0	0	0	0
	11	19.2	0	0	0	0	0
	12	27.2	0	0	0	0	0

*The number of particles counted in 10-second period.

Particle Size Distributions of Microfog Sprays

	Channel	Size (μm)	Particle Size Distribution*				
			2 cfm	3 cfm	4 cfm	5 cfm	6 cfm
Sunthetic 18HB							
Nozzle No. 1							
	1	0.6	265	1083	1007	826	973
	2	0.9	270	1619	1417	878	1144
	3	1.2	214	1344	1322	617	862
	4	1.7	27	251	268	92	94
	5	2.4	0	5	4	2	1
	6	3.4	1	0	0	2	0
	7	5.8	0	38	28	12	82
	8	6.8	0	0	0	0	6
	9	9.6	0	0	0	0	0
	10	13.6	0	0	0	0	0
	11	19.2	0	0	0	0	0
	12	27.2	0	0	0	0	0

*The number of particles counted in 10-second period.

Particle Size Distributions of Microfog Sprays

	Channel	Size (μm)	Particle Size Distribution* 2 cfm	3 cfm	4 cfm	5 cfm	6 cfm
Sunthetic 18HB							
Nozzle No. 2							
	1	0.6	260	1004	763	392	564
	2	0.9	280	1387	752	315	533
	3	1.2	295	1347	516	178	392
	4	1.7	17	188	31	12	56
	5	2.4	0	5	0	0	2
	6	3.4	0	1	0	0	1
	7	5.8	0	23	19	11	0
	8	6.8	0	1	1	0	0
	9	9.6	0	0	0	0	0
	10	13.6	0	0	0	0	0
	11	19.2	0	0	0	0	0
	12	27.2	0	0	0	0	0

*The number of particles counted in 10-second period.

Particle Size Distributions of Microfog Sprays

	Channel	Size (μm)	Particle Size Distribution*				
			2 cfm	3 cfm	4 cfm	5 cfm	6 cfm
Sunthetic 18HB							
Nozzle No. 3							
	1	0.6	257	768	556	254	370
	2	0.9	282	991	488	241	288
	3	1.2	235	995	387	154	230
	4	1.7	46	135	45	14	39
	5	2.4	0	2	0	2	0
	6	3.4	0	0	0	0	0
	7	5.8	0	0	0	0	0
	8	6.8	0	0	0	0	0
	9	9.6	0	0	0	0	0
	10	13.6	0	0	0	0	0
	11	19.2	0	0	0	0	0
	12	27.2	0	0	0	0	0

*The number of particles counted in 10-second period.

Particle Size Distributions of Microfog Sprays

	Channel	Size (μm)	Particle Size Distribution*				
			2 cfm	3 cfm	4 cfm	5 cfm	6 cfm
Sunthetic 18HB							
Nozzle No. 1A							
	1	0.6	138	808	830	801	747
	2	0.9	110	1002	1169	1055	1025
	3	1.2	132	975	1084	934	1096
	4	1.7	31	187	214	162	305
	5	2.4	0	6	2	6	19
	6	3.4	0	0	0	0	0
	7	5.8	0	0	23	0	182
	8	6.8	0	0	4	0	23
	9	9.6	0	0	0	0	2
	10	13.6	0	0	0	0	0
	11	19.2	0	0	0	0	0
	12	27.2	0	0	0	0	0

*The number of particles counted in 10-second period.

Particle Size Distributions of Microfog Sprays

	Channel	Size (μm)	Particle Size Distribution*				
			2 cfm	3 cfm	4 cfm	5 cfm	6 cfm
Sunthetic 18HB							
Nozzle No. 3A							
	1	0.6	104	416	626	434	642
	2	0.9	46	448	649	429	742
	3	1.2	62	430	533	297	748
	4	1.7	16	126	134	45	178
	5	2.4	0	3	6	3	3
	6	3.4	0	0	0	0	0
	7	5.8	0	0	0	0	0
	8	6.8	0	0	0	0	0
	9	9.6	0	0	0	0	0
	10	13.6	0	0	0	0	0
	11	19.2	0	0	0	0	0
	12	27.2	0	0	0	0	0

*The number of particles counted in 10-second period.

Particle Size Distributions of Microfog Sprays

	Channel	Size (μm)	Particle Size Distribution*				
			2 cfm	3 cfm	4 cfm	5 cfm	6 cfm
Esso Turbo 4040							
Nozzle No. 1							
	1	0.6	626	390	537	637	367
	2	0.9	1464	1693	1710	1548	1697
	3	1.2	2014	2336	2261	1918	2408
	4	1.7	966	1520	1067	767	1596
	5	2.4	41	142	113	75	152
	6	3.4	0	1	1	1	2
	7	5.8	491	593	437	350	912
	8	6.8	84	142	112	113	351
	9	9.6	6	2	6	12	73
	10	13.6	0	0	0	0	0
	11	19.2	0	0	0	0	0
	12	27.2	0	0	0	0	0

*The number of particles counted in 10-second period.

Particle Size Distributions of Microfog Sprays

	Channel	Size (μm)	Particle Size Distribution*				
			2 cfm	3 cfm	4 cfm	5 cfm	6 cfm
Esso Turbo 4040							
Nozzle No. 2							
	1	0.6	698	596	599	454	683
	2	0.9	1453	1801	1683	1638	1491
	3	1.2	2281	2225	2114	2121	1501
	4	1.7	872	966	811	884	317
	5	2.4	35	37	26	23	10
	6	3.4	0	0	0	0	0
	7	5.8	460	352	164	81	187
	8	6.8	71	36	14	10	39
	9	9.6	5	0	1	0	7
	10	13.6	0	0	0	0	1
	11	19.2	0	0	0	0	0
	12	27.2	0	0	0	0	1

*The number of particles counted in 10-second period.

Particle Size Distributions of Microfog Sprays

	Channel	Size (μm)	Particle Size Distribution*				
			2 cfm	3 cfm	4 cfm	5 cfm	6 cfm
Esso Turbo 4040							
Nozzle No. 3							
	1	0.6	643	691	589	630	739
	2	0.9	1446	1665	1717	1415	1446
	3	1.2	2072	2131	2109	1567	1530
	4	1.7	902	586	801	560	299
	5	2.4	43	16	11	52	10
	6	3.4	1	0	1	3	2
	7	5.8	377	349	271	124	218
	8	6.8	58	23	31	10	51
	9	9.6	2	2	0	0	9
	10	13.6	0	0	0	0	0
	11	19.2	0	0	0	0	0
	12	27.2	0	0	0	0	0

*The number of particles counted in 10-second period.

Particle Size Distributions of Microfog Sprays

	Channel	Size (μm)	Particle Size Distribution*				
			2 cfm	3 cfm	4 cfm	5 cfm	6 cfm
Esso Turbo 4040							
Nozzle No. 1A							
	1	0.6	771	796	606	395	426
	2	0.9	869	1474	1538	1194	1184
	3	1.2	742	1543	1911	1783	1699
	4	1.7	116	330	1023	1817	1601
	5	2.4	4	9	110	659	512
	6	3.4	0	0	4	45	31
	7	5.8	45	239	674	998	1071
	8	6.8	8	40	210	636	863
	9	9.6	1	3	21	229	474
	10	13.6	0	0	0	0	12
	11	19.2	0	0	0	0	0
	12	27.2	0	0	0	0	0

*The number of particles counted in 10-second period.

Particle Size Distributions of Microfog Sprays

	Channel	Size (μm)	Particle Size Distribution*				
			2 cfm	3 cfm	4 cfm	5 cfm	6 cfm
Esso Turbo 4040							
Nozzle No. 3A							
	1	0.6	511	696	618	190	424
	2	0.9	380	1256	1530	1445	1592
	3	1.2	220	1247	1962	2120	2380
	4	1.7	31	294	863	2580	1649
	5	2.4	2	11	64	814	208
	6	3.4	0	0	0	24	4
	7	5.8	15	182	712	1074	1231
	8	6.8	0	23	178	519	727
	9	9.6	2	3	16	117	178
	10	13.6	0	0	0	0	2
	11	19.2	0	0	0	0	0
	12	27.2	0	0	0	0	0

*The number of particles counted in 10-second period.

Particle Size Distributions of Microfog Sprays

	Channel	Size (μm)	Particle Size Distribution*				
			2 cfm	3 cfm	4 cfm	5 cfm	6 cfm
Ucon 50-HB-5100							
Nozzle No. 1							
	1	0.6	491	1044	939	957	773
	2	0.9	294	1588	1650	1542	1763
	3	1.2	124	1667	1794	1414	2017
	4	1.7	4	272	404	392	546
	5	2.4	0	2	8	29	20
	6	3.4	0	0	0	0	0
	7	5.8	0	131	259	176	270
	8	6.8	0	1	35	27	39
	9	9.6	0	0	1	1	1
	10	13.6	0	0	0	0	0
	11	19.2	0	0	0	0	0
	12	27.2	0	0	0	0	0

*The number of particles counted in 10-second period.

Particle Size Distributions of Microfog Sprays

	Channel	Size (μm)	Particle Size Distribution*				
			2 cfm	3 cfm	4 cfm	5 cfm	6 cfm
Ucon 50-HB-5100							
Nozzle No. 2							
	1	0.6	352	950	1008	1032	1005
	2	0.9	223	1595	1438	966	1401
	3	1.2	100	1755	1325	561	990
	4	1.7	2	307	146	26	76
	5	2.4	0	1	1	0	0
	6	3.4	0	0	0	0	0
	7	5.8	0	207	100	11	20
	8	6.8	0	18	4	1	2
	9	9.6	0	0	0	0	0
	10	13.6	0	0	0	0	0
	11	19.2	0	0	0	0	0
	12	27.2	0	0	0	0	0

*The number of particles counted in 10-second period.

Particle Size Distributions of Microfog Sprays

	Channel	Size (μm)	Particle Size Distribution*				
			2 cfm	3 cfm	4 cfm	5 cfm	6 cfm
Ucon 50-HB-5100							
Nozzle No. 3							
	1	0.6	364	955	973	1128	1091
	2	0.9	226	1571	1532	1150	1302
	3	1.2	104	1853	1539	768	928
	4	1.7	4	398	226	45	44
	5	2.4	0	4	1	0	0
	6	3.4	0	0	0	0	0
	7	5.8	0	165	187	21	22
	8	6.8	0	10	11	0	0
	9	9.6	0	0	0	0	0
	10	13.6	0	0	0	0	0
	11	19.2	0	0	0	0	0
	12	27.2	0	0	0	0	0

*The number of particles counted in 10-second period.

Particle Size Distributions of Microfog Sprays

	Channel	Size (μm)	Particle Size Distribution* 2 cfm	3 cfm	4 cfm	5 cfm	6 cfm
Ucon 50-HB-5100							
Nozzle No. 1A							
	1	0.6	150	1117	1060	913	967
	2	0.9	61	1105	1370	1185	1193
	3	1.2	28	697	1203	1142	1126
	4	1.7	0	50	190	198	264
	5	2.4	0	0	10	10	13
	6	3.4	0	0	1	0	2
	7	5.8	0	32	73	145	171
	8	6.8	0	1	10	18	26
	9	9.6	0	1	2	2	2
	10	13.6	0	0	0	0	0
	11	19.2	0	0	0	0	0
	12	27.2	0	0	0	0	0

*The number of particles counted in 10-second period.

Particle Size Distributions of Microfog Sprays

	Channel	Size (μm)	Particle Size Distribution* 2 cfm	3 cfm	4 cfm	5 cfm	6 cfm
Ucon 50-HB-5100							
Nozzle No. 3A							
	1	0.6	129	836	961	967	993
	2	0.9	42	556	1002	1240	1190
	3	1.2	23	269	807	1039	1059
	4	1.7	0	24	100	192	189
	5	2.4	0	0	3	2	3
	6	3.4	0	0	0	0	0
	7	5.8	0	14	90	145	132
	8	6.8	0	0	8	18	12
	9	9.6	0	1	0	1	1
	10	13.6	0	0	0	0	0
	11	19.2	0	0	0	0	0
	12	27.2	0	0	0	0	0

*The number of particles counted in 10-second period.

APPENDIX D

WETTING RATE DETERMINATIONS

APPENDIX D-1

Wetting Rate Study (XRM-177F; Nozzle No. 1)

Item	Run No.	Temp. (°F)	Gas Flow Rate (ft^3/min) at 45 psi & 200°F	Oil Flow Rate (gm/min)	Wetting Time, sec. 3/4"	1"	1-1/2"	1-3/4"	2"	Wetting Rate (Fract. area covered/sec.)
1	M31-1	600	2	0.40			1.24		3.75	0.25
2	M31-2	600	3	0.85		0.31	0.62	0.91	1.25	0.77
3	M31-3	600	4	1.35		0.17	0.33	0.58	0.75	1.15
4	M28-1	600	5	1.93		0.16	0.22	0.39	0.50	1.60
5	M23-1	600	6	2.52		0.13	0.31	0.44	0.56	1.58
6	M32-1	700	2	0.40		0.47	2.16		5.03	0.16
7	M34-3	700	3	0.85		0.56			1.35	0.82
8	M34-4	700	4	1.35		0.30	0.42		0.53	2.00
9	M29-2	700	5	1.93		0.28	0.41	0.49	0.55	2.00
10	M24-1	700	6	2.52		0.22	0.44	0.64	0.81	1.54
11	M33-1	800	2	0.40		0.67	3.72	6.50	7.70	0.10
12	M33-2	800	3	0.85		0.13	0.31	0.64	0.88	0.84
13	M33-3	800	4	1.35		0.13	0.29	0.34	0.38	3.00
14	M30-2	800	5	1.93		0.25	0.41	0.45	0.55	2.00
15	M25-1	800	6	2.52		0.13	0.23	0.31	0.38	3.00

Wetting Rate Study (XRM-177F; Nozzle No. 2)

Item	Run No.	Temp. (°F)	Gas Flow Rate (ft^3/min) at 45 psi & 200°F	Oil Flow Rate (gm/min)	Wetting Time, sec. 3/4"	1"	1-1/2"	1-3/4"	2"	Wetting Rate (Fract. area covered/sec.)
1		600	2	0.40						
2		600	3	0.85	NO WETTING (10+ sec.)					
3		600	4	1.35						
4	M28-2	600	5	1.93					2.66 - streaks to edge	
5	M23-2	600	6	2.52					0.422 - streaking to edge	
6		700	2	0.40						
7		700	3	0.85	NO WETTING (10+ sec.)					
8		700	4	1.35						
9	M29-3	700	5	1.93					1.69 - no apparent wetting	
10	M24-2	700	6	2.52					0.17 - streaks - no full coverage	
11		800	2	0.40						
12		800	3	0.85	NO WETTING (10+ sec.)					
13		800	4	1.35						
14	M30-3	800	5	1.93	No visible oil film					
15	M25-2	800	6	2.52	Stain in center - no wetting					

Wetting Rate Study (XRM-177F; Nozzle No. 3)

Item	Run No.	Temp.	Gas Flow Rate (ft^3/min) at 45 psi & 200°F	Oil Flow Rate (gm/min)	Wetting Time, sec. 1/2"	3/4"	1"	1-1/2"	1-3/4"	2"	Wetting Rate (Fract. area covered/sec.)
1	M5-1	600	2	0.40		Streaks of oil film					0.01
2	M12-1(M5-2)	600	3	0.85	0.94	1.33	2.19	2.97 (3.30)	4.60	7.13 (7.06)	0.12
3	M15-1(M5-3)	600	4	1.35			0.91	1.56 (1.97)	2.73	3.50 (3.90)	0.25
4	M15-4	600	5	1.95			0.52	1.42	2.19	2.88	0.30
5	M23-3	600	6	2.52			0.43	0.78	1.47	2.34	0.37
6	M6-1	700	2	0.40		No visible wetting					-
7	M6-2	700	3	0.85	1.17	2.02	3.10	4.63	5.62	7.06	0.19
8	M6-3(M10-1)	700	4	1.35		0.78	1.40 (1.84)	2.45 (2.17)		4.15 (4.25)	0.25
9	M14-4	700	5	1.93			0.42	1.15	2.04	2.64	0.33
10	M24-3	700	6	2.52			0.22	0.83	1.50	1.88	0.43
11	M7-1	800	2	0.40		No visible wetting					-
12	M7-2	800	3	0.85	2.0	3.05	4.45	7.18	9.52		0.10
13	M7-3	800	4	1.35	0.89		1.97	3.03		4.75	0.23
14	M7-4(M13-1)	800	5	1.93			1.11 (1.28)	1.55 (1.80)	2.76	3.42 (3.68)	0.29
15	M25-3	800	6	2.52			0.34	1.60	2.69	3.38	0.40

Wetting Rate Study (XRM-177F; Nozzle No. 1A)

Item	Run No.	Temp. (°F)	Gas Flow Rate (ft^3/min) at 45 psi & 200°F	Oil Flow Rate (gm/min)	Wetting Time, sec. 3/4"	1"	1-1/2"	1-3/4"	2"	Wetting Rate (Fract. area covered/sec.)
1	M31-4	600	2	0.40		4.53	11.7		17.30	0.06
2	M34-7	600	3	0.85		1.66			3.02	0.33
3	M34-8	600	4	1.35			1.0		1.75	0.56
4	M28-3	600	5	1.93			0.49	0.74	0.98	1.11
5	M23-4	600	6	2.52		0.25	0.73		1.11	0.91
6	M32-4	700	2	0.40		5.58	10.70		14.40	0.07
7	M34-2	700	3	0.85			0.75	1.08	1.47	0.60
8	M32-6	700	4	1.35			0.812	1.06	1.19	0.75
9	M29-4	700	5	1.93		0.24	0.48	0.69	1.00	0.90
10	M24-4	700	6	2.52		0.23	0.50	0.75	0.94	0.90
11	M33-6	800	2	0.40		2.16	4.60	5.85	5.98	0.13
12	M34-1	800	3	0.85				1.14	1.40	0.69
13	M33-4	800	4	1.35		0.28	0.74		1.22	0.83
14	M30-4	800	5	1.93			0.23	0.37	0.45	1.30
15	M25-4	800	6	2.52		0.25	0.66	0.80	0.97	1.06

Wetting Rate Study (XRM-177F; Nozzle No. 3A)

Item	Run No.	Temp. (°F)	Gas Flow Rate (ft^3/min)	Oil Flow Rate (gm/min	Wetting Time, sec. 3/4"	1"	1-1/2"	1-3/4"	2"	Rate (Fract. Area covered/sec.)
1	M34-5	600	2	0.40		7.04			11.4	0.17
2	M31-8	600	3	0.85			0.52	0.83	1.14	0.75
3	M31-9	600	4	1.35		0.41	0.71		0.94	1.43
4	M28-4	600	5	1.93		0.75	1.24		1.36*	1.43
5	M23-5	600	6	2.52		0.32	1.17	1.41	1.57*	1.25
6	M32-7	700	2	0.40		6.92	12.00		14.52	0.18
7	M32-8	700	3	0.85			1.06	1.42	1.66	0.67
8	M32-9	700	4	1.35			0.86	1.07	1.18	1.25
9	M29-5	700	5	1.93		0.94	1.24	1.53	1.72*	1.00
10	M24-5	700	6	2.52		0.72	1.12		1.70*	0.77
11	M33-7	800	2	0.40		6.20	11.25	13.17	13.85	0.16
12	M33-8	800	3	0.85		0.59	1.00	1.20	1.55	0.77
13	M33-9	800	4	1.35		0.29	0.50	0.69	0.79	1.25
14	M30-5	800	5	1.93		0.50	0.94	1.17	1.25*	1.00
15	M25-5	800	6	2.52		0.61	0.93	1.09	1.37*	1.00

Wetting Rate Study (Hercolube-F; Nozzle No. 1)

Item	Run No.	Temp. (°F)	Gas Flow Rate (ft^3/min)	Oil Flow Rate (gm/min)	Wetting Time, Sec. 1/2"	1"	1-1/4"	1-1/2"	1-3/4"	2"	Wetting Rate (fract. area covered/sec.)
1	HF2-4	600	2	1.09	0.34	0.47	0.80	1.53	3.0	3.64	0.22
2	HF2-3	600	3	2.20	0.14	0.25		0.64	1.02	1.35	0.71
3	HF2-2	600	4	3.19	0.10	0.17		0.38	0.52	0.69	1.45
4	HF2-1	600	5	4.62	0.11	0.16		0.30	0.37	0.49	1.92
5	HF1-3	600	6	6.08		0.11	0.14	0.28	0.39	0.51	2.02
6	HF3-5	700	2	1.09		0.45	0.97	1.85	3.57	4.59	0.17
7	HF3-4	700	3	2.20	0.22	0.30	0.40		0.74	1.03	1.00
8	HF3-3	700	4	3.19	0.11	0.14	0.17	0.24	0.39	0.72	1.14
9	HF3-2	700	5	4.62	0.05	0.13	0.17	0.24	0.36	0.64	1.23
10	HF1-1	700	6	6.08		0.14		0.23		0.59	1.45
11		800	2	1.09	No run made						-
12	HF8-1	800	3	2.20		0.18	0.37	0.50			0.86
13	HF7-3	800	4	3.19		0.13	0.22	0.40	0.88	1.32	0.52
14	HF7-2	800	5	4.62		0.13	0.27	1.20	2.22	4.05	0.15
15	HF1-11	800	6	6.08	Flooding - heavy streaks						-

Wetting Rate Study (Hercolube-F; Nozzle No. 2)

Item	Run No.	Temp. (°F)	Gas Flow Rate (ft^3/min)	Oil Flow Rate (gm/min)	Wetting Time, Sec. 1/2"	1"	1-1/4"	1-1/2"	1-3/4"	2"	Rate (Fract./sec
1		600	2	1.09							
2		600	3	2.20	NO WETTING: 10+ sec. spray						
3		600	4	3.19							
4		600	5	4.62							
5	HF1-4	600	6	6.08	A trace of oil film but no oil film movement						
6		700	2	1.09							
7		700	3	2.20	NO WETTING: 10+ sec. spray						
8		700	4	3.19							
9		700	5	4.62							
10	HF1-2	700	6	6.08							
11		800	2	1.09							
12		800	3	2.20	NO WETTING: 10+ sec. spray						
13		800	4	3.19							
14		800	5	4.62							
15		800	6	6.08							

Wetting Rate Study (Hercolube-F; Nozzle No. 3)

Item	Run No.	Temp. (°F)	Gas Flow Rate (ft^3/min)	Oil Flow Rate (gm/min)	Wetting Time, Sec. 1/2"	1"	1-1/4"	1-1/2"	1-3/4"	2"	Wetting Rate (Fract./sec.)
1		600	2	1.09	No apparent wetting						
2	HF2-7	600	3	2.20	0.06	0.53	0.82	2.20			0.17
3	HF2-5	600	4	3.19	0.05	0.19	0.97		1.40	2.20	0.36
4	HF2-6	600	5	4.62	0.06	0.17	0.53	1.14		1.53	0.59
5	HF1-5	600	6	6.08				0.83		1.41	0.70
6		700	2	1.09	No run made						
7	HF3-8	700	3	2.20		1.40	3.50	Streaking - lacquer			
8	HF3-7	700	4	3.19		0.58	2.08	Streaking - lacquer			
9	HF3-6	700	5	4.62		1.60	2.03	2.50	Streaking - heavy flooding		0.31
10	HF1-8	700	6	6.08							
11		800	2	1.09	No run made						
12	HF7-1	800	3	2.20			5.13	No oil film advancement after 1-1/4"; light streaks and deposits.			
13	HF6-5	800	4	3.19	No visible oil film movement - after 8 sec. spray, plate appears to be flooded and deposit completely covers plate.						
14	HF6-4	800	5	4.62							
15	HF1-12	800	6	6.08	No apparent film movement.						

Wetting Rate Study (Hercolube-F; Nozzle No. 1A)

Item	Run No.	Temp. (°F)	Gas Flow Rate (ft^3/min)	Oil Flow Rate (gm/min)	Wetting Time, sec. 1/2"	1"	1-1/4"	1-1/2"	1-3/4"	2"	Wetting Rate (Fract./sec.)
1	HF2-11	600	2	1.09	1.00	1.58	2.96	4.07	5.80	7.32	0.14
2	HF2-10	600	3	2.20	0.05	0.20	0.36	0.55	1.12	1.48	0.53
3	HF2-9	600	4	3.19	0.03	0.17	0.34	0.60	0.89	1.20	0.71
4	HF2-8	600	5	4.62	0.03	0.20	0.30	0.45	0.60	0.72	1.35
5	HF1-6	600	6	6.08			0.26	0.34		0.56	2.00
6	HF4-1	700	2	1.09	0.312	0.703	1.14	1.47	1.94	2.28	0.42
7	HF3-11	700	3	2.20		0.45	0.73	1.22	1.63	1.83	0.50
8	HF3-10	700	4	3.19		0.30	0.52	0.80	1.30	1.50	0.58
9	HF3-9	700	5	4.62		0.22	0.33	0.57	0.83	1.08	0.84
10	HF1-9	700	6	6.08			Flooding - heavy streaks				-
11		800	2	1.08			No run made				-
12	HF6-3	800	3	2.20		0.20	0.31	0.52	0.81	1.11	0.73
13	HF6-2	800	4	3.19		0.11	0.20	0.44		1.14	0.65
14	HF6-1	800	5	4.62		0.09	0.16		0.70	1.07	0.70
15	HF1-13	800	6	6.08			0.30	0.42	Heavy streaks		

Wetting Rate Study (Hercolube-F; Nozzle No. 3A)

Item	Run No.	Temp. (°F)	Rate (ft^3/min)	Rate (gm/min)	Wetting Time, Sec. 1/2"	1"	1-1/4"	1-1/2"	1-3/4"	2"	Wetting Rate (Fract./sec.)
1	HF3-1	600	2	1.09		0.45	0.91	2.68	4.08	5.22	0.15
2	HF2-14	600	3	2.20	0.12	0.15	0.41	0.62	0.94	1.33	0.63
3	HF2-13	600	4	3.19	0.05	0.1	0.27	0.53	0.78	1.00	0.84
4	HF2-12	600	5	4.62	0.05	0.1	0.27	0.47	0.62	0.84	1.12
5	HF1-7	600	6	6.08		0.1	0.27	0.49	0.69	0.93	0.94
6	HF4-5	700	2	1.09		0.33	0.58	0.92	1.31	1.61	0.57
7	HF4-4	700	3	2.20	0.16	0.31	0.50	0.69	1.19	1.45	0.62
8	HF4-3	700	4	3.19		0.06	0.12	0.37	0.56	0.69	1.25
9	HF4-2	700	5	4.62		0.02	0.18	0.29	0.47	0.66	1.21
10	HF1-8	700	6	6.08		Heavy streaks - flooding					
11		800	2	1.09		No run made					
12	HF5-4	800	3	2.20		0.15	Heavy streaks				
13	HF5-3	800	4	3.19		0.09	0.19	0.34		0.59	1.53
14	HF5-2	800	5	4.62		0.05	0.16	0.28	0.47	0.58	1.50
15	HF1-14	800	6	6.08		0.10	Heavy streaks				

Wetting Rate Study (Sunthetic 18 HB; Nozzle No. 1)

Item	Run No.	Temp. (°F)	Gas Flow Rate (ft^3/min. @ 45 psi, 200°F)	Oil Flow Rate (gm/min.)	Wetting Time, Sec. 1"	1-1/4"	1-1/2"	1-3/4"	2"	Wetting Rate (Fract. area covered/sec.)
1	S1-4	600	2	0.21	3.62	7.52	12.23	15.94		0.04
2	S1-3	600	3	0.65	0.62	1.94	3.47	5.84	7.27	0.11
3	S1-2	600	4	1.02	0.30	0.59	1.13	1.48	1.81	0.44
4	S1-1	600	5	1.39	0.25	0.62	1.09	1.72	2.00	0.45
5	S12-3	600	6	1.71	0.39	0.73	1.27	2.02	2.75	0.32
6	S5-3	700	2	0.21	1.94	4.48	8.65	12.72	17.28	0.05
7	S5-2	700	3	0.65	0.34	0.94	1.64	2.56	3.59	0.23
8	S5-1	700	4	1.02	0.20	0.33	0.69	1.14	1.37	0.56
9	S4-4	700	5	1.39	0.23	0.42	0.70	1.03	1.13	0.91
10	S14-2	700	6	1.71	0.52	0.87	1.63	2.36	2.89	0.32
11	S9-4	800	2	0.21	1.64	4.17	7.36	13.01	16.30	0.05
12	S9-3	800	3	0.65	0.45	0.75	1.34	2.05	2.86	0.30
13	S9-2	800	4	1.02	0.50	0.84	1.36	1.81	2.13	0.44
14	S9-1	800	5	1.39	0.56	0.77	1.22	1.56	1.87	0.56
15	S15-3	800	6	1.71	0.19	0.34	0.69	1.22	1.69	0.51

Wetting Rate Study (Sunthetic 18 HB; Nozzle No. 3)

Item	Run No.	Temp.	Gas Flow Rate (ft^3/min. @ 45 psi, 200°F)	Oil Flow Rate (gm/min)	1"	1-1/4"	1-1/2"	1-3/4"	2"	Wetting Rate (Fract. area covered/sec.)
1	S18-2	600	3	0.65		3.00		13.94	17.23	0.05
2	S18-1	600	4	1.02	1.00	2.92	7.97	10.75	13.81	0.06
3	S17-2	600	5	1.39	1.59	3.11	6.03	9.61	11.59	0.08
4	S13-1	600	6	1.71	3.52	7.71				0.04
5	S20-2	700	4	1.02	1.94	3.78	6.25	10.08	14.45	0.06
6	S6-1	700	5	1.39	2.81	6.97				0.04
7	S14-3	700	6	1.71	4.11	9.38	15.40			0.03
8	S10-2	800	4	1.02	3.44	13.12	20.80			0.02
9	S10-1	800	5	1.39	2.64					
10	S15-4	800	6	1.71	2.28	4.53			10.79	0.09

Wetting Rate Study (Sunthetic 18 HB; Nozzle No. 1A)

Item	Run No.	Temp. (°F)	Gas Flow Rate (ft^3/min. @ 45 psi, 200°F)	Oil Flow Rate (gm/min)	Wetting Time, Sec. 1"	1-1/4"	1-1/2"	1-3/4"	2"	Wetting Rate (Fract. area covered/sec.)
1	S4-3	600	2	0.21	8.19	12.60				0.03
2	S4-2	600	3	0.65	2.00	3.05	4.69			0.08
3	S4-1	600	4	1.02	2.41	4.75	6.90	9.07	9.30	0.08
4	S20-1	600	5	1.39	1.94	2.45	3.63	5.00	6.72	0.15
5	S13-2	600	6	1.71	1.56	2.94	4.45	7.26	8.60	0.11
6	S7-4	700	2	0.21	7.09	11.72				0.02
7	S7-3	700	3	0.65	1.47	2.45	3.78	4.80	6.05	0.16
8	S7-2	700	4	1.02	0.88	1.44	2.60	3.80		0.18
9	S7-1	700	5	1.39	0.52	1.03	1.84	3.05	4.13	0.22
10	S15-1	700	6	1.71	0.09	0.23	0.83	1.38	1.75	0.48
11	S11-4	800	2	0.21	5.98	8.65	13.19			0.04
12	S11-3	800	3	0.65	1.12	2.03	3.25	4.70	6.60	0.13
13	S11-2	800	4	1.02	0.84	1.58	3.03	5.31	6.90	0.12
14	S11-1	800	5	1.39	0.59	1.56	2.97	4.30	5.80	0.15
15	S16-1	800	6	1.71	0.56	1.09	2.19	3.21	4.09	0.21

Wetting Rate Study (Sunthetic 18 HB; Nozzle No. 3A)

Item	Run No.	Temp. (°F)	Gas Flow Rate (ft^3/min @ 45 psi, 200°F)	Oil Flow Rate (gm/min)	Wetting Time, sec. 1/2"	1"	1-1/4"	1-1/2"	1-3/4"	2"	Wetting Rate (Fract. area covered/sec.)
1	S19-1	600	3	0.65		1.84	3.39	6.50	11.60	16.70	0.03
2	S19-2	600	4	1.02		3.00	4.59	6.47	8.47	9.94	0.10
3	S19-3	600	5	1.39		1.41	2.06	2.92	3.97	4.88	0.22
4	S14-1	600	6	1.71		1.97	3.24	4.69	6.31	7.54	0.15
5	S8-3	700	3	0.65		3.80	5.51	7.31	10.28	12.50	0.08
6	S8-2	700	4	1.02		2.22	3.56	5.38	7.45	8.91	0.11
7	S8-1	700	5	1.39		1.66	2.66	3.55	4.85	5.42	0.23
8	S15-2	700	6	1.71		0.16	0.41	0.69	1.19	1.69	0.47
9	S12-2	800	4	1.02		2.11	3.10	4.22	5.75	6.87	0.15
10	S12-1	800	5	1.39		1.59	2.91	4.66	6.72	7.66	0.11
11	S16-2	800	6	1.71		2.03	3.34	4.90	7.85	9.85	0.10

Wetting Rate Study (Turbo Oil 4040; Nozzle No. 1)

Item	Run No.	Temp. (°F)	Gas Flow Rate (ft^3/min. @ 45 psi, 200°F)	Oil Flow Rate (gm/min)	Wetting Time, sec. 1"	1-1/4"	1-1/2"	1-3/4"	2"	Wetting Rate (Fract. area covered/sec.)
1	Es 33-3	600	2	1.38	12.65					-
2	Es 34-1	600	3	2.85	0.11	0.22	0.39	0.61	0.78	1.17
3	Es 34-2	600	4	5.07	0.09	0.19	0.39	0.69	0.99	0.85
4	Es 34-3	600	5	7.39	0.44	1.45	2.59	3.33	3.91	0.21
5	Es 1-1	600	6	10.23	0.06	0.11	0.17	0.22	0.25	3.0
6	Es 27-3	700	2	1.38	0.47	1.25	23.62			0.01
7	Es 28-1	700	3	2.85	0.91	6.25	12.62	28.56		0.02
8	Es 28-2	700	4	5.07	0.91	1.91	3.56	6.13	7.50	0.10
9	Es 29-1	700	5	7.39	0.28	1.47	2.66	3.78	4.50	0.17
10	Es 2-2	700	6	10.23	0.13	0.28	0.38			0.90
11	Es 2-3	800	6	10.23	0.38					

Wetting Rate Study (Turbo Oil 4040; Nozzle No. 2)

Item	Run No.	Temp. (°F)	Gas Flow Rate (ft^3/min. @ 45 psi, 200°F)	Oil Flow Rate (gm/min.)	Wetting Time, sec. 1"	1-1/4"	1-1/2"	1-3/4"	2"	Wetting Rate (Fract. area covered/sec.)
1	Es 34-4	600	3	2.85	Irregular flooding					
2	Es 35-1	600	4	5.07	Immediate flooding 0.16					
3	Es 35-2	600	5	7.39	0.06	0.16	0.63	0.91	1.19	0.79
4	Es 1-2	600	6	10.23	0.06	0.11	0.74	1.13	1.56	0.55
5	Es 29-2	700	4	5.07	3.13	6.10	11.56	13.64	15.00	0.06
6	Es 29-3	700	5	7.39		0.03	0.08	0.28	0.55	1.16
7	Es 2-1	700	6	10.23	Could not follow oil flow					
8	Es 2-4	800	6	10.23	Could not follow oil flow					

Wetting Rate Study (Turbo Oil 4040; Nozzle No. 3)

Item	Run No.	Temp. (°F)	Gas Flow Rate (ft^3/min. @ 45 psi, 200°F)	Oil Flow Rate (gm/min)	Wetting Time, sec. 1"	1-1/4"	1-1/2"	1-3/4"	2"	Wetting Rate (Fract. area covered/sec.)
1	Es 35-3	600	3	2.85	2.44	7.95	10.54	13.40		0.06
2	Es 24-1	600	4	5.07	1.02	3.61	5.75	7.53	8.58	0.13
3	Es 24-2	600	5	7.39	1.09	2.32	3.32	4.54	5.65	0.19
4	Es 1-3	600	6	10.23	0.06	0.09	0.22	0.27	0.31	2.25
5	Es 20-4	700	4	5.07	3.20	6.40	10.36	12.98	14.44	0.09
6	Es 30-1	700	5	7.39		0.19	1.97	2.92	3.56	0.26
7	Es 1-8	700	6	10.23	0.03	0.09	0.14	0.22	0.38	2.25
8	Es 2-5	800	6	10.23	Could not follow oil flow					

Wetting Rate Study (Turbo Oil 4040; Nozzle No. 1A)

Item	Run No.	Temp. (°F)	Gas Flow Rate (ft^3/min. @ 45 psi, 200°F)	Oil Flow Rate (gm/min)	Wetting Time, sec. 1"	1-1/4"	1-1/2"	1-3/4"	2"	Wetting Rate (Fract. area covered/sec.)
1	Es 25-1	600	2	1.38	1.94					-
2	Es 25-2	600	3	2.85	0.58	1.51	4.54	8.86	11.46	0.07
3	Es 36-1	600	4	5.07	2.58	3.94	5.25	5.85	7.50	0.16
4	Es 26-1	600	5	7.39		0.05	0.16	0.25	0.33	2.73
5	Es 1-4	600	6	10.23	0.14	0.25	0.45	0.63	0.84	1.00
6	Es 30-2	700	4	5.07	1.62	3.13	4.47	5.94	6.87	0.14
7	Es 30-3	700	5	7.39	2.28	3.06	4.06	5.65	6.40	0.18
8	Es 1-7	700	6	10.23	0.34	0.50	1.42	2.22	2.58	0.31
9	Es 32-3	800	4	5.07	4.32	7.24	9.40	11.89	13.28	0.08
10	Es 32-4	800	5	7.39	2.03	2.76	3.66	5.22	6.38	0.15
11	Es 2-6	800	6	10.23	1.34	2.88	4.32	5.97		0.11

Wetting Rate Study (Turbo Oil 4040; Nozzle No. 3A)

Item	Run No.	Temp. (°F)	Gas Flow Rate (ft^3/min. @ 45 psi, 200°F)	Oil Flow Rate (gm/min)	Wetting Time, sec. 1"	1-1/4"	1-1/2"	1-3/4"	2"	Wetting Rate (Fract. area covered/sec.)
1	Es 36-2	600	2	1.38	1.41	4.72	16.26	25.30		0.02
2	Es 36-3	600	3	2.85	0.22	0.42	0.55	1.08	1.41	0.61
3	Es 27-1	600	4	5.07	0.16	0.47	1.09	1.53	1.78	0.45
4	Es 27-2	600	5	7.39	0.81	1.87	2.75	3.34	4.00	0.25
5	Es 1-5	600	6	10.23	0.34	0.39	0.44	0.50	0.55	2.0
6	Es 30-4	700	2	1.38	6.10	No more oil spread				
7	Es 31-1	700	3	2.85	Unusuable - film gate trouble					
8	Es 32-1	700	4	5.07	3.47	6.00	9.47	11.00	12.24	0.15
9	Es 32-2	700	5	7.39		0.38	1.70	2.38	3.19	0.30
10	Es 1-6	700	6	10.23	0.05	0.09	0.19	0.27	0.39	2.50
11	Es 33-1	800	4	5.07	0.06	0.59	2.25	4.06	5.04	0.14
12	Es 33-2	800	5	7.39	4.06	6.88	8.28	10.79	12.50	0.10
13	Es 2-7	800	6	10.23	0.39	1.44	3.94			0.09

Wetting Rate Study (Ucon 50 - HB 5100; Nozzle No. 1)

Item	Run No.	Temp. (°F)	Gas Flow Rate (ft^3/min. @ 45 psi, 200°F)	Oil Flow Rate (gm/min	Wetting Time, sec. 1"	1-1/4"	1-1/2"	1-3/4"	2"	Wetting Rate (Fract. area covered/sec.)
1	Uc 1-4	600	2	0.20	4.30	8.75	13.56	23.50	25.70	0.04
2	Uc 1-3	600	3	0.51	0.61	1.53	2.52	4.37	5.59	0.15
3	Uc 1-2	600	4	1.07	0.30	0.67	1.20	1.91	2.41	0.38
4	Uc 1-1	600	5	1.43	0.09	0.27	0.47	0.70	1.00	0.86
5	Uc 11-5	600	6	1.89	0.31	0.67	1.15	1.87	2.53	0.38
6	Uc 6-1	700	2	0.20	4.32	6.27	11.35	22.40		0.02
7	Uc 5-6	700	3	0.51	0.37	1.13	2.00	3.06	4.06	0.20
8	Uc 5-5	700	4	1.07	0.16	0.37	0.78	1.23	1.59	0.60
9	Uc 5-4	700	5	1.43	0.19	0.39	0.67	1.08	1.44	1.00
10	Uc 10-6	700	6	1.89	0.25	0.47	0.73	1.15	1.50	1.00
11	Uc 8-3	800	3	0.51	0.36	0.92	1.64	2.83	3.75	0.22
12	Uc 8-2	800	4	1.07	0.13	0.28	0.61	0.89	1.28	0.69
13	Uc 8-1	800	5	1.43	0.13	0.22	0.31	0.59	0.75	1.16
14	Uc 10-1	800	6	1.89	0.09	0.23	0.42	0.64	0.89	0.95

Wetting Rate Study (Ucon 50 - HB 5100; Nozzle No. 2)

Item	Run No.	Temp. (°F)	Gas Flow Rate (ft^3/min. @ 45 psi, 200°F)	Oil Flow Rate (gm/min)	Wetting Time, sec. 1"	1-1/4"	1-1/2"	1-3/4"	2"	Wetting Rate (Fract. area covered/sec.)
1	Uc 2-2	600	4	1.07	No oil film movement					
2	Uc 2-1	600	5	1.43	No oil film movement					
3	Uc 12-1	600	6	1.89	7.13		15.41			0.04
4	Uc 11-1	700	6	1.89	No visible oil film					
5	Uc 10-2	800	6	1.89			7.69			

Wetting Rate Study (Ucon 50 - HB 5100; Nozzle No. 3)

Item	Run No.	Temp. (°F)	Gas Flow Rate (ft^3/min. @ 45 psi, 200°F)	Oil Flow Rate (gm/min)	Wetting Time, sec. 1"	1-1/4"	1-1/2"	1-3/4"	2"	Wetting Rate (Fract. area covered/sec.)
1	Uc 3-3	600	3	0.51			2.95	16.19		0.04
2	Uc 3-2	600	4	1.07			2.76	5.80	9.09	0.07
3	Uc 3-1	600	5	1.43			3.78	5.30	7.94	0.08
4	Uc 12-2	600	6	1.89			1.69	3.24	5.47	0.12
5	Uc 6-3	700	4	1.07			1.31	2.82	4.16	0.16
6	Uc 6-2	700	5	1.43			1.47	3.99	4.92	0.17
7	Uc 11-2	700	6	1.89	2.64	No further oil film advancement				
8	Uc 8-5	800	4	1.07			1.41	2.23	4.47	0.12
9	Uc 8-4	800	5	1.43	0.16	0.33	0.62	0.92	1.22	0.67
10	Uc 10-3	800	6	1.89			1.17	2.48	4.13	0.16

Wetting Rate Study (Ucon 50 - HB 5100; Nozzle No. 1A)

Item	Run No.	Temp. (°F)	Gas Flow Rate (ft^3/min. @ 45 psi, 200°F)	Oil Flow Rate (gm/min)	Wetting Time, sec. 1"	1-1/4"	1-1/2"	1-3/4"	2"	Wetting Rate (Fract. area covered/sec.)
1	Uc 4-4	600	2	0.20	23.80					
2	Uc 4-3	600	3	0.51	2.32	3.58	5.66	9.42	12.35	0.07
3	Uc 4-2	600	4	1.07	0.88	1.44	2.25	3.39	4.28	0.21
4	Uc 4-1	600	5	1.43	0.47	0.66	0.92	1.37	1.78	0.56
5	Uc 12-3	600	6	1.89	0.56	0.75	1.00	1.56	2.46	0.46
6	Uc 7-3	700	3	0.51	1.72	2.53	3.89	5.72	7.29	0.13
7	Uc 7-2	700	4	1.07	0.81	1.22	2.00	3.28	4.55	0.18
8	Uc 7-1	700	5	1.43	0.62	0.92	1.27	1.95	2.54	0.36
9	Uc 11-3	700	6	1.89	0.53	0.77	1.03	1.28	1.56	0.83
10	Uc 9-2	800	3	0.51	1.72	2.94	4.50	6.98	8.52	0.11
11	Uc 9-1	800	4	1.07	0.39	0.89	1.48	2.44	3.52	0.23
12	Uc 8-6	800	5	1.43	0.38	0.48	0.77	1.06	1.61	0.56
13	Uc 10-4	800	6	1.89	0.38	0.56	0.84	1.17	2.00	0.50

Wetting Rate Study (Ucon 50 - HB 5100; Nozzle No. 3A)

Item	Run No.	Temp. (°F)	Gas Flow Rate (ft^3/min. @ 45 psi, 200°F)	Oil Flow Rate (gm/min)	Wetting Time, sec. 1"	1-1/4"	1-1/2"	1-3/4"	2"	Wetting Rate (Fract. area covered/sec.)
1	Uc 5-3	600	3	0.51	3.83	5.66	8.38	11.80	13.90	0.12
2	Uc 5-2	600	4	1.07	0.89	1.42	2.26	3.20	3.80	0.24
3	Uc 5-1	600	5	1.43	0.62	1.24	1.68	2.58	3.20	0.30
4	Uc 12-4	600	6	1.89	0.67	1.14	1.87	2.69	3.44	0.27
5	Uc 7-6	700	3	0.51	2.00	3.12	4.60	6.75	8.35	0.11
6	Uc 7-5	700	4	1.07	0.69	1.23	1.81	2.56	3.47	0.27
7	Uc 7-4	700	5	1.43	0.50	0.88	1.25	1.77	2.47	0.37
8	Uc 11-4	700	6	1.89	0.67	1.01	1.39	1.81	2.42	0.41
9	Uc 9-5	800	3	0.51	3.12	4.67	6.94	9.45	11.28	0.09
10	Uc 9-4	800	4	1.07	0.97	1.56	2.42	3.50	4.40	0.22
11	Uc 9-3	800	5	1.43	0.38	0.62	0.91	1.45	2.19	0.42
12	Uc 10-5	800	6	1.89	0.45	0.81	1.30	1.81	2.50	0.37

Appendix D-2

Wetting Study of XRM-177F in the Presence of Air

Item	Run No.	Temp. (°F)	Gas Flow Rate (ft^3/min. @ 45 psi, 200°F	Oil Flow Rate (gm/min)	Wetting Time, Sec. 1"	1-1/4"	1-1/2"	1-3/4"	2"	Wetting Rate (Fract. area covered/sec.)
	Nozzle No. 1									
1	Ma 1-1	500	3	0.85	0.28	0.53	0.98	1.47	2.03	0.42
2	Ma 1-2	500	5	1.93	0.08	0.13	0.22	0.37	0.47	1.92
3	Ma 1-9	550	3	0.85	0.20	0.44	0.69	1.25	1.84	0.45
4	Ma 1-10	550	5	1.93	0.08	0.11	0.19	0.31	0.41	2.14
5	Ma 3-2	600	3	0.85	0.16	0.34	0.59	0.94	1.25	0.69
6	Ma 3-3	600	5	1.93	0.06	0.11	0.22	0.31	0.42	2.14
	Nozzle No. 3									
7	Ma 5-3	500	3	0.85				4.25	7.78	0.08
8	Ma 5-2	500	5	1.93		0.19	0.34	0.78	1.22	0.58
9	Ma 5-1	550	3	0.85				3.69	6.65	0.09
10	Ma 4-4	550	5	1.93		0.22	0.34	0.91	1.56	0.47
11	Ma 4-3	600	3	0.85				3.47	6.65	0.09
12	Ma 4-2	600	5	1.93		0.22	0.58	0.88	1.20	0.67
	Nozzle No. 1A									
13	Ma 1-5	500	3	0.85	1.00	1.47	2.24	2.96	3.92	0.26
14	Ma 1-6	500	5	1.93		0.22	0.37	0.49	0.57	1.67
15	Ma 2-3	550	3	0.85	0.67	1.22	1.87	2.61	3.28	0.31
16	Ma 2-4	550	5	1.93	0.16	0.19	0.34	0.45	0.56	1.67
17	Ma 3-6	600	3	0.85	0.28	0.75	1.20	1.66	2.11	0.42
18	Ma 3-7	600	5	1.93	0.11	0.20	0.33	0.45	0.59	1.67
	Nozzle No. 3A									
19	Ma 1-7	500	3	0.85	0.56	0.94	1.42	2.10	2.89	0.31
20	Ma 1-8	500	5	1.93	0.13	0.23	0.48	0.63	0.88	0.98
21	Ma 2-5	550	3	0.85	1.08	1.41	2.00	2.84	3.38	0.33
22	Ma 3-1	550	5	1.93	0.19	0.31	0.52	0.72	0.84	1.11
23	Ma 3-8	600	3	0.85	0.42	0.84	1.36	1.87	2.28	0.41
24	Ma 3-9	600	5	1.93	0.16	0.31	0.50	0.69	0.88	1.10

Appendix D-3

Wetting Rate as a Function of Oil/Gas Mass Flow Ratio and of Impaction Velocity (XRM-177F; Nozzle No. 3)

Item	Run No.	Temp. (°F)	Gas Flow Rate, cfm Generator	Diffuser	Oil Flow Rate (gm/min)	Oil/Gas Mass Flow Ratio $Q^* \times 10^3$	Wetting Time, sec. 1/2"	3/4"	1"	1-1/2"	1-3/4"	2"	Wetting Rate (Fract. area covered/sec.)
1	M 5-1	600	2	0	0.40	1.91	Streaks of oil films						-
2	M 16-2	600	2	2	0.40	0.96	1.75		7.03	9.08			0.01
3	F 12-1	600	3	0	0.85	2.67	0.94	1.33	2.19	2.97	4.60	7.13	0.12
4	M 12-2	600	3	1	0.85	2.00			2.31	3.97		7.10	0.12
5	M 12-3	600	3	2	0.85	1.60			1.81	2.44		7.16	0.11
6	M 12-4	600	3	3	0.85	1.34			1.60	2.97	5.44	7.22	0.13
7	M 15-1	600	4	0	1.35	3.20			0.91	1.56	2.73	3.50	0.25
8	M 15-2	600	4	1	1.35	2.56			0.56	1.31	1.98	3.17	0.22
9	M 16-1	600	4	2	1.35	2.14				0.97		2.99	0.23
10	M 15-3	600	4	3	1.35	1.83			0.45	1.25	2.28	3.09	0.27
11	M 15-4	600	5	0	1.93	3.66			0.52	1.42	2.19	2.88	0.30
12	M 15-5	600	5	1	1.93	3.05			0.75	1.60	2.22	3.06	0.28
13	M 15-6	600	5	2	1.93	2.62			0.63	1.14	1.98	2.74	0.32

Appendix D-3 (Cont'd)

Wetting Rate as a Function of Oil/Gas Mass Flow Ratio and of Impaction Velocity (XRM-177F; Nozzle No. 3)

Item	Run No.	Temp. (°F)	Gas Flow Rate, cfm		Oil Flow Rate (gm/min)	Oil/Gas Mass Flow Ratio Q*x10³	Wetting Time, sec.						Wetting Rate (Fract. area covered/sec.)
			Generator	Diffuser			1/2"	3/4"	1"	1-1/2"	1-3/4"	2"	
14	M 6-2	700	3	0	0.85	2.67	1.17	2.02	3.10	4.63	5.62	7.06	0.19
15	M 9-2	700	3	1	0.85	2.00	0.95		2.02	3.78		7.78	0.11
16	M 9-3	700	3	2	0.85	1.60		1.37	1.47	2.80		7.50	0.10
17	M 9-4	700	3	3	0.85	1.34			3.01	4.85		7.42	0.17
18	M 10-1	700	4	0	1.35	3.20		0.88	1.84	2.17		4.25	0.25
19	M 10-2	700	4	1	1.35	2.56	0.72		2.06	3.14		4.62	0.23
20	M 10-3	700	4	2	1.35	2.14		1.02	2.39			5.35	0.22
21	M 14-1	700	4	3	1.35	1.83			0.59	1.48	2.00	3.02	0.27
22	M 14-4	700	5	0	1.93	3.66			0.42	1.15	2.04	2.64	0.33
23	M 14-2	700	5	1	1.93	3.05			0.50	0.72	1.61	2.61	0.30
24	M 14-3	700	5	2	1.93	2.62	0.22		0.34	1.26	2.09	3.02	0.28

Appendix D-4

Surface Velocity and Thickness of Thin Oil Films *

(Nozzle No. 1A)

Item	Plate Temp. (°F)	Gas Flow Rate (cfm)	Wetting Rate (Fract. area covered/sec.)	Specific Flow Rate (g/cm-sec.) x 10^4	Mean Surface Velocity (cm/sec.)	Oil Film Thickness (μm)
1	600	2	0.06	0.47	0.11	12.4
2	600	3	0.33	6.67	0.58	33.3
3	600	4	0.56	9.32	0.98	27.6
4	600	5	1.11	11.44	1.94	17.1
5	600	6	0.91	12.95	1.59	23.6
6	700	2	0.07	0.47	0.12	
7	700	3	0.60	6.67	1.05	
8	700	4	0.75	9.32	1.31	
9	700	5	0.90	11.44	1.57	
10	700	6	0.90	12.95	1.57	
11	800	2	0.13	0.47	0.23	
12	800	3	0.69	6.67	1.20	
13	800	4	0.83	9.32	1.45	
14	800	5	1.30	11.44	2.28	
15	800	6	1.06	12.95	1.85	

*Test conditions used: XRM-177F AND 1A nozzle

Appendix D-4

Surface Velocity and Thickness of Thin Oil Films *

Item	Plate Temp. (°F)	Gas Flow Rate (cfm)	Wetting Rate (Fract. area covered/sec.)	Specific Flow Rate (g/cm-sec.) x 10^4	Mean Surface Velocity (cm/sec.)	Oil Film Thickness (μm)
1	600	2	0.17	0.45	0.30	4.4
2	600	3	0.75	8.06	1.31	17.8
3	600	4	1.43	12.25	2.52	14.1
4	600	5	1.43	13.42	2.52	15.4
5	600	6	1.25	13.57	2.19	18.0
6	700	2	0.18	0.45	0.32	
7	700	3	0.67	8.06	1.17	
8	700	4	1.25	12.25	2.19	
9	700	5	1.00	13.42	1.75	
10	700	6	0.77	13.57	1.35	
11	800	2	0.16	0.45	0.28	
12	800	3	0.77	8.06	1.35	
13	800	4	1.25	12.25	2.19	
14	800	5	1.00	13.42	1.75	
15	800	6	1.00	13.57	1.75	

*Test conditions used: XRM-177F and 3A nozzle

D-5. Flow in the Oil Film

For a laminar film flow, the Navier-Stokes equation for two-dimensional flow may be used to relate the velocity distribution and the volumetric flow in the oil film to the drag of the gas at the interface.

$$\frac{\partial u}{\partial t} + u\frac{\partial u}{\partial x} + v\frac{\partial u}{\partial y} = -\frac{1}{\rho}\frac{\partial P}{\partial x} + \frac{\mu}{\rho}\frac{\partial^2 u}{\partial y^2} - \frac{\partial \Omega}{\partial x} \qquad (1)$$

For an oil film with a stable thickness under a steady-state flow condition

$$v = 0, \quad \frac{\partial u}{\partial x} = 0, \quad \frac{\partial u}{\partial t} = 0$$

Thus, Equation (1) becomes

$$\frac{1}{\rho}\frac{\partial P'}{\partial x} = \frac{\mu}{\rho}\frac{\partial^2 u}{\partial y^2} \qquad (2)$$

Where $P' = P + \rho\Omega$

If the boundary conditions

$$u = 0 \quad \text{at} \quad y = 0$$

$$\frac{\partial u}{\partial y} = \frac{\tau_i}{\mu} \quad \text{at} \quad y = \delta$$

are employed, Equation (2) may be integrated to give

$$u = \frac{1}{2\mu}\left(\frac{dP'}{dx}\right)(y^2 - 2y\delta) + \frac{\tau_i y}{\mu} \qquad (3)$$

By integrating Equation (3) over the film thickness, δ, the mean velocity is found to be

$$< \bar{u} > = \frac{1}{\delta} \int_0^{\delta} u(y)dy = - \frac{1}{3\mu}\left(\frac{dP'}{dx}\right) \delta^2 + \frac{\tau_i \delta}{2\mu} \quad (4)$$

the total specific flow rate is given by

$$\Gamma = \int_0^{\delta} \rho u(y)dy = - \frac{\rho}{2\mu} \left(\frac{dP'}{dx}\right) \delta^3 + \frac{\rho \tau_i \delta^2}{2\mu}$$

$$= \rho\delta < \bar{u} > \quad (5)$$

From Equation (5), the velocity distribution of oil film for various simplified cases with different boundary conditions, starting with one of the simplest possible case, which is closely related to this study.

Laminar Film Flow Motivated by Interfacial Shear

For a laminar film flow with an interfacial shear, the velocity of the film is given by taking $\frac{dP'}{dx} = 0$ in Equation (3)

$$u(y) = \frac{\tau_i y}{\mu} \quad (6)$$

and at the surface of the oil film, the velocity is

$$u(\delta) = \frac{\tau_i \delta}{\mu} \quad (7)$$

The total specific flow rate is given by

$$\Gamma = \int_0^{\delta} \rho u(y)\,dy = \frac{\rho \tau_i \delta^2}{2\mu} \qquad (8)$$

D-6. Stability Criterion

Consider a thin film of oil flowing uniformly over the isothermal surface of a flat plate, for example, the flow due to an interfacial shear applied from a high speed gas stream. If the flow rate of oil is reduced sufficiently (near to minimum wetting rate), the oil film will break away from the edges of the plate or else disrupt over the central area giving rise to one or more dry patches to develop streaky flow. An idealized case (no temperature, surface tension or viscosity gradients) is depicted in Figure 66. When a uniform stream of oil with a mean velocity of $< \bar{u} >$ flows on to the upper edge AB of a rectangular plate ABCD, and a dry patch FGHJ is formed centrally.

If the dry patch is stable, the surface tension forces along G_1 G_3 must balance the stagnation pressure of the oil film over G_1 G_3. Thus the point G will be in static equilibrium.

$$\sigma\ (1-\cos\theta) = \int_0^{\delta^*} \frac{\rho u^2(y)}{2}\,dy \qquad (9)$$

Now, if u(y) is defined for any given system, the critical film thickness, δ^*, at a minimum wetting rate can be easily estimated from Equation (9).

Applying Equation (9) to the case for a laminar film flow motivated by interfacial shear, we obtain for the minimum oil film thickness from the force criterion:

$$\delta^* = 1.82 \left[\{\sigma(1-\cos\theta)\} \left(\frac{\mu}{\tau_i}\right)^2 \right]^{1/3} \qquad (10)$$

and the minimum wetting rate is

$$\Gamma^* = 3.30 \left[\left(\frac{\rho\mu}{\tau_i}\right) \{\sigma(1-\cos\theta)\}^2 \right]^{1/3} \qquad (11)$$

Figure 66

DRY PATCH FORMATION ON THIN OIL FILM FLOWING OVER A SOLID SURFACE

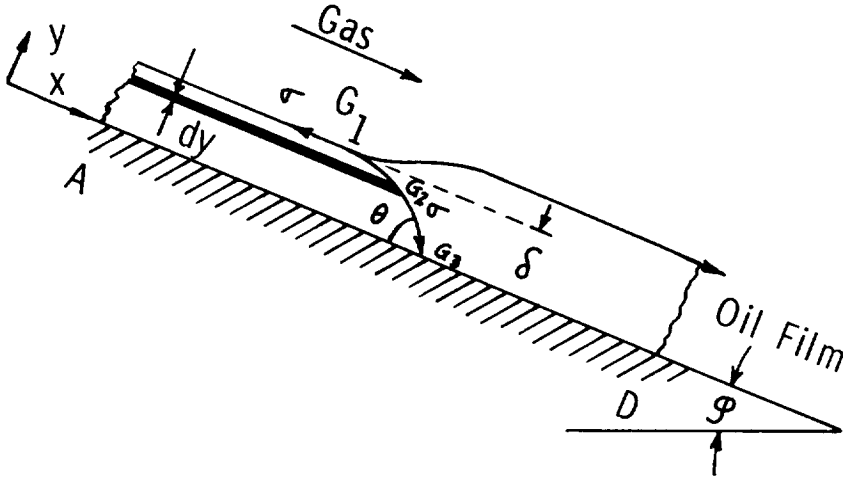

(a)

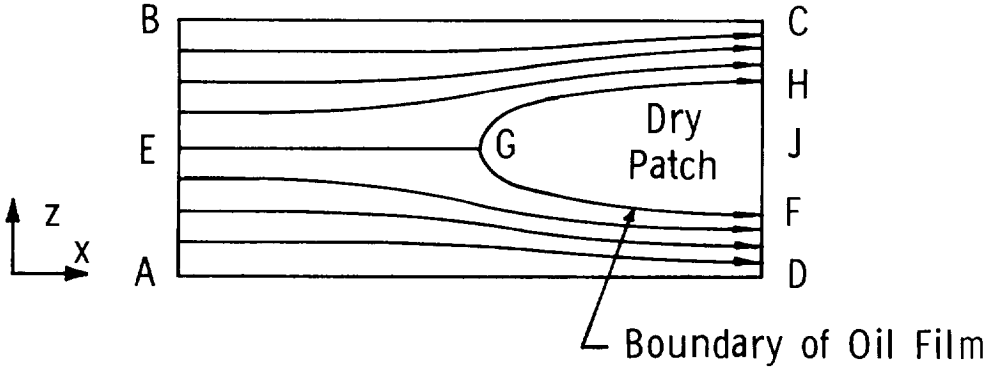

(b)

FINAL REPORT DISTRIBUTION LIST FOR CONTRACT NAS 3-9400

Addressee	Number of Copies
1. NASA-Lewis Research Center Aeronautics Procurement Section 21000 Brookpark Road Cleveland, Ohio 44135 Attention: John H. DeFord, MS 77-3	1
2. NASA-Lewis Research Center Technical Utilization Office 21000 Brookpark Road Cleveland, Ohio 44135 Attention: P. E. Foster, MS 3-19	1
3. NASA-Lewis Research Center Fluid System Components Division 21000 Brookpark Road Cleveland, Ohio 44135	
Attention: A. Ginsburg, MS 5-3	1
E. E. Bisson, MS 5-3	1
C. H. Voit, MS 5-3	1
R. L. Johnson, MS 23-2	1
W. R. Loomis, MS 23-2	3
M. A. Swikert, MS 23-2	1
W. J. Anderson, MS 23-2	1
E. V. Zaretsky, MS 6-1	1
D. P. Townsend, MS 6-1	1
4. FAA Headquarters 800 Independence Avenue, SW Washington, D. C. 20553	
Attention: General J. C. Maxwell	1
F. B. Howard	1
5. NASA Headquarters 600 Independence Avenue, SW Washington, D. C. 20546 Attention: N. F. Rekos (RAP)	1
6. NASA-Langley Research Center Langley Station Hampton, Virginia 23365 Attention: Mark R. Nichols	1
7. Air Force Aero Propulsion Laboratory Wright-Patterson AFB, Ohio 45433 Attention: APEL, J. L. Morris	1

Addressee	Number of Copies
8. NASA-Lewis Research Center Air-Breathing Engines Division 21000 Brookpark Road Cleveland, Ohio 44135 Attention: J. H. Childs, MS 60-4	1
9. Air Force Materials Laboratory Wright-Patterson AFB, Ohio 45433 Attention: MANL, R. Adamczak	1
10. Air Force Systems Engineering Group Wright-Patterson AFB, Ohio 45433 Attention: SEJDF, S. Prete	1
11. United Aircraft Corporation Pratt and Whitney Aircraft Division East Hartford, Connecticut Attention: R. P. Shevchenko P. Brown	1 1
12. General Electric Company Gas Turbine Division Evendale, Ohio Attention: B. Venable	1
13. NASA-Lewis Research Center 21000 Brookpark Road Cleveland, Ohio 44135 Attention: Library, MS 60-3 Fred Macks, MS 3-15	1 1
14. NASA-Lewis Research Center 21000 Brookpark Road Cleveland, Ohio 44135 Attention: Reports Control Office, MS 5-5	1
15. NASA-Scientific and Technical Information Facility P. O. Box 33' College Park, Maryland 20740 Attention: NASA Representative	6
16. Department of the Army U. S. Army Aviation Material Labs. Fort Eustis, Virginia 23604 Attention: J. W. White Propulsion Division	1

Addressee	Number of Copies
17. Avco Corporation Lycoming Division 550 Main Street Stratford, Connecticut Attention: Mr. Saboe	1
18. Allison Division General Motors Corporation Plant #8 Indianapolis, Indiana	1
19. Boeing Aircraft Company Aerospace Division Materials and Processing Section Seattle, Washington Attention: J. W. Van Wyk	1
20. Battelle Memorial Institute 505 King Avenue Columbus, Ohio Attention: C. Allen	1
21. Lockheed Aircraft Corporation Lockheed Missile and Space Co. Material Science Laboratory 3251 Hanover Street Palo Alto, California Attention: Francis J. Clauss	1
22. North American Rockwell Corporation Los Angeles Division, International Airport Los Angeles, California 90209 Attention: Frank J. Williams	1
23. EPPI Precision Products Company 227 Burlington Avenue Clarendon Hills, Illinois 60514 Attention: C. Dean	1
24. Midwest Research Institute 425 Volker Boulevard Kansas City 10, Missouri Attention: V. Hopkins & A. D. St. John	1
25. McDonnell-Douglas Aircraft Company 3000 Ocean Park Boulevard Santa Monica, California Attention: Robert McCord	1
26. The Marlin-Rockwell Corporation Jamestown, New York Attention: Arthur S. Irwin	1

Addressee	Number of Copies
27. Chicago Rawhide Manufacturing Co. 1311 Elston Avenue Chicago, Illinois Attention: Richard Blair	1
28. IIT Research Institute 10 West 35th Street Chicago, Illinois 60616 Attention: Waren Jamison	1
29. E. I. duPont de Nemours and Co. Petroleum Chemicals Division Wilmington, Delaware 19898 Attention: Neal Lawson	1
30. Sinclair Research, Inc. 400 E. Sibley Boulevard Harvey, Illinois Attention: M. R. Fairlie, Director of Products Division	1
31. Fairchild Hiller Corporation Republic Aviation Division Space Systems and Research Farmingdale, Long Island, New York 11735 Attention: R. Schroeder	1
32. Hercules Powder Company, Inc. 900 Market Street Wilmington, Delaware Attention: R. G. Albern	1
33. AiResearch Manufacturing Company Department 93-3 9851 Sepulveda Blvd. Los Angeles, California 90009 Attention: Hans J. Poulsen	1
34. General Electric Company Silicone Products Department Waterford, New York 12188 Attention: J. C. Frewlin	1
35. Curtiss-Wright Corporation Wright Aeronautical Division 333 West 1st Street Dayton, 2 Ohio Attention: S. Lombardo	1

Addressee	Number of Copies
36. Bray Oil Company 1925 North Marianne Avenue Los Angeles, California 80032 Attention: Martin Fainman	1
37. Stauffer Chemical Company 299 Park Avenue New York, New York 10017 Attention: T. M. Downer, Jr.	1
38. Shell Development Company Emeryville, California Attention: Dr. C. L. Mahoney	1
39. Gulf Research and Development Company P. O. Drawer 2038 Pittsburgh 30, Pennsylvania Attention: Dr. H. A. Ambrose	1
40. California Research Corporation Richmond, California Attention: Neil Furby	1
41. Dow Chemical Company Abbott Road Buildings Midland, Michigan Attention: Dr. R. Gunderson	1
42. Pennsylvania Refining Company Butler, Pennsylvania	1
43. Kendall Refining Company Bradford, Pennsylvania Attention: F. I. I. Lawrence	1
44. Aerojet-General Corporation 20545 Center Ridge Road Cleveland, Ohio Attention: D. B. Rake	1
45. Pennsylvania State University Dept. of Chemical Engineering University Park, Pennsylvania 19406 Attention: Dr. E. E. Klaus	1
46. Rocketdyne Division of North American Aviation Canoga Park, California Attention: Library	1

Addressee	Number of Copies
47. Southwest Research Institute San Antonio, Texas 78205 Attention: P. M. Ku	1
48. Stewart-Warner Corporation 1826 Diversey Parkway Chicago, Illinois 60614	1
49. Westinghouse Electric Corporation Research Laboratories Beulah Road, Churchill Borough Pittsburgh, Pennsylvania 15235 Attention: J. Boyd S. M. DeCorso	1 1
50. Texaco, Incorporated P. O. Box 509 Beacon, New York Attention: Dr. G. B. Arnold	1
51. Olin Mathieson Chemical Corporation Organics Division 275 Winchester Avenue New Haven 4, Connecticut Attention: Dr. C. W. McMullen	1
52. Heyden Newport Chemical Corp. Heyden Chemical Division 290 River Drive Garfield, New Jersey Attention: D. X. Klein	1
53. C. A. Norgren Company Englewood, Colorado Attention: D. G. Faust	1
54. Crucible Steel Company of America The Oliver Building Mellon Square Pittsburgh 22, Pennsylvania	1
55. Dow Corning Corporation Midland, Michigan Attention: R. W. Awe & H. M. Schiefer	1
56. Mechanical Technology, Inc. Latham, New York Attention: S. F. Murray & M. B. Peterson	1

Addressee	Number of Copies
57. U. S. Naval Air Material Center Aeronautical Engine Laboratory Philadelphia, Pennsylvania 15212 Attention: Engine Lubrication Branch A. L. Lockwood	1
58. U. S. Naval Research Laboratory Washington, D. C. 20390 Attention: Charles Murphy	1
59. Department of the Navy Washington, D. C. Attention: Bureau of Naval Weapons A. B. Nehman, RAAE-3	1
C. C. Singleterry, RAPP-44	1
Bureau of Ships Harry King, 634A	1
60. U. S. Army Ordnance Rock Island Arsenal Laboratory Rock Island, Illinois 61201 Attention: R. LeMar	1
61. Industrial Tectonics, Inc. Research and Development Division 18301 Santa Fe Avenue Compton, California Attention: Heinz Hanau	1
62. Alcor Incorporated 2905 Bandera Road San Antonia, Texas Attention: Mr. L. Hundere	1
63. Monsanto Chemical Company 800 North Lindbergh Boulevard St. Lowis, Missouri 63166 Attention: Ken McHugh	1
64. Monsanto Research Corporation Everett Station Boston 49, Massachusetts Attention: Dr. John O. Smith	1
65. The Koppers Company, Inc. Metal Products Division Piston Ring and Seal Dept. 7709 Scott Street Baltimore, Maryland 21203 Attention: T. C. Kuchler	1

Addressee	Number of Copies
66. Sinclair Refining Company 600 5th Avenue New York 20, New York Attention: C. W. McAllister, Mgr. Aviation Sales & Tech.	1
67. Union Carbide Chemicals Company Division of Union Carbide Corporation Tarrytown, New York Attention: W. M. Millett	1
68. Sun Oil Company Automotive Laboratory Marcus Hook, Pennsylvania Attention: J. Q. Griffith	1
69. Rohm and Haas Company Washington Square Philadelphia, 5 Pennsylvania Attention: V. Ware & P. M. Carstensen	1
70. Crane Packing Company 6400 W. Oakton Street Morton Grove, Illinois	1
71. Stein Seal Company 20th and Indiana Avenue Philadelphia, Pennsylvania 19132	1
72. Sealol Company 100 Post Road Providence, Rhode Island	1
73. Fafnir Bearing Company 37 Booth Street New Britain, Connecticut Attention: Mr. H. B. VanDorn	1
74. General Electric Company General Engineering Laboratory Schenectady, New York	1
75. Fairchild Engine and Airplane Corporation Stratos Division Bay Shore, New York	1
76. Borg-Warner Corporation Roy C. Ingersoll Research Center Wolf and Algonquin Roads Des Plaines, Illinois	1

Addressee	Number of Copies
77. General Motors Corporation New Departure Division Bristol, Connecticut Attention: W. O'Rourke	1
78. Eaton Yale and Towne, Inc. Farval Division 3249 East 80th Street Cleveland, Ohio 44104 Attention: E. J. Gesdorf	1
79. Esso Research and Engineering Company P. O. Box 8 Linden, New Jersey Attention: Jim Moise Director, Government Research Lab.	1 1
80. Sun Oil Company Research and Development Marcus Hook, Pennsylvania 19061 Attention: G. H. Hommer	1
81. Eaton, Yale and Towne, Inc. Research Center 26201 Northwestern Highway Southfield, Michigan 48075 Attention: H. M. Reigner W. Mannhardt	1 1
82. SKF Industries, Inc. Engineering and Research Center 1100 First Avenue King of Prussia, Pennsylvania 19406 Attention: L. B. Sibley H. Mahncke	1 1
83. Chevron Research Company 576 Standard Avenue Richmond, California 94804 Attention: Douglas Godfrey	1